University of Liège
Faculty of Applied Science

Discrete Element Method Modeling of Ball Mills
-
Liner Wear Evolution

by

Dominik BOEMER

Submitted to the Department of Mechanical Engineering
on June 4th, 2015, in partial fulfillment
of the requirements for the degree of

Master of Mechanical Engineering

Jury		
Prof. Dr. Ir. Jean-Philippe PONTHOT	University of Liège	Academic supervisor
Ir. Serge RYCERSKI	Magotteaux International S.A.	Industrial supervisor
Prof. Dr. Ir. Pierre DUYSINX	University of Liège	President
Prof. Dr. Ir. Maarten ARNST	University of Liège	Member
Dr. Ir. Romain BOMAN	University of Liège	Member
Prof. Dr. Ir. Eric PIRARD	University of Liège	Member

2014 - 2015

Discrete Element Method Modeling of Ball Mills Liner Wear Evolution

by
Dominik BOEMER

Submitted to the Department of Mechanical Engineering
on June 4th, 2015, in partial fulfillment
of the requirements for the degree of
Master of Mechanical Engineering

Abstract

Ball mills, i.e. rotating cylindrical drums filled with a feed material and metal balls, also known as the charge, are a major category of grinding devices in mineral processing and cement production. Since the grinding process is excessively energy-intensive and aggressive in terms of wear, a profiled and wear-resistant liner is installed in the mill to transfer energy to the grinding charge more efficiently and to protect the mill shell. Because of the harsh environment inside of the mill and the relatively long lifespan of its liner, the optimization of the liner by the classical way, i.e. experimental testing, is a difficult and slow process.

In this thesis, a procedure for predicting the charge motion and the power draw of a ball mill based on the discrete element method (DEM) is calibrated and validated by means of photographs of the charge, and power draw measurements of a 1:5-scale laboratory mill, which were kindly provided by the company Magotteaux International S.A. . This computational method essentially renders future experimental testing unnecessary with respect to these characteristics.

Based on this first method, a generic process for predicting the wear distribution and the progressive shape evolution of liner surfaces is developed and validated by the wear profiles of the shell liner in the first chamber of a 5.8 m diameter cement mill monitored during a decade by Magotteaux International S.A. . The energy dissipated by tangential damping defined by the linear spring-slider-damper DEM contact law was found to be the best fitting wear model with respect to the real wear data. The progressive update of the liner geometry by a multi-step procedure delivers relatively accurate results for liners without axial height variation while further investigations are still required for almost fully variable geometries. Nevertheless, detailed phenomena, like the creation of grooves in the liner, were for the first time numerically modeled in this thesis.

Keywords: ball mill, discrete element method, liner wear

Academic supervisor: Prof. Dr. Ir. Jean-Philippe PONTHOT, University of Liège
Industrial supervisor: Ir. Serge RYCERSKI, Magotteaux International S.A.

Acknowledgments

I am deeply grateful to have met a number of people, who contributed more to this thesis than they might sometimes expect, during the past four months.

First, I would like to thank the academic members of the jury for their time and interest in my work. I am especially grateful to my supervisor Jean-Philippe Ponthot for the exact right amount of guidance, with enough freedom to explore any aspect of the problem but also his immediate availability when questions arose. Moreover, I thank Pierre Duysinx for his enthusiastic encouragements during my studies, Maarten Arnst and Romain Boman for our interesting discussions, which went far beyond the scope of the thesis, and Eric Pirard for being the precious link between the Geological and Mechanical Engineering Departments. Furthermore, I would like to thank the Non Linear Computational Mechanics (LTAS/MN2L) research group and Stoyan Gaydardzhiev for their curiosity and helpful advice.

I also enjoyed working at Magotteaux, partially because of my work, but even more because of my colleagues. First and foremost, I would like to thank my industrial supervisor Serge Rycerski for his efforts to make my internship as instructive as possible but also for his friendship. In addition, I wish to thank Jean Vis for teaching me that people, who are yelling at me, can also be quite likable, as well as Marc Kassé, Xavier Prignon, François Lepoint and Frédéric Oger for providing me with valuable experimental data and their curiosity, which was a great motivation. I would also like to thank Gilles Recoules for his confidence in my passion for solving problems and René Schleiss without whom I would never have met these people. Finally, my other fellow colleagues shall not be forgotten; thank you for being one of the reasons why I am always looking forward to coming to work.

Besides my professors at the University of Liège and my colleagues at Magotteaux, I wish to thank Mark Sawley, CEO of Granulair Technologies and professor at the EPFL, for sharing his long-lasting experience in DEM simulations with me. Furthermore, I would like to thank the YADE community and especially Anton Gladky, Bruno Chareyre, Jan Stránský, Raphaël Maurin, François Kneib and Jérôme Duriez for keeping this project alive and for kindly answering my questions about the software.

Last but not least, I would like to express my deepest gratitude to my family, especially my parents, who have always encouraged and motivated me in an extraordinary way during my studies and my whole life.

Contents

Introduction

In the following lines, the general introduction of the research in the framework of this thesis is presented. The research *context* is discussed in the first section. The *objectives* and the *structure* of this document are described in the two following sections. Finally, the last section gives an *overview of the new contributions* to the fields of DEM ball mill modeling and liner wear prediction.

Context

Comminution or particle size reduction is an essential component of mineral processing or cement production. *Grinding* is the final stage of comminution consisting in breaking small particles into much smaller ones in order to enhance their chemical and physical properties. A major category of grinding devices are *tumbling mills*, i.e. rotating cylindrical drums filled with a feed material and the grinding media. In particular, *ball mills* are tumbling mills whose grinding media are metal balls.

The overall *objectives of grinding* are to maximize the mill throughput with the required reduction ratio while minimizing the operating costs. Grinding is, however, not only excessively energy-intensive, but also highly aggressive in terms of wear. A profiled, replaceable and abrasion-resistant liner is therefore installed to *transfer energy to the grinding charge more efficiently* and to *protect the mill shell* at the same time. Hence, the operational performance of the mill depends not only on the operating conditions, i.e. mainly the rotation speed and the filling ratio, but also on the liner itself. For this reason, the slightest improvement of the *liner design* becomes a significant competitive advantage.

In general, the liner design depends on its *material* and its *initial shape*. Due to the collisions between the balls, the ore and the liner, its surface material is progressively worn away and its shape changes. Consequently, it might be expected that less energy is transferred to the charge and that the particle flow pattern adapts to this change by reducing the mill throughput. Moreover, the liner also looses little by little its protective capability because of the increasing material loss due to wear after several ten thousand hours. Developing a liner with a uniform wear distribution and globally low wear rates thus saves the cost of frequent relining and more importantly avoids production losses during the mill downtime. Accordingly, the liner design

should not only depend on the initial shape of the liner but also on its *change in geometry due to wear* over time.

Because of the harsh internal mill environment and the relatively long lifespan of the liner, the optimization of the liner design by the classical way, i.e. experimental testing, is a difficult and slow process. This is why, *computational engineering* becomes more and more popular as an alternative way to solve this problem. In particular, the recent advances in computing hardware rendered it possible to simulate the motion of the balls in a mill by the *discrete element method* (DEM) on almost every personal computer in a decent amount of time. The objectives, which we will try to achieve by means of this method, are explained in the next section.

Notice that this thesis was written during an internship at the company Magotteaux International S.A., the leading global provider of high performance wear resistant products to industries where crushing, grinding, and other comminution processes are an essential step in the value chain. The connection between the research and its application is therefore more direct and the numerical results will be calibrated and validated by detailed experimental data of shell liner plates in the first compartment of clinker grinding cement tube mills[1].

Objectives

This thesis has essentially two *objectives*, which consist in developing a method to predict:

- the *charge motion* and the *power draw* of a ball mill;
- the *wear distribution* and the *wear evolution*, i.e. the shape modification, of the shell liner in a ball mill as a function of time and the operating conditions.

Structure

This thesis is divided into three chapters:

- Chapter 1: in the first chapter, the general *theoretical background* of the models, which are used in the following chapters, is explained by means of an extensive literature review. First, the *ball mill* and its mode of operation are described. Then, the most promising charge motion model, i.e. the *discrete element method*, is defined. In the third section, the most popular *wear models* are introduced. In the last section of this chapter, the ball mill, the discrete element method and the wear models are combined to clarify the underlying principles and the current state of the art in the *wear modeling of ball mill liners*.

[1] As will be explained in the first chapter, tube mills are balls mills with a length to diameter ratio between 3 and 5.

- Chapter 2: the aim of the second chapter is to explain and to assess the solution to the first objective of the thesis, i.e. the *DEM ball mill simulation*. First, the *experimental data* (charge photographs and power measurements), which was recorded in a 1:5-scale laboratory mill, is introduced to calibrate and validate the DEM model. Then, we select the *DEM software*, which is used to predict the charge motion and the power draw of the laboratory mill. On the basis of the *DEM model* defined in the third section, the *numerical results* are analyzed in the forth section in order to assess the capability of the discrete element method to predict the charge motion and the power draw of the ball mill.

- Chapter 3: in the last chapter, a general procedure to predict the wear distribution and the change in geometry of liner surfaces due to wear by the interaction with granular materials is presented. In this thesis, the emphasis is put on the *liner wear simulation* of an industrial ball mill but it was tried to keep the algorithm as general as possible in order to apply it to other comminution devices in the future. In a similar way to the second chapter, the *experimental data* (wear profiles) is described in the first section of this chapter. Then, the *charge motion simulation* model is defined in order to sample the numerical wear data. In the last section, the *wear simulation* as such is explained. In particular, the best fitting wear model and its wear constant are determined on the basis of the experimental data. By means of the resulting wear distribution, a multi-step method is then introduced to predict the progressive change in the geometry of the liner.

The different appendices are referenced in the text, except for the appendix E. This appendix gives some guidelines about how the simulation data of this project can be used in future projects by means of the CD, which was distributed with this document.

Original contributions

Some *new contributions*[2] to the fields of DEM ball mill modeling and liner wear prediction in this document are briefly mentioned and referenced in order to simplify the search for new information by readers, who are already very familiar with these topics:

- introduction of a *position density limit* on the basis of the position density plot in order to compare more easily the global charge motion in the pseudo steady state of mills with different operating conditions and different liner profiles (section 2.3.4);

- calculation of the *power components* of the linear spring-slider-damper contact law, i.e. the normal, tangential and sliding power, in order to show by which idealized mechanism the power in a ball mill is mainly dissipated (sections 2.3.1 and 2.4.2);

[2] Saying that these contributions are *new* might be an exaggeration. Nevertheless, we did not find them explicitly in the articles, books and websites mentioned in the bibliography, and we therefore believe that they might be interesting to specialists in these fields.

- detailed study of the *influence of the contact parameters* (of the linear spring-slider-damper contact law, e.g. the normal stiffness, the tangential coefficient of restitution, ...) on the global charge motion and the power draw of the mill (section 2.4.2);
- explicit *superposition of the DEM results and the photographs* of the real charge motion in order to prove their agreement from this point of view (section 2.4.2);
- position density plots showing the charge distribution from the top of the mill and illustrating the creation of a *structured ball motion* in the presence of an axial obstruction like end walls without tangential interaction (section 3.3.2);
- determination of the *best fitting wear model and its wear constant* a posteriori by the correlation of the real wear data and several numerical data sets corresponding to six different wear models (section 3.3.4). A similar approach was, however, already introduced in [Cleary et al., 2009];
- creation of *grooves* in the liner plate by the numerical model leading to the conclusion that a *liner design with grooves similar to the real grooves might increase the lifespan of the liner* (section 3.3.7).

Chapter 1

Theoretical Background

In this chapter, the theoretical background of ball mill liner wear modeling will be summarized by explaining the three main components of this method: the *ball mill*, the *discrete element method* (DEM) and the *wear modeling*. In the forth section, these elements will be combined to outline the *current state of the art* in ball mill liner wear modeling.

1.1 Ball Mills

To design a model which accurately simulates the ball mill liner wear, it is essential to understand what a ball mill is. In this section, we will therefore show the place of ball mills in the general context of comminution, describe its structure, analyze its mode of operation and introduce the characteristic parameters used in practice to specify its operating conditions.

1.1.1 Comminution

Particle size reduction, also known as *comminution*, is an essential component of *mineral processing* and the *cement production*. It usually starts with the removal of rocks from their natural beds by explosives. The *blasting* of the rock is then followed by the crushing of rather massive fragments.

Crushing is accomplished by direct compression or impact of the ore (or the limestone in the case of the cement production) against sufficiently rigid surfaces in primary and secondary crushers. Heavy-duty *primary crushers*, like jaw and gyratory crushers, reduce the ore to a size appropriate for transport and for feeding to secondary crushers. *Secondary crushers*, like cone crushers and hammer mills, further reduce the rocks to a size suitable for grinding[1].

[1]Detailed explanations of the different steps, crusher types and differences between the mineral processing procedure and the cement production are deliberately not provided here as the purpose of this section is to determine the place of the ball mill in the field of comminution from a bird's eye perspective. Further information can, however,

Grinding is finally the last stage of comminution. The ore particles are ground mainly by abrasion and impact from around 5 - 250 mm to 40 - 300 μm. This relatively high reduction ratio[2] in comparison to primary and secondary crushing (reduction ratio from three to six in each stage) is necessary to increase the ratio of the surface area to the volume of the ore, which enhances its physical and chemical properties. In consequence, grinding is the most energy-intensive comminution operation in mineral processing or the cement production. For instance, around 110 kWh of electrical energy are consumed per ton of cement produced. 70% of this energy are needed to grind the raw material and the clicker [Kawatra, 2006]. This is why, even the slightest improvement in terms of energy efficiency can lead to a considerable economic impact. Grinding can be performed by tumbling and stirred mills, high pressure grinding rolls (HPGR), vertical roller mills (VRM) and some other machines. Here we will focus only on tumbling mills to eventually locate the position of ball mills in the field of comminution.

Roughly speaking, *tumbling mills* are cylindrical drums closed by flat or conical end walls. These drums are filled with the *mill charge*, or simply the charge[3], i.e. the feed material and the grinding media. The *grinding media* are hard and heavy grinding bodies, like metal balls or rods. Because of the tumbling mill's rotation around the horizontal axis of the drum, the charge is lifted up by friction against its walls and the loosely moving grinding media take part in the comminution of the feed material. Depending the grinding media, different tumbling mill types can be distinguished, like rod mills, ball mills, autogenous mills (AG mills, the ore is the grinding medium) and semi-autogenous mills (SAG mills, steel balls are used in addition to the feed material).

1.1.2 Structure of a ball mill

As mentioned earlier, *ball mills* are tumbling mills whose grinding media are metal balls with typical diameters from 10 to 150 mm, thus weighting 1 g to over 4 kg. On average, ball mills have a 4 m diameter and consume around 5 to 10 MW of power (figure 1.1). Their length to diameter ratio varies between 1 and 1.5. Longer ball mills with a length to diameter ratio between 3 and 5 are called *tube mills* (figure 1.2).

The cylindrical drum of the ball mill is called the *mill shell*. The mill shell commonly rotates at constant speed around its horizontal axis by being supported on oil-lubricated or roller-type bearings at its ends. In tube mills, the cylindrical drum is sometimes divided into several compartments with decreasing bulk material size; for instance, this is the case for clinker grinding in the cement industry [Cleary, 2009] (figure 1.3).

Because of the very aggressive impacting and abrasion environment inside of the mill, it is *protected* by liners (figure 1.4). *Liners* are very wear-resistant, replaceable metal or rubber

be found in [Wills & Napier-Munn, 2005] or [Kawatra, 2006].

[2]The reduction ratio can be defined as the ratio of the maximum particle size entering and the maximum particle size leaving the crusher or grinding machine.

[3]The mill charge, or charge, has not to be mistaken with the ball charge. The ball charge are the balls without the feed material, as explained later on.

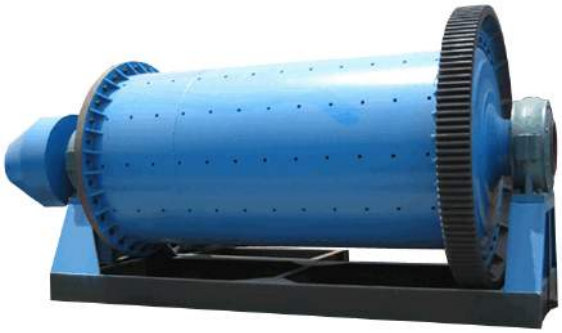

Figure 1.1: Ball mill [Longding, 2015] (adapted).

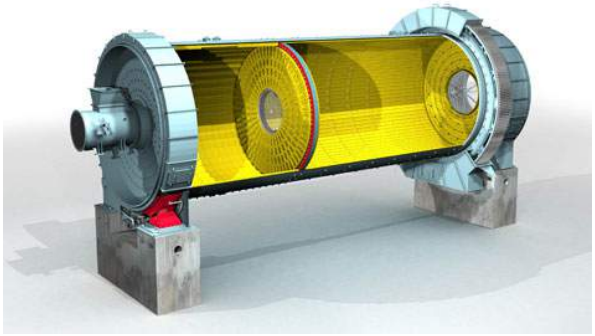

Figure 1.2: Cross-section of a tube mill with two chambers [FLSmidth, 2015].

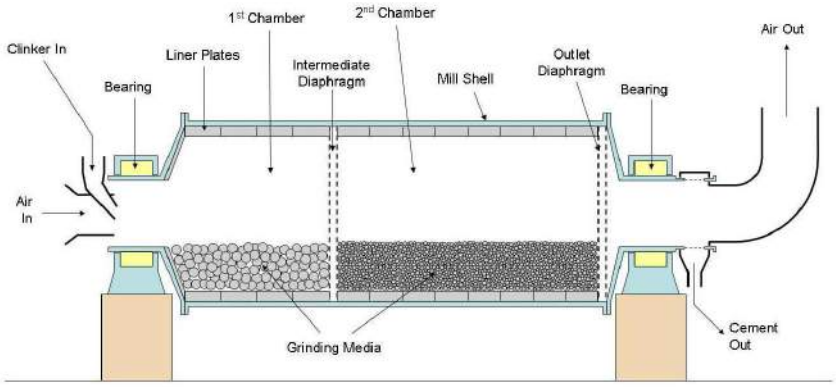

Figure 1.3: Two chamber clinker grinding cement tube mill [Wikipedia, 2015].

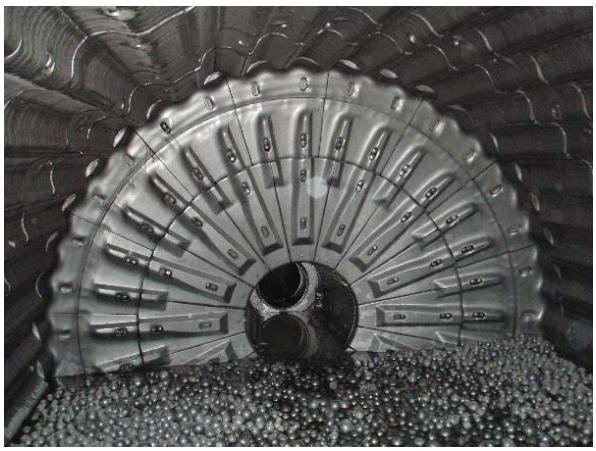

Figure 1.4: Head liner, shell liner and balls inside of a ball mill [Magotteaux S.A., 2015].

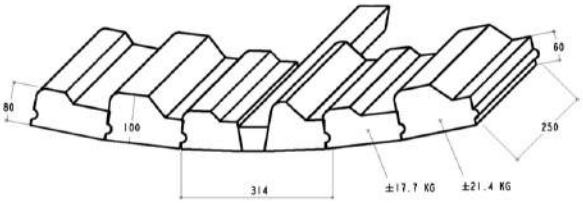

Figure 1.5: Part of a boltless liner row with its principal dimensions. In particular, this figures shows the *keystone* of the vaulted liner, which is the only liner plate bolted to the mill shell. Length dimensions in mm [Magotteaux S.A., 2015].

working faces attached to the inside of the mill. Liners can be divided into two categories[4]: head liners and shell liners. *Head liners* can be conical or flat liners which protect the head, i.e. the lateral end walls of the cylindrical mill. *Shell liners* take the form of arched plates attached to the mill shell either by bolts, by vault effect (boltless lining), i.e. the wedge-shaped liner plates interlock themselves similar to the stones of a masonry arch, or by direct bonding to the inner surface in case of rubber linings. As shown in the figure 1.5, the liner plates are assembled along the circumference of the mill to build ring-like structures, called *rows*. Several rows put together along the axial direction, then form the entire shell liner.

Liner plates are usually made from chromium, manganese, molybdenum and nickel alloys. These alloys have the advantage to be relatively hard and abrasion-resistant but more and more brittle with increasing hardness. Their counterpart are therefore rubber liners, which are particularly well adapted to normal impacts because of their high elasticity, i.e. they deform easily and resume their shape, when the forces are removed. Rubber/steel composites also exist as well as more sophisticated magnetic liners protected by thick rubber layers which are themselves protected by the attracted mill charge [Powell et al., 2006]. In this work, we will, however, only focus on *metallic shell liners*.

Besides the protection of the mill shell, the liner's second primary function is the *energy transfer* to the charge from the rotary motion of the mill, which ultimately leads to the grinding of the feed material. To promote the most favorable motion of the charge, liners have different *profiles* (figure 1.6), which should enhance the size reduction by adding impact crushing and higher abrasion efficiency to the comminution process through its lifting action. *Lifting* literally

[4]It is possible add a third category, i.e. *classifying liners*, which are usually installed in the second chamber of cement tube mills. This liner category will, however, not be analyzed in this thesis.

consists in moving the charge to a higher position in the mill by the combination of centrifugal and friction forces. Ultimately, the charge falls down under the action of gravity and impacts itself, thus increasing the grinding rate. The characteristic part of the liner profile, which enhances the lifting of the charge, is simply called a *lifter*[5].

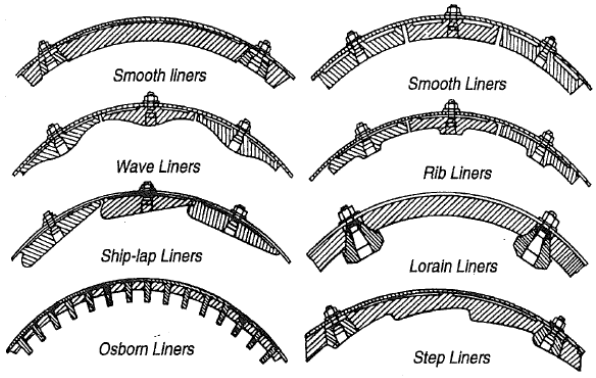

Figure 1.6: Different liner profiles [Wills & Napier-Munn, 2005].

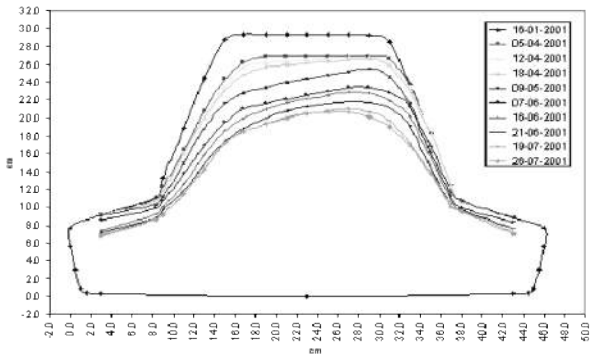

Figure 1.7: Wear profile of a lifter in a 7 m diameter SAG mill [Powell et al., 2006].

With increasing wear of the liner, it gradually looses its lifting capacity (figure 1.7). This is also the reason why some tumbling mills are equipped with removable lifters attached to the liner plates since they have to be exchanged more often due to their high exposure to abrasion. A typical liner lifespan in the first compartment of a cement tube mill is around 5 to 10 years.

In addition to the minimal liner thickness for the protection of the mill shell, the *preservation of the liner profile* is therefore a fundamental requirement for a long liner life. Moreover, relining represents a major *cost* in the operation of a mill not only because of its manufacturing and material cost but also because of the limited throughput of the plant and the employment of additional staff during the relining. For these reasons, liner profile validation and optimization in terms of wear are necessary steps during the liner design.

1.1.3 Charge motion

The figure 1.8 shows the ball charge motion[6], its different zones and characteristic positions. The charge is lifted by the rising side of the liner profile due to the combined action of rotation and friction. Once gravity exceed the resultant of the centrifugal and friction forces, the charge either cascades or cataracts down the free surface formed by the other particles. More precisely, at lower rotation speeds, the charge *cascades* down, i.e. the balls roll down, and at higher speeds,

[5] In practice, lifters are replaceable parts of a liner, which are attached to a liner plate. The previous definition is therefore a little more general since a wave of the liner plate, which enhances the lifting of the charge, would also be considered to be a lifter.

[6] In addition to the balls and the feed material, balls mills might also contain a slurry, when grinding is performed *wet*. In this work, we will, however, focus only on dry ball milling or at least, neglect this effect.

the balls fly down until colliding with the balls and feed material in the impact zone. This *cataracting* motion leads to comminution by impact, while cascading balls rather reduce the material size by abrasion.

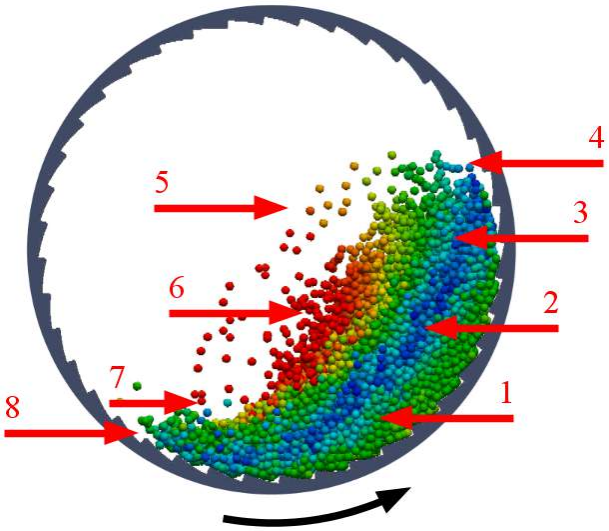

Figure 1.8: Ball charge motion in a ball mill. The straight arrows point to the centers of different characteristic zones and positions: 1. Grinding zone; 2. Dead zone (in blue); 3. Tumbling zone; 4. Shoulder; 5. Cataracting charge in the flight zone; 6. Cascading charge; 7. Crushing/Impact zone; 8. Toe. The curved arrow shows the orientation of the rotation. The color code indicates the translation velocity: blue is slow and red is fast.

The position at which the highest point is reached by the charge is called the *shoulder*. For a low rotation speed, this position is clearly defined, while it becomes more difficult to identify for the cataracting charge motion at higher speeds. For this reason, [Cleary et al., 2003] defines a lower and an upper limit of the shoulder position. These limits are respectively located at the points where the particles near the liner begin to diverge from it and where the charge reaches its highest position. The counterpart of the shoulder is the *toe*. It is the position down to which the bodies cascade or cataract from the shoulder. Its lower limit is situated at the intersection of the charge free surface and the mill liner, while its upper limit can be defined at the position below which the largest concentration of cataracting particles have impacted on the liner[7]. Usually the shoulder and the toe are specified by the shoulder and toe *angles*, θ_s and θ_t, which will be defined with respect to the 6 o'clock position, by convention, positive in both directions. It seems not necessary to mention that these parameters are quite subjective despite the definition of a lower and an upper limit[8].

[7]Here, we interchanged the definitions of the lower and upper limit provided in [Cleary et al., 2003], because they depend on the definition of the toe angle.

[8]In cases, in which a strict numerical values is not needed, we will therefore try to superpose the simulated or photographed charge shapes in order to validate the numerical results instead of measuring and comparing these angles.

Five zones represented in the figure 1.8 can be defined according to [Radziszewski & Morrell, 1998]:

- *grinding* zone: ball layers slide over another, grinding the material trapped between them.
- *dead* zone: balls are practically without motion in this zone, i.e. grinding is locally very low.
- *tumbling* zone: balls roll over one another and break material in relatively low energy breakage compared to the breakage in the grinding zone.
- *flight* zone: balls fly along a parabolic path under the action of gravity.
- *crushing/impact* zone: balls in flight impact the charge and crush rock particles at relatively high energies.

Theses zones are obviously not clearly separated; their definition is only used to qualitatively separate the different zones in the mill and to ease the description of the mill charge motion. In terms of liner wear, it is very important to notice that the *lower toe limit is not always located in the impact region*. At high rotation speeds, for a low filling of the mill or poorly designed liner profiles, the mill charge, and most importantly the cataracting balls, might impact the liner directly, which ultimately leads to greatly accelerated liner wear. In addition, the milling efficiency might also decrease because the collisions with the highest impact energy occur against the liner instead of on the toe.

1.1.4 Characteristic parameters

In practice, the mill operation can be described by two values: the percentage of critical speed and the filling ratio.

Percentage of critical speed The *percentage of critical speed* quantifies the constant rotation speed of a ball mill, which is usually equal to 75% in clinker grinding tube mills. This percentage is defined by the ratio of the current speed to the critical speed. The *critical speed* is the speed of the mill for which its charge would be centrifuged. Thus, the critical speed is reached when the centrifugal force equals the force exerted by gravity on a ball:

$$m\,v^2/R = m\,g \tag{1.1}$$

where the linear velocity v of a ball of mass m can be written as a function of the rotation speed N of the mill in [rpm] and the radius to the center of rotation $R = (D-d)/2$ with D and d being respectively the diameter of the mill and the diameter of the ball:

$$v = \frac{2\,\pi\,N\,R}{60} \tag{1.2}$$

As mentioned earlier, the ball diameter is negligible in comparison to the mill diameter. For this reason, the critical speed N_c is commonly defined by the following formula:

$$N_c = \frac{42.3}{\sqrt{D}} \text{ [rpm]} \tag{1.3}$$

Filling ratio In addition to the percentage of critical speed, the mill operation is characterized by the filling ratio (related to the balls), if no complete *ball charge distribution* is available. The ball charge distribution is based on the partitioning of the ball charge into groups according to their diameter. Each group is defined by an interval of diameters, which allows to calculate the mean diameter. Knowing the ball material density and the mass of each ball group, it is possible to deduce a number of balls for each mean diameter. It is important to notice that, even though the balls are also ground, i.e. their form is altered and their radius reduced, their size distribution is kept uniform by continuously adding new balls. Thus, the *ball size distribution in the mill seems not to change over time*.

If this relatively precise information is not known, the filling ratio can be used to determine the quantity of balls in the mill. The *filling ratio* is the percentage of volume occupied by the balls (and their interstices, without the feed material) with respect to the total volume of the mill. The total volume of the mill can be calculated by means of the mean diameter of the liner profile and the mill length. In the first chamber of a clinker grinding tube mill, the filling ratio commonly takes a value between 20 and 40%.

1.2 Discrete Element Method

To predict the liner shape evolution due to wear, it is essential to understand and to quantify the motion of the mill charge and its resulting interaction with the mill liner. The most promising method in this field is the *discrete element method* (DEM). For this reason, we will first describe the method in general and then focus on its application in the field of ball mill modeling.

1.2.1 General description

The *discrete element method* (DEM), originally termed the distinct element method, is a numerical method used to simulate the kinematic and dynamic behavior of granular materials. The method was first formulated in [Cundall, 1971] for the analysis of rock movement mechanics. The initial formulation was based on the definition of circular bodies interacting according to a contact law. Later, more sophisticated models with deformable 3D bodies of almost any shape were developed [Bićanić, 2005]. Here we will, however, concentrate on a *3D sphere element model with a linear spring-slider-dashpot contact law*. To understand the following principles, it is necessary to mention that the discrete element method is based on the *Lagrangian* description of discrete bodies interacting by a *soft contact model*, i.e. the spheres may slightly overlap during the simulation, and on an *explicit time integration scheme* of the equations of motion.

These essential characteristics of DEM simulations will be explained by summarizing a classical *simulation loop*. This computational sequence describes the iterative steps which are necessary to get from the current *state* in time to the next state. The simulation loop successively passes through three stages related to the bodies, their interactions and the time integration.

Bodies

The bodies in DEM simulations can be classified into two categories: *discrete elements* and *boundary elements*.

Discrete elements The discrete element method is based on the definition of *bodies* or *elements* whose motion is described by *Newton's second law* and a *contact law* in terms of a Lagrangian formalism, i.e. the motion of each particles is tracked individually. In ball mill modeling, these bodies are generally spheres representing the balls. Each sphere j is characterized by the following properties:

- *state* properties: center position $\mathbf{x}_j$, translation velocity $\dot{\mathbf{x}}_j$, angular velocity $\boldsymbol{\omega}_j$, translation acceleration $\ddot{\mathbf{x}}_j$, angular acceleration $\dot{\boldsymbol{\omega}}_j$, force applied to its center $\mathbf{F}_j$ and the moment of force, i.e. torque, around its center $\mathbf{M}_j$;
- *shape* properties: diameter d_j (or radius r_j);

- *material* properties: density ρ_j and contact parameters (explained hereinafter).

These spheres are floating in space according to Newton's second law (translation and rotation):

$$m_j \ddot{\mathbf{x}}_j = \mathbf{F}_j \quad (1.4)$$
$$I_j \dot{\boldsymbol{\omega}}_j = \mathbf{M}_j \quad (1.5)$$

where $m_j = 4\pi \rho_j r_j^3/3$ is the mass of the particle and $I_j = 2m_j r_j^2/5$ the moment of inertia. Notice that we simplified the general equilibrium equation in rotation because of the sphere's symmetry, i.e. the inertia tensor is diagonal.

Boundary elements In addition to spherical elements, it is necessary to include one more category of elements in the simulation. Strictly speaking, these elements are no real discrete elements because their motion is restricted and not governed by Newton's law. For this reason, we will call them *boundary elements*. A very versatile category of three-dimensional boundary elements are triangulated surfaces. By assigning a specific motion to the resulting surface mesh, it is possible to model very complex environments with which the particles interact, for instance, a ball mill liner. The triangular elements of the mesh will be called *facets*. The next step of a simulation is to manage the interactions between the bodies.

Interactions

Interactions result either from collisions between bodies, i.e. sphere-sphere or facet-sphere[9], or from other forces, like gravity. The critical algorithmic issue of DEM simulations is the *contact detection* between elements. Once the contacts are known, *contact laws* are used to calculate the interaction forces.

Contact detection *Contact detection* is crucial because of the possible number of bodies in the simulation [Bićanić, 2005]. For instance, in most industrial applications, typical minimum problem sizes range from 20,000 to 100,000 particles [Cleary & Sawley, 2002]; tube mills have around 50,000 balls in their first compartment. Considering also the bulk material in tumbling mills, as it is usually done in AG and SAG mills, several hundred thousand particles or even millions are necessary to accurately model the charge motion. For instance, in a recent study of a full 3D cement tube mill simulation, the *Cundall number* (number of particle time steps per CPU second) was around 170,000 on a single 3.6 GHz CPU [Cleary, 2009]. In consequence, for a simulation with 50,000 particles, a typical time step of 10^{-6} s and a simulated time of 10 s, around 8 hours of computation are necessary to complete the simulation. Hence, in terms of algorithmic complexity, it is necessary that the collision detection is clearly not $\mathcal{O}(n^2)$ but rather

[9] Facet-facet collisions are not mentioned here, because this type of collision never happens in ball mills. In other circumstances, it is certainly possible to define facet elements whose motion is governed by Newton's law.

$\mathcal{O}(n\ \log n)$ or even $\mathcal{O}(n)$ with $\mathcal{O}$ and n being the big O notation and the number of particles, respectively. Notice that the intuitive algorithm, which consists in checking for each particle, if it is in contact with another particles, requires $n(n-1)/2$ inspections; these inspections simply consist in checking the distance between the centers of spherical bodies as they may slightly overlap during the simulation. To limit the calculation time, numerous contact detection algorithms are described in the literature [Munjiza, 2005]. To give a glimpse of how contact detection can be managed efficiently, we will briefly describe two algorithms, i.e. the sweep and prune insertion sort algorithm and the category of grid algorithms.

Both algorithms are based on a two phase strategy. During the first phase, a fast and approximate collision detection is performed, while the exact local contact resolution is determined in a second phase. The *sweep and prune insertion sort algorithm* is the standard contact detection algorithm in the Yade plateform [Šmilauer et al., 2014], an open-source DEM solver. The keystone of this algorithm are axis-aligned bounding boxes, i.e. rectangular parallelepipeds which contain each a sphere or a facet, and whose edges are aligned with the axes of the coordinate system. A 2D example is provided in the figure 1.9. This figure shows that two bodies can only be in contact, if their bounding boxes are. In the first phase, it is thus only necessary to check for contacts of the bounding boxes. These boxes can be represented as three lists, one for each dimension, which contain the bounds of the bodies ($\tilde{B}_j^{i0}$ and $\tilde{B}_j^{i1}$ values in the figure 1.9). Besides the bounds, each element in a list further contains a reference to the corresponding body and a flag which indicates whether it is the lower or the upper bound. At the beginning, these lists have to be sorted. This operation has a complexity of $\mathcal{O}(n\ \log n)$ in the best case but it is only performed once. The key of the collision detection algorithm is surprisingly the *insertion sort* algorithm[10]. In fact, the three boundary box lists are initially sorted and the collisions are known. At the next iteration, the elements of the list are updated and it might happen that some elements are not sorted anymore, i.e. one box enters or leaves another box[11]. The collisions are then detected and managed by the insertion sort of the three lists. If the insertion sort swaps a lower and an upper bound of two distinct bodies, a new contact either appears or disappears depending on the swap direction. Because of the small time step in DEM simulations, it seems acceptable to admit that only few elements are swapped during each iteration. Hence, the complexity of the insertion sort is rather $\mathcal{O}(n\ \log n)$ than $\mathcal{O}(n^2)$, which leads to the efficiency of the method.

The category of *grid algorithms*, also referred to as boxing or binning algorithms, is based

[10] In simple words, the insertion sort builds a sorted array by sweeping through the unsorted array. For instance, if the array should be sorted in an increasing order, the algorithm starts at the second element. If this element is lower than the first element, both elements are swapped. Then the algorithm continues with the third element and sorts it with respect to the two first elements, i.e. if it is smaller than the second element, they swap their position, ... The algorithm then continues with the forth element and so on. A simple example is given by the following sequence: (4 3 2 1); (3 4 2 1); (3 2 4 1), (2 3 4 1); (2 3 1 4), (2 1 3 4), (1 2 3 4).

[11] Notice that this is a consequence of the explicit time integration and the soft contact method. More precisely, as the time step in the explicit integration schemes is rather small, i.e. around 10^{-6} s in DEM simulations, a particle moves only a little bit between two successive time steps. As the soft contact method allows particles to slightly overlap, the little displacement between time steps might lead to the slight overlapping of two particles. In consequence, the value associated the bound of one particle becomes smaller than the respective bound of the other particle.

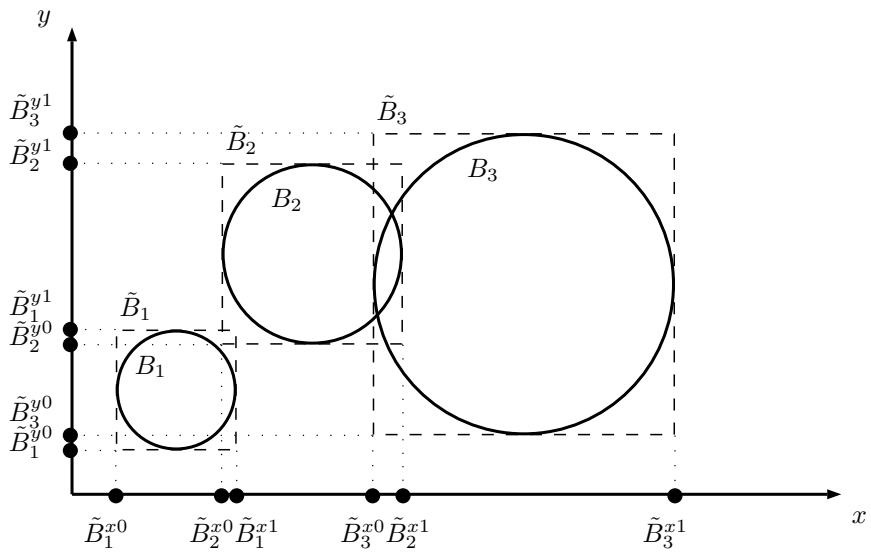

Figure 1.9: Sweep and prune insertion sort collision detection algorithm illustrated in 2D, where three spherical bodies B_1, B_2 and B_3, and their axis-aligned bounding boxes $\tilde{B}_1$, $\tilde{B}_2$ and $\tilde{B}_3$ are represented.

on the discretisation of the simulation space into cubic cells whose edge length is specified by the size of the largest particle in the simulation. The center of a particle is always inside of a cell, called the center cell. Because of the specific cell size, a particle can only be in contact with particles which either share the same center cell or which have their center located in one of the immediate neighboring cells. If the size distribution of particles is sufficiently restricted, the algorithm's complexity is $\mathcal{O}(n)$, because only particle pairs in a near-neighbor interaction list have to be checked for contact [Munjiza, 2005].

In conclusion, the sweep and prune insertion sort algorithm is efficient in DEM simulations with a large size distribution of the particles, i.e. with small and big particles at the same time, while the category of grid-based algorithms is very efficient if the particles have similar sizes.

Contact laws Once the contact has been detected, *contact or interaction laws* are used to determine the forces created during the interaction. In DEM simulations, a *soft contact* method is usually used, which means that the contacting bodies overlap slightly. The amount of overlap gives then rise to the interaction forces. Various contact laws have been defined and the most promising models are the *linear spring-slider-damper model*, the *non-linear spring-damper Hertz-Mindlin model* and the *elastic perfectly plastic model* [Mishra, 2003a]. To understand the essence of a contact law, we will present the formulation of the easiest one, i.e. the linear spring-slider-damper model [Pournin et al., 2001], in the context of the contact between two spheres (figure 1.10).

Let B_1 and B_2 be two spherical bodies entering into contact at a point C (figure 1.11). Let $\mathcal{P}$ be the plane tangent to B_1 and B_2. The unit vector normal to $\mathcal{P}$ and pointing to B_2 can be defined

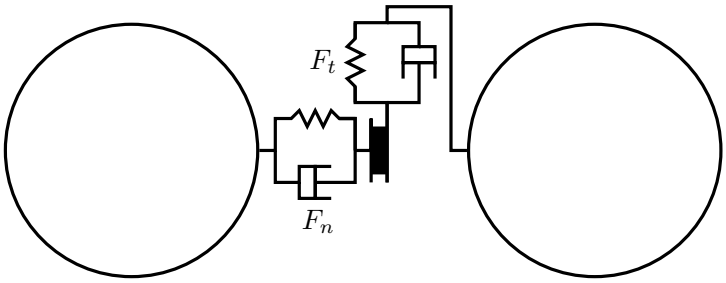

Figure 1.10: Schematic representation of the linear spring-slider-damper contact law with its normal and tangential components F_n and F_t.

as

$$\mathbf{u}_n = \frac{\mathbf{x}_2 - \mathbf{x}_1}{\|\mathbf{x}_2 - \mathbf{x}_1\|} \tag{1.6}$$

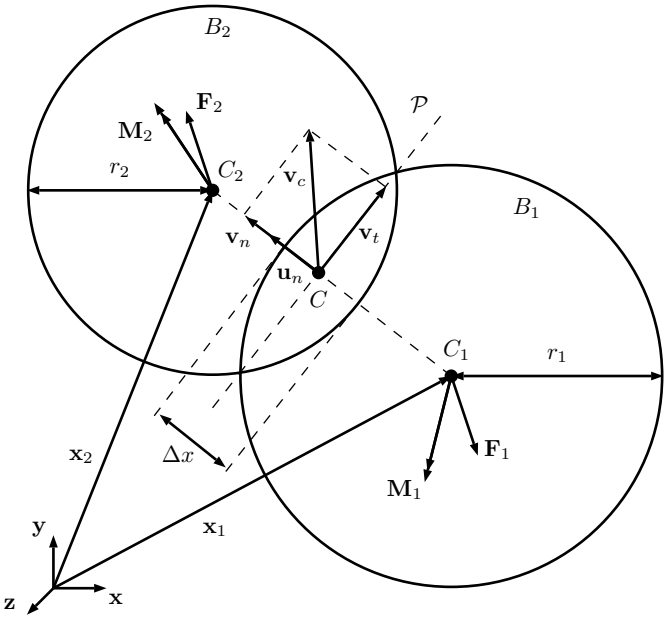

Figure 1.11: Geometric contact representation to derive the linear spring-slider-damper interaction law.

The relative velocity of B_1 and B_2 at point C is then calculated by the following formula:

$$\mathbf{v}_c = \dot{\mathbf{x}}_2 - \dot{\mathbf{x}}_1 + \mathbf{u}_n \times (\tilde{r}_1 \boldsymbol{\omega}_1 + \tilde{r}_2 \boldsymbol{\omega}_2) \quad \text{with} \quad \begin{cases} \tilde{r}_1 & = \|\mathbf{C}_1\mathbf{C}\| \\ \tilde{r}_2 & = \|\mathbf{C}_2\mathbf{C}\| \end{cases} \tag{1.7}$$

The *normal* component $\mathbf{F}_n$ of the contact force is a function of the overlap Δx and the normal

velocity $\mathbf{v}_n$ weighted by the equivalent[12] normal stiffness k_n of the linear spring and the equivalent normal damping coefficient c_n of the dashpot, respectively:

$$\mathbf{F}_n = \begin{cases} F_n\,\mathbf{u}_n & \text{, if } F_n \geq 0 \\ \mathbf{0} & \text{, otherwise.} \end{cases} \quad \text{with} \quad \begin{cases} v_n &= -\mathbf{u}_n \cdot \mathbf{v}_c \\ \Delta x &= r_1 + r_2 - \|\mathbf{x}_2 - \mathbf{x}_1\| \\ F_n &= k_n\,\Delta x + c_n\,v_n \end{cases} \tag{1.8}$$

In this formula, F_n might be negative because of the viscous damping. To prevent any attraction forces it is thus necessary to change its value depending on its sign. The *tangential* component $\mathbf{F}_t$ of the interaction force can be calculated by the following formula:

$$\mathbf{F}_t = \begin{cases} \mu\,\|\mathbf{F}_n\|\,\overline{\mathbf{F}}_t / \|\overline{\mathbf{F}}_t\| & \text{, if } \|\overline{\mathbf{F}_t}\| > \mu\,\|\mathbf{F}_n\| \\ \overline{\mathbf{F}_\mathbf{t}} & \text{, otherwise.} \end{cases} \quad \text{with} \quad \begin{cases} \mathbf{v}_t &= \mathbf{v}_c - (\mathbf{v}_c \cdot \mathbf{u}_n)\mathbf{u}_n \\ \overline{\mathbf{F}}_t &= k_t \int_* \mathbf{v}_t\,dt + c_t\,\mathbf{v}_t \end{cases} \tag{1.9}$$

The integral[13] term in this formula represents the spring that stores energy from the relative tangential motion and models the elastic tangential deformation of the contacting forces. The tangential force is limited by the Coulomb friction limit, at which point the surfaces begin to slide over each other.

Finally, the forces and moments applied at the center of each sphere are equal to:

$$\mathbf{F}_1 = -\mathbf{F}_n + \mathbf{F}_t \tag{1.10}$$
$$\mathbf{F}_2 = -\mathbf{F}_1 \tag{1.11}$$
$$\mathbf{M}_1 = \mathbf{C}_1\mathbf{C} \times \mathbf{F}_t \tag{1.12}$$
$$\mathbf{M}_2 = -\mathbf{C}_2\mathbf{C} \times \mathbf{F}_t \tag{1.13}$$

Previously, we presented a quite rigorous formulation of the model. In practice, it is usually represented by the following set of equations, which is certainly less rigorous but easier to understand:

$$F_n = k_n\,\Delta x + c_n\,v_n \tag{1.14}$$
$$F_t = \min\left(\mu\,F_n,\; k_t \int v_t\,dt + c_t\,v_t\right) \tag{1.15}$$

[12] Notice that the equivalent stiffness or the equivalent damping ratios are different from the elementary ones. The equivalent structural components, i.e. springs and dampers, are obtained by the connection in series of the elementary components. For instance, if two bodies have the elementary stiffness coefficients k_{n1} and k_{n2}, the equivalent stiffness is $k_n = k_{n1}k_{n2}/(k_{n1}+k_{n2})$. In this thesis, we will always use the equivalent coefficients in order to simplify the explanations; one should, however, be aware of this additional layer of abstraction.

[13] The star sign $*$ in the integral represents an operation, which is far from being trivial and therefore not described here [Šmilauer et al., 2014]. This operation consists in taking into account the invariance of the tangential elastic component of the contact force to a change in orientation of the particles, when their relative positions are unchanged with respect to each other.

The purpose of this section is to give a broad but sufficiently detailed overview of the general DEM method. For this reason, we will neither define the standard values of the parameters nor explain the advantages and drawbacks of this model in this section. As the reader might anticipate, we will obviously revisit the linear spring-slider-damper model in the literature review section about the DEM modeling of ball mills.

Other forces As mentioned earlier, interactions between spheres and spheres or spheres and facets are not the only interactions. The particles might also interact with other factors, like gravity. The force due to gravity $m_j\,\mathbf{g}$ is simply added to the forces, which are already acting on the spheres[14]. Once all the forces applied to a particle have been determined, its new acceleration, velocity and position can be determined by Newton's second law and the numerical time integration scheme presented in the following section.

Time integration

The last part of the discrete element method, which makes this explanation complete, is the time integration of the dynamic equilibrium equations 1.4 and 1.5. *Conditionally stable explicit time integration schemes* are usually used to solve these equations in DEM applications [Bićanić, 2005]; especially, the *leap frog algorithm* has been quite successful [Mishra, 2003a]. In fact, at each time step, the forces and moments acting on the different particles are determined as explained before. In consequence, the translation and angular accelerations are immediately known by Newton's law:

$$\ddot{\mathbf{x}}_j = \mathbf{F}_j/m_j \tag{1.16}$$

$$\dot{\boldsymbol{\omega}}_j = \mathbf{M}_j/I_j \tag{1.17}$$

The translation velocities and positions are then updated as follows[15], from iteration n to $n+1$ with a constant time step Δt:

$$\dot{\mathbf{x}}(t_{n+1/2}) = \dot{\mathbf{x}}(t_{n-1/2}) + \ddot{\mathbf{x}}(t_n)\,\Delta t \tag{1.18}$$

$$\mathbf{x}(t_{n+1}) = \mathbf{x}(t_n) + \dot{\mathbf{x}}(t_{n+1/2})\,\Delta t \tag{1.19}$$

The instantaneous velocity is then calculated as:

$$\dot{\mathbf{x}}(t_n) = \frac{\dot{\mathbf{x}}(t_{n+1/2}) + \dot{\mathbf{x}}(t_{n-1/2})}{2} \tag{1.20}$$

Similar formulas are used to determine the rotation velocity. The angular position is usually not determined for spheres because of their symmetry.

[14] Again, it would make no sense to apply gravity on the facets because they are considered to be boundary bodies in this project, i.e. their movement is explicitly prescribed.

[15] The notation $t_{n+1/2}$ has the meaning $t_n + \Delta t/2$. Likewise, $t_{n-1} = t_n - \Delta t$ and $t_{n+1} = t_n + \Delta t$.

The leap frog algorithm is *second order accurate*, i.e. the error on the position is $\mathcal{O}(\Delta t^2)$ due to the time discretisation. More specifically, this means that the error on the displacement is divided by 4 if the time step is divided by 2. In addition, the algorithm is *conditionally stable*. In simple terms, this means that the error introduced by the explicit integration is not amplified for time steps which are sufficiently small $\Delta t \leq \Delta t_{\text{cr}}$. The critical time step Δt_{cr} and a strategy to choose the time step Δt are presented in the following section.

In conclusion, the *discrete element method* is based on discrete bodies, mainly spheres and boundary facets, interacting by contact laws, like the linear spring-slider-damper law, and floating through space according to Newton's second law, which is solved by an explicit conditionally stable time integration scheme.

1.2.2 Review of DEM ball mill modeling

In this section, we will briefly summarize the modeling process of ball mills by the discrete element method in order to choose the most promising *contact law*, *geometrical approximation* and *simulation parameters*. Moreover, the major *validation methods* of DEM results in the context of tumbling mill modeling will be introduced. Detailed reviews can be found in [Mishra, 2003a, Mishra, 2003b] or more recently in [Weerasekara et al., 2013].

Contact laws

Previously, we described the linear spring-slider-damper law, which is certainly the most used contact law in DEM simulations of tumbling mills. This law was first applied to ball mills by [Mishra & Rajamani, 1992] and later Cleary certainly aided its spread within the scientific community by his significant work in this field, i.a. [Cleary, 1998]. Other researchers used the Hertz-Mindlin non linear contact law, which seems to have gained popularity because of its implementation in the EDEM discrete element solver, i.e. one of the leading commercial solvers [Khanal & Morrison, 2008, McBride & Powell, 2006, Powell et al., 2011, Rezaeizadeh et al., 2010a]. A third alternative is an elastic perfectly plastic contact law summarized in [Mishra, 2003a]. Before briefly explaining each model, it is necessary to understand, that these models and the resulting interaction forces should not be over-interpreted in terms of physical significance; the contact is idealized.

Linear spring-slider-damper contact law The *linear spring-slider-damper contact law*[16] is the simplest model to account for energy transfers from one particle to another while dissipating some of this energy during their interaction. Without the tangential force component and the dampers, neither the particle rotation, nor the energy dissipation during collisions could be simulated, respectively. Moreover, the total tangential force is limited by the Coulomb friction limit allowing particles to slide over each other. All these different mechanisms are necessary to

[16] A more rigorous definition of the model was provided in the section 1.2.1.

model a ball mill with the discrete element method[17]. In a simplified way, the law can be written as follows, where F_n and F_t are the normal and tangential components of the contact forces applied at the contact point:

$$F_n = k_n \Delta x + c_n v_n \tag{1.21}$$

$$F_t = \min\left(\mu F_n,\ k_t \int v_t\, dt + c_t v_t\right) \tag{1.22}$$

Despite the apparent simplicity of the model, it contains already 5 material parameters: the normal stiffness k_n, the tangential stiffness k_t, the normal damping coefficient c_n, the tangential damping coefficient c_t and the friction coefficient μ. In the following section, we will explain how these parameters can be determined. The correct choice of the parameters seems to be key in finding accurate results with the linear spring-slider-damper contact law [Dong & Moys, 2002], even though the shearing and sliding mechanisms seem to be inadequately or at least approximately modeled [Chandramohan & Powell, 2005].

Hertz-Mindlin contact law The *Hertz-Mindlin contact law* is very similar to the linear spring-slider-damper law. The difference consists mainly in the definition of the stiffness and damping coefficients, which are not constant anymore. The Hertz-Mindlin law is based on the quite popular problem of contact between two spheres in linear elasticity theory [Timoshenko & Goodier, 1951]. The stiffness coefficients are thus partly derived from the elastic properties of the material: the Young modulus and the Poisson ratio. It is, however, very important to notice that a reduced Young modulus is used in practice due to the relation between the critical time step and the elastic properties of the system, i.e. the real Young modulus leads to excessively small time steps. Furthermore, the model can be criticized because a fine layer of crushable material might be located between the impacting balls in a ball mill. This layer might be the cause of a completely different pressure distribution in comparison to the Hertzian theory. The Hertz-Mindlin contact law is therefore not necessarily a better contact model than the previous linear model.

Elastic perfectly plastic contact law A third contact law which should be mentioned is the *elastic perfectly plastic contact law*. The damping coefficients in the linear spring-slider-damper law and in the Hertz-Mindlin law are in general determined by the restitution coefficient. This will be shown in the next section for the linear model. The restitution coefficient is, however, not an intrinsic material parameter, like the Young modulus, i.e. it changes with the ball diameter and the impact velocity. The elastic perfectly plastic contact law tries to alleviate this shortcoming by linking the restitution directly to the plastic dissipation during contact. A detailed comparison of the different contact models can be found in [Thornton et al., 2013].

In conclusion, the *linear spring-slider-damper model* seems to be the best contact law for ball mill simulations because of its sufficient and necessary simplicity. On the one hand, we did

[17] The *dissipation* makes it possible to calculate the mill's power draw. A ball without *rotation* about itself seems to be quite non physical. And finally, the *sliding* between the balls themselves and the liner is one of the origins of grinding.

not find any evidence in the literature showing that one contact law leads to a significantly better correlation with the reality than another law (in the field of tumbling mill DEM simulations), i.e. the linear contact law is sufficient. This justification is also related to the limited validation data available for ball mills [Cleary, 2001b], as we will point out later on. On the other hand, the law is able to model the different phenomena observed in a real mill, i.e. transfer of the angular moment from one ball to another, energy dissipation and sliding of the ball charge. For this reason, the model is also necessary.

Geometrical approximation

Dimensionnality Ball mills were first modeled in *two dimensions* by the discrete element method in [Mishra & Rajamani, 1992]. With the advent of more powerful computers, *3D full scale* simulations with several million particles have become possible. For instance, an entire two chamber cement tube mill has been simulated by [Cleary, 2009]; the second chamber contained 3.81 million particles and the calculations took 56 CPU days for 1.5 revolutions. An intermediate stage between the 2D and the full 3D simulations is a *3D model with a periodic boundary condition*. Such a condition makes it possible to simulate an axial slice of the complete mill; it is called *periodic* because the balls which are leaving the mill on one side are reentering by the other side. Even though the influence of the end walls can not be modeled with this condition, the computation time can be significantly lowered because of the reduced number of particles. In some cases, it might even be desirable to neglect the influence of the end walls. For instance, this is true if the performance of the liner profile per se has to be evaluated (figure 1.12).

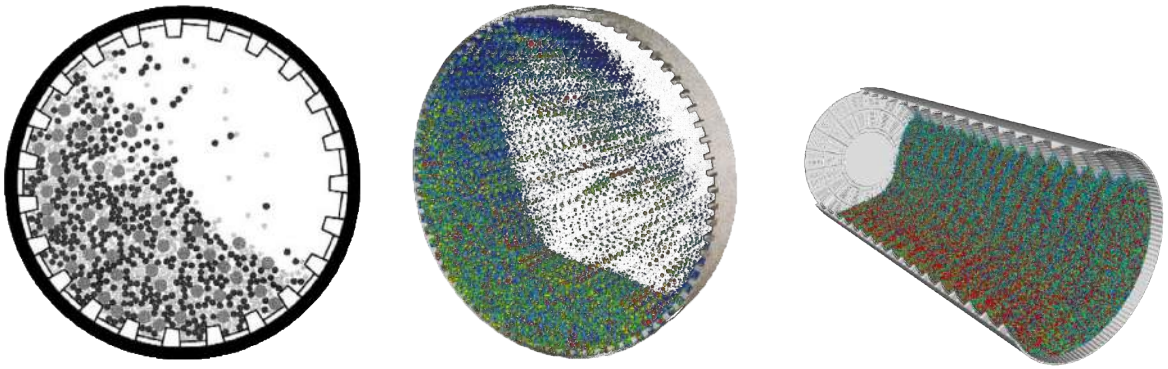

(a) 2D DEM simulation of a 7 m diameter SAG mill with around 5000 particles [Cleary, 2001a] (adapted).

(b) 3D DEM simulation of a 0.5 m slice of a 10 m diameter SAG mill with 185,000 particles [Cleary, 2001c] (adapted).

(c) 3D DEM full scale simulation of the second chamber in a cement tube mill with 3.81 million particles [Cleary, 2009] (adapted).

Figure 1.12: Simulations in different dimensions.

In the context of SAG mills, [Cleary et al., 2003] compares these three different ways of

approximating the geometry in terms of its dimension (2D, 3D or 3D slice). It is demonstrated that 2D circular particle DEM models consistently under-predict the shoulder and toe positions, i.e. the shoulder is too low and the toe too high in comparison to experimental results. This can be explained by the *limited strength of the 2D particle structure against shear*. In fact, the axial compression of the particles in a 3D simulation makes the failure of this structure much more difficult. The results of the 3D slice model are in between the 2D and the full scale 3D model because the friction of the charge against the end walls is neglected in this model. In conclusion, if an entire mill has to be analyzed, a full scale 3D DEM simulation is certainly the best choice, while a 3D axial slice seems to be sufficient to analyze the intrinsic properties of the liner profile. Nevertheless the full scale 3D simulation is commonly replaced by the simulation of the axial slice because of its important computation time.

Liner modeling In addition to the choice of the dimension, the mill and its content have to be geometrically modeled in a DEM simulation. The important parts of the *mill* in terms of this simulations are its boundaries, i.e. the shell liner and the end walls. The simplest surface representing a shell liner is the outer surface of a cylinder, i.e. the extrusion of a circle along the axial direction. Because of their very limited lifting action, liner profiles are in practice not circular, as we mentioned earlier. In consequence, a liner is better represented by the axial extrusion of the liner's profile curve, which might be a stepped or undulated curve. Such a liner may be called a 1D liner design because its height varies only along the azimuthal direction, i.e. that, in cylinder coordinates, where the z axis is aligned with the rotation axis of the mill, the liner surface can be parameterized by $r = r(\theta)$, where r is the distance between the profile and the rotation axis, and where θ is the azimuthal angle about this axis. For instance, Magotteaux's previous liners, like the *Duolift* and *XLift* liners, are 1D liner designs. More recently, 2D designs are considered. The height of these liners varies not only along the azimuthal direction but also along the axial direction, i.e. the liner profile surface can be parametrized by the relation $r = r(\theta, z)$ in cylindrical coordinates, where z represents the axial coordinate. Magotteaux's *New Duostep* liner therefore is a 2D liner.

In DEM simulations, liner profiles are approximated by segments in 2D or by surface meshes of facet boundary elements in 3D. Notice that 2D liner designs cannot be fully modeled in 2D DEM simulations since the profile curve of the liner changes along the axial direction; this is an additional reason for simulating ball mills in 3D.

The liner surface can either be approximated by triangular or quadrangular elements. Quadrangular facets are at best used to model 1D liner designs because they reduce the number of necessary facets, if two opposed edges of each quadrangular facet are aligned with the rotation axis (figure 1.13). Triangular elements are used to approximate 2D liner design because of their better capability to capture the curvature of the surface, even though the total number of boundary elements increases significantly.

Charge modeling Finally, the mill *charge* has also to be approximated in geometrical terms. The easiest, computationally least expensive and most common way to model the ball charge and

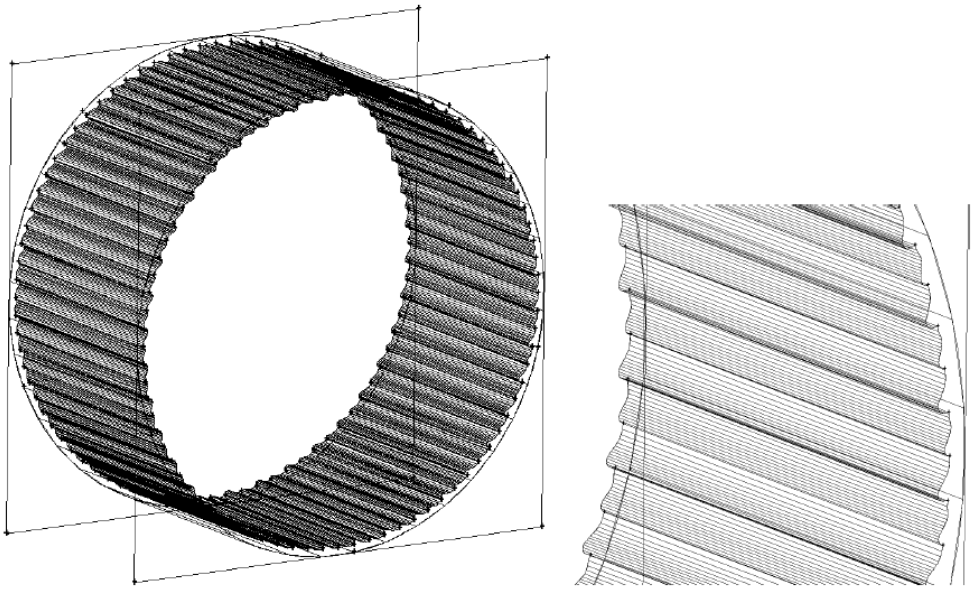

Figure 1.13: Surface mesh of a 1D liner with quadrangular elements (full view and zoom). The end walls are modeled by big quadrangular elements which rotate with the mesh of the shell liner [Sawley, 2006] (adapted).

the bulk material are spheres (or circles in 2D). Because of their three-dimensional symmetry, the exact contact detection and the calculation of the interaction forces is straightforward. Alternatives to spheres are clusters (rigidly connected spheres) [Šmilauer et al., 2014], super-quadrics [Bićanić, 2005] or polygonal elements [Feng & Owen, 2004]. In general, the consequence of non-spherical bodies in DEM simulations is the increase in shear strength of the mill charge due to the more efficient interlocking of non-spherical particles; hence, the height of the shoulder is raised as well as the power consumption[18] (at sub-critical speeds) [Cleary, 1998, Cleary, 2001c, Cleary, 2001a, Cleary et al., 2003]. Despite their better capability of modeling the real geometry of the feed material (or worn balls), non-spherical bodies are, however, not used if they are not absolutely necessary because of their computational cost. For instance, super-quadrics have a computational cost between 2 and 5 times that of spheres [Cleary et al., 2008]. But even simulations with spherical balls can take quite a long time, e.g. 5.7 CPU hours for two rotations of a 53,000 particle model [Cleary, 2009]; notice that this CPU time is rather short, i.e. the solver seems to be very efficient.

Anticipating what will be explained in the next section (wear modeling), it seems reasonable to suppose that the balls are the predominant *source of liner wear* because of their greater size and mass (density of steel: 7800 kg/m^3; density of clinker, the ground material in the cement

[18]The power consumption of the mill will be explained hereinafter. At this point, it is only necessary to know that the power consumption is the power necessary to mechanically keep the mill in rotation at a constant angular velocity. In other words, it is the power dissipated by the dampers and sliding devices of the contact model in the simulation.

mill: 1400 kg/m^3), as well as their higher hardness with respect to the feed material (hardness of clinker: 500 HV; hardness of steel liner: 700 HV). This material might, however, indirectly be the source of wear despite our previous hypothesis, which states that the balls are the predominant factor. In fact, the ground material might contain a small mass percentage of very hard particles, like silica SiO_2 (1000 HV, approximately), i.e. quartz, the most common constituent of sand. This leads to the conclusion, that the ground material intervenes indirectly in the wear process by minor contributions of very hard particles, while it can geometrically be neglected due to its smaller size and mass in comparison to the ball charge. Notice that the *volume occupied by the feed material* in a ball mill (clinker grinding) is only equal to the volume of the interstices between the balls at rest. Although it thus seems *acceptable to not model the feed material in a geometrical sense*, one should bear in mind that it might still be incorporated indirectly in the DEM simulation through the contact law (and the wear constants, as explained later on), e.g. a specific feed material might increase the sliding of the charge; in consequence, the coefficient of friction in the contact law decreases.

In a broader sense, material breakage will obviously not be simulated in this study even though a significant research interest exists in this field [Herbst & Nordell, 2001, Morrison & Cleary, 2004, Morrison & Cleary, 2008, Powell & McBride, 2006, Powell & Morrison, 2007, Powell et al., 2008]. Notice also that the ball charge will be approximated by spheres while balls can become highly non spherical due to wear [Sawley, 2006]; the majority is, however, almost spherical.

Simulation parameters

In one of the previous sections, we discussed why the linear spring-slider-damper contact law is sufficient and necessary for DEM simulations of balls mill. This model depends on several parameters, i.e. the normal and tangential stiffness, the normal and tangential damping coefficients, and the friction coefficient. In addition to these material parameters, one more value has to be chosen, i.e. the time step of the numerical time integration scheme. In this section, we will try to find some guidelines about how to choose the values of these parameters.

Time step As we mentioned in the general description of the discrete element method (section 1.2.1), the equations of motion are numerically solved by an explicit conditionally stable time integration scheme. This scheme is stable, i.e. numerical errors are not amplified from one iteration to the next, if the time step Δt is smaller than a critical time step Δt_{cr}. A linear undamped oscillatory system is thus stable if the time step Δt is smaller than the following value [O'Sullivan & Bray, 2004]:

$$\Delta t_{cr} = \frac{2}{\omega_{max}} \tag{1.23}$$

The variable ω_{max} stands for the greatest natural frequency in the system. In a single degree of freedom system, the critical time step is simply defined by the following formula, in which

m represents the mass of a point particle attached to a rigid fixation in space by a spring of stiffness k:

$$\Delta t_{\text{cr}} = 2\sqrt{\frac{m}{k}} \tag{1.24}$$

This formula has been extensively used in DEM simulations and should, however, be strongly criticized according to [O'Sullivan & Bray, 2004] because the 1D result can not simply be extrapolated to 3D DEM cases which are subjected to more complex contact conditions. By explicitly calculating the mass and stiffness matrices of numerous interaction conditions with a linear spring contact law, O'Sullivan and Bray showed that the resulting eigenvalues (representing the natural frequencies) are significantly higher than the eigenvalues of the single degree of freedom system. Hence, in DEM simulations, the critical time step should satisfy the following condition, where m is the minimum mass of a particle and where k is the smaller of k_n and k_t, i.e. the smaller of the normal and tangential stiffness of a linear spring contact law:

$$\Delta t_{\text{cr}} \leq 0.22\sqrt{\frac{m}{k}} \tag{1.25}$$

This time step is around 7 times smaller than the critical time step previously mentioned. In consequence, the question rises whether all former DEM simulations based on the 1D critical time step are false in a certain way. The answer is obviously no, even though one has to bear in mind that any numerical simulation is false to some extent. The specific reason of this answer is that the simulation should accurately integrate the collision in addition to the stability requirement. More precisely, the time step is commonly chosen in order to recover the coefficient of restitution from which the damping coefficient was chosen. For instance, [Cleary, 1998] uses about 20 to 50 time steps for a sphere-sphere collision. According to the results in the appendix A.1.3, the collision time of this system is equal to $\pi\sqrt{m_{\text{eff}}/(k_n(1-\zeta^2))}$ in the normal direction, where $\zeta = c_n/(2\sqrt{m_{\text{eff}}\,k_n})$ is the normal damping ratio and m_{eff} the effective mass, which is equal to $m/2$ if particles of the same mass m collide. Usually, the damping ratio is relatively small so that the time step can be chosen equal to $\Delta t = \pi/20\sqrt{m/(2k_n)}$ in the worst case (with the factor 20 suggested by Cleary); this time step is around two times smaller than the critical time step[19]. In consequence, this time step leads not only to a stable integration but it is also sufficiently energy consistent, i.e. the coefficient of restitution is recovered. To choose a time step which is admissible for all particles in the simulation, it is important to calculate the time step with the material properties of the particle with the greatest normal stiffness and the smallest mass. A typical DEM time step takes a value between 10^{-3} and 10^{-6} s according to Cleary, i.a. [Cleary, 1998].

For the sake of completeness, we will mention one last condition related to the time step which is usually not mentioned because the previous requirements generally imply the satisfaction of this condition. More precisely, if the time step is too large or the speed of the particle too

[19]This result is partially based on the fact the k_t, the tangential stiffness, should in theory have a value between 2/3 and 1 of k_n, the normal stiffness, according the Hertz-Mindlin contact theory, which is at the origin of the Hertz-Mindlin contact law [Mishra, 2003a]. Thus, the time step is minimal for the normal stiffness.

high, it might happen that one *particle moves (numerically) through another particle* because of the explicit time integration scheme. This is generally not true for DEM simulations of ball mills since the velocities remain relatively low with respect to the time step.

Stiffness As explained earlier, the interactions are calculated by a *soft particle method*, i.e. the particles are allowed to overlap and the interaction forces are determined on the basis of this overlap and the overlapping velocity.

The maximum overlap $\Delta x_{\max}$ depends on the normal stiffness and is usually limited to a value between 0.1 and 1% with respect to the particle diameter [Cleary, 2001b], thus requiring a *normal stiffness* between 10^6 to 10^7 N/m in 2D and 10^4 to 10^6 in 3D according to [Cleary et al., 2003]. The normal stiffness is lower in 3D than in 2D since the mass of spherical particles is lower than that of cylinders of unit length (in 2D), for a given maximum percentage of overlap [Cleary & Sawley, 1999]. There is, however, no perfect value of maximum overlap; maybe 10% would still lead to satisfying results even though the geometrical interaction seems to be significantly altered in comparison to the reality where steel balls never overlap that much. In addition, the desire to decrease the overlap is mitigated by the necessary reduction of the time step when the stiffness increases. In simple words, a lower overlap implies a longer computation time. The following formula gives the maximum overlap, which is reached during the normal collision of two particles colliding at a relative velocity v_r and having each a mass m (see appendix A.1.3)[20]:

$$\Delta x_{\max}^{**} = v_r \sqrt{\frac{m}{2k_n}} \tag{1.26}$$

If $p_{\Delta x}$ is the percentage of maximum overlap with respect to the particle diameter d, the stiffness coefficient can be written as a function of this percentage:

$$k_n = \frac{v_r^2\, m}{d^2\, p_{\Delta x}^2} \tag{1.27}$$

The average relative velocity v_r in this formula can for instance be determined by the diameter of the ball mill. Supposing that a ball falls from a height equal to around half the diameter D of the mill on the toe, its terminal velocity can be calculated by the conservation of energy:

$$\frac{1}{2}\, m v_r^2 = mg\frac{D}{2} \qquad \Rightarrow \qquad v_r = \sqrt{gD} \tag{1.28}$$

Besides this quite artificial evaluation of the normal stiffness, [Mishra & Rajamani, 1992] determined its value by experiments. These experiments consisted in the measurement of the strain waves in a 5 m long steel rod when a steel ball is dropped on it. Stiffness coefficients of the order of 10^8 N/m were measured for metal-metal contact. Such coefficients would lead

[20] The normal dashpot was neglected in this formulation. On the one hand, its influence is usually rather small in comparison to the spring. On the other hand, it is possible to obtain a rather practical worst case formula by not considering the damping. In fact, the overlap is higher without than with damping, for a constant stiffness.

to excessively small time steps and very long computation times. Moreover, pure metal-metal impacts are less likely to occur in a ball mill which is grinding the feed material. For this reason, they also performed a series of experiments with a layer of quartz particles between the colliding bodies. In these experiments, the resulting stiffness rather had an order of magnitude equal to $3 \cdot 10^5$ N/m, probably due to the progressive brittle breakage of the quartz. Spring constants of this order of magnitude are used in numerous studies and led to a good correlation with validation data, i.a. [Cleary et al., 2003, Sawley, 2003, Kalala et al., 2005a, Kalala et al., 2005b, Rajamani et al., 2000a].

Since the determination of the normal stiffness is more an art than a science, the *tangential stiffness* k_t is even harder to evaluate and only very few information could be found about its value. Mainly [Mishra & Rajamani, 1992] and [Mishra, 2003a] recommend to chose a tangential stiffness varying between 2/3 and 1 of the normal stiffness k_n according to the Hertz-Mindlin contact theory.

Damping coefficient The *normal damping coefficient* c_n is commonly expressed in terms of the coefficient of restitution ε_n representing the ratio of the relative speeds after and before an impact of two bodies. As we explained earlier, the coefficient of restitution is no intrinsic material property but rather a function of the impact velocity, the particle geometry and its material properties. According to the proof in the appendix A.1.3, the following relation exists between the normal[21] damping coefficient and the normal coefficient of restitution for a linear spring-slider-damper model:

$$c_n = -2\ln(\varepsilon_n)\sqrt{\frac{m_{\text{eff}}\,k_n}{\pi^2+\ln^2(\varepsilon_n)}} \quad \text{with} \quad m_{\text{eff}} = \frac{m_1\,m_2}{m_1+m_2} \tag{1.29}$$

where m_{eff} and k_n are the effective mass of the two colliding particles (m_1 and m_2 being their individual mass), and the normal stiffness coefficient, respectively.

Typical coefficients of restitution have a value between 0.3 and 0.8; the lower value is commonly used for ball-liner impacts and the upper value for ball-ball impacts [Cleary, 1998, Cleary, 2009, Datta et al., 1999, Kalala et al., 2005b, McBride & Powell, 2006, Mishra & Rajamani, 1992, Rajamani et al., 2000a]. [Mishra & Rajamani, 1992] determined the coefficient of restitution by dropping balls from a fixed height on a thick metal plate and recording the rebound heights. They found out that ε_n varies between 0.4 and 0.6 in this case. The ball-ball contact was also studied with a pendulum device and it was concluded that $\varepsilon_n = 0.97$. As the power draw of a tumbling mill is more sensitive to the coefficient of restitution and the coefficient of friction than the stiffness of the material, these coefficients are a convenient way to calibrate the model based on the experimental power draw [Kalala, 2008]. This sensitivity seems, however, to be relatively small for the coefficient of restitution according to [Cleary, 1998]; the power draw of the mill increases only by around 5% if the (normal) damping ratio is changed from 0.3 to 0.5. It is not mentioned whether the tangential damping ratio was also changed but we suppose that Cleary

[21] Similar relations exist for the tangential damping coefficient in [Pournin et al., 2001].

chose $c_t = c_n$. This observation can be explained by the fact that it matters little whether a single or several collisions in a rapid sequence are required to dissipate any relative motion. The same conclusion was drawn by [Sawley, 2003].

In a similar way to the tangential stiffness, only very few consistent strategies to determine the *tangential damping coefficient* c_t were found in the literature. In fact, the most direct hypothesis is seemingly to suppose that $c_t = c_n$.

Coefficient of friction The coefficient of friction μ limits the total tangential force conforming to Coulomb's law of friction. As stated in [Kalala, 2008] and [Sawley, 2003], the power draw of tumbling mills is more sensitive to the coefficient of friction than the stiffness and the damping coefficient. Indeed, when the coefficient of friction decreases, the sliding of the charge increases and the shoulder angle decreases. As less charge is lifted up, less torque, i.e. less power, has to be supplied to the mill. In the same way as for the coefficient of restitution, the coefficient of friction spans a wide range in the literature even though the same materials were supposed to be modeled, i.e. rocks and steel balls: 0.1 in [Mishra & Rajamani, 1992], 0.2 to 0.4 in [Dong & Moys, 2002, Kalala, 2008], 0.5 in [Datta et al., 1999, Rajamani et al., 2000a], 0.4 in [Djordjevic, 2005], 0.5 or 0.75 in [Cleary, 1998, Cleary, 2009]. This explains the necessity of the following subject, i.e. validation.

Validation

Previously, we noticed that it is not obvious which parameters have to be used in the model to accurately simulate the real material. Two dependent reasons seems to be at the origin of this parameter variability. On the one hand, the parameters seem to have no significant influence on the results, which can be validated, like the power draw. On the other hand, only very few results can be validated because of the very harsh milling environment. Below, we will briefly describe the most used validation parameters of the discrete element method in the field of tumbling mill simulations.

Power draw In practice, the power draw by the mill can be directly determined by the torque applied to the mill shell measured by a torque-meter. In DEM simulations, this value is calculated by summing the contribution of the individual torques created by the collisions of the ball charge with the liner. An additional way of computing the power by the discrete element method is to integrate the energy dissipation for each collision and to divide it by the simulation time. This way of calculating the power is, however, much more difficult and less accurate since it is based of many small contributions (numerical problem) [Cleary, 2001a]. According to [Cleary et al., 2003, Datta et al., 1999, Makokha et al., 2007, Mishra, 2003b, Rajamani et al., 2000a, Rajamani et al., 2014, Sawley, 2003], the discrete element method is able to predict the power draw of the mill relatively precisely but its validity depends on the accuracy of the real power measurements. In fact, the power used by real mills is not entirely transferred to the mill shell due to mechanical looses in the drive or bearings.

Moreover, quantitatively good power predictions do not necessarily imply that the DEM model delivers reliable results in terms of other parameters, like the charge motion or the contact forces [Moys et al., 2000] because of its synthetic or global character. For this reason, further validation parameters were introduced.

Charge motion The charge motion in a ball mill can be examined mainly by three methods. The first method consists in taking *photographs* of the mill along the axial direction, where one end wall has been replaced by a transparent PMMA (Plexiglas) or tempered glass window [Cleary et al., 2003, Van Nierop et al., 2001, Dong & Moys, 2002, Prignon & Lepoint, 2001, Sawley, 2003] (figure 1.14). As expected such a study is usually only carried out in a laboratory ball mill with a reduced diameter because of the reduced cost. A side effect of the smaller mill size is the lower impact and abrasion energy, which makes it possible to not have to change the window after each test since the window gets progressively opaque.

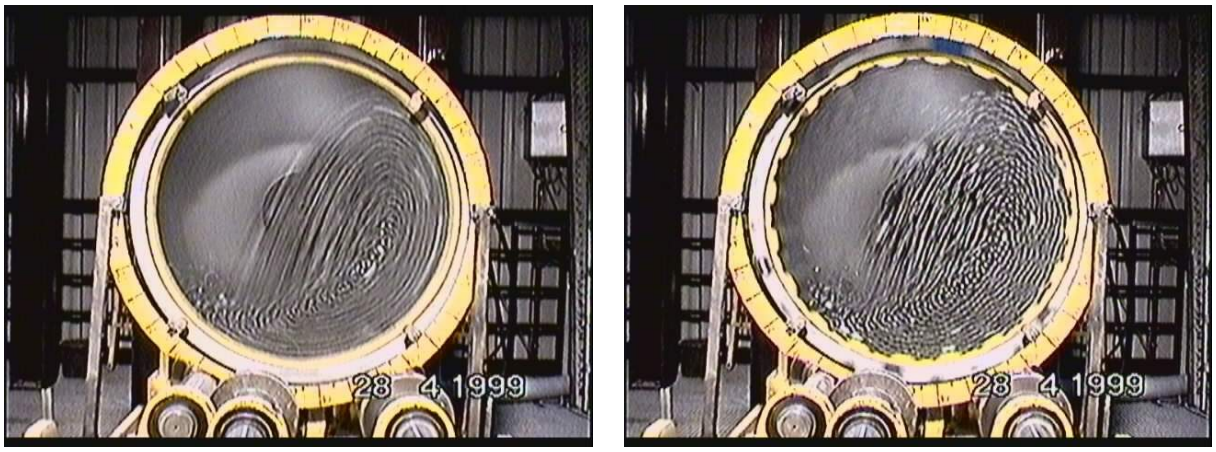

(a) Shutter speed equal to 1/12 s. **(b)** Shutter speed equal to 1/50 s.

Figure 1.14: Photographic validation data of the charge motion in a laboratory mill and influence of the shutter speed [Prignon & Lepoint, 2001].

Important parameters of this study are the finite focal length of the camera, its shutter speed (exposure time) and the finite depth-of-field of the images. Due to the *finite focal length*, the pictures show a noticeable amount of perspective. In computer geometry visualizations, this perspective is usually created by an isometric projection. Thus, it is important to compare the pictures with post-processed simulation data projected in a similar way, e.g. not by using a parallel projection with a focal point at infinity. The *finite shutter speed* allows the experimenter either to observe the particle at their instantaneous position or their pathlines, i.e. their trajectories during the time over which the film or the sensor is exposed (figure 1.14). Finally, the *finite depth-of-field of the images* is a consequence of the camera's focus, i.e. the balls just in front of the window can be clearly distinguished on the pictures while the balls, which are further away, are blurred.

More recent methods are x-ray filming [Govender, 2005] and Positron Emission Particle Tracking (PEPT), summarized in [Rajamani et al., 2014] and [Weerasekara et al., 2013]. X-ray filming consists in tracking the 3D trajectories of the charge particles by generating two orthogonal x-ray images and applying an edge detection algorithm, achieving a 0.15 mm accurate reconstruction at 100 frames per second. X-ray filming has been extended by *Position Particle Emission Tracking* (PEPT). This technique makes it possible to track individual particles by labeling them with a radio active tracer decaying with the emission of positrons.

Force on the liner To complete the energetic and kinematic validation, [Moys et al., 2000] introduced the *dynamic* validation by *instrumenting a lifter* with strain gauges measuring the normal and tangential forces applied to this lifter in a 0.55 m diameter ball mill (figure 1.15a). The 2D behavior of the charge motion was studied because of the large 9.5 mm average diameter of the balls with respect to the length of the mill, which was only equal to 23 mm. This study is explained in more detail by [Kalala, 2008]. Despite the pronounced standard deviation of the signal a relatively good correlation between the real and the simulated forces was achieved (figure 1.15b).

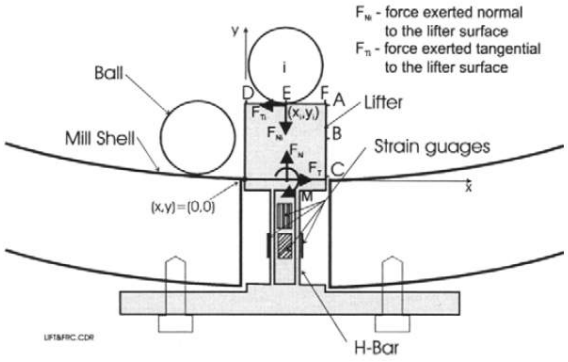

(a) Instrumented lifter [Moys et al., 2000].

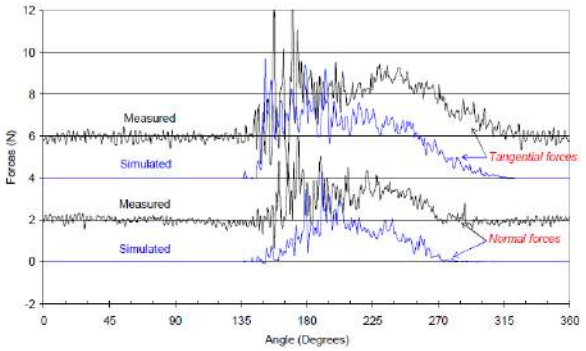

(b) Numerical and experimental results [Kalala, 2008].

Figure 1.15: Illustration of the dynamic validation based on measuring the force exerted on an instrumented lifter.

1.3 Wear Modeling

In a general sense, *wear* is the progressive removal of material from solid surfaces due to their mechanical interaction. It is a complex phenomenon and its physical mechanisms are still not completely understood. [Meng & Ludema, 1995] surveyed 5466 papers in the *Wear* journal between 1957 and 1992 and the *Wear of Materials* conferences from 1977 to 1991; their conclusion was that no single predictive equation could be found for general use. Nevertheless, several types of wear and the corresponding mathematical models have been established by modern research.

In the field of ball mill liner wear, it is possible to classify wear models into two categories:

- *impact (or normal) collision wear* resulting from the normal force created during the collision of high-speed cataracting/cascading balls on the liner surface. This type of wear is supposed to occur preferentially in the toe region where the lifters enter again into the ball charge.
- *tangential collision wear* resulting from the shear forces created by the sliding motion of the balls subjected to gravity and by the liner profile which lifts them from the toe to the shoulder.

Tangential collision wear could also be called abrasion wear, which is probably easier to understand but misleading. By intention, we did therefore not use this term. More precisely, anticipating what will be explained later on, impact wear can for instance be caused by the abrasion wear mechanism due to microscopic sliding of the colliding surfaces in the presence of abrasive hard particles. In this case, the distinction between impact and abrasion wear is incoherent and a classification according to the impact direction seems to be more consistent while it remains, however, an imperfect idealization.

In the following sections, we will take a closer look at different wear models used to simulate the wear of liners. First, the *major wear mechanisms* will be explained. Then, some *derived models* from these mechanisms, which have already been used in the context of the mill liner wear, will be presented.

1.3.1 Major wear mechanisms

The classification of wear according to different mechanisms is complex because of their interdependent nature. Nevertheless, four major mechanisms of wear, i.e. adhesion, abrasion, corrosion and surface fatigue wear, were established in [Archard, 1980, Rabinowicz, 1995]. These four mechanisms will be explained hereinafter in the context of metal wear.

Adhesive wear

Adhesive wear is the most common form of wear and occurs whenever two solid surfaces slide over each other. Its origin are adhesive forces created when atoms come into intimate contact. Such a contact is created when two surfaces are brought together. As real surfaces are microscopically rough, atom-to-atom contact appears only locally in regions called junctions. If the adhesive forces at junctions are sufficiently strong, they are able to break the material through a surface inside one of the contacting solids instead of through the previous interface of the contact during their relative motion. In consequence, when the surfaces are separated again, a small fragment is removed from one of the original surfaces, i.e. an adhesive wear particle is created (figure 1.16).

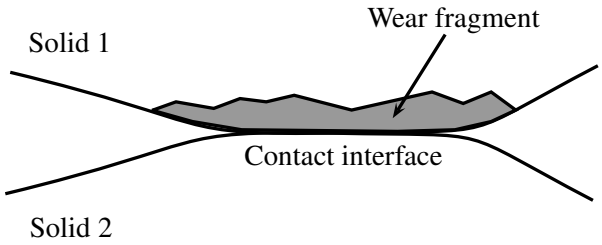

Figure 1.16: Creation of an adhesive wear fragment at a junction since the material breaks inside of the solid 1 instead of along the interface of the contact.

This phenomenon might seem to be unlikely, which explains why adhesive wear is a very slow process. Further theories were developed to explain why breakage inside of the material would occur. For instance, the IBM fatigue theory assumes that the junctions are stressed by fatigue during normal or sliding contact, which ultimately leads to the breakage of surface asperities by defect propagation.

Adhesive wear can be quantitatively described by the *Archard wear equation* [Archard, 1953, Archard, 1980]. Sliding wear experiments revealed that the volume V, which is worn away when two bodies slide over each other, depends on the normal load F_n, the sliding distance x_s and the penetration hardness of the material H. The *penetration hardness* represents the highest stress (in Pa or MPa) that a material surface can withstand without plastic yielding. In practice, it is generally determined by the Vickers hardness test. The Archard equation combines these different factors as follows:

$$V = K_{\text{adh}} \frac{F_n \, x_s}{H} \tag{1.30}$$

This equation can be determined by means of a few hypotheses in order to find the meaning behind the *wear constant* K_{adh}. As mentioned earlier, real surfaces are rough. Hence, the *real area of contact* A_r, where surface asperities are actually in contact, is lower than the apparent, i.e. macroscopic, area of contact A_a. By supposing that the real area of contact is so small that the interfacial asperities yield due to the normal force, a minimum value of this contact area is

suggested by the following formula:

$$A_r = \frac{F_n}{H} \tag{1.31}$$

Assuming also that the contact between surface asperities leads to circular junctions of radius a, the total number of junctions at any instant is the number n (figure 1.17):

$$A_r = n\,\pi\,a^2 \qquad \Rightarrow \qquad n = \frac{A_r}{\pi\,a^2} = \frac{F_n}{\pi\,H\,a^2} \tag{1.32}$$

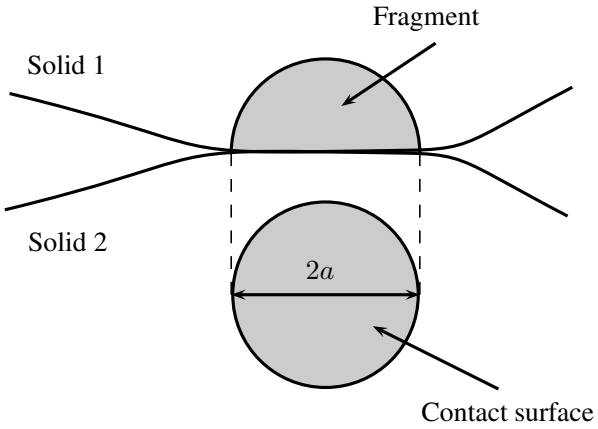

Figure 1.17: Idealized microscopic asperity contact representation with a circular contact surface of radius a and a potential hemispherical adhesive fragment production. The circular contact surface has been represented two times in this figure: once between the two surfaces (only a line is visible) and once projected to show its circular shape.

It seems reasonable that each junction is broken after a sliding distance $2a$. Therefore, the total number of broken junctions along a sliding distance x_s is N

$$N = \frac{n\,x_s}{2a} = \frac{F_n\,x_s}{2\pi\,a^3\,H} \tag{1.33}$$

As explained earlier, breakage may happen at the interface of a contact or along a surface inside one of the solids, thus producing an adhesive wear fragment. The *probability of creating a fragment* is denoted by k and the shape of the fragment is supposed to be a hemisphere of radius a. In consequence, the total volume lost due to adhesive wear for a sliding distance of solids subjected to a normal force F_n is V:

$$V = k\,N\,\frac{2}{3}\pi\,a^3 \tag{1.34}$$

$$= \frac{k\,F_n\,x_s}{3\,H} \tag{1.35}$$

The shape factor 3 and the fragment creation probability k are commonly combined in the non-dimensional constant $K_{\text{adh}} = k/3$, called the *wear constant*. For adhesive wear of unlubricated low carbon steel, the wear coefficient has in general a value between 10^{-4} and 10^{-3}.

The Archard equation was explicitly used in [McBride & Powell, 2006, Glover & De Beer, 1997, Qiu et al., 2001, Radziszewski & Tarasiewicz, 1993a, Radziszewski & Tarasiewicz, 1993b] to predict the liner wear in tumbling mills.

Abrasive wear

Abrasive wear occurs, when a hard solid body slides against a softer solid body or when two bodies of similar hardness slide against each other in the presence of harder particles in the contact region. The harder body or the particles plow grooves in the softer body. Wear fragments are eventually created due to the degradation of the surface integrity.

A mathematical model can be derived by supposing that the hard asperities or particles have a conical form. The penetration of this abrasive grain into the softer surface can indirectly be expressed by a, the radius of the cone at the surface of the softer contacting body (figure 1.18):

$$\Delta F_n = H\, \Delta A = H\, \pi a^2 \tag{1.36}$$

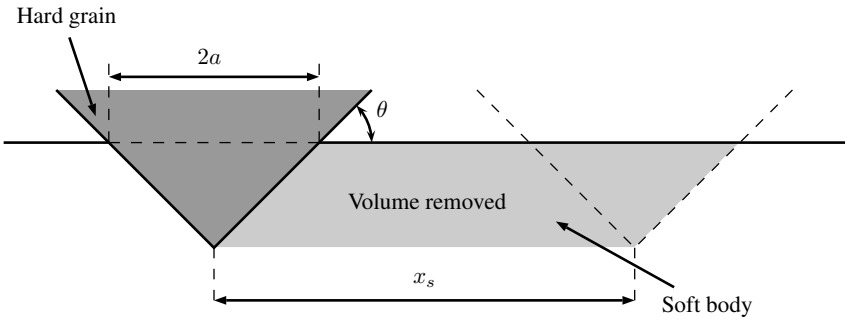

Figure 1.18: Simplified abrasive wear model consisting of a conical hard grain or surface asperity penetrating the surface of a softer body and removing material from this body over a sliding distance x_s.

The variables ΔF_n and H denote the normal force exerted on the individual asperity and the penetration hardness of the softer material. When the cone moves a distance x_s, a volume ΔV will be removed:

$$\Delta V = a^2\, \tan(\theta)\, x_s = \frac{\tan(\theta)\, \Delta F_n\, x_s}{\pi\, H} \tag{1.37}$$

Adding all the contributions from the different asperities or grains, and supposing that $\overline{\tan(\theta)}$ is the weighted average over all the cones, the total volume loss V of the soft body for a sliding

distance x_s is determined by the following equation, which will be called the *abrasion wear equation*:

$$V = \frac{\overline{\tan(\theta)}\, F_n\, x_s}{\pi\, H} \tag{1.38}$$

Finally, the volume loss can also be written in an similar form as the Archard wear equation, which will be called the *general* abrasion wear equation:

$$V = K_{\text{abr}}\, \frac{F_n\, x_s}{H} \tag{1.39}$$

The abrasion wear constant $K_{\text{abr}} = \overline{\tan(\theta)}/\pi$ has a similar or even slightly higher order of magnitude in the two-body case, i.e. hard and soft body contact, than the adhesive wear constant K_{adh}: $K_{\text{abr}} = 6 \cdot 10^{-3}$ to $6 \cdot 10^{-2}$. In the presence of hard particles between two soft bodies, the constant is about an order of magnitude smaller, i.e. $K_{\text{abr}} = 3 \cdot 10^{-4}$ to $3 \cdot 10^{-3}$, probably because the abrasive grains spend some time rolling between the surfaces instead of cutting them [Rabinowicz, 1995]; these values are very similar to those given for K_{adh} previously.

Due to the similarity with the Archard equation, the general abrasion wear model was implicitly used in all the studies about liner wear simulation, in which the Archard equation was used. The described *mechanism* of abrasive wear is, however, explicitly the basis of other models like Radziszewki's abrasion energy model [Radziszewski & Tarasiewicz, 1993a, Radziszewski & Tarasiewicz, 1993b, Radziszewski, 1997, Radziszewski et al., 2005], Rezaeizadeh's pressure model [Rezaeizadeh et al., 2010a], Powell's wear model with diameter [Powell et al., 2011] or even Finnie's law [Finnie, 1972]. These models will be briefly explained in the section about derived wear models.

Corrosion wear

Corrosion wear is a third wear mechanism, which can be seen as an *amplifying factor* of the two previous wear mechanisms, i.e. adhesion and abrasion wear. In fact, if the contacting surfaces interact chemically with their environment, for instance with the slurry in a tumbling mill, these surfaces tend to form a film on top of themselves, like rust for oxidizing steels. Oxides are usually harder and more brittle than the surfaces they are covering. In consequence, when the film reaches a critical thickness, it can be removed as a result of the sliding that takes place in the contact region. The worn volume might not only be increased by the brittleness of the layer, which allows it to flake off completely at one time, but in addition, the hard particles might act as abrasive grains. Corrosion is a complex phenomenon because it combines chemical kinetics with mechanical interactions. For this reason, it is currently not possible to take corrosion *explicitly* into account in the liner wear model. Notice that corrosion might, however, *implicitly* be taken into account by the wear constants K_{adh} or K_{abr}, which contain in a certain way all the uncertainties related to wear.

Surface fatigue

Surface fatigue at the microscopic level is very similar to macroscopic fatigue which generally results in the failure of the structure by breakage. Due to the repeated loading of a surface, inherent material discontinuities (dislocation) will increase in size and form cracks. These cracks will eventually result in the breakup of the surface with the formation of large fragments. Surface fatigue has been extensively studied in the field of rolling contact elements, like ball-bearings. In a broader perspective, surface fatigue might also be associated to a more general concept of wear modeling, i.e. *fracture mechanics*. Slow surface wear can be due to surface fatigue, while fast wear (impact) might arise from surface fracture.

In conclusion, it is interesting to notice that this presentation followed the general trend of wear modeling in the literature as pointed out in the extensive review by [Meng & Ludema, 1995]: wear modeling started with empirical relations, then contact-mechanics-based equations were introduced and finally wear models based on material failure mechanisms appeared.

1.3.2 Derived wear models in the context of liner wear

While some of the previous models were directly included in mill liner wear simulations, like the Archard equation or the similar general abrasion wear equation, other formulations of the previous mechanisms have been used to model the liner wear in grinding mills. In the following lines, these models will be categorized according to the collision direction, as explained earlier, i.e. impact wear, tangential collision wear and combined wear models. Unfortunately, some of the following models were not always clearly presented in the literature. We tried, however, to capture their essence as best as possible.

Impact wear models

Rabinowicz's general description of impact wear *Impact wear* occurs when two surfaces collide in the normal direction at high speed. The literature on impact wear is divided as to the cause of this wear process. First, the *adhesive wear* mechanism can be considered due to microscopic sliding between the surfaces during their collision. [Rabinowicz, 1995] suggests therefore the following mathematical model:

$$V = K \frac{I\, n}{H} \tag{1.40}$$

where I is the energy per impact and n the total number of impacts. The wear constant K depends on the proportion of the total impact energy expended in interfacial slip. The law was derived from the Archard equation in a similar way than Finnie's erosion law will be derived from the general abrasion wear equation in one of the following sections. This explanation clearly shows that impact wear is not a wear mechanism by itself, like adhesion, abrasion, corrosion or surface fatigue, but rather a way in which the constituents leading wear can be applied. This explanation

also emphasizes why we preferred to use the terms impact and tangential collision wear instead of impact and abrasion wear. Besides adhesion wear, *abrasion* might also be the cause of wear due to impact if hard particles are present in the interaction. In his impact experiments, Rabinowicz concluded that no correlation exists between the material loss and the hardness of the material; the hardness could thus be removed from the previous equation for normal impacts. Very brittle materials, which are usually relatively hard, have, however, high wear rates.

Impact wear can thus also be caused by *surface fatigue* which is directly related to surface fracture. In fact, if the material is rather ductile and if the impact energy is sufficiently low, the cracks simply propagate slowly (fatigue), like described in classical fracture mechanics [Zehnder, 2012]. If, however, the material is brittle and if the impact energy is large, rapid material removal occurs. Therefore, it seems reasonable to suppose that impact wear is proportional to the kinetic energy, more precisely:

$$V \propto m\, v_n^2 \tag{1.41}$$

where V, m and v_n are the volume loss due to impact wear, the mass of the ball and the relative normal velocity at the moment of the collision, respectively.

Two impact wear models will be briefly explained hereinafter. As the corresponding articles were not available, the following description is only based on third party information found in [Arekar, 2004] and [Kalala, 2008].

Sheldon-Kanhere impact wear model Sheldon and Kanhere studied the impingement erosion process of large single particles on an aluminum surface and derived a mathematical model of the volume loss due to wear [Sheldon & Kanhere, 1972]. The volume of material V removed by the wear mechanism is computed by the empirical relation:

$$V = K\, d^3\, v^3 \left(\frac{\rho}{H}\right)^{3/2} \tag{1.42}$$

where K, d, v, ρ and H are the wear constant, the particle diameter, the impact velocity (direction not specified), the material density of the ball and the hardness (not specified of which body, probably the aluminum surface), respectively. Arekar criticizes the exponent 3 of the velocity based on Finnie's law which has only an exponent 2. This critique can neither be affirmed nor denied because of the lack of information.

Wellinger-Breckel impact wear model Wellinger and Breckel investigated the relationship between physical values and wear of metallic materials tested by repetitive impacts [Wellinger & Breckel, 1969]. Their experiments showed that the volume loss V due to impact wear is proportional to v^n, where v is the impact velocity (its direction has not been specified) and where n is an exponent between 1.5 and 2.2.

Tangential collision wear models

Radziszewki's abrasion energy model Based on experimental studies using an abrasion wheel [Radziszewski et al., 2005], Radziszewki develops the following wear equation to quantify the volume loss due to abrasion:

$$V = \frac{\overline{\tan(\theta)}\ \mu\ F_n\ x_s}{\pi\ H} \tag{1.43}$$

This equation can be rewritten in terms of the abrasion energy:

$$V = \frac{\overline{\tan(\theta)}\ E_{\text{abr}}}{\pi\ H} \tag{1.44}$$

In the first equation, the coefficient of friction μ seems, however, to come out of nowhere if this equation is based on the abrasion wear model derived previously (equation 1.38). Hence, Radziszewki's abrasion energy model might be incoherent with respect to the general wear equation in theory. In practice, his model might lead to more accurate data, though; unfortunately no validation results were provided.

To *reconcile* this model with the *general* abrasion wear equation (equation 1.39), it is more meaningful to introduce the tangential force F_t in the abrasion wear equation by using Coulomb's law of friction, $F_t = \mu\ F_n$, where μ is the coefficient of friction:

$$V = \frac{\overline{\tan(\theta)}\ \mu\ F_n\ x_s}{\pi\ \mu\ H} = \frac{\overline{\tan(\theta)}\ F_t\ x_s}{\pi\ \mu\ H} = \frac{\overline{\tan(\theta)}\ E_{\text{abr}}}{\pi\ \mu\ H} \tag{1.45}$$

It might be difficult to use this equation as a predictive model, i.e. obtaining good quantitative estimates of wear by replacing its variables by their values, because the determination of these values is complex. To reduce the complexity, the individual variables can again be combined in a non-dimensional constant[22] $K^*_{\text{abr}} = \overline{\tan(\theta)}/(\pi\ \mu)$, obtained in practice by the calibration of the model, which leads to the *abrasion energy equation*:

$$V = K^*_{\text{abr}}\ \frac{E_{\text{abr}}}{H} \tag{1.46}$$

This model is equivalent to Radziszewki's model, if the abrasion wear constant is defined differently: $K^{**}_{\text{abr}} = \overline{\tan(\theta)}\ \mu/\pi$.

Rezaeizadeh's pressure model Rezaeizadeh's model is a direct particularization of the general abrasion wear equation [Rezaeizadeh et al., 2010b]. In fact, the height Δh lost due to wear during a time Δt can be written in terms of the sliding velocity v_s and the average pressure on the surface of the liner p_{ave}:

$$\frac{\Delta h}{\Delta t} = K_{\text{abr}}\frac{p_{\text{avg}}\ v_s}{H} \tag{1.47}$$

[22] This variable is called a constant but it might actually change as a function of the material, the normal force, the sliding velocity and so on.

Powell's wear model with diameter Powell introduces a wear model based on the abrasion wear mechanism but takes explicitly into account the ball diameter [Powell et al., 2011]. In fact, he supposes that the volume loss V due to wear from a ball-liner contact can be approximated by a rectangular cross-section having the dimensions $d\ h$, which is extruded along the sliding distance[23] $x_s = v_s\, t$ (figure 1.19):

$$V = d\ v_s\ t\ h \tag{1.48}$$

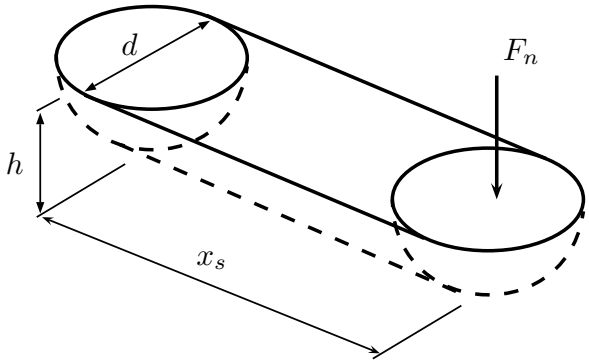

Figure 1.19: Powell's wear model of a ball having a diameter d sliding along a distance x_s and penetrating the surface by a (strongly amplified) distance h due to the normal force F_n.

The variables d, v_s, t and h denote the diameter of the ball, the sliding velocity, the sliding time and the penetration depth h of the ball into the liner surface, which is implicitly supposed to be softer than the ball. Moreover, the penetration depths is assumed to be proportional to F_n and inversely proportional to the hardness H of the liner. Hence, the volume loss for one ball-liner contact is given by:

$$V = K\,\frac{d\ F_n\ v_s\ t}{H} \tag{1.49}$$

This equation is similar to the general abrasion wear equation, except for the diameter d, which turns K into a *dimensional* wear constant. This model can thus be criticized because it implies that a ball with a greater diameter produces a greater volume loss for the same normal force, sliding distance and wear constant. This is not necessarily true because this model takes not into account that the penetration depth decreases with the diameter since the force is distributed over a higher surface area[24], e.g. it is easier to stick a pointed object (small diameter) in the ground than a blunted one (great diameter). For this reason, Powell's model has to be used with precaution.

[23] It is important to notice that we use the sliding velocity and not the total velocity in the following equation. In the related paper, Powell explains that he did not account for the angle of impact in his simulations, i.e. he did not project the relative velocity into the sliding plane. It is unclear why he used a different technique in the simulations than in his explanation of the wear model.

[24] This characteristic is exactly what makes disappear the radius a in the general abrasion wear equation.

Finnie's law Finnie's law was developed to model erosion wear of ductile metals struck at grazing angle by hard abrasive grains [Finnie, 1972]. *Erosion* is the wear process related to surfaces impinged by solid particles carried in a fluid, like in sand blasting. It might thus be surprising to find out that this model has been used to model ball mill liner wear in [Cleary, 1998]. Nevertheless, Finnie's law is essentially nothing else than an alternative form of the abrasive wear equation (equation 1.38), which might be more convenient to implement in some cases. Before showing the connection between both theories, the wear model will briefly be presented from Finnie's perspective.

Finnie calculated the material removal by solving the equations of motion of a hard particle when it removes the surface material of a ductile solid in a way similar to metal cutting (figure 1.20). The resulting volume V removed from a surface with hardness H by a mass M of eroding particles having an individual mass m, inertia moment I, average radius r and a velocity v is equal to the following quantity:

$$V = \frac{c\,M\,v^2}{4\,H\left(1+\frac{m\,r^2}{I}\right)}\left(\cos(\alpha)^2 - \left(\frac{\dot{x}_t}{v}\right)^2\right) \tag{1.50}$$

where α is the collision angle and c the fraction of particles cutting in an idealized manner.

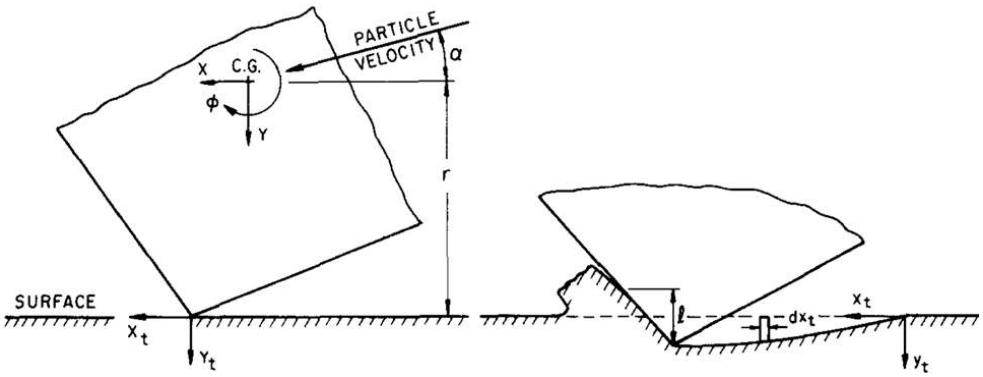

Figure 1.20: Idealized representation of an abrasive particle striking a soft surface at a collision angle α and removing its material [Finnie, 1972].

The horizontal velocity of the particle's tip $\dot{x}_t$, when the cutting ceases, can either be zero (i.e if $\tan(\alpha) > 1/3$, empirical result) or the particle may leave the surface while its tip is still moving forward. Finnie's law can therefore take the following simplified form, supposing that only one particle impacts the surface [Finnie et al., 1992]:

$$V = K\,f(\alpha)\,\frac{m\,v^2}{H} \quad \text{with} \quad f(\alpha) = \begin{cases} 1/3\,\cos(\alpha)^2 & \text{, if } \tan(\alpha) > 1/3 \\ \sin(2\alpha) - 3\sin(\alpha)^2 & \text{, otherwise.} \end{cases} \tag{1.51}$$

The non-dimensional constant K is the wear constant which contains the shape factors and the ideal cutting probability c, while f represents the angular dependence in the collision angle

α. The form of this equation already resembles the abrasion wear equation (equation 1.38). More precisely, Finnie's law can be derived from this equation:

$$V = \frac{\overline{\tan(\theta)}\, F_n\, x_s}{\pi\, H} = \frac{\overline{\tan(\theta)}\, F_t\, x_s}{\pi\, \mu\, H} = \frac{\overline{\tan(\theta)}\, E_{\text{abr}}}{\pi\, \mu\, H} \tag{1.52}$$

where the normal force has again been replaced by the tangential force estimated from Coulomb's law $F_t = \mu\, F_n$ in order to express the lost volume as a function of the abrasion energy $E_{\text{abr}} = F_t\, x_s$. If we suppose that this energy is a fraction w (dependent on the impact angle) of the kinetic energy $1/2\, mv^2$ of a particle, which collides on the surface, the volume loss due to abrasion can be rewritten as follows:

$$V = \frac{\overline{\tan(\theta)}\, w(\alpha)\, m\, v^2}{\pi\, \mu\, H} = K\, w(\alpha)\, \frac{m\, v^2}{H} \tag{1.53}$$

Eventually, we found again Finnie's law starting from the abrasive wear equation. The wear constant K might have a slightly different definition but it remains non-dimensional. In any case, this constant has to be directly determined by experimental data and hence, it is not calculated by combining the components of its definition, which are highly variable themselves (e.g. coefficient of friction) or very complex to measure in practice (e.g. ideal cutting probability or shape factors).

Combined wear models

Radziszewki-Tarasiewski's model A surprising combination of wear models was chosen in [Radziszewski & Tarasiewicz, 1993a, Radziszewski & Tarasiewicz, 1993b, Radziszewski, 1997], where the adhesive wear equation (equation 1.35) and the abrasion wear equation (equation 1.38) were explicitly added to give the total volume loss. Instead of combining these equations in one single equation and calibrating a single wear constant due to their similar form, the adhesion probability P and the cutting angle θ were separately determined. The separation seems to stem from the assumption that different wear mechanisms are active in different parts of the mill.

Kalala's wear model Based on the previous wear models, Kalala concludes that adhesion, abrasion and impact are the main types of wear in ball mills [Kalala, 2008]. Adhesion and abrasion wear can both be predicted by the Archard wear equation, where the constant $K_{\text{adh/abr}}$ represents the wear constant which takes into account the contributions from adhesion and abrasion wear:

$$V = K_{\text{adh/abr}}\, \frac{F_n\, x_s}{H} \tag{1.54}$$

To further simplify the model, the hardness and the wear coefficient are combined in the wear rate coefficient W, such that the volume loss due to adhesion and abrasion can be written:

$$V = \frac{K}{H}\, F_n\, x_s = W\, E_{\text{adh/abr}} \tag{1.55}$$

The coefficient of friction was omitted in the expression of the adhesion/abrasion energy $E_{\text{adh/abr}}$ as it is anyways multiplied by a weighting factor, i.e. W.

The previous equation shows that there is no wear, if there is no sliding motion between the grinding media and the mill liner. In the literature we found, however, that wear can occur without tangential relative motion, i.e. by impact. Sheldon-Kanhere's and Wellinger-Breckel's impact wear models therefore lead to the definition of an impact term in the wear equation, which is equal to[25]:

$$V = \frac{K}{H} E_{\text{imp}} \quad \text{with} \quad E_{\text{imp}} = \frac{m\, v^2}{2} \tag{1.56}$$

The exponent 2 of the velocity was chose as it is related to the kinetic energy, despite the fact that the exponent 3 was found in [Wellinger & Breckel, 1969]. It is unclear whether the variable v represents the absolute value of the velocity or only the relative normal impact velocity. This later choice would be more rigorous as the macroscopic sliding action should not be taken into account in the impact term; in fact, it is already contained in the tangential collision term, i.e. the abrasion/adhesion component. The impact model and the adhesion/abrasion model are finally combined by taking the sum of the different wear contributions:

$$V = W(a_{\text{adh/abr}}\, E_{\text{adh/abr}} + a_{\text{imp}}\, E_{\text{imp}}) \tag{1.57}$$

It is not clear why Kalala uses three different material factors instead of two; maybe his intention is to normalize $a_{\text{adh/abr}}$ and a_{imp}, which are weighting factors associated to the different wear mechanisms.

Cleary's four component wear model Cleary's four component wear model is finally the most general model of wear prediction [Cleary, 2001c, Cleary et al., 2009]. Impact and abrasion wear will each be determined by two components, which are unfortunately not described by mathematical formulas in the article; their meaning can, however, be deduced approximately from the description.

Impact wear is determined from the following two contributions:

- the normal work, i.e. the energy dissipated in the normal direction between the particles and the liner. The normal work can be calculated by integrating the normal component F_n of the force provided by the spring-slider-damper DEM contact law multiplied by the normal relative velocity v_n over time; it is the energy dissipated by the normal damper.
- the excess kinetic energy of impact for collisions above a threshold collision velocity, e.g. 0.1 m/s. Low-speed impacts, which are high in number, only deform the liner surface elastically, while high-speed impacts lead to significant liner damage due to the quadratic dependence of the kinetic energy in the velocity.

[25] In the reference, the variable K denotes the wear constant for abrasion/adhesion or impact wear. In both cases, the values of the variables is probably not the same, which explains the introduction of the variables $a_{\text{adh/abr}}$ and a_{imp} hereinafter.

Tangential wear is calculated on the basis of:

- the shear work, i.e. the energy dissipated along the tangential direction due to sliding between the particles and the liner. The shear work is determined by integrating the tangential component F_t of the force provided by the spring-slider-damper DEM contact law multiplied by the tangential velocity v_t over time. This way, the model includes the viscous tangential damping as well as the sliding dissipation, when the Coulomb friction limit has been exceeded.
- the kinetic energy of collision with a strong angular dependence; this measure of abrasion wear is similar to Finnie's law, which explains the angular dependence; in fact, shallow oblique collisions produce more abrasion wear than normal or orthogonal impacts with respect to the liner surface.

It is interesting to notice that the individual components of each wear type (normal impact wear/tangential wear) try to account for similar mechanisms in rather different ways: *numerical contact mechanics* (spring-slider-damper law) and *experimental wear models* (Wellinger-Breckel/Archard). Notice that the second way is the one used by Kalala [Kalala, 2008], who replaced Finnie's law by the almost equivalent Archard equation[26]. The different components of the wear model are then each multiplied by some weighting factor, i.e. the wear constant of each component, and added to obtain the total volume loss due to wear.

[26]Even though the Archard equation is associated to the adhesion wear mechanism, its form is identical to the general abrasion wear equation, except for the wear constant, which is determined by experimental calibration in any case. Moreover, Finnie's law can be deduced partially from the general abrasion wear equation. This explains, why we suppose that Finnie's law is almost equivalent to the Archard equation.

1.4 Ball Mill Liner Wear Modeling

The *efficiency of ball mill liners* progressively declines over time due to *wear*. On the one hand, the thickness of the liner decreases, which reduces the protection of the mill shell. On the other hand, the specific liner profile changes and it loses its capability to lift the charge to a specific height, i.e. the throughput of the mill drops due to the reduced energy available for breakage. In consequence, wear defines the lifespan of the liner and it thus has a significant economical impact, not only because of the direct relining cost and the progressive production losses but also due to the downtime of the mill during relining. At production outputs of around 300 tons/hour, it is easily understandable that the downtime has to be reduced as much as possible.

In ball mills, liner wear arises from the interactions between the balls, the feed material and the liner, which implies that it is necessary to *model the charge motion* inside of the mill, for instance by the discrete element method. Such a model should make it possible to predict the kinematic, dynamic and energetic behavior of the ball charge, and specifically in the context of wear, the normal force, the impact velocity, the sliding distance and so on.

To estimate the liner wear, *material wear models* are the connection between the mechanical data obtained from ball charge simulations, and the liner profile transformation. This transformation can be divided into two stages. First, the local loss of material has to be determined on the basis of the charge motion. Once the lost volume of material is known, the *liner profile geometry* is updated.

The goal of this section is therefore to review the *charge motion simulation*, the *wear modeling* and *geometry modification strategies* suitable for predicting the liner wear evolution in ball mills. These three elements will be explained in a general way. Afterwards, particular principles will be highlighted in the context of the major case studies related to liner wear simulations found in the literature.

Previous reviews of liner wear simulations can be found in [Arekar, 2004], [Kalala, 2008] and more recently in [Sawley, 2014].

1.4.1 Charge motion simulation

Different models can be used to predict the charge motion in tumbling mills. In order to transform this motion into a volume loss due to wear, it is necessary to extract some data of the charge motion model. For this reason, this section explains the *charge motion models* and the *data extraction strategies* necessary to numerically simulate the liner wear evolution.

Charge motion models

Wear models express the relation between the volume loss of material due to wear and the kinematic, dynamics and energetic characteristics of the charge motion. For instance, if the impact

velocity between a ball and a liner is higher, the wear is expected to be higher, too. Hence, it is necessary to extract sufficiently accurate interaction data between the liner and the balls from a *charge motion model*.

In the literature, mainly three charge motion models in relation to wear modeling have been developed. These models can be sorted by increasing complexity, computation time and accuracy:

- a *simplified ball charge model*: this method is based on empirical relations, the analytic calculation of characteristics of the ball charge, like the point of flight and the toe stability, and a discretization of space to assign the ball positions [Arekar, 2004, Radziszewski & Tarasiewicz, 1993a, Radziszewski & Tarasiewicz, 1993b, Radziszewski, 1997, Radziszewski & Morrell, 1998]. It is unclear how the balls move from one position to the next on the basis of these articles. Despite its expected low computation time, further investigations of the method are omitted in this review due to the limited physical meaning of its results, e.g. represented in the figure 1.21.

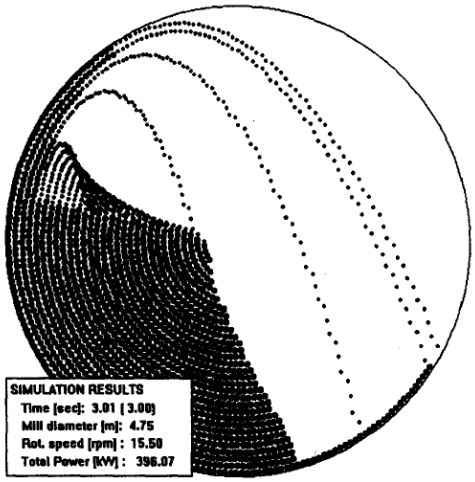

Figure 1.21: Ball charge motion obtained by the simplified ball charge model in [Radziszewski & Morrell, 1998].

- *2D DEM simulations*: discrete element simulations are far ahead of the previous method in terms of accuracy because the individual motion of each ball, the interactions between the balls themselves as well as the interactions between the balls and the liner are modeled. 2D DEM simulations with circular discs have the advantage to limit the *computation time and post-processing data* but are unable to model the increase in shear strength of the charge due to the axial effect [Cleary, 2001c]; this effect has been explained earlier in section 1.2.2. Moreover, 2D liners, with a an axial height variation, and the influence of the end walls of the mill can not be modeled by 2D DEM simulations. This type of charge motion model was used in [Cleary, 1998, Glover & De Beer, 1997, Kalala, 2008] to predict the liner wear.

- *3D DEM simulations*: the shortcomings of the previous methods are solved by the 3D discrete element method which seems currently to be the most accurate method to determine the charge motion for wear simulation [Cleary, 2001c, Cleary et al., 2009, McBride & Powell, 2006, Qiu et al., 2001, Rezaeizadeh et al., 2010a, Powell et al., 2011]. To limit the CPU time and the size of the post-processing data, liner wear simulations might be based only on the charge motion in a short axially periodic slice of the mill.

The 3D discrete element method eventually seems to be the most promising charge motion model. Nevertheless, the *computation time* is significantly longer than the simulated time, e.g. 1 second of simulated time requires on average 1 hour of CPU time (rough estimation). For this reason, it is simply impossible to simulate the entire collision history between the balls and the liner in real time. The goal is therefore to determine kinematic, dynamic and energetic average data from several simulated rotations of the mill which should be sufficiently *representative* of the long-term stress[27] on the liner. As ball mill DEM simulations generally start with having their charge at rest, around two rotations are usually necessary to reach the *pseudo steady state*[28]. Once this state has been reached, the charge motion data is sampled over around two additional rotations.

Data extraction

DEM simulations produce large amounts of data as the motion of each particle is tracked. The typical size of the post-processing data is measured in gigabytes. *Data extraction techniques* have therefore to be well though out. Essentially two strategies were used in previous liner wear studies: the *explicit* and the *synthesized* data extraction.

On the one hand, the data related to each collision with the liner, like the impact force or the sliding distance, as well as the contact position[29] on the liner could be *stored at each time step or at a reduced sampling frequency*. This technique would allow a very flexible post-processing since the collision data is explicitly stored and it could thus be applied to various wear models during the post-processing. The unwanted side-effect is obviously the large amount of information which has to be stored, e.g. 40,000 collisions in 0.5 s [McBride & Powell, 2006].

On the other hand, this information could be *synthesized* during the simulation. The base element of the data synthesis is a binning structure. More precisely, the lifters are discretized into geometrical regions, called bins. In DEM simulations, the definition of bins is a natural consequence of the surface mesh used to represent the geometry of the liner, i.e. the elements of the mesh could be the bins. These facets are, however, not required to be bins. For instance, the liner could be approximated by line segments in 2D DEM simulation in order to reduce the computational cost of the contact detection. Each segment is then discretized into bins to

[27] The word *stress* denotes here not only the mechanical stress representing a force to area ratio, but any kind of mechanical factor leading to wear.

[28] This state is not simply called steady state since the balls are still moving, i.e. it is a pseudo steady state.

[29] The contact position is necessary to map the collision data onto the liner geometry afterwards.

extract the data for wear predictions (figure 1.22). These bins are used to accumulate or average the local collision data, like the impact velocity or the normal force, during the simulation. By accumulating for instance the local impact energy or the relative volume loss due to wear, which are additive quantities, only one value per quantity and per bin is necessary to be stored at the end of the simulation. This strategy thus reduces significantly the amount of stored information in contrast to the first strategy where the information is stored for each or almost each time step. Nevertheless, the post-processing becomes less flexible as only the synthesized, i.e. accumulated or averaged, data is available at the end of the simulation.

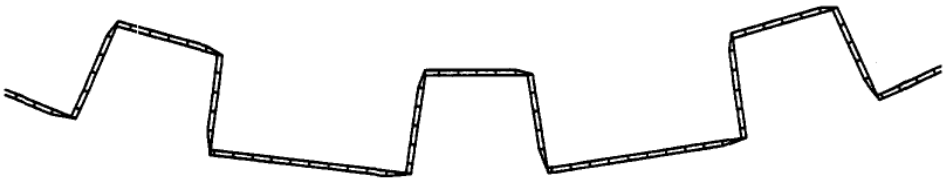

Figure 1.22: Discretized lifters into line segments which are themselves discretized into bins [Cleary, 2001c].

The *binning structure* is necessary to synthesize the collision data during the DEM simulation. It will, however, also be used for the post-processing of the data extracted by the explicit strategy. More precisely, the modification of the liner geometry due to wear, implies the discretization of the liner surface in any case since a mesh seems to be the simplest geometrical representation of the liner, which can be modified. To take advantage of this discretization and the periodic positioning of identical lifters on the circumference of the mill, the binning structure should be symmetric[30], too. The statistical representativity of the sampling could then by increased by its mapping (average) on a representative master lifter. For instance, if a mill has 22 identical lifters and if it is simulated for one second of simulated time in the pseudo steady state, the data accumulated in the bins could be averaged over the 22 lifters which would lead to a result having a statistical value equivalent to 22 seconds of simulated time for one lifter. In addition, if the liner is a 1D liner, i.e. a curve extruded along the axial direction, and if the binning structure, or simply the discretization, was well chosen, it is also possible to calculate an average along the axial direction. This axial and azimuthal averaging will be called the *master lifter mapping technique* hereinafter.

1.4.2 Material wear models and calibration

As explained earlier, the charge motion data is usually associated to spatial regions of the liner called bins. For each bin, the *relative* volume loss due to wear can either be calculated during

[30]In other words, each lifter should be represented by the same mesh which is simply duplicated and rotated by an angular increment to obtain the full mill liner, which is assembled of identical lifters.

(synthesized data extraction) or after the DEM simulation (explicit data extraction) by *material wear models*. These models were extensively described in the section 1.3.

The next step is to predict the *absolute* volume loss by the *calibration* of the wear constants. Calibration is based on the geometry of real worn liners after a given operation duration. In practice, two techniques are used to measure this geometry besides weighting the worn lifters. The first technique uses a mechanical profiling gauge composed of rods (figure 1.23) [Powell et al., 2006]. These rods are displaced when an imprint of the liner profile is taken. By measuring their displacement, the profile of the worn liner is obtained. In the case of more complex geometries, like 2D liners, a more sophisticated measuring technique is used, i.e. laser scanning of the mill [Cleary et al., 2009].

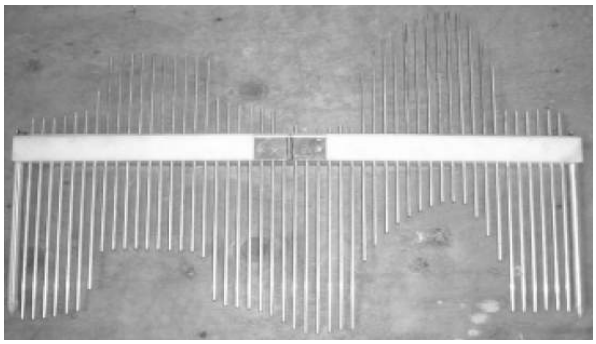

(a) Measurement with a mechanical profiling gauge [Powell et al., 2006].

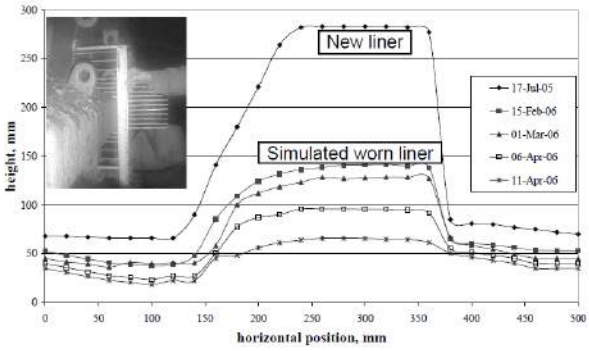

(b) Graphical data obtained from liner measurements [McBride & Powell, 2006].

Figure 1.23: Liner profile measurement.

In addition to the geometrical data of the worn liner, it is also necessary to record its *operating duration* when the measurements are taken. Otherwise, it would be impossible to estimate the absolute wear rates, e.g. mm/year of liner height loss.

Two steps are then necessary to transform the wear data determined in a simulation, like the normal damping energy for each facet, into a real volume loss: *relative/absolute wear conversion* and *time amplification*. On the one hand, the relative wear volume determined by the model has to be divided by the simulated time to obtain the relative wear rate. Similarly, the real wear volume is divided by the number of operating hours to compute the real wear rate. According to the previous explanation about the wear models, the proportionality constant between both wear rates is the wear constant, or more precisely, the wear constant divided by the hardness of the material. The wear constants can be determined by usual data fitting techniques, like a linear regression analysis of the real wear rate versus the simulated wear rate, over all the bins.

On the other hand, the liner wear in real ball mills is accumulated over several million rotations, which would simply be impossible to reproduce on a personal computer. This is why the wear rate was previously estimated by multiplying the relative wear rate by the wear constant. Finally, by multiplying the wear rate by a certain number of operating hours, we obtain the ab-

solute volume loss of each facet, i.e. bin, after these hours. Hence, the next step is to modify the geometry of the liner to account for the volume loss.

Notice also that recently some effort was put into developing a tumbling mill steel media abrasion wear test (abrasion wheel) by [Radziszewski et al., 2005] to calibrate the wear constants for wear simulations based on the discrete element method. Currently, calibration with real wear profiles has, however, been preferred despite this seemingly more predictive test.

1.4.3 Liner geometry modification

Due to the discrete bin size and the relatively short simulation time to reduce the computation time, the binned data tends to be rather discontinuous along the geometry. Real liner surfaces are, however, smooth. *Spatial smoothing* of the data is therefore a necessity in any liner geometry modification. Several techniques were proposed in the literature. For instance, a moving average filter or a cubic spline smoothing can be applied. Kalala even formulated the geometry modification as an optimization problem [Kalala, 2008]. Once the data has been smoothed, the liner profile is displaced normally to itself to satisfy approximately the volume loss constraint. This finally leads to a new liner profile. Older studies of liner wear simulations end their analysis at this point. More recent studies, however, push things a little further.

More precisely, while more and more material is removed in a real mill due to wear, the charge motion changes over time due to this modification of the lining geometry. A *multi-step procedure* was introduced to account for this strong coupling between the charge motion and the geometry. This procedure is an iterative method which progressively updates the liner profile. In fact, it starts from the initial geometry. Then, a DEM simulation and the associated wear model lead to the first geometry update. The simulation continues with the new geometry and the charge flow adapts to its new boundary conditions. Because the charge motion is different, the liner wear will most likely be different, too. In consequence, a new liner geometry is obtained and so on.

Besides accounting for the coupling between the charge motion and the wear, this approach has the additional benefit of simply *continuing the simulation*. Usually, when a new geometry is used, the charge motion starts from rest and thus needs several rotations until reaching the pseudo steady state. In a multi-step procedure, it would be possible to restart a simulation for the updated liner from the state of the particles just before the liner update. The tedious simulation time necessary to reach the pseudo steady state could thus be reduced. It is also important to notice that this advantageous strategy is premised on the enlargement of the mean radius of the mill as a result of wear, i.e. there is no risk of having a ball being outside of the liner after its update. Cleary suggests that it is, however, necessary to wait for around 1 to 2 revolutions until the new pseudo steady state of the charge motion is reestablished [Cleary et al., 2009]. He also assumes that around 4 to 10 steps are sufficient to capture the feedback of charge motion due to the change in geometry.

1.4.4 Review of ball mill linear wear modeling

Previously, we presented the charge motion simulation, the wear modeling and liner geometry modification strategies necessary to predict liner wear in general. In this section, we will explain these methods and some results found in the literature[31] from their particular point of view. This presentation in two stages (general/particular) was chosen since some principles only make sense for some simulation strategies. Trying to fit all these principles in a general explanation may have been detrimental to the understanding. This section will be structured according to the charge motion model which was used in the respective article.

Nevertheless, this section is *not absolutely necessary to understand the methods of the following chapters*. Moreover, the data found in the literature was sometimes relatively vague and not always clear. To optimize the information exchange, the following section can therefore be skipped, if the reader is in a hurry. The most interesting section is certainly *Cleary et al. (2009)*.

Simplified ball charge model

Radziszewski and Tarasiewicz (1993, 1997) Using the *simplified charge motion model* described in [Radziszewski & Morrell, 1998], Radziszewski and Tarasiewicz predicted the wear evolution of a wave and a bevel liner [Radziszewski & Tarasiewicz, 1993a, Radziszewski & Tarasiewicz, 1993b, Radziszewski, 1997]. The wear was calculated with the Archard and the abrasion equations (equation 1.35 and 1.38) for the balls and only with the *abrasion equation* for the liner. At each time step, small elements of the liner discretization (figure 1.24a) were removed from the initial surface depending on the predicted volume loss. As shown in the figure 1.24b, the simulated profiles are qualitatively realistic. Unfortunately, these profiles were not compared with real validation measurements.

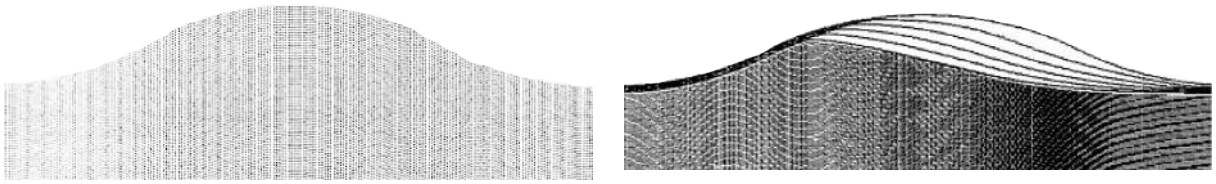

(a) Discretization. **(b)** Liner wear evolution.

Figure 1.24: Wave liner in a 2.6 m diameter mill simulated by [Radziszewski & Tarasiewicz, 1993b].

Arekar (2004) Using a simplified 2D ball charge model based on Radziszewski's theory, the same liner profile of a 10 m diameter SAG mill as in [Qiu et al., 2001] was analyzed in [Arekar,

[31] The articles, which will be summarized and commented are the major articles in the field of liner wear simulation, i.e. this review is essentially complete.

2004]. The wear was calculate by the *abrasion wear equation* (equation 1.38) and *Bitter's erosion wear equation*, which is similar to Finnie's law but containing more material parameters. The results of the material wear laws were amplified to simulate the liner wear in reasonable time. Then, the liner was *discretized* by 2D square elements but it is unclear how this discretization is updated by means of the volume loss due to wear. It was observed that the liner profiles were not always smooth after running a simulation. Therefore, a cubic spline *smoothing* was combined with a *Tukey smoothing* technique. The numerical results, which are shown in the figure 1.25, are coherent with the experimental measurements; it remains, however, unclear if the method is predictive after the calibration of the parameter i.e. able to predict the wear profiles of a similar mill without any artificial fine-tuning of the parameters for each new scenario. The charge motion in the figure 1.25 is in any case physically questionable.

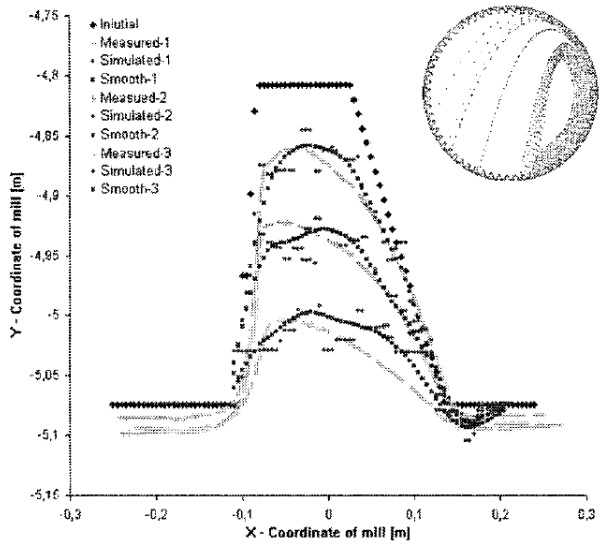

Figure 1.25: Comparison of the simulated and measured evolution of the liner profile due to wear with the corresponding charge motion [Arekar, 2004].

2D DEM

Glover and de Beer (1997) The article was not accessible. This summary is thus based on [Arekar, 2004, Kalala, 2008, Sawley, 2014]

A two-dimensional DEM ball charge model was used to predict the wear of a double wave liner. The liner was *discretized* by line segments. During the contact of a ball with the liner, the normal force and the sliding distance were combined by the *Archard equation* to predict the local volume loss. In consequence, the line segments are displaced by an amount proportional to the wear and the profile is *smoothed using a three point moving average*. The figure 1.26 shows the simulated evolution of the liner profile which is obviously non realistic since the profile shape becomes sharper.

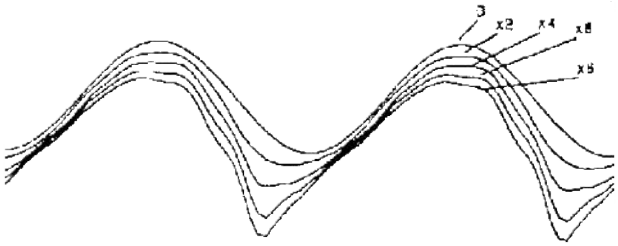

Figure 1.26: Simulated wear evolution of a double wave liner [Glover & De Beer, 1997].

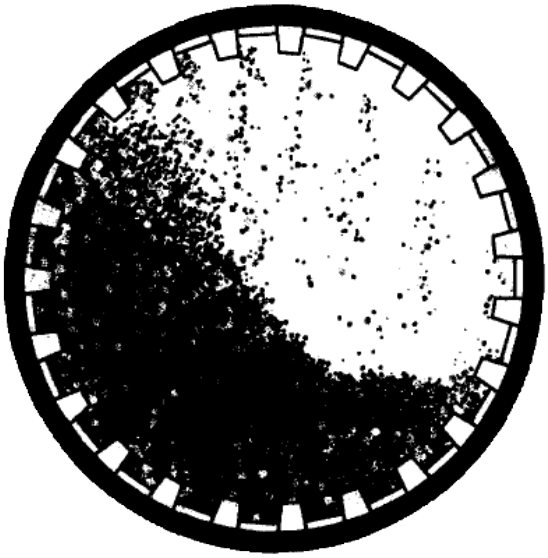

Figure 1.27: Illustration of the geometry and charge motion of the 5 m diameter ball mill [Cleary, 1998].

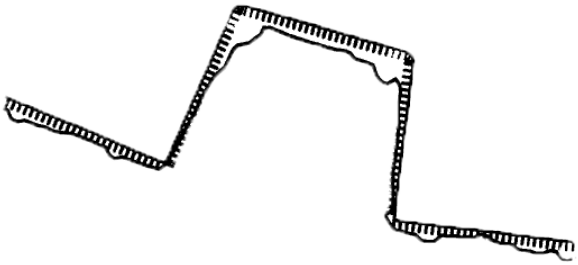

Figure 1.28: Binning structure for the wear data collection on a ball mill liner with the resulting wear profile [Cleary, 1998].

Cleary (1998) Cleary simulated the charge motion by a 2D DEM simulation of a 5 m diameter ball mill (figure 1.27) to estimate the liner wear [Cleary, 1998]. The DEM contact law is the spring-slider-damper model with the normal stiffness coefficient $k_n = 10^6 - 10^7$ N/m, the normal damping ratio $\varepsilon_n = 0.3$ and the coefficient of friction $\mu = 0.75$. The definition of the tangential parameters is not provided but they were probably given by $k_t = k_n$ and $c_t = c_n$.

The charge motion data used for the wear prediction was collected by a *binning* strategy. The figure 1.28 shows a typical set of bins for a part of a ball mill liner. Cleary smoothed the data in the bins with a *Demmler-Reinsch formulation of the cubic spline smoothing algorithm.*

The wear was predicted by *Finnie's law* on the basis of the binned impact velocity. As the data was collected along the entire mill and as the binning distribution was identical for each lifter, the wear for each bin of the first lifter was averaged with the matching bins of the other

22 lifters. By choosing the *cutting constant c* in Finnie's law equal to 0.1, by *amplifying* the wear rate by the ratio of the real time to the simulated time, by moving the center point of each bin inward according to the respective volume loss and by smoothing the data, Cleary obtained the wear profile, which is shown in the figure 1.28. This profile is not as smooth as it would in practice be expected.

Kalala (2008) Kalala's work in the field of ball mill liner wear simulation is probably the most extensive one because of his PhD thesis [Kalala, 2008], under the guidance of M.H. Moys [Moys et al., 2000], and the related publications [Kalala & Moys, 2004, Kalala et al., 2005a, Kalala et al., 2005b, Kalala et al., 2008].

Kalala simulated the ball charge motion with the 2D discrete element method and the spring-slider-damper contact law in the Itasca PFC software (particle flow code) originated by Cundall. The material parameters are $k_t = 3/4k_n = 4 \cdot 10^5$ N/m and $c_t = 3/4c_n$, where c_n is calculated by means of the coefficient of normal restitution. The coefficients of normal restitution and friction were different for ball-ball and ball-wall interactions. Their values were calibrated by means of experimental data (power, charge motion and force on lifter) and have a value between 0.2 - 0.4 (restitution) and 0.4 - 0.7 (friction), respectively.

To record the impact data and to modify the liner profile geometrically, two liner *discretization* strategies were implemented: the vertical and the radial discretization of 1D liners; the first method was also generalized to 2D liners. More specifically, this discretization includes two concepts: first, the discretization of the liner profile curve into discrete segments and second, the determination of the directions along which the end points of the segments will be displaced due to wear. Both geometrical strategies are illustrated in the figure 1.29. This figure also shows the reason why a radial discretization is sometimes necessary. In fact, the points of the vertical discretisation can only be displaced vertically, which would lead to no wear at all in the case represented in the figure 1.29a.

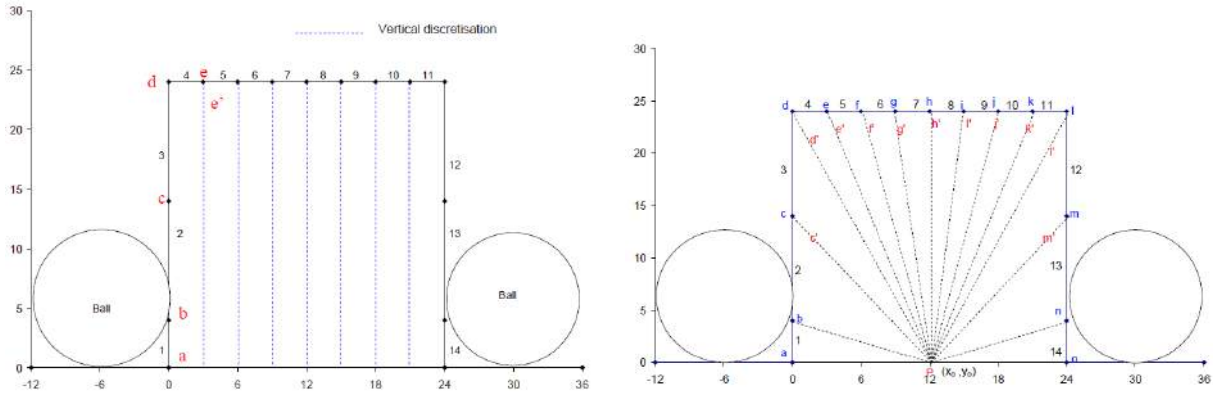

(a) Vertical discretization. **(b)** Radial discretization.

Figure 1.29: Discretization strategies applied to a rectangular lifter [Kalala, 2008].

The relation between the charge motion and the removed volume was determined by *Kalala's wear model*, which was explained earlier. The charge motion data related to wear was therefore accumulated for each segment of the discretized liner during the simulation. The wear constants K, $a_{\text{adh/abr}}$ and $a_{\text{adh/abr}}$ were determined recursively to match the measured worn profiles; it is unclear how this was exactly done.

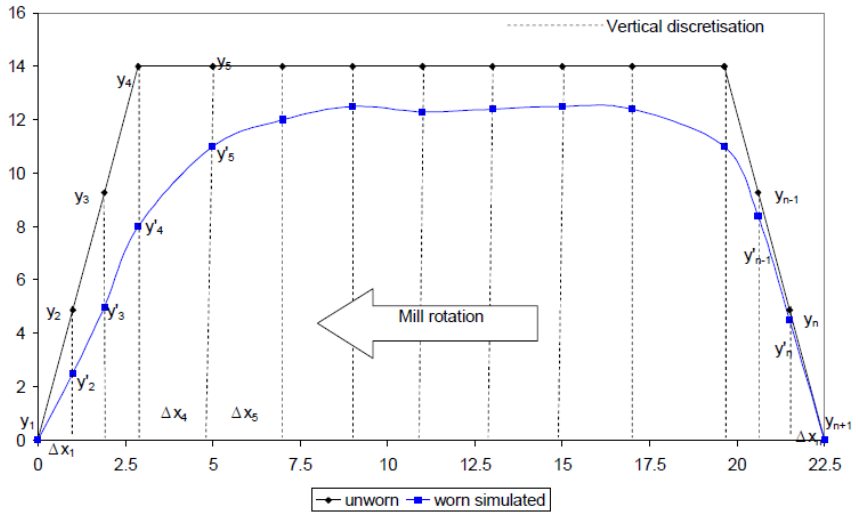

Figure 1.30: Vertical discretization of a trapezoidal lifter and the worn profile to illustrate the geometry updating strategy [Kalala, 2008].

Once the volume loss V_i per discretized segment was known, Kalala introduced an original method to update the geometry while preserving a *smooth* liner, i.e. an *optimization problem*. The objective function S, which had to be minimized, was the weighted sum of fours components, which will be expressed here in mathematical terms for the vertical discretization based on the notations given in the figure 1.30:

- S_1 is associated to the predicted volume loss V_i and the volume, which is actually removed after the update of the geometry:

$$S_1 = \sum_{i=1}^{n} \left[\left(\frac{(y_i - y'_i) + (y_{i+1} - y'_{i+1})}{2} \Delta x_i \, L \right) - V_i \right]^2 \tag{1.58}$$

  where Δx_i and L are the width, i.e. the horizontal distance, of a vertical discretization and the length of the mill (in its axial direction), respectively. The other variables are defined in the figure 1.30.

- S_2 is a smoothing term which tries to minimize the difference between the slope of neighboring discretized segments in the updated liner geometry:

$$S_2 = \sum_{i=1}^{n-1} \left(\frac{y'_{i+2} - y'_{i+1}}{\Delta x_{i+1}} - \frac{y'_{i+1} - y'_i}{\Delta x_i} \right)^2 \tag{1.59}$$

- S_3 minimizes the difference in slope of the current and the updated geometry to prevent any dramatic change in the profile:

$$S_3 = \sum_{i=1}^{n} \left(\frac{y'_{i+1} - y'_i}{\Delta x_i} - \frac{y'_{i+1} - y'_i}{\Delta x_i} \right)^2 \tag{1.60}$$

- S_4 ensures that the profile is strictly decreasing and strongly penalizes increasing profile heights:

$$S_4 = \sum_{i=1}^{n+1} e^{\beta(y'_i - y_i)} \tag{1.61}$$

  where β is a large number.

Finally, the components are combined in the global objective function S:

$$S = S_1 + \lambda\, S_2 + \alpha\, S_3 + S_4 \tag{1.62}$$

where λ and α are weighting factors influencing the smoothing. The objective function is then minimized and the coefficients adjusted to obtain the necessary smoothing of the result.

Finally, a multi-step procedure was introduced to account for the modification of the charge motion due to the geometry modification. Relatively good results were obtained and the models seems to posses some predictive potential, i.e. three industrial coal mill liners were apparently analyzed (figure 1.31) with the same values of the material and smoothing parameters.

3D DEM

Qiu et al. (2001) Based on the *Archard equation*, the liner wear of a 10 m diameter SAG mill was predicted [Qiu et al., 2001]. The wear profiles were compared with real measurements and a good agreement was found (figure 1.32). The exact way, in which the wear model was implemented, is not explained in the article; therefore, it is unknown why Qiu et al. obtained smooth results with the Archard equation and Glover and de Beer did not. It is only reported that 1.5 rotations of the mill were sufficient to gather enough charge motion data to extract the volume loss. This loss was amplified to account for the limited simulated time. It was observed that the wear rate $W = K_{\text{adh}}/H$ in the Archard equation was not constant. Hence, Qiu et al. supposed that this variation was due to a change in the hardness of the feed material. By applying a correction factor $C = a\, H_{\text{ore}}^b$ to the wear rate, they obtained seemingly better results; it is, however, unclear how this factor was introduced in the model.

Cleary (2001) Cleary simulated the profile wear of a 10 m diameter SAG mill [Cleary, 2001c]. The DEM spring-slider-damper contact law was used with Cleary's usual parameters, i.e. normal stiffness $k_n = 10^6$ N/m, normal damping ratio $\varepsilon_n = 0.3$ and coefficient of friction $\mu = 0.75$. The filling degree of the mill was 30 % and it rotated at 78% of its critical speed (10 rpm). A 0.5

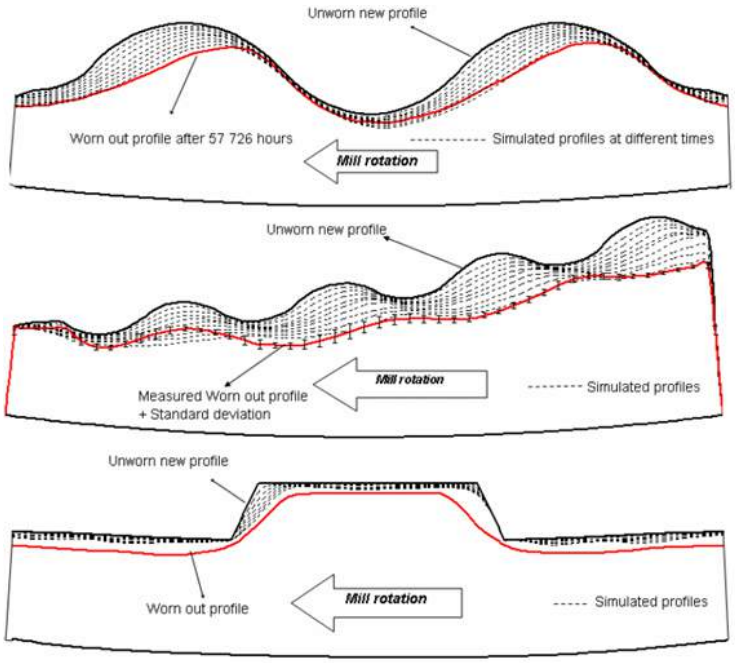

Figure 1.31: Simulation results of three lifters in coal grinding ball mills. For the last lifter only the first stage of its usage was simulated. In practice, these lifters are reversed once they reach a critical profile from one side [Kalala, 2008].

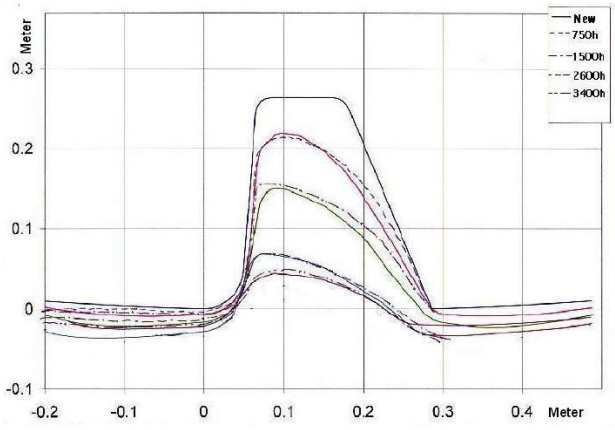

Figure 1.32: Simulated and measured evolution of a lifter in a 10 m diameter SAG mill [Qiu et al., 2001].

m axial slice of the mill with a periodic boundary condition and a minimum particle diameter size of 25 mm was used to predict the wear distribution on the liner (balls and feed material); a total of 185,000 particles were simulated. Around 31 CPU hours were necessary per second of simulated time on a 500 MHz EV6 alpha workstation. The liner was tessellated by *triangular elements* having an average length of 20 mm, which is smaller than the smallest particle in the simulation. The stress and wear data were *accumulated* (averaged) for each triangular facet during around two rotations of the mill. Due to the 1D liner configuration (axially extruded curve), it was possible to *aggregate the data across the depth* of the mill slice to obtain better statistical estimates of them. Nevertheless, the data was also smoothed (no information about the particular technique was provided) to eliminate the noise at the particle size level.

The figure 1.33 shows the resulting stress distribution. It illustrates how important the fluctuations of the stresses along the liner can be, even after smoothing their values; the same is true for the numerical wear measures, which are not represented here. It is also interesting to notice that the normal stress is around 3 times higher than the shear stress for an average impact; the general distribution of the stresses is, however, similar in both cases. By applying *Cleary's four component wear model*, the relative wear of each component was determined along the lifter. In particular, the normal work was around two times higher than the shear work. This implies, however, not necessarily that the dominant wear mechanism is impact instead of tangential collision wear, which some might call abrasion wear. Indeed, it might be expected that the liner steel is very resistant to impact and erodes mainly by tangential abrasion/adhesion wear. No experimental data was available and the contribution of each wear component could therefore not be determined. The model calibration and validation was performed in Cleary's future work [Cleary et al., 2009] for another type of mill.

Cleary et al. (2009) Cleary et al. quantitatively predicted and validated the wear evolution in a Hicom nutation mill [Cleary et al., 2009]. The mill was simulated with the 3D discrete element method and the spring-slider-damper contact law. Cleary's standard material parameter values were used, i.e. $k_n = 10^6$ N/m, $\varepsilon_n = 0.3$ and $\mu = 0.75$. Only the grinding media was represented in the model, i.e. around 50,000 spherical balls. The charge motion data related to wear was accumulated on a triangular surface mesh during the simulation. This data was transformed into wear by Cleary's four component wear model. In contrast to Cleary's previous studies, a multi-step procedure and the calibration of the wear constants was introduced in this article; spatial smoothing was, however, not mentioned.

The *calibration* of the four wear constants was rendered possible by high-quality measurements. A 3D laser scanned digitization of the real worn liner was used to obtain the real absolute wear rates. These rates represent the material loss of the liner per unit of time, e.g. mm/day. Without this calibration data, the *relative importance of the wear components* in the model could not be determined. Furthermore, it would also be impossible to obtain estimates of the *liner wear as a function of time*. In this latter case, only patterns of the wear could be explored but no estimation of the liner profile at a given time could be obtained by simulation. The wear rates, or simply the wear of the real mill at the moment of the measurement, i.e. after a specified number

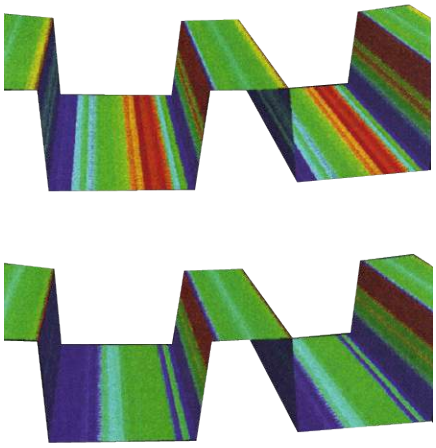

(a) Stress distribution on the liner: normal stress (top), shear stress (bottom).

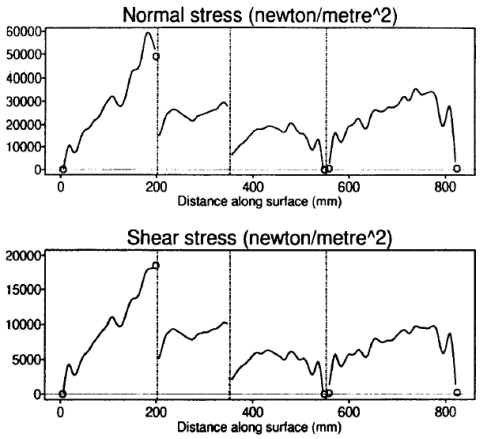

(b) Stress distribution along the liner. The regions (lifter front, top, rear and plate) are separated by vertical lines.

Figure 1.33: Rather strongly fluctuating stress distribution on the 10 m diameter SAG liner [Cleary, 2001c] (adapted).

of working hours, was calculated by taking the difference between the worn and new liner and by mapping it on the new liner (figure 1.34a); the exact way of doing this was not explained. By visual inspection, it was then observed that the wear component related to the Finnie model (one of the four numerical wear components in Cleary's wear model) delivered the best qualitative matching with the real wear distribution (figure 1.34b).

To quantify this observation, a *multiple linear regression analysis* of the real wear data versus the DEM results was performed and the Finnie-based abrasion component was eventually the best fitting wear model. One of the most interesting discoveries in this study was its capability of predicting that the floor of the liner was made of a much harder abrasion resistant material (figure 1.35), which was actually confirmed by the manufacturer.

Finally, the progressive wear of the liner was simulated by a multi-step procedure in five steps. The data of each step is collected over 2.5 revolutions. It is important to notice that the wear rate of one simulation was chosen such that it leads to one fifth of the total wear. Ultimately, a strong correlation between the predicted and actual worn liner displacements was found.

McBride and Powell (2006) An 8 m diameter SAG mill reduced to a 0.25 m axial slice with a periodic boundary condition was simulated by the 3D discrete element method. The real charge was truncated at 22 mm to obtain the simulated charge, which consisted in 38,000 particles. The simulation of 4 rotations (two rotations to mix the charge and to reach the pseudo steady-state, and two additional rotations to acquire the data for the wear prediction) at 75% of the critical velocity (11.4 rpm) with the commercial DEM software EDEM took approximately 3 weeks

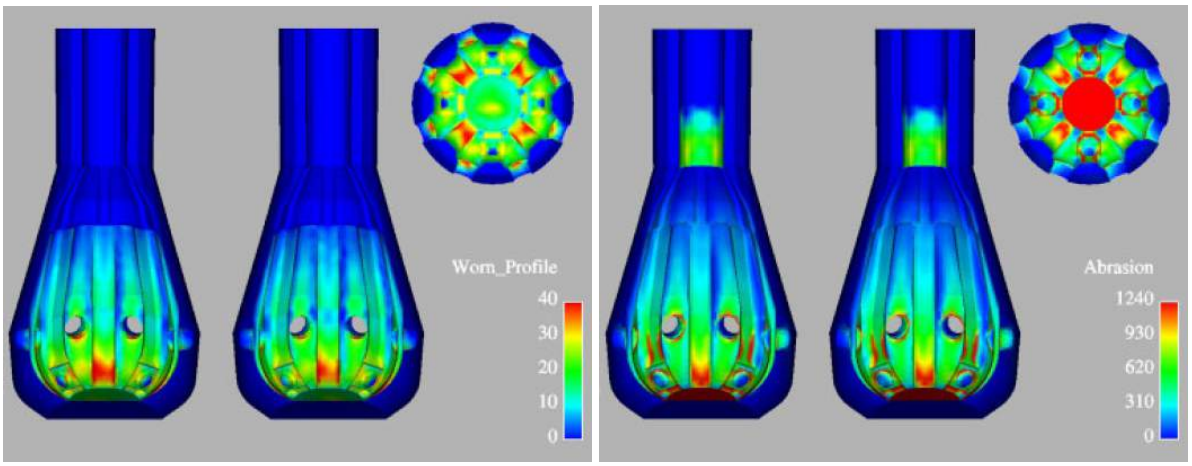

(a) Real liner wear mapped on the new liner surface.

(b) Relative predicted liner wear by the Finnie-based abrasion wear component.

Figure 1.34: Choice of the wear model based on the qualitative comparison between the real liner wear mapped on the new liner surface and the predicted liner wear by the Finnie-based abrasion wear component of Cleary's wear model [Cleary et al., 2009].

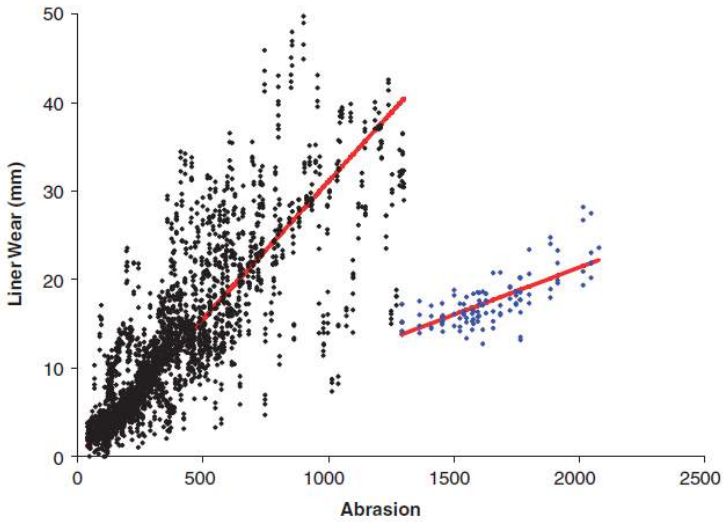

Figure 1.35: Regression lines of the measured real wear versus the Finnie-based abrasion wear [Cleary et al., 2009]. The smaller point cloud is associated to the floor of the mill, which was made of a more abrasion resistant material.

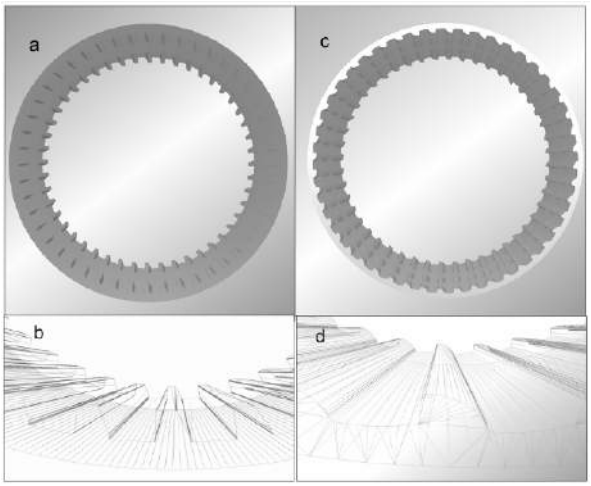

Figure 1.36: (a) Mill with the new lifters, (b) DEM mesh of the mill with new lifters, (c) Mill with the worn lifters, (d) DEM mesh of the worn lifters.

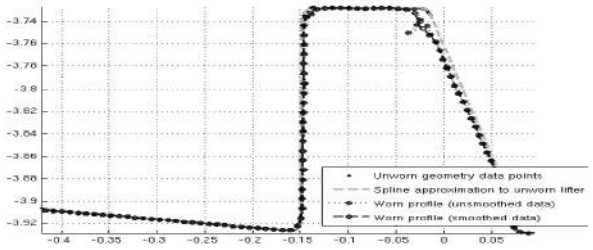

Figure 1.37: Original and worn (smoothed and non-smoothed) master lifter profiles. The dots of the worn profile, which were seemingly associated to the center of each bin give an idea of the small bin size.

on a 3.6 GHz processor. The Hertz-Mindlin contact law was used to model the interactions between particles. Different contact parameters for the contact between different materials were chosen, i.e. different parameters for steel-steel, steel-rock and rock-rock interactions. Neither the validation of these parameters nor a reference to the validation study is provided in the paper. The figure 1.36 shows the new liner and the worn liner with their meshes as used in the DEM simulations; it seems that quadrangular elements were used to model the 1D liner, i.e. its height does not change along the axial direction. Only the new liner is used for the wear prediction.

To estimate the worn liner profile, each collision event during the DEM simulation was recorded and mapped to a master lifter thanks to the azimuthal symmetry. This master lifter was then divided into 100 equally spaced and rather small 1D bins, as the liner is 1D (figure 1.37). Notice that the geometry was *not binned a priori* but only once the collisions are known; thus the binning structure is not identical to the discretisation of the geometry in the DEM simulation. The material loss was determined by the Archard equation on the basis of the charge motion data; no information about the model calibration was provided in the article. The non-smooth numerical wear data along the lifter was *smoothed in two steps*. First, a cubic spline was used to smooth the collision data before applying the Archard equation. After applying this equation, a least squares smoothing spline was applied to predict the resulting worn liner profile. It is unclear why the data was smoothed two times. Finally, a *multi-step procedure* was used to estimate the liner wear by taking the charge motion modification into account. More precisely, the liner profile was updated after some simulated time but the simulation was not restarted. Update after update, the worn profile was finally obtained, when a specified volume loss was attained. The results in the figure 1.37 show only a very small change in the geometry, which was not compared with the validation data illustrated in the article.

Powell (2011) In the most recent liner wear study, Powell simulated a slice of a 8 m diameter ball mill containing 110,000 spherical particles (feed material and balls) with the Hertz-Mindlin contact law (EDEM software) [Powell et al., 2011]. The liner was carefully meshed to form meaningful elements for wear modeling, i.e. the collision data is stored per mesh element (binning strategy) and more elements were used where higher wear was expected. The volume loss was calculated by means of *Powell's wear model with diameter*, which was explained earlier. Knowing the volume loss per element, its thickness loss perpendicular to its surface was then calculated by dividing the volume loss by the area of the element. Without any specific smoothing technique (at least it was not mentioned), the new relative liner profile was then determined. On the basis of the measurement of the real liner wear profiles of the mill, the wear parameter Kd/H was estimated to be equal to $6.08 \cdot 10^{-12}$ s^2/kg on average. This value changed, however, locally between the front and the rear faces of the lifter in a systematic way, indicating that some kind of wear mechanism was not accounted for in the wear model. It was not clear why a single constant did not fit the wear equation but Powell suggests that he did not incorporate the angle of impact in the model, i.e. the total impact energy was used in the wear model instead of the energy in the sliding plane.

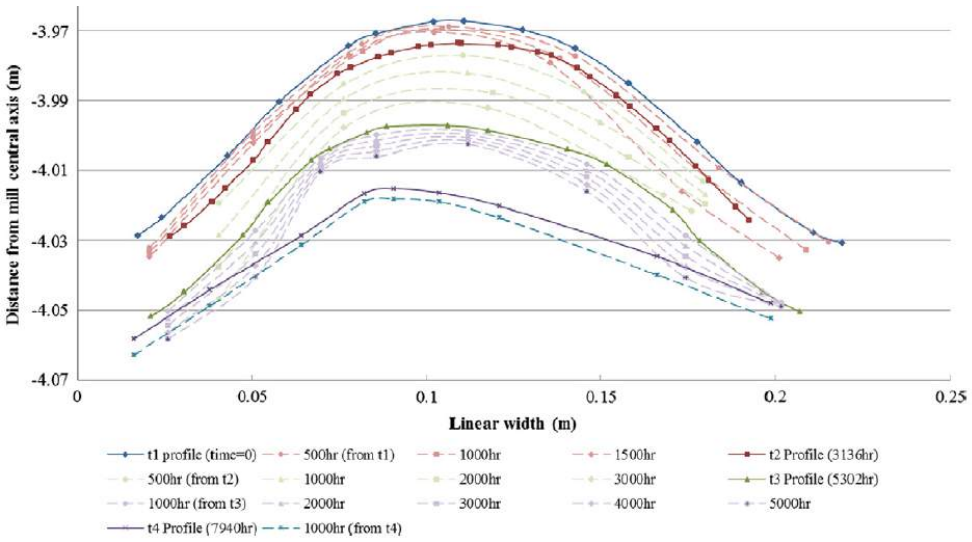

Figure 1.38: Measured (solid lines) and predicted (dashed lines) wear profiles. The mill rotates anticlockwise, i.e. from the left to the right with respect to the lifter. The predicted wear profiles were always estimated on the basis of a DEM simulation with a liner profile of the closest measured profile.

The figure 1.38 shows four measured wear profiles and the predicted profiles. The predicted profiles were restarted from each measured profile, i.e. the predicted profiles are based on a DEM simulation with the measured profile. The wear is then simply amplified by a constant factor for the different time intervals following a measured profile.

Chapter 2

DEM Ball Mill Simulation

In the previous chapter, we explained that the discrete element method is currently the most promising method to model the charge motion in ball mills. Nevertheless, different types of DEM models and a large spectrum of parameter values were used in the literature. In consequence, it seems absolutely necessary to *calibrate* the DEM model and to *validate* the numerical results before using this model as a predictive tool. In other words, the objective of this chapter is to determine the values of the simulation parameters, to assess the capability of the discrete element method to model the charge motion and to analyze the influence of the parameters on the results.

Therefore, this chapter starts with the description of the *experimental data* obtained in a 0.8 m diameter laboratory ball mill at the company Magotteaux International S.A. [Prignon & Lepoint, 2001]. To simulate the charge motion in this mill, a *DEM software* will be chosen in the second section of this chapter. In the third section, the *DEM model* and in particular, the modeling hypotheses and procedure will be explained by following the structure of the simulation control script. Finally, the *numerical results* will be presented in three stages: the elementary collision, the laboratory mill and the extension to the industrial mill.

2.1 Experimental Data

Experimental data is a fundamental requirement of computational engineering to calibrate the numerical parameters and to validate the results of the simulations. It was explained in the section 1.2.2, that the experimental data available for DEM simulations of ball mills are mainly power draw measurements, charge motion photographs and force on lifter measurements. In this section, we will focus on power draw measurements and charge motion photographs taken by [Prignon & Lepoint, 2001] at Magotteaux International S.A. .

First, the *experimental setup* will be described before selecting some of the *experimental results* for the model calibration and validation.

2.1.1 Experimental setup

The *experimental setup* is illustrated in the figure 2.1. It consists of a laboratory mill with removable liners which is closed at one end by a window of tempered glass. The mill is driven by an electric motor which is connected to the mill by a torquemeter.

(a) Laboratory mill supported on driving shafts with a Duolift liner and closed by an end wall of tempered glass.

(b) Torquemeter between the electric motor and the mill shell.

Figure 2.1: Experimental setup for the power draw measurement and the charge motion determination in a laboratory mill [Prignon & Lepoint, 2001].

The characteristics of the setup are the following ones:

- shell *diameter*: $D = 800$ mm
- mill *length*: $L = 400$ mm, with flat end walls
- *liner*: 1D liner, i.e. no variation of the liner height along the axial direction, with 7 different profiles of a 4 m diameter mill reduced by a factor 1/5 (geometrical similarity). Each liner is characterized by its exact geometry and its average diameter $\overline{D}$. This diameter is equal to the diameter of the circle which delimits the same area than the liner profile curve (figure 2.2). The liner plates in the laboratory mill are made of steel with a slightly rougher surface condition (striation due to metal cutting) than that of the real liner plates.
- *filling*: almost spherical steel balls having a diameter $d \approx 15$ mm, a material density $\rho_{\text{balls}} = 7640$ kg/m^3 and a bulk density $\rho_{\text{bulk}} = 4580$ kg/m^3. The filling ratio (with respect to the

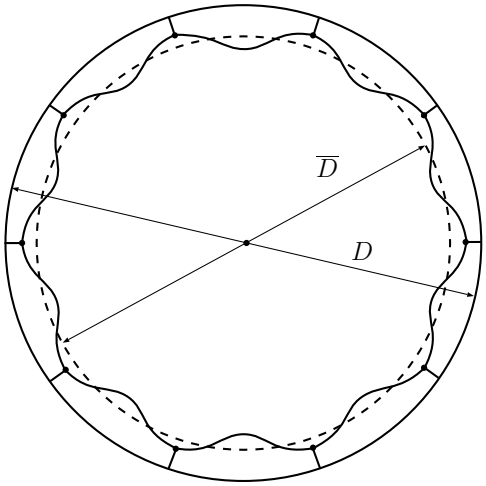

Figure 2.2: Illustration of the mill cross-section with the shell diameter D and the average diameter $\overline{D}$ of the 1D liner profile.

average liner diameter $\overline{D}$ and the bulk density) is equal to one of the following values: 20, 25, 30, 35 and 40 %. Only balls, i.e. no feed material, are inside of the mill.

- *rotation speed*: the rotation speed is deduced from the percentage of critical velocity with respect to the average diameter $\overline{D}$. It is equal to one of the following values: 60, 65, 70, 75 or 80 %.

For each of the 7 profiles and for each combination of the filling ratio and the rotation speed, photographs of the charge motion were taken with different shutter speeds (1/12, 1/25, 1/50 s and almost instantaneous photographs[1]). Moreover, the power draw was measured for each testing case with the torquemeter.

In the following section, we will justify our choice of the specific liner profiles, filling ratios and rotations speeds chosen for the parameter calibration and validation.

2.1.2 Experimental results

Concerning the *liner*, two different profiles will be chosen. Thus, the material parameters can be calibrated based on one liner profile and validated with the other profile. In this way, we can demonstrate that the model is able to simulate the charge motion in mills with different liners. Magotteaux's *Perfecto ABAB* liner (figure 2.3) will be used to calibrate the model as it was already used in a similar study [Sawley, 2003]. Therefore, the choice of this liner allows us to compare our results with the DEM results in this previous study. To obtain similar simulation

[1]The shutter speed of these photographs is not known but it is sufficiently high to instantaneously capture the balls which are seemingly at rest.

conditions, we also choose a filling ratio of 30% and a percentage of critical velocity equal to 70% or 80%; these values correspond to typical operating conditions. To capture the influence of the filling ratio, we will also consider the *Perfecto ABAB* liner with an increased filling ratio of 40 %.

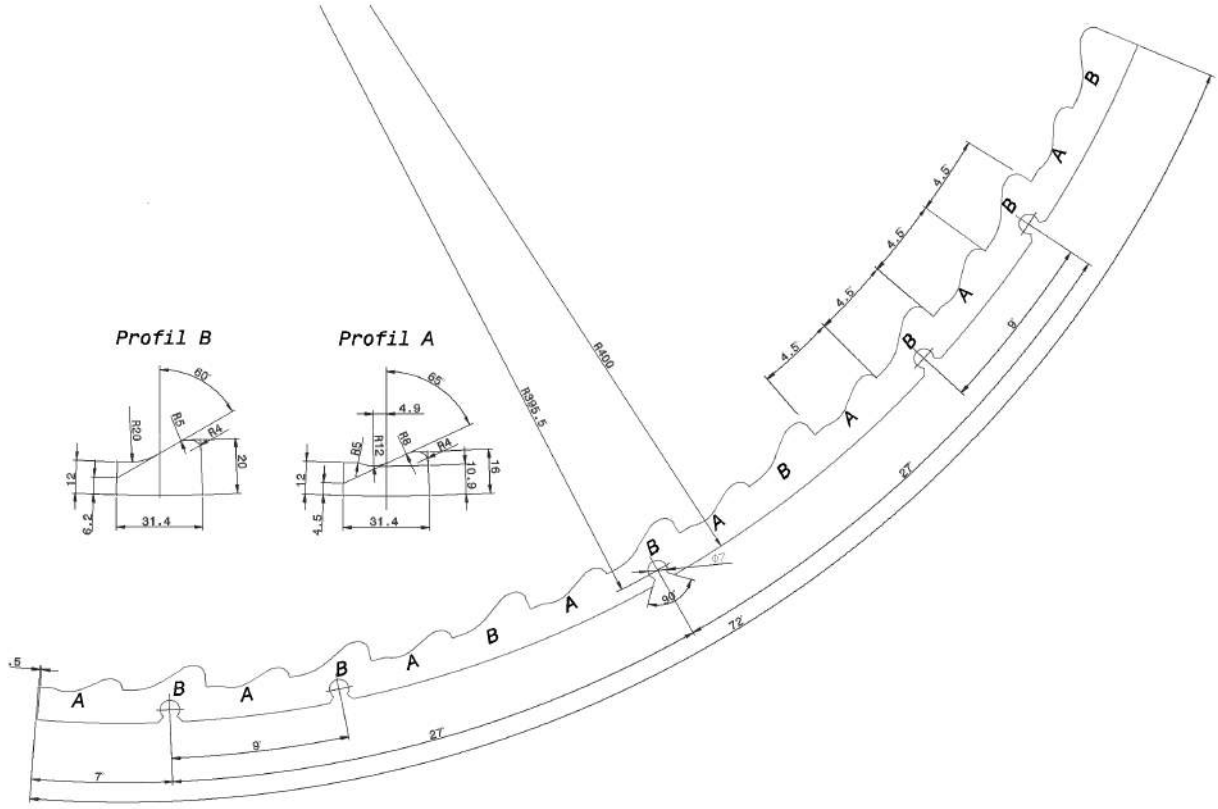

Figure 2.3: *Perfecto ABAB* liner profile in the 0.8 m diameter laboratory mill [Prignon & Lepoint, 2001].

In addition to the *Perfecto ABAB* liner, the *Duolift* (EU) liner (figure 2.4) will be examined to check if the DEM results are still valid for another liner geometry. This liner type was chosen due to its similarity to the liner, which will be used to calibrate the wear model in the following chapter.

The different calibration and validation cases considered in this study are summarized in the table 2.1. This table also contains the *average net power draw*[2] of the mill, i.e. the difference between the average power consumed by the charged mill in the pseudo steady state[3] and the average power consumed by the empty mill[4]. One may notice that the power increases with the

[2]The average net power draw has previously simply been called the power draw. Hereinafter, we will continue to use this shorter designation.

[3]As will be explained afterwards, the *pseudo steady state* is the state reached by the charge motion when its average characteristics do not change anymore, if the rotation speed of the mill remains constant.

[4]In fact, the power consumed by the rotation of the empty mill is negligible.

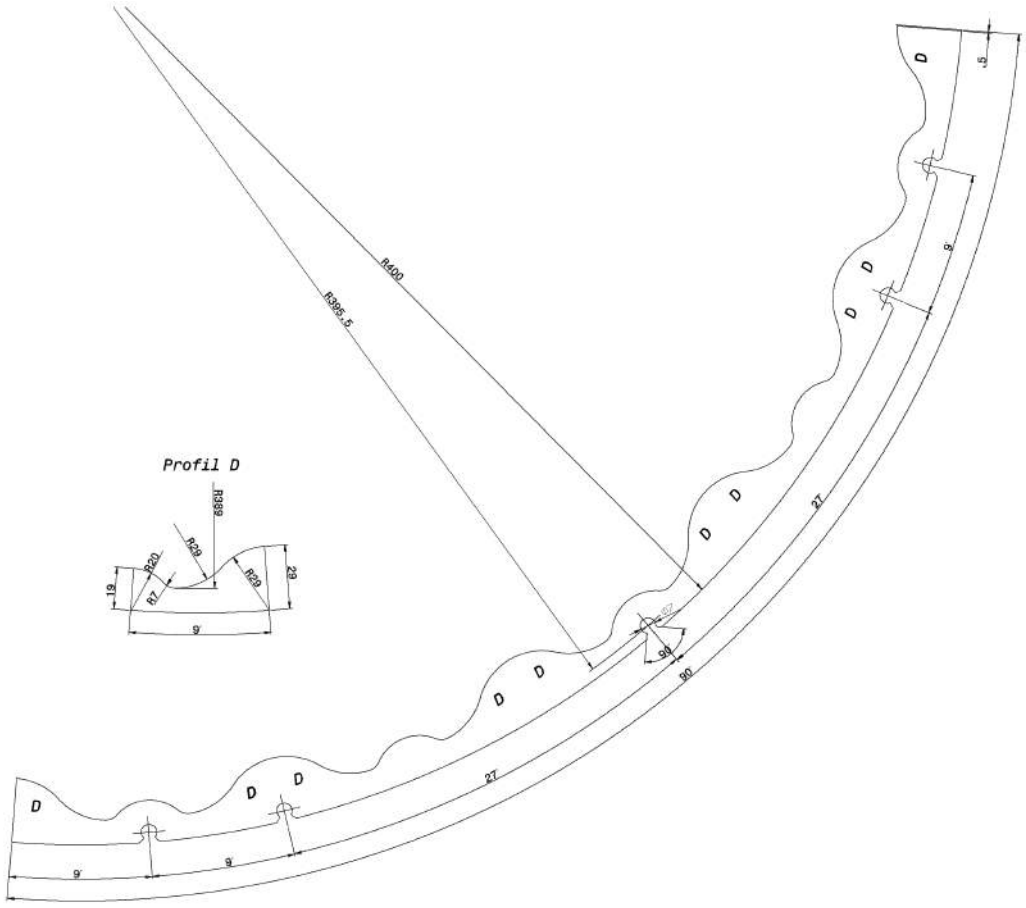

Figure 2.4: *Duolift* (EU) liner profile in the 0.8 m diameter laboratory mill [Prignon & Lepoint, 2001].

filling ratio and the rotation speed; this is generally true for sub-critical rotation speeds [Cleary, 2001a]. The power draw for the *Duolift* liner is approximately equal to the power draw for the *Perfecto ABAB* liner with the same operating conditions.

The photographs of the charge motion in the different cases are represented in the figure 2.5. To focus on the general characteristics of the charge motion, we chose only the pictures obtained with a 1/12 s exposure time. Due to this relatively long exposure time, the pathlines of the balls are visible. In consequence, these pictures give a better idea about the average charge motion than the instantaneous photographs. Obviously, it is difficult to extract quantitative data of these photographs due to the variable density of the balls in space, especially in the cataracting region, and the quality of the pictures, in particular the finite depth-of-field.

We tried, however, to draw the contour of the charge in each mill and superimposed them in the figure 2.6. Hence, the charge is far more dispersed, i.e. the void ratio increases, at *higher rotation speed* (e.g. figures 2.5a and 2.5b). In other words, the rotation speed increases the number of cataracting balls and the shoulder angle. This is also true for the filling ratio, which

(a) Case 1.

(b) Case 2.

(c) Case 3.

(d) Case 4.

Figure 2.5: Photographs of the charge motion for the different testing cases in the pseudo steady state with an exposure time of 1/12 s [Prignon & Lepoint, 2001].

Name	Liner	Filling ratio [%]	Percentage of critical velocity [%]	Power [W]
Case 1	Perfecto ABAB	30	70	1,449
Case 2	Perfecto ABAB	30	80	1,656
Case 3	Perfecto ABAB	40	80	1,893
Case 4	Duolift	30	70	1,429

Table 2.1: Experimental cases used to calibrate (case 1) and validate (cases 2, 3 and 4) the numerical model.

increases these characteristics even more. While the rotation speed has only a negligible influence on the toe angle in our testing cases, the *filling ratio* clearly increases the toe angle. Finally, the difference in the charge motion resulting from changing the liner profile is relatively small. Nevertheless, the charge cloud for the *Duolift* liner seems to be pushed slightly inward, i.e. closer to the center of the mill, with respect to the *Perfecto ABAB* liner rotating with the same operating conditions. This might also explain why the power draw of the *Duolift* liner is marginally lower than the power draw of the *Perfecto ABAB* liner (for the same operating conditions). In fact, the power draw can be calculated on the basis of the position of the center of gravity of the charge. If this point is closer to the center of the mill along the horizontal direction, the torque necessary to rotate the mill is lower. Hence, the power draw for the *Duolift* profile is lower than the power draw of the *Perfecto ABAB* profile.

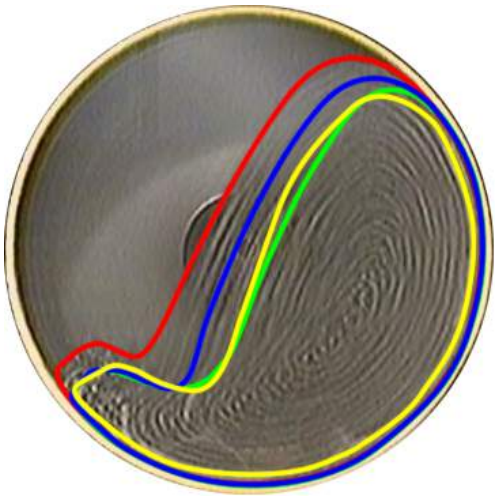

Figure 2.6: Superimposed charge contours for the cases 1 (green), 2 (blue), 3 (red) and 4 (yellow) with the background being the case 3. This contour is not uniquely defined due to the decreasing position density of cataracting balls and the quality of the pictures.

For the sake of completeness, the table 2.2 contains the mean diameter of the liner profiles from which the number of balls and the rotation speed for each testing case were deduced. The lower mean diameter of the *Duolift* liner might explain why the charge seems to be pushed more

to the center of the mill with respect to the *Perfecto ABAB* liner.

Name	Mean diameter [mm]	Number of balls [-]	Rotation speed [rpm]
Case 1	772	19,054	33.70
Case 2	772	19,054	38.51
Case 3	772	25,406	38.51
Case 4	763.6	18,642	33.88

Table 2.2: Mean liner diameter, number of balls and rotation speed of each testing case.

2.2 DEM Software

Even though DEM simulations might initially seem to be rather simple and more intuitive than Eulerian methods, like classical FEM or CFD, their complexity, however, rises from the typical problem size, which requires not only sophisticated algorithms but also efficient programming techniques. Instead of implementing a new DEM solver from scratch, it seems therefore to be more reasonable to choose an existing software and to modify it in order to meet our requirements. In this section, we will explain for what reasons, the YADE (Yet Another Dynamic Engine) software was chosen to simulate the ball mill.

Currently, a large number of DEM solvers exist[5]. Some of these programs have successfully been used to model the charge motion in ball mills:

- EDEM[6] (DEM Solutions Ltd.) is one of the leading commercial DEM solvers.
- PFC[7] (Particle Flow Code, Itasca Consulting Group Inc.), initiated by P.A. Cundall, is a commercial alternative to the EDEM solver.
- LIGGGHTS[8] (LAMMPS Improved for General Granular and Granular Heat Transfer Simulations) is an extensive open source discrete element solver based on LAMMPS, a classical molecular dynamics code, which adds moving geometry meshes and classical granular contact laws, like the spring-slider-damper law or the Hertz-Mindlin law. LIGGGHTS is programmed in C++ and uses an MPI parallelization with dynamic load balancing (grid collision detection algorithm) to reach high performance. Simulations are controlled by a scripting language particular to the software or by a quite limited PYTHON wrapper.
- YADE [Šmilauer et al., 2014] is a very versatile open source software mainly focused on DEM simulations. The program is written in C++ with an OpenMP parallelization (axis-aligned bounding box collision detection algorithm) controlled by PYTHON scripts.

The requirements related to the choice of the software can be grouped into two categories: versatility and performance. We consider *versatility* to be the ability of the software to solve our problem, i.e. its ability to adapt its general functionality to our particular case. Versatility is therefore not only defined by the existing features of the software but also by the potential simplicity of adding new features. Especially due to the wear modeling in the next section, it is necessary to have a good low-level control of the code, e.g. for the synthetic data extraction. For this reason and their cost, *open source* software seems to be a better choice than commercial software. Its drawback is usually the more complex usage, which is compensated by a better understanding of the underlying principles in the long run. Considering again the main programs

[5] http://en.wikipedia.org/wiki/Discrete_element_method
[6] http://www.dem-solutions.com/
[7] http://www.itascacg.com/software/pfc
[8] http://www.cfdem.com/liggghts-open-source-discrete-element-method-particle-simulation-code

used for DEM ball mill modeling, EDEM and PFC can be eliminated as they are commercial software.

Furthermore, YADE was designed with the objective of being extremely versatile [Kozicki & Donzé, 2009]. In fact, it is build on a very general base structure which assembles packages. Thus, adding a new feature to the software, like an element shape or a material law, does not require to change the entire program but only requires implementing and loading a new package into the base structure. Moreover, this structure is designed in such a way that the scene construction, the simulation and the post-processing can be managed by PYTHON scripts. These scripts are able to read and modify the data, e.g. the velocity of a particle, during the simulation, while the C++ code assures the performance. Such a structure turns the software into a very flexible tool. In LIGGGHTS, the PYTHON wrapper is far less developed and less connected to the underlying C++ code than in YADE, which makes their interaction more difficult. In terms of versatility, it should also be mentioned that LIGGGHTS is a relatively large software with respect to Yade, i.e. it contains around 8 times more source code files (around 8000) than YADE. As a result, adding or modify the source code is potentially more time-consuming in LIGGGHTS.

Nonetheless, LIGGGHTS has a better performance than YADE with respect to the computation time, probably due to the spatial decomposition of the domain for the collision detection combined with the MPI parallelization [Cleary & Sawley, 2002]. In fact, we carried out a short benchmark study to compare their relative performance. The study was premised on exactly the same simulation which will be explained afterwards, but the liner mesh was generated differently[9]. Nevertheless the same data was used in both programs, i.e. the same mesh of the mill, the same number of balls, the same material parameters, the same time step, the same simulated time, ... For a 10 s simulation of a ball mill meshed with 20,224 facets and containing 20,000 balls with a time step equal to $5 \cdot 10^{-6}$ s, the calculations took 3.46 hours in LIGGGHTS and 8.65 hours in YADE. On average, LIGGGHTS is thus around 2.5 times faster than YADE.

In conclusion, LIGGGHTS and YADE are versatile enough to simulate the charge motion in ball mills. Despite LIGGGHTS' superior performance, we are, however, constrained to use YADE because of its higher versatility (PYTHON interface and straightforwardness of the C++ source code) and the limited time span of this project[10].

[9] Instead of extruding the mesh and closing its ends by infinite planes, a surface mesh of the entire mill was created. Therefore, it contains more elements and the computation time is longer than for the mesh, which will be used in the following calibration and validation study.

[10] This last reason is especially true for the wear simulations in the third chapter, which require to have a very deep knowledge of the low-level source code in order to implement the wear models and to retrieve the resulting wear values. Due to YADE's extremely flexible programming structure and its reduced size with respect to LIGGGHTS, it allows acquiring this knowledge quicker than with LIGGGHTS. In the long term, it might, however, be more interesting in terms of performance to adapt the principles introduced in YADE to LIGGGHTS.

2.3 DEM Model

To predict the charge motion and the power draw of the laboratory mill, a standard procedure was developed by combining CAD (FREECAD and/or CATIA), meshing (GMSH), DEM (YADE), data analysis (MATLAB, OCTAVE or PYTHON) and visualization (PARAVIEW) software. This procedure is obviously centered on the DEM solver YADE. A simulation in YADE is controlled by a PYTHON script. To simplify the explanations, we will therefore follow the structure of this control script, which is included[11] in the appendix B.

The modeling hypotheses and procedure will be described by starting with the definition of the *material* (contact law) and the *geometry* (mill and filling), followed by the description of the *simulation* and the *post-processing*.

2.3.1 Material

In DEM charge motion simulations of ball mills, the material characteristics are the *density* of the filling material, the *contact model* and the *contact parameters*.

Density

As the laboratory mill is only filled with steel balls having a high mass percentage of chromium (around 20 %), their *density* can simply be measured; it is equal to around 7640 kg/m^3.

Contact law

According to our explanation in the section 1.2.2, the *soft-particle linear spring-slider-damper contact law* seems to be the least sophisticated law able to model the collisions with sufficient accuracy, while, however, remaining an idealization. To ensure that this law is implemented in line with our expectations, we added our *own contact law* (`SprSldDmpPM.hpp` and `SprSldDmpPM.cpp`) to YADE by creating a new material package. It is based on the theoretical definition in the section 1.2.1 and the existing viscoelastic law in YADE (`ViscoElasticPM.hpp` and `ViscoElasticPM.cpp`). To offer the reader full insight into our contact model, it was added in the appendix C. The critical points will, however, be summarized hereinafter.

Tangential spring The tangential spring component of the force is the most complex component of the model since it depends on the *history* of the interaction (see the integral in equation 1.9).

[11] It is questionable whether this script should be included in this report. In contrast to numerous articles about DEM validation, we want, however, give the reader the opportunity to understand the slightest detail of this validation study.

On the one hand, the spring stores or loses energy due to the relative motion between the elements. In consequence, the tangential velocity can not simply be integrated in global coordinates in order to determine the strain of the spring. This problem is solved by rotating the spring force simultaneously with the colliding elements [Šmilauer et al., 2014, p. 133].

On the other hand, this force has to be changed properly, when two elements *slide* over each other. In the existing implementation of the viscoelastic contact law (`ViscoElasticPM.hpp` and `ViscoElasticPM.cpp`), this interaction was handled in an incoherent way. In fact, elements started to slide, when the spring component of the tangential force exceeded the friction limit *independently of the viscous component*[12]. In the new material law, we added this tangential viscous force component to the friction limit test and ensured that the history of the tangential spring component is adapted appropriately.

Power dissipation Besides the forces, the power dissipated during the collisions is calculated in the material law. Essentially three different mechanisms dissipate power: normal damping, tangential damping and sliding by Coulomb friction. Nonetheless, there also exist two other sources of power dissipation.

On the one hand, the tangential spring stores energy during the collision of two bodies. If, however, these bodies are not overlapping anymore, the energy stored in the spring is simply lost, i.e. dissipated.

On the other hand, the tangential spring force has to be rotated, as explained earlier, since its energy is not modified, when the relative position (and orientation) between the two contacting bodies is unchanged. This rotation is an approximate rotation, which may lead to the artificial creation of numerical energy. Fortunately, only small quantities of energy are created numerically, i.e. at most around 5% (for the material parameters used hereinafter). Due to the general acceptance of the rotation algorithm [Šmilauer et al., 2014] (where other authors are cited) and the moderated quantities of numerical energy, the rotation algorithm was not improved.

Hence, the total power dissipated in the system can be calculated by the following formulas, which are written by using the notations of the section 1.2.1:

- power dissipated along the normal direction by the normal damper, called *normal power*:

$$P_{\text{normal}} = c_n \, v_n^2 \tag{2.1}$$

- power dissipated along the tangential[13] direction (when the friction limit has *not* been reached), called *tangential power*:

$$P_{\text{tangential}} = \mathbf{F}_t \cdot \mathbf{v}_t \quad \text{if} \quad F_t < \mu \, F_n \tag{2.2}$$

[12] This problem was already partially pointed out but not entirely fixed: `http://www.mail-archive.com/yade-users@lists.launchpad.net/msg01391.html`

[13] Notice that this attribute (i.e. *tangential*) might be ambiguous since the sliding force also acts in the tangential direction. Nevertheless, we did not find an adjective, which describes more accurately the power dissipated along the tangential direction by tangential damping, lost contact and approximate rotation of the tangential spring force.

- power dissipated by sliding (when the friction limit has been reached), called *sliding power*:

$$P_{\text{sliding}} = \mathbf{F}_t \cdot \mathbf{v}_t \quad \text{if} \quad F_t \geq \mu \, F_n \tag{2.3}$$

In addition to the tangential damping power, it is important to notice that $P_{\text{tangential}}$ also includes the power transferred to and from the tangential springs, which is not dissipated because of the elasticity of the spring. As a result, this power component $P_{\text{tangential}}$ includes the artificial creation of numerical energy by the approximate rotation of the spring force as well as the power which is lost, when the contact between bodies ceases even though the tangential spring is still stressed. This explains why, the tangential power dissipation is not simply equal to $c_t \, v_t^2$, the tangential damping power. In the pseudo steady state, the power $P_{\text{tangential}}$ becomes, however, equal to the total power *dissipated* along the tangential direction (without sliding) since the total energy stored by all the tangential springs in the simulation does not change on average (by definition of the pseudo steady state).

Defining the previous components is finally a way of *controlling the artificial creation of energy* in the system. Since the rotation power[14] accounts for the power injected into the system and since the sum of the previous power components accounts for the power dissipated in the system, their difference directly gives the artificial power.

Wear Different wear models were also added to the material law in order to calculate the wear accumulated during the interactions. These models will be explained in the next chapter.

Contact parameters

The spring-slider-damper contact law contains *5 parameters*: the normal stiffness k_n, the tangential stiffness k_t, the normal damping coefficient c_n, the tangential damping coefficient c_t and the coefficient of friction μ. Due to this important number of parameters, it would be delusional to use different values for ball/ball and ball/mill interactions at the current stage of the ball mill modeling. The remaining 5 parameters will be determined in the section 2.4 by following the below-mentioned steps:

- initially, we will adopt the *material parameters*, which were used in a previous DEM study of the charge motion in the laboratory mill, i.e. $k_n = k_t = 10^5$ N/m, $\varepsilon_n = 0.3$ (coefficient of normal restitution for a sphere/sphere collision, i.e. $c_n = 18.6$ Ns/m according to the appendix A.1), $c_t = c_n$, $\mu = 0.75$ [Sawley, 2003]. These values were also used in numerous studies by Cleary, i.a. [Cleary et al., 2003], who, however, chose a higher value for the stiffness in general, i.a. around 10^6 N/m, which is certainly related to the analysis of larger mills (overlap limitation of heavier balls).

[14]The definition of the *rotation power* will be provided in the section 2.3.4. In simple words, it is the power necessary to rotate the mill.

- based on the order of magnitude of these values, we will first *validate the material law by existing analytic solutions* of elementary collisions to ensure the correctness of the implementation (trajectory and dissipated power).
- the next step is to understand the *influence of the material parameters on the interaction of the balls*, in particular to limit the *overlap* of the colliding bodies and to choose a *time step*, which allows us to recover the coefficient of restitution.
- after the elementary collision analysis, we will study the influence of the material law on the *global charge motion and the power draw* of the mill to achieve the best correlation between the model and the reality.

2.3.2 Geometry

The laboratory ball mill will be modeled by a *full-scale 3D model* in order to take into account the influence of the end walls and the increased shear strength of the charge in 3D.

The *mill* will be represented geometrically by three elements: two flat end walls and the shell liner. On the one hand, the *end walls* are modeled by infinite planes to reduce the computation time. These planes rotate at the same speed than the mill. On the other hand, the *shell liners* are modeled by surface meshes. The *Perfecto ABAB* liner and the *Duolift* liner have 1D profiles, i.e. there is no variation of the liner profile along the axial direction. As a result, the computation time can be reduced by choosing an efficient surface meshing technique, which reduces the number of facets.

More precisely, the profile of a liner plate[15] is first *drawn* by a conventional CAD software (FREECAD or CATIA), and exported into the standard exchange file format `.step` (figure 2.7).

This profile curve is then *discretized* into line segments. In DEM simulations, the surface mesh simply *approximates the geometry* and has no significant influence on the results like in the classical finite element method, where the mesh is also the basis of the displacement field interpolation. For this reason, the necessary mesh refinement depends on the production and assembly tolerances of the liner plates, which are equal to around 1 mm (deviation of the liner profile curve from the theoretical curve). The objective of the profile curve discretisation is therefore to obtain the best approximation with the smallest number of points. To reach this objective, we implemented a *1D curvature meshing* algorithm in MATLAB (or OCTAVE). In contrast to standard mesh generators, in which the average element size is prescribed, this algorithm adds more elements where the curvature of the shape is high. In this way, the geometry can be better approximated with less elements. To convert the `.step` geometry file into data points, we used GMSH. A very fine mesh (around 1000 vertices) was creates in this software and exported in

[15] Strictly speaking, the *Perfecto ABAB* liner is composed of two different plates, i.e. the A and the B plates. Nevertheless, we designate by *liner plate* the (unique) entity which is periodically repeated in space around the rotation axis of the mill. For the *Perfecto ABAB* liner, a liner plate is thus the combination of an A and a B plate.

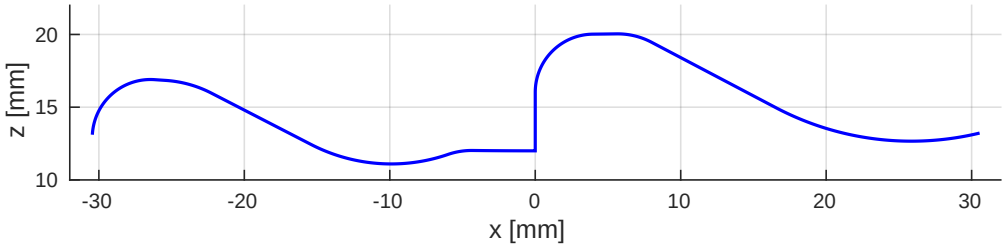

Figure 2.7: Profile curve of the *Perfecto ABAB* liner plate. The curve is plotted in such a way that the rotation axis (aligned with the y-axis) of the mill passes through the point (0, 0, 400) mm, i.e. the circle of the mill shell (800 mm diameter) passes through the origin. Moreover, the profile curve is contained in the lower 9° sector of this circle, whose bisector is aligned with the z-axis.

the `.mesh` format. This file was then read in MATLAB and a restricted number of vertices was selected on the basis of the curvature criteria.

Although we mentioned that the mesh has only a geometrical influence, its fineness might also have a dynamical consequence. As a matter of fact, typical surface meshes are by definition discrete, i.e. different facets are assembled along edges and vertices. In DEM simulations with spheres and surface meshes, it might happen that a sphere does not collide with the facet as such but rather with one of its edges or vertices, i.e. the normal projection of the center the sphere onto the plane of the facet is not located on this facet. In YADE, this *regularization problem* is simply solved by allowing multiple collisions. Hence, if a sphere collides with the edge between two neighboring facets, the program handles this case as if the sphere collides with the edge of the first facet and then with the edge of the second facet, even though these edges are geometrically identical. The same is true for the collision with a vertex, where the sphere might, however, be in potential contact with more than 2 facets (usually 6 in 3D meshes with triangular facets). In conclusion, the contact locally stiffens since more than one spring and one damper (along the normal or tangential direction) determine the interaction forces. To check whether the mesh refinement has an influence on the results or not, we created three discretizations of the *Perfecto ABAB* liner plate profile curve (figure 2.8). Only a medium refined mesh was generated for the *Duolift* liner plate profile curve (figure 2.9). Interestingly, less vertices were necessary to discretize the *Duolift* liner (for a same circular sector) with a specified accuracy due to its lower average curvature.

These curves were then extruded along the axial direction to obtain the surface mesh of one liner plate. As YADE contains only triangular boundary elements and as the mesh has only a geometrical importance (except for the regularization), the initial liner profile curve was simply duplicated, translated and connected to the initial curve by triangular facets (figure 2.10). For 2D liners, whose height changes along the axial direction, the surface mesh of the liner plate can simply be obtained by classical average element size meshing, even though the number of elements rises quickly with the refinement.

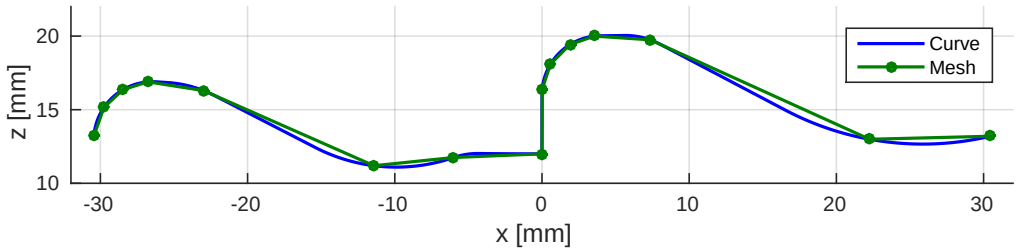

(a) Coarse mesh: 15 vertices.

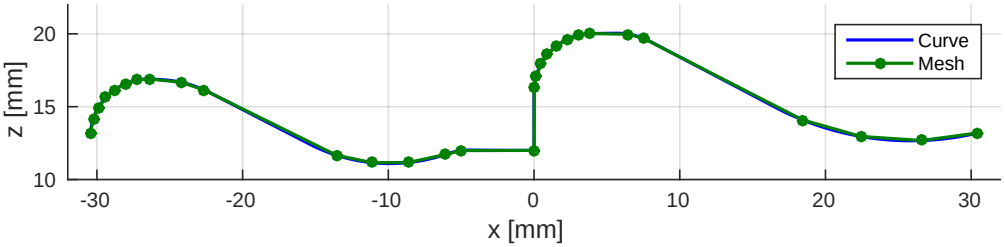

(b) Medium mesh: 30 vertices.

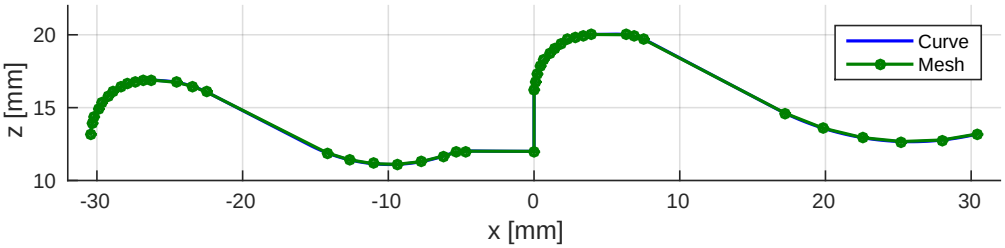

(c) Fine mesh: 45 vertices.

Figure 2.8: Profile curve of the *Perfecto ABAB* liner plate and its discretization based on curvature with increasing refinement. The curve is plotted in such a way that the rotation axis (aligned with the y-axis) of the mill passes through the point (0, 0, 400) mm, i.e. the circle of the mill shell (800 mm diameter) passes through the origin. Moreover, the profile curve is contained in the lower 9° sector of this circle, whose bisector is aligned with the z-axis.

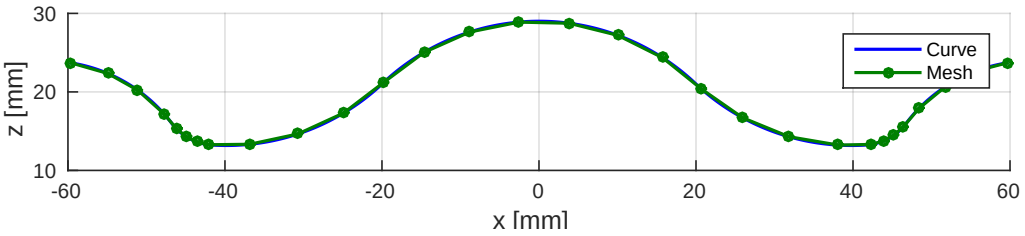

Figure 2.9: Profile curve of the *Duolift* liner plate and its medium discretization based on curvature (30 vertices). The curve is plotted in such a way that the rotation axis (aligned with the y-axis) of the mill passes through the point (0, 0, 400) mm, i.e. the circle of the mill shell (800 mm diameter) passes through the origin. Moreover, the profile curve is contained in the lower 18° sector of this circle, whose bisector is aligned with the z-axis.

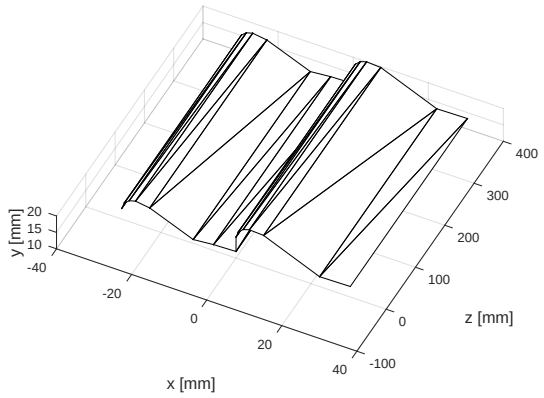

Figure 2.10: Axial extrusion of the coarse *Perfecto ABAB* liner profile curve discretization (figure 2.8a) to illustrate the generation of the liner plate mesh composed of triangular facets.

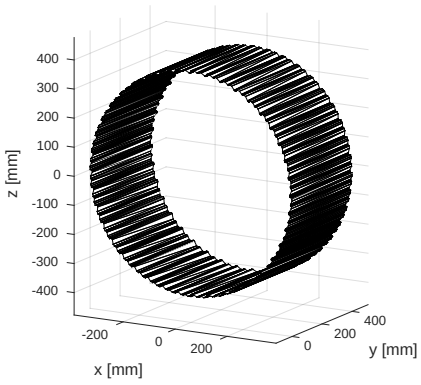

Figure 2.11: Assembly of the coarse liner plate meshes of the *Perfecto ABAB* liner to obtain the entire shell liner mesh represented in the coordinate system which will be used throughout the calibration and validation study.

Finally, the surface mesh of the liner plate is reproduced 40 times for the *Perfecto ABAB* liner and 20 times for the *Duolift* liner before being rotated[16] to assemble the mesh of the entire shell liner (figure 2.11). This mesh is then saved again in the `.mesh` format, which is imported into YADE. The coarse, medium and fine meshes of the *Perfecto ABAB* liner contain 1120, 2320 and 3520 triangular facets. The equivalent number of quadrangular elements in the medium mesh is thus almost identical to the 1200 quadrangular elements, which were used in a previous study [Sawley, 2003]. The *Duolift* liner mesh contains only 1120 triangular facets (same number of facets than in the coarse *Perfecto ABAB* liner mesh) due to its reduced average curvature.

Concerning the filling material, the *balls* are the only mobile elements inside of the mill. Geometrically, they will be modeled by spherical discrete elements having a diameter of 15 mm. Their initial positions are defined by filling the mill from the bottom to the top along horizontal planes while avoiding any initial contact between the balls and the liner (figure 2.12). In consequence, the balls will first fall during a fraction of a second under the influence of gravity before colliding with the liner.

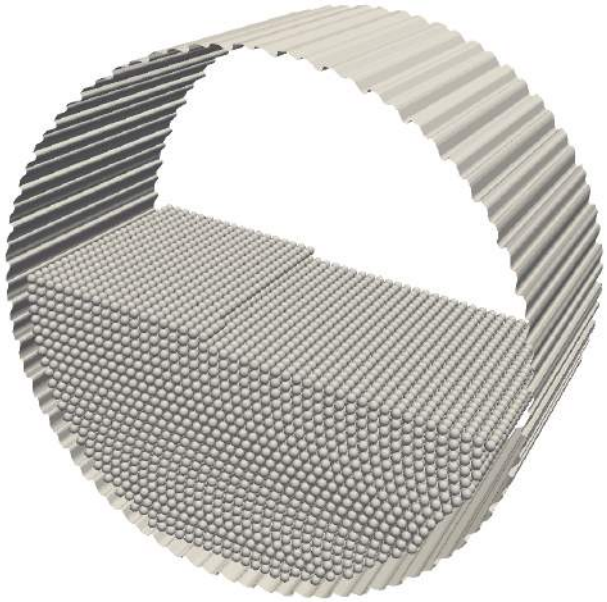

Figure 2.12: Initial positions of the balls based on the simulation script in the appendix B with the medium *Perfecto ABAB* liner mesh.

[16] Instead of creating each unique liner plate, it is also possible to draw the complete liner profile curve (i.e. not the liner *plate* profile curve), to discretize it and to extrude it along the axial direction. We did not choose this method, since it does not necessarily allow us to map all the lifters on one master lifter since the relative position of each vertex in each liner plate mesh might be different. This technique will, however, only be used in the next chapter to achieve a better statistical representativity of the wear data during the liner wear analysis.

2.3.3 Simulation

When the material and the geometry have been defined, the interaction between the bodies can be calculated by starting the simulation. In YADE, a simulation takes the form of different engines, which are called periodically at each time step until the total simulated time is reached. Therefore, it is necessary to define the different *simulation engines*, the *time step*, the *total simulated time* and the *computational requirements* of the simulation.

The *simulation engines* are for instance used to detect the collisions, to apply the contact law, to perform the time integration, ... Since the underlying principles of these engines have already been explained[17], we will only focus on two particular engine features, which are the reasons for the ball collisions: gravity and the rotation of the mill. On the one hand, *gravity* is simply introduced in the model by applying a constant acceleration equal to -9.81 m/s^2 along the z-axis. On the other hand, the *rotation engine* is responsible for rotating the mill at the constant rotation speed, which was defined in the section related to the experimental data. Looking along the y-direction in the figure 2.11, the liner will rotate anticlockwise, i.e. the less aggressive side of the liner profile lifts the charge, which is typical for liner profiles in cement mills. The rotation will start immediately with simulation. In other words, no simulation time will be wasted on simulating the resting phase[18] of the charge under the influence of gravity since we are interested in the pseudo steady state characteristics of the ball charge motion.

As we explained earlier, the *time step* will be chosen by finding the compromise between the computation time and the recovery of the restitution coefficient to integrate the individual collisions as best as possible (section 2.4.1). In the earlier study of the laboratory mill [Sawley, 2003], the time step Δt was equal to 10^{-5} s, which ensured that each collision lasted for at least 50 time steps according to the author.

The total *simulated time* should be sufficient to reach the pseudo steady state of the charge motion and to sample enough data to obtain representative averages of the charge motion and the power draw. The necessary simulated time has thus to be determined by the simulation itself (section 2.4.2). In the previous study [Sawley, 2003], a total simulated time of 10 s was used and the charge motion started to stabilize after around 2.5 s, i.e. after around 1.5 rotations.

In terms of the *computational requirements*, it is important to notice that DEM simulations are usually run in parallel on several processors to reduce the computation time. YADE solves this problem by an *OpenMP* shared memory parallelization. Due to the splitting of the problem in sub-problems and their recombination, the computation time on several computation cores is not simply equal to the computation time on one core divided by the total number of cores used for the simulation. To minimize the computation time, we studied the evolution of this time as a function of the number of cores. The reference simulation is based on the PYTHON control script in the appendix B used with the medium mesh of the *Perfecto ABAB* liner. The simulations were

[17] Some additional explanations can, however, be found in the comments of the PYTHON control script in the appendix B.

[18] The resting phase describes the evolution of the ball positions from their unstable initial positions to their stable position after colliding with the liner (at rest) under the influence of gravity.

run on a single Intel Core i7-4790 processor clocked at 3.6 GHz with 4 cores virtually divided into 8 cores by *hyper-threading*, i.e. Intel's simultaneous multithreading implementation. During a simulation only around 250 MB of RAM were required. The figure 2.13 shows that using two cores leads to the highest decrease in calculation time with respect to previous calculation time (one core less), while using more than 4 cores has no real advantage. It seems that running simultaneously 4 simulations in parallel on 2 cores each or running 2 simulations in parallel on 4 cores each are the best strategies to run a large number of simulations in a minimum amount of time. Nevertheless, this conclusion neglects the processor load of the operating system and the other processes, as well as the influence of the hardware. In particular, since hyper-threading is the *virtual* duplication of parts of the hardware (loosely speaking), it is questionable whether running *simultaneously* 2 simulations in parallel on 4 cores each is actually two times faster than running these simulations *successively* on 4 cores and having 4 (virtually) idle cores; this would explain why running the simulation on more than 4 cores led to no significant improvement (in addition to the problem splitting/combination overhead). A compromise[19] is therefore to run 3 simulations simultaneously on 2 cores each, which leaves 2 cores idle to work with other programs.

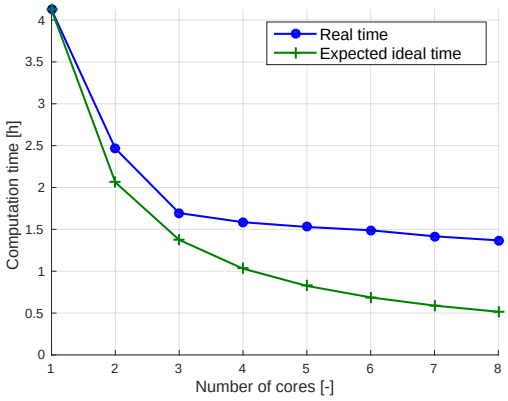

Figure 2.13: Computation time (real time, i.e. not CPU time) required to run the script, which is provided in the appendix B, with the medium *Perfecto ABAB* liner mesh as a function of the number of cores. The other cores were idle during the simulation except for the execution of the operating system and the background processes. The expected ideal time, which is equal to the simulation time on one core divided by the respective number of cores, has also been represented.

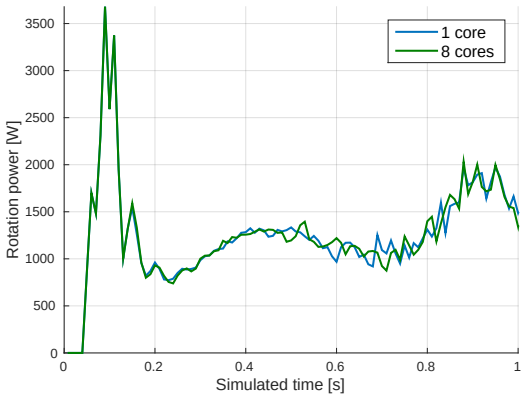

Figure 2.14: Illustration of the nondeterminism, when large scale DEM simulations are executed in parallel on several processing cores. The rotation power was calculated with the control script in the appendix B and the medium *Perfecto ABAB* liner mesh on 1 or 8 cores. Initially both results are the same but their difference increases gradually.

Finally, it is interesting to notice that DEM simulations, which are executed in parallel, are *nondeterministic* [Šmilauer et al., 2014]. Because of the finite precision arithmetic of floating

[19] It is certainly possible to analyze this problem more in detail but it is not critical for this study, which is why we will not continue its analysis.

point numbers, which are combined pseudo-randomly on different computation cores, the exact same simulation input might lead to different results. The figure 2.14 shows the power draw of the mill (rotation power[20]) obtained by the simulations on 1 core and on 8 cores of the previous study of the computation time. It is clearly visible that the results are initially identical but diverge progressively. Fortunately, their mean values in the pseudo steady state, i.e. the averages of the recorded rotation power from 2.5 to 5 s (simulated time), remain almost identical: $P_{1\text{ core}} = 1399.8$ W and $P_{8\text{ cores}} = 1396.8$ W.

2.3.4 Post-processing

Since the experimental data consists of photographs of the charge motion and power draw measurements, the same data should be exported from the simulation. This data, which will be defined more precisely hereinafter, is recorded at a reduced *sampling frequency*, i.e. not at each time step, due to the large data creation in DEM simulations. The sampling frequency should therefore be sufficiently low to reduce the storage requirements while being sufficiently high to obtain representative data of the simulation. The most stringent criteria rises from the creation of an animation of the simulation. In fact, if the sampling frequency is too high, it might be impossible to determine the rotation direction based on the profile movement alone. This behavior is known as the *reverse rotation effect*, e.g. of filmed car wheels. For the experimental data, the critical sampling period is slightly larger than 0.01 s. Hence, a reasonable choice[21] seems to be a recording period equal to $\Delta t_{\text{rec}} = 0.01$ s.

Concerning the charge motion, the position and the velocity of the balls and facets are saved in the `.vtu` VTK format for unstructured meshes. These files can be post-treated in the PARAVIEW visualization application to create expressive illustrations of the charge motion by rendering the spheres and the facets (figure 2.15). Moreover, the coordinates of the spheres are also saved explicitly to perform some data analysis in MATLAB. For instance, it is possible to determine if the pseudo steady state has been reached by analyzing the global center of gravity of the spheres over time. Once the steady state has been reached, the general charge motion can be analyzed by a more sophisticated method, i.e. by position density plots [Kalala, 2008]. *Position density plots* show the number of occurrences of balls at a specific position in the mill. More precisely, the space taken up by the mill in the *xz*-plane is discretized by a rectangular plane grid. For each cell, the number of balls having their center projection in this specific cell is accumulated for all the time steps. After dividing this number by the total number of recorded time steps,

[20] The *rotation power* will defined in the next section. In simple words, it is the power necessary to rotate the mill.

[21] Notice that it might be tempting to use an even smaller sampling period to increase the representativity of the results, which would then allow to reduce the total simulated time. More precisely, this strategy can be explained as follows. Hereinafter, the duration, over which the data will be sampled and averaged, will be equal to 2.5 s. Since the transient component of the charge motion disappears after around 2.5 s, the total simulated time will be equal to 5 s. To reduce this simulated time, one may try to reduce the sampling duration to 2 s and the sampling period Δt_{rec} to $8 \cdot 10^{-3}$ s, hence, obtaining the same number of sampling points. Nevertheless, this strategy focuses more and more on the local behavior of the charge motion instead of its global average motion. Therefore, it is impossible to reduced the sampling period and the simulated time while maintaining the representativity of the results unchanged.

we obtain the position density plot (figure 2.16). The cell size will be equal to the shell diameter divided by 150; this value leads to a sufficiently detailed representation (more cells) with a medium density (less cells). The position density plot has the additional benefit of introducing a relatively objective way to determine the influence of the charge motion to different parameters, like the material parameters or the operating conditions. In fact, it is possible to plot the *contour curve* (represented in red in the figure 2.16), which separates the main charge zone from the zone where the balls are less likely to occur. This curve will be called the *position density limit*. The limiting value has been chosen equal to the average of the average number of balls per cell over all the non-zero occurrence cells[22] divided by 10. For instance, in the figure 2.16, the average of the average number of balls per cell over all the non-zero occurrence cells is equal to around 2.5. Hence, the limiting value in the contour plot is 0.25.

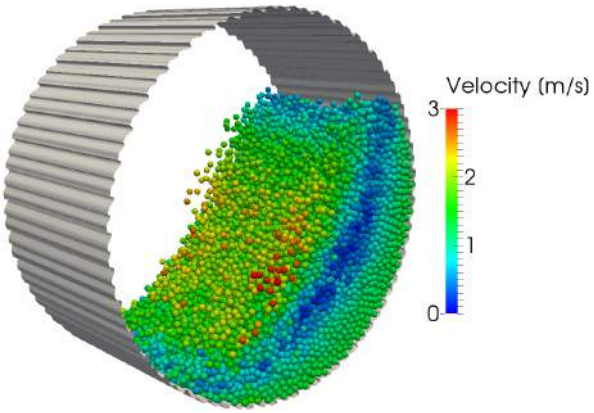

Figure 2.15: Illustration of the visual capabilities of PARAVIEW. The charge motion was represented with a color code depicting the translation velocity of the balls.

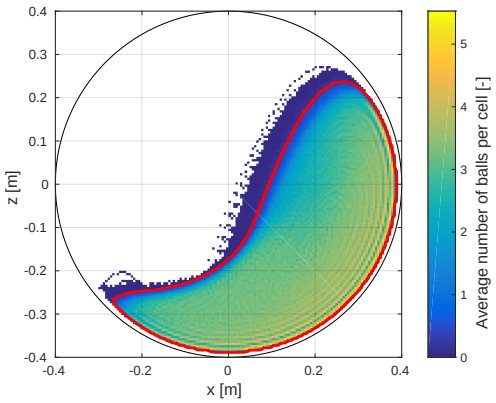

Figure 2.16: Position density plot of the charge motion in the pseudo steady state (simulated time: 2.5 s to 5 s) obtained with the control script in the appendix B and the medium *Perfecto ABAB* liner mesh. The underlying grid is divided into 150 cells along each direction. The red line is the position density limit.

Besides the charge motion, the *power draw* of the mill is the second category of experimental validation data. As explained in the previous chapter, the power draw can numerically be estimated either on the basis of the torque exerted by each ball on the liner (rotation power) or by the power dissipated during the interactions, i.e. by damping and sliding[23]. Only in the pseudo

[22] It is important to calculate the average over the *cells in which ball occurrences have actually been accumulated* to take into account the average degree of dispersion of the charge cloud. Indeed, if the average would be calculated over all the cells it would be constant, if the filling ratio and the geometry of the mill are unchanged. For instance, the charge cloud is more expanded at a higher rotation speed than at a lower one. Hence, the limiting value would be too restrictive for expanded charge clouds where the average number of balls per cell is smaller than at low angular speeds.

[23] The normal, tangential and sliding dissipation power measures were defined in the section 2.3.1. Their actual implementation can be found in the appendix C. The implementation of the rotation power calculation is provided in

steady state, these different measures take on average identical values due to the conservation of energy. Their comparison might give an idea about the influence of the material (contact) parameters on the different types of power dissipation, like increased sliding dissipation, when the friction coefficient decreases. For this reason, the rotation power P_{rotation} (torque times rotation speed), the power dissipated along the normal direction P_{normal}, the power dissipated along the tangential direction $P_{\text{tangential}}$ and the power dissipated by sliding P_{sliding} will be saved for each $\Delta t_{\text{rec}} = 0.01$ s.

the appendix B. Notice that there also exists a third way of numerically calculating the rotation power in the pseudo steady state. More precisely, if the center of gravity of the balls is determined, its horizontal distance to the rotation axis gives the lever arm of the charge. By multiplying this lever arm by the mass of the charge and the acceleration of gravity, the torque applied to the mill is known. Finally, multiplying the torque by the angular speed leads to the rotation power in the pseudo steady state.

2.4 Numerical Results

In this section, the *numerical results* of the DEM model will be analyzed to judge its capability of predicting the charge motion and the power draw of ball mills. First, the *elementary collisions* between spheres, facets and walls will be studied, then the results of the *laboratory mill* will be discussed, and finally, the influence of the size of the *industrial mill* with respect to the laboratory mill will be examined.

2.4.1 Elementary collision

In this first section about the numerical results, the elementary collision between the discrete bodies will be studied to *analytically validate* the new contact law in YADE, to understand the influence of the material parameters on the normal *overlap* of the spheres during their collision and to determine the *time step* of the integration.

Analytic validation

To ensure that the new linear spring-slider-damper contact model implemented in YADE (appendix C) delivers correct results, some elementary interactions were simulated. Since these interactions are sufficiently simple, it was possible to derive their analytic solutions. The figure 2.17 summarizes the different scenarios for which the *displacement* (or rotation) and the respective *power dissipation* (normal, tangential and sliding power) were calculated numerically and analytically. Due to the lengthy derivation of the analytic laws and the pass-fail comparison, the entire study will not be described here but in the appendix A.

In conclusion, the new contact model deliveres correct results with respect to the normal and tangential components (with and without sliding) of the contact law for sphere, facet (triangular surface) and wall (infinite place) elements in YADE.

Overlap limitation

As explained in the section 1.2.2, a common technique used to choose the value of the normal stiffness k_n is to limit the overlap between colliding spheres. In this section, we will therefore write the *percentage of overlap as a function of the contact parameters*, i.e. the normal stiffness k_n and the coefficient of normal restitution ε_n. The percentage of overlap $p_{\Delta x}$ is defined with respect to the diameter d of the colliding spheres:

$$p_{\Delta x} = \frac{\Delta x}{d} \tag{2.4}$$

In the case of the laboratory mill, $d = 15$ mm. According to the explanation in the appendix A, the maximum overlap Δx during a collision (with the linear spring-slider-damper con-

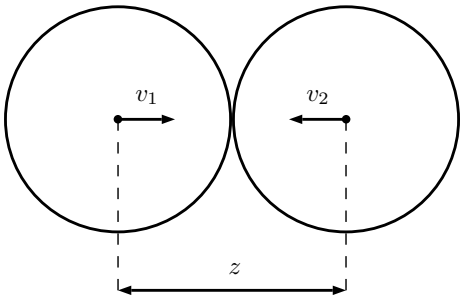

(a) Normal collision between two spheres moving at the velocities v_1 and v_2.

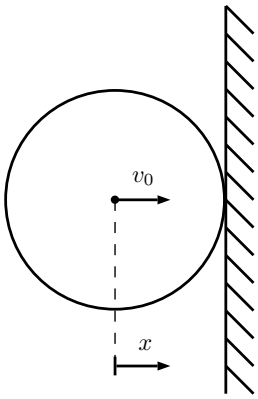

(b) Normal collision of a sphere on a facet with an initial velocity v_0.

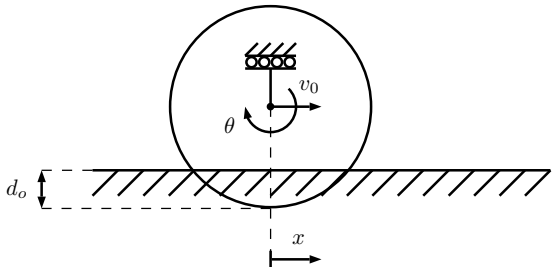

(c) Tangential collision of a sphere on a wall with an initial velocity v_0. The overlap was imposed to be equal to d_o in order to ensure the tangential interaction. The friction coefficient was increased sufficiently to study the interaction without sliding.

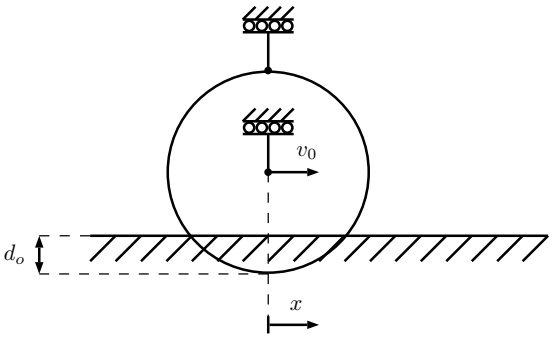

(d) Tangential collision of a sphere on a wall with an initial velocity v_0. The overlap was imposed to be equal to d_o in order to ensure the tangential interaction. The tangential stiffness was increased sufficiently and the rotation blocked to study the sliding component of the contact law solely.

Figure 2.17: Interaction scenarios, which were used in the appendix C to analytically validate the implementation of the new spring-slider-damper contact law in YADE.

tact law) is defined by the following formula:

$$\Delta x = \frac{v_r}{\omega_d}\, e^{-\zeta\, \omega_0\, t^*}\, \sin\left(\omega_d\, t^*\right) \quad \text{with} \quad t^* = \frac{1}{\omega_d}\, \arctan\left(\frac{\sqrt{1-\zeta^2}}{\zeta}\right) \tag{2.5}$$

where the natural frequency ω_0, the damping ratio ζ and the damped frequency ω_d are defined by:

$$\omega_0 = \sqrt{\frac{k_n}{m_{\text{eff}}}} \qquad \zeta = \frac{c_n}{2\sqrt{k_n\, m_{\text{eff}}}} \qquad \omega_d = \omega_0\, \sqrt{1-\zeta^2} \tag{2.6}$$

The definition of the effective mass depends on the type of the interaction. If a sphere collides with another sphere (freely moving), $m_{\text{eff}} = m_1 m_2/(m_1+m_2)$, where m_1 and m_2 are the respective masses of the spheres. For spheres of identical mass, $m_{\text{eff}} = m/2$, where m is the mass of one sphere. If a sphere collides with a rigid facet, $m_{\text{eff}} = m$. The material density of the spheres is again equal to 7640 kg/m^3.

The last variable, which has to be defined to calculate the percentage of overlap, is the relative velocity v_r. This velocity can either be estimated by the lifting height of the charge (velocity by energy conservation) or its peripheral rotation speed:

$$v_r = \sqrt{2\, g\, h} \qquad v_r = r_{\text{mean}}\, \omega \tag{2.7}$$

where g, h, r_{mean} and ω are the gravitational acceleration 9.81 m/s^2, the average lifting height h, which can be approximated by the average liner diameter (around 770 mm, worst case scenario), the mean radius of the liner profile (around 385 mm) and the rotation speed of the mill (around 40 rpm). The maximum relative speed is therefore equal to around 4 m/s by selecting the greater value of the previous estimates, i.e. the velocity reached due to gravity.

Moreover, we will write the normal damping coefficient c_n as a function of the coefficient of normal restitution ε_n, which represents the ratio of the relative separation speed to the relative speed of approach (appendix A):

$$c_n = -2\ln(\varepsilon_n)\, \sqrt{\frac{m_{\text{eff}}\, k_n}{\pi^2 + \ln^2(\varepsilon_n)}} \tag{2.8}$$

Finally, it is possible to calculate the *maximum percentage of overlap as a function of the normal stiffness k_n and the coefficient of normal restitution ε_n*. The results are shown in the figure 2.18 for common values of k_n and ε_n. This figure highlights the fundamental fact that a stiffer spring is harder to strain, i.e. the overlap decreases mainly with the stiffness of the normal spring.

In conclusion, it seems reasonable to chose the lower limit of the normal stiffness equal to 10^5 N/m because the percentage of overlap is then roughly limited to 10%; it should be noticed that the previous reasoning is based on the maximum overlap, i.e. on the maximum velocity.

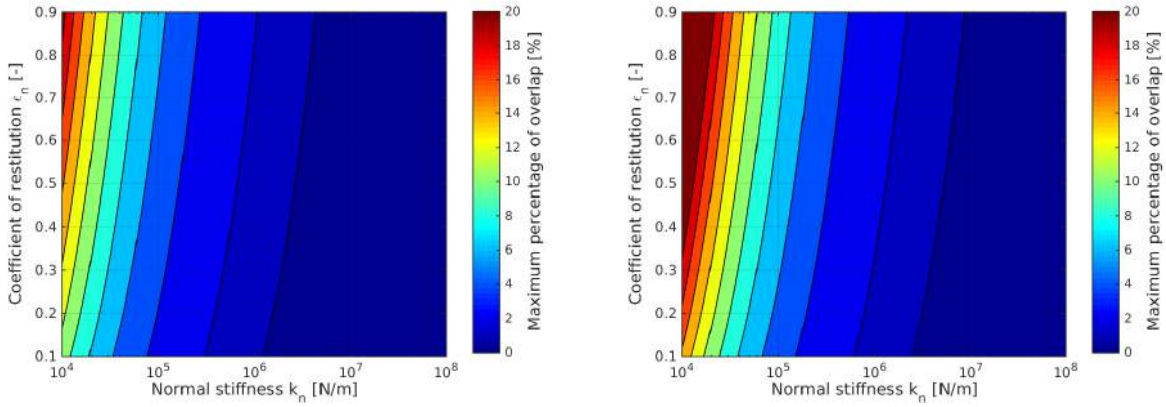

(a) Collision between two (freely moving) spheres.

(b) Impact of a sphere on a rigid facet.

Figure 2.18: Maximum percentage of overlap with respect to the diameter (of one sphere) for the linear spring-slider-damper contact law. The spheres have a 15 mm diameter and a density equal to 7640 kg/m^3. The relative normal impact velocity is equal to 4 m/s. The frontiers in the contour diagrams are associated to the following percentages: 1, 2, 4, 6, 8, 10, 12, 14, 16, 18 and 20 %.

On average, the impact velocities are, however, far below 4 m/s as will be shown hereinafter. Concerning the upper limit of the normal stiffness, a greater value than 10^7 N/m seems to lead to no significant reduction of the overlap, which is anyways below 1% for this value. The influence of the stiffness on the global charge motion and the power draw will be analyzed in the section 2.4.2.

It is also interesting to notice that the overlap resulting from the static stress applied to the balls by gravity is negligible with respect to the impacts. In fact, if one supposes that a column of balls as high as the mill shell diameter rests on one balls, the resulting overlap due to gravity is only equal to around $7 \cdot 10^{-5}$ m for a normal stiffness $k_n = 10^5$. This value correspond to a percentage of overlap smaller than 0.5%. In comparison, the maximum percentage of overlap due to an impact is far greater, i.e. 4% - 6% for a sphere/sphere impact at $v_0 = 4$ m/s (depending on ε_n).

Time step

It was previously explained (section 1.2.2) that the time step has to be sufficiently small to integrate accurately the equations of motion. On the one hand, it is necessary that the explicit integration scheme is *stable*, i.e. approximation errors are not amplified. For a linear spring contact law, this condition is the following one [O'Sullivan & Bray, 2004], where $k = \min(k_n, k_t)$ and m is the mass of the sphere elements:

$$\Delta t_{\text{cr}} \leq 0.22 \sqrt{\frac{m}{k_n}} \tag{2.9}$$

Therefore, the time step Δt should at maximum be equal to $8.08 \cdot 10^{-5}$ s, $2.56 \cdot 10^{-5}$ s or $8.08 \cdot 10^{-6}$ s for $k_n = 10^5$, 10^6 or 10^7 N/m, supposing that $k_t \leq k_n$ and that the damping is sufficiently small[24]. The mass of the balls in the laboratory mill (around 13.5 g) was obviously used to determine these values.

On the other hand, the time step can be determined by trying to *recover the coefficient of normal restitution*, when a sphere collides with another sphere (identical speed with opposite directions). The *sphere-sphere* collision is considered since the contact time between two spheres is smaller than the contact time between a sphere and a facet for the same parameters (appendix A), i.e. it is the worst case scenario[25]. Moreover, the normal collision is studied since the contact parameters in the tangential direction have the same order of magnitude. Hence, it seems reasonable to suppose that the results in the normal direction can be extrapolated to the behavior in the tangential direction.

The coefficient of normal restitution is influenced by the time step as follows. Due to the explicit time integration, the force at the current position of the sphere is used to update its velocity and its position. If the time step increases, the sphere travels further before being slowed down, when approaching the other sphere. As a consequence, the impacting spheres get closer to each other (figure 2.19a). Since the overlap is directly proportional[26] to the force created by the normal spring component of the contact law, greater forces are created when the impacting particles separate. Hence, the velocity of the spheres after the impact increases with the time step. In other words, when the number of time steps per collision increases, the error of the coefficient of restitution decreases. This phenomenon can be observed in the figure 2.19b, which illustrates the coefficient of restitution as a function of the number of time steps per collision. It might be surprising to see that the coefficient of restitution in this figure does not converge to the imposed theoretical coefficient, which is equal to 0.3. In fact, this is a consequence of the particular implementation of the contact law, which prohibits attractive forces (created by the damper) between separating elements.

To complete this first part of the explanation, which will be extended by energetic considerations, it is important to define the relation between the number of time steps per collision and the time step per se, as well as the relation between the imposed theoretical coefficient of normal restitution ε_n and the effective coefficient of restitution $\overline{\varepsilon}_n$. The time step Δt can be defined based on the *number of time steps per collision* by dividing the theoretical contact time $t_c = \pi/\omega_d$ (appendix A) by the number of time steps per collision. This contact time is represented in

[24] Since our contact law contains a viscous component, the critical time step should also be dependent on the damping coefficient. Nevertheless, no conclusive results were found in the literature; the result in [O'Sullivan & Bray, 2004] seems to contain an error. Due to the complexity of determining the critical time step of discrete spring-slider-damper systems, we will rather develop a simplified strategy for choosing the time step hereinafter and control the results by the different power measures (rotation power, normal power, tangential power and sliding power) in the simulation of the charge motion.

[25] Multi-sphere collisions might lead to an even worse scenario. Because of their complexity, we will rather try to generalize the results of the elementary collision to the multi-collision scenario instead of analyzing this scenario as such.

[26] The damping component of the force is not mentioned here to simplify the explanation.

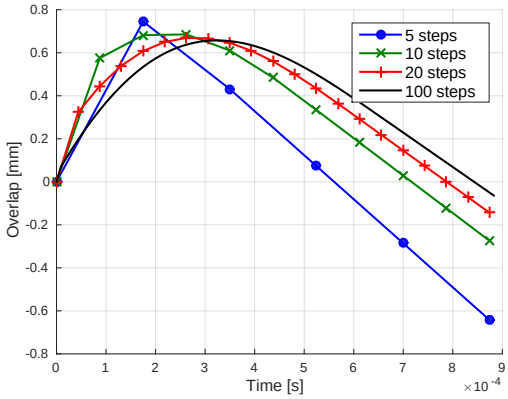

(a) Increasing overlap when the number of time steps per collision decreases.

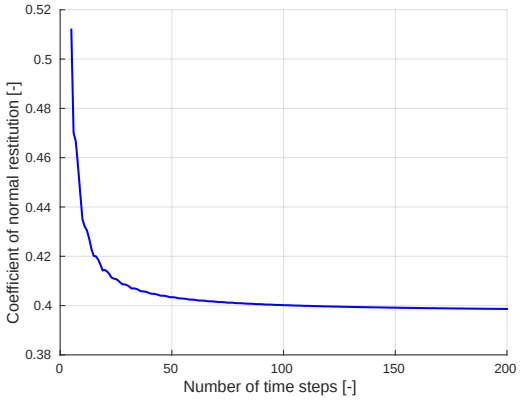

(b) Decreasing coefficient of normal restitution when the number of time steps per collision increases.

Figure 2.19: Influence of the time step on the normal collision of two spheres (density $\rho = 7640$ kg/m^3, diameter $d = 15$ mm) with an impact velocity $v_0 = 4$ m/s, i.e. 2 m/s each (opposite directions). The stiffness and the coefficient of restitution of the normal component of the spring-slider-damper contact law are equal to $k_n = 10^5$ N/m and $\varepsilon_n = 0.3$. The time step was calculated by dividing the theoretical contact time ($t_c = \pi/\omega_d$) by the respective number of time steps. These results were obtained by the DEM solver YADE.

the figure 2.20 for the sphere/sphere collision. In a typical DEM simulation, the contact time therefore varies between 10^{-3} s and 10^{-4} s.

As explained earlier, the effective coefficient of normal restitution $\overline{\varepsilon}_n$, i.e. the coefficient of restitution in the simulation for a large number of times steps per collision in order to neglect the influence of the explicit integration, e.g. 10,000, is different from the theoretical coefficient of normal restitution ε_n since the normal force between impacting bodies (in the contact law implementation) is equal to zero, when it becomes attractive. This is usually the case when the separating normal velocity is relatively high so that the normal damper creates an attractive force which is stronger than the repulsive force of the spring. The relation between the theoretical coefficient of restitution ε_n and the effective coefficient of restitution $\overline{\varepsilon}_n$ is shown in the figure 2.21 for the sphere/sphere collision. The effective coefficient of restitution $\overline{\varepsilon}_n$ is greater than the theoretical coefficient of restitution ε_n especially for low values of ε_n. This is the consequence of the higher normal damping coefficient c_n for these values of ε_n.

A more rigorous but equivalent way of choosing the time step is the *recovery of energy* instead of the coefficient of restitution. Since the resulting coefficient of restitution increases with the time step, the separation velocity of the particles increases as well, i.e. less energy is dissipated. Instead of loosing less energy, the *reverse* argument states that artificial energy is created numerically. According to this reasoning, minimizing the time step minimizes the creation of numerical energy. The figure 2.22 shows the percentage of numerical energy with respect to the

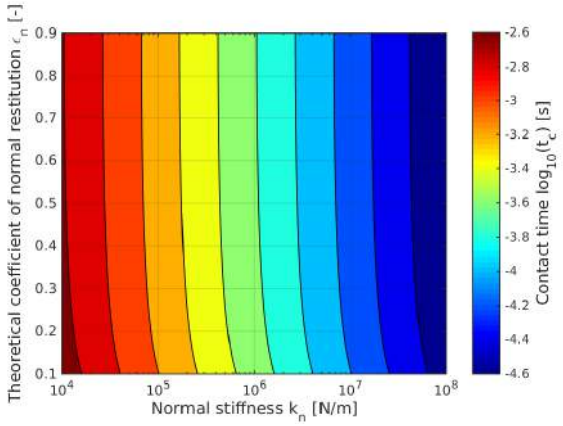

Figure 2.20: Logarithm (basis 10) of the theoretical contact time t_c between two identical spheres (density $\rho = 7640$ kg/m^3, diameter $d = 15$ mm). This contact time is independent of the impact velocity v_0 and therefore depends only on the mass of the spheres m, the normal stiffness k_n and the coefficient of normal restitution ε_n. The frontiers on the contour plot are associate to the following values: -4.4, -4.2, -4, -3.8, -3.6, -3.4, -3.2, -3, -2.8 and -2.6 (from the right to the left).

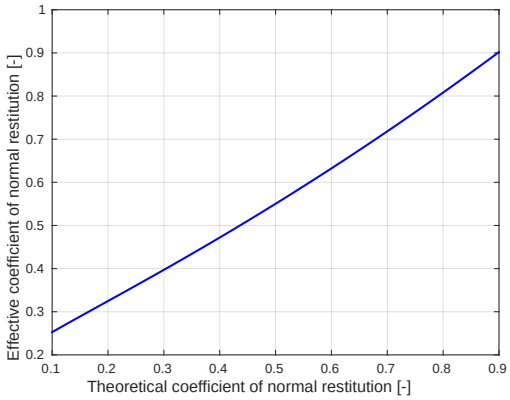

Figure 2.21: Relation between the theoretical and the effective coefficient of normal restitution, i.e. ε_n and $\overline{\varepsilon}_n$. The figure was created for two spheres (density $\rho = 7640$ kg/m^3, diameter $d = 15$ mm) colliding with an impact velocity $v_0 = 4$ m/s, i.e. 2 m/s each (opposite directions). The normal stiffness was equal to $k_n = 10^5$ N/m. Nevertheless, the result is independent of the particle mass m, the impact velocity v_0 and the normal stiffness k_n, i.e. it depends only on the theoretical coefficient of restitution ε_n and the number of time steps per collision, which was equal to 10,000 in order to neglect the influence of the time step.

non-artificial energy after the collision as a function of the number of time steps per collision. A very important conclusion drawn during the creation of this figure is its independence[27] of the normal stiffness k_n, the impact velocity v_0 and the mass of the sphere m. In other words, the percentage of numerical energy created during a normal collision between two spheres only depends on the theoretical coefficient of normal restitution ε_n and the number of time steps used to integrate the collision.

The figure 2.22 shows only the percentage of numerical energy created in a single collision of two spheres. The objective is, however, to obtain numerical results, which are sufficiently independent of the time step, by limiting the percentage of the *total* numerical energy. For

[27] The underlying results of this conclusion, i.e. the curves for *different* values of k_n, m and v_0, were not represented since they are identical to the curves in the figure 2.22. Nevertheless, we can try to understand the reason behind this independence. For the analytic solution of the contact law, it is clear that the normal stiffness k_n and the mass m have no influence on the speed of the sphere after the impact since the coefficient of restitution defines this speed on the basis of the impact velocity. Hence, the stiffness k_n does not change the remaining energy after the impact (in the analytic solution). Moreover, the mass has no influence on the percentage of numerical energy, since it cancels out by calculating this percentage (fraction with m in the numerator and denominator). It is, however, unclear why the *numerical* result is not dependent on the stiffness and the impact velocity v_0 because of the time discretization. More detailed investigations would be necessary to understand this behavior of the explicit time integration.

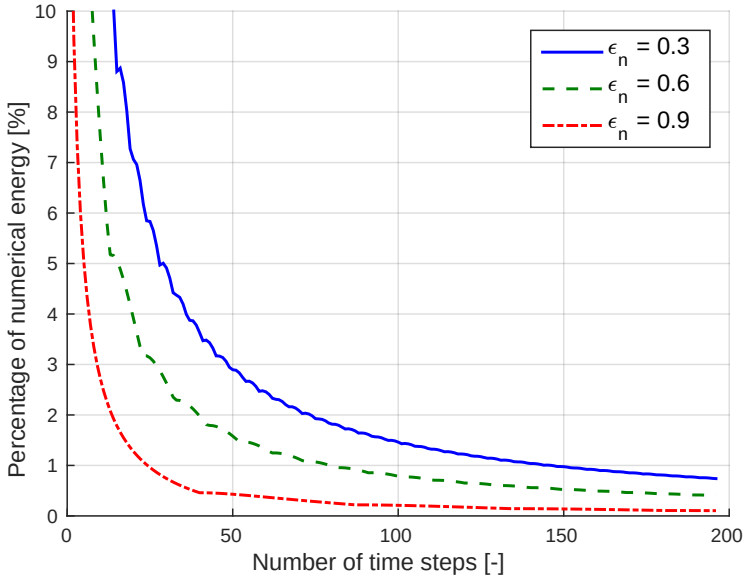

Figure 2.22: Decreasing percentage p_n of the numerical energy created during the normal impact of two spheres (density $\rho = 7640$ kg/m^3, diameter $d = 15$ mm) with a velocity $v_0 = 4$ m/s, i.e. 2 m/s each (opposite directions) for different theoretical coefficients of normal restitution ε_n. The normal stiffness is equal to $k_n = 10^5$ N/m. The results depend, however, only on the theoretical coefficient of normal restitution ε_n and the number of time steps per collision. The percentage of numerical energy was calculated with respect to the remaining energy after the collision obtained by a simulation with 10,000 time steps (per collision). For this number of time steps, the creation of numerical energy is negligible.

instance, the percentage of numerical energy might be lower for a single collision of a particle with a higher coefficient of restitution. Nevertheless, this particle might collide more often than a particle with a lower coefficient of restitution since less energy is lost per collision. Hence, more artificial energy could be created in the long run. A formula for the worst case scenario will be derived hereinafter to finally determine the time step Δt as a function of the normal stiffness k_n, the theoretical coefficient of normal restitution ε_n and the percentage of the admissible creation of numerical energy (in the worst case).

Let E be the total energy initially in the system and p_n the percentage of numerical energy created during a *single* impact of two spheres. This percentage is defined with respect to the energy after the single impact simulated with 10,000 time steps (per collision) like in the figure 2.22, i.e. $\overline{\varepsilon}_n^2\, E$. For this number of time steps, the creation of numerical energy is negligible. Consequently, when all the particles in the system collide once with a relatively large time step, the total energy after the impact is equal to $(1 + p_n)\, \overline{\varepsilon}_n^2\, E$ of which $p_n\, \overline{\varepsilon}_n^2\, E$ is the artificially created energy. In the worst case, the particles collide an infinite number of times. Hence, the

total artificial energy E_a created during all these collisions is equal to[28]:

$$E_a = \left[p_n\,\overline{\varepsilon}_n^2 + p_n\,(1+p_n)\,\overline{\varepsilon}_n^4 + p_n\,(1+p_n)^2\,\overline{\varepsilon}_n^6 + \ldots\right] E \tag{2.10}$$

$$= p_n\,\overline{\varepsilon}_n^2\,E \sum_{i=0}^{+\infty} (1+p_n)^i\,\overline{\varepsilon}_n^{2i} \tag{2.11}$$

$$= \frac{p_n\,\overline{\varepsilon}_n^2}{1-(1+p_n)\overline{\varepsilon}_n^2}\,E \tag{2.12}$$

In the worst case, the *percentage p_{ntot} of the total numerical energy with respect to the total energy injected in the system*, is given by the following equation according to the previous reasoning:

$$p_{ntot} = \frac{p_n\,\overline{\varepsilon}_n^2}{1-(1+p_n)\overline{\varepsilon}_n^2} \tag{2.13}$$

To understand the influence of the effective coefficient of normal restitution on the total percentage of numerical energy, the previous equation was plotted in the figure 2.23. As expected, this figures shows that the percentage of total numerical energy increases strongly for high effective coefficients of normal restitution $\overline{\varepsilon}_n$ since the corresponding particles do not loose as much energy in a single collision and can collide more often, thus, creating more numerical energy.

In conclusion, the previous explanation can be used as a *strategy to choose the time step*. For instance, we will try to determine the time step Δt necessary to integrate interactions with a normal stiffness $k_n = 10^5$ N/m and a theoretical coefficient of normal restitution $\varepsilon_n = 0.3$ while allowing a maximum percentage of numerical energy $p_{ntot} = 1\%$. The figure 2.21 shows that the theoretical coefficient of normal restitution $\varepsilon_n = 0.3$ is equivalent to the effective coefficient of normal restitution $\overline{\varepsilon}_n \approx 0.4$. The formula 2.13 or the figure 2.23 can then be used to determine the corresponding percentage of numerical energy for one collision $p_n \approx 5.2\%$. This percentage can be converted in a number of time steps per collision by the figure 2.22: around 27 time steps. Finally, the figure 2.20 shows us that the theoretical contact time for $k_n = 10^5$ N/m and $\varepsilon_n = 0.3$ is equal to approximately $10^{-3.1}$ s. Hence, the time step Δt, which satisfies our requirements, is equal to more or less $2.94 \cdot 10^{-5}$ s. This time step is smaller than the critical time step calculated previously, provided that the damping is relatively low.

2.4.2 Laboratory mill

By combining the DEM model of the laboratory mill (section 2.3) with the results of the previous section, it is finally possible to simulate the charge motion and the power draw of the mill. It is, however, still necessary to determine when starts the pseudo steady state of the charge motion and for how long it should be recorded to obtain sufficiently representative prediction of this motion and the power draw. Accordingly, some *general results* of the mill simulation, will first

[28] The line over the ε_n is a line and not a minus sign.

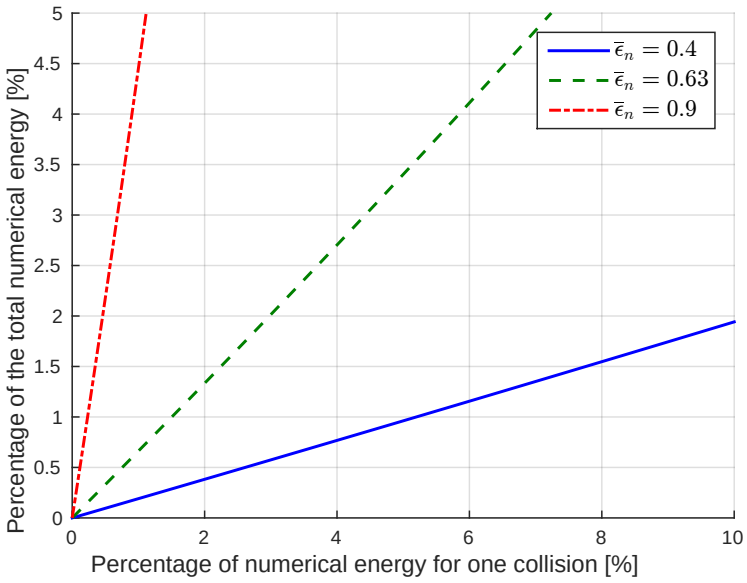

Figure 2.23: Percentage of the total numerical energy p_{ntot} with respect to the total energy injected in the system as a function of the percentage of numerical energy created during one collision p_n with respect to the *real* remaining energy after the collision, i.e. the remaining energy after the collision obtained by a simulation with 10,000 time steps. This figures was created by means of the formula 2.13. The effective coefficients of normal restitution $\overline{\varepsilon}_n = 0.4$, 0.63 and 0.9 correspond to the theoretical coefficients of normal restitution $\varepsilon_n = 0.3$, 0.6 and 0.9 according to the figure 2.21.

be described. Then, the liner mesh and the material parameters will be studied to understand their influence on the results and to ultimately *calibrate* these latter parameters on the basis of the experimental data summarized previously (case 1, section 2.1.2). Finally, the calibrated model will be *validated* to ensure its predictive capability in different milling scenarios (case 2, 3 and 4, section 2.1.2).

General results

The numerical results in this section were obtained by simulating the case 1 of the experimental data (section 2.1.2): *Perfecto ABAB liner* (medium mesh), filling ratio 30% and percentage of critical velocity 70%. The material parameters are identical to those used in a previous study of the laboratory mill [Sawley, 2003]: equivalent normal stiffness $k_n = 10^5$ N/m, equivalent tangential stiffness $k_t = 10^5$ N/m, (theoretical) coefficient of normal restitution (for a sphere/sphere collision) $\varepsilon_n = 0.3$ ($c_n \approx 18.6$ Ns/m, appendix A.1), equivalent tangential damping coefficient $c_t = c_n$ and the friction coefficient $\mu = 0.75$. If 1% of numerical power with respect to the total power is allowed to be created in the system, the time step Δt should be equal to around $3 \cdot 10^{-5}$ s at most (according to the strategy explained in the section 2.4.1). We choose, however,

$\Delta t = 10^{-5}$ s to keep the recording period equal to $\Delta t_{rec} = 0.01$ s (multiple of 10^{-5} s) and for reasons of simplifying standardization[29]. The *total simulated time* is chosen to be equal to 10 s, which is equivalent to almost 6 full rotations of the mill. This value was chosen by supposing that one rotation is necessary to allow the charge to be lifted up and fall down. One additional rotation is then necessary to leave the transient state. And finally, one more rotation is needed to record the characteristics in the pseudo steady state. Hence, three rotations seem to be necessary to extract the data, which is needed in this analysis. Nevertheless, this number of rotations was doubled to check whether the pseudo steady state is actually reached after 2 rotations or in other words, to check whether the data recorded during the last rotation is sufficiently representative of the characteristics (mainly the power draw) in the pseudo steady state.

Concerning the *general charge motion*, the figure 2.24 shows the charge, which falls onto the liner, which is then lifted up and which finally, cascades and cataracts down to the toe. After around 2.5 s, the transient motion seems to disappear and the *pseudo steady state* has been reached. The *maximum amplitude of the translation velocity* is 3 m/s. This value is relatively close to the 4 m/s, which was determined previously by considering the full diameter of the mill as drop height. The figure 2.25 clearly illustrates the *influence of the end walls*, which enhance the lifting capability of the liner due to the friction between the walls and the balls.

To determine more objectively, when the *pseudo steady state* has been reached, the figure 2.26 shows the center of gravity of the balls as a function of time along x and z, x being the horizontal axis and z being the vertical axis (e.g. figure 2.11). The center of gravity reaches the pseudo steady state in the lower front quadrant of the mill after approximately 2.5 s. Hence, *the characteristics in the pseudo steady state (average charge position and power draw prediction) should only be based on the recorded data after 2.5 s of simulated time*.

Besides the charge motion, some general conclusions about the *power* can be drawn. The figure 2.27 represents the rotation power P_{rot}, i.e. the power necessary to rotate the mill, and the dissipated power in collisions $P_{dissip} = P_{normal} + P_{tangential} + P_{sliding}$, along the normal direction, along the tangential direction (without sliding) and by sliding. The first peak is due to the artificial impact of the balls, when they fall onto the liner. Then, the charge is lifted up, which explains the high rotation power, before avalanching down to the toe and leading to a significant amount of energy, which is dissipated in damping and sliding collisions. Since the balls are moving in a relatively chaotic way, the power oscillates randomly around a medium value in the pseudo steady state. Most importantly, *the rotation power is on average equal to the power dissipated in collisions* in this state, i.e. the same amount of energy which is injected into the system is dissipated by it. For instance, by calculating the mean of both power measures from 7.5 s to 10 s, we obtain $P_{rot} = 1392.3$ W and $P_{dissip} = 1395.2$ W; these values are thus almost identical.

To reduce the computation time in future simulations, it is questionable whether the system has already reached the steady state after 2.5 s and if 2.5 additional seconds are sufficiently representative of the average power. Hence, we calculated the mean of both power variations

[29] As will be pointed out in the section about the influence of the material parameters, choosing this smaller time step makes it also possible to use the same time step for all the simulations with a normal stiffness equal to 10^5 N/m. For reasons of standardization, we thus prefer to use a single value of the time step for a specific normal stiffness.

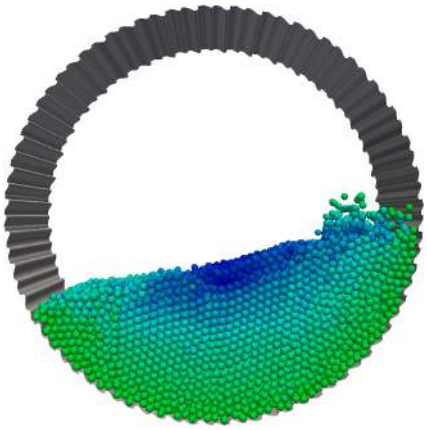

(a) Charge falling onto the liner (t = 0.2 s)

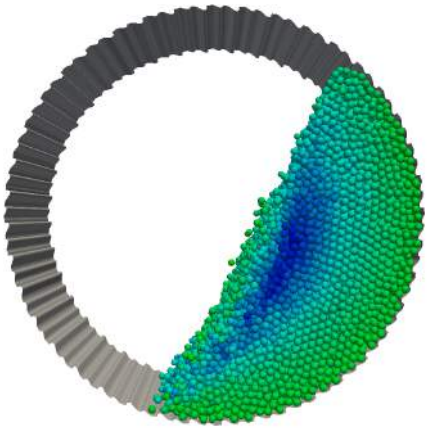

(b) Lifted up charge (t = 0.5 s)

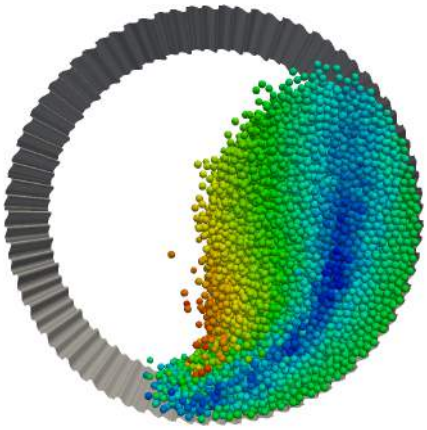

(c) Cascading and cataracting charge (t = 0.75 s)

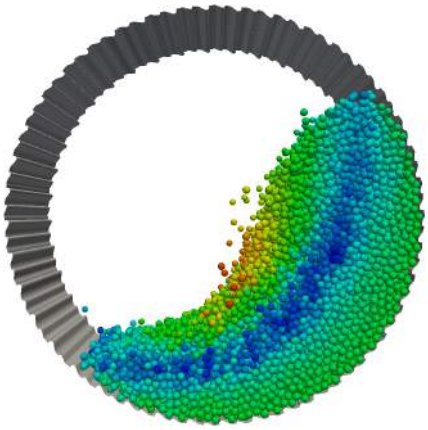

(d) Charge in the pseudo steady state (t = 2.5 s)

Figure 2.24: General charge motion in the laboratory mill. The color code indicates the amplitude of the translation velocity: 0 m/s (blue) to 3 m/s (red).

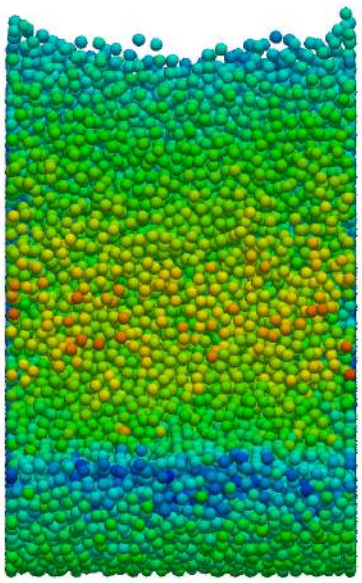

Figure 2.25: Parallel projection of the charge along the x-direction ($t = 3$ s). The influence of the end walls is shown by the enhanced lifting at the left and the right sides. The color code indicates the amplitude of the translation velocity: 0 m/s (blue) to 3 m/s (red).

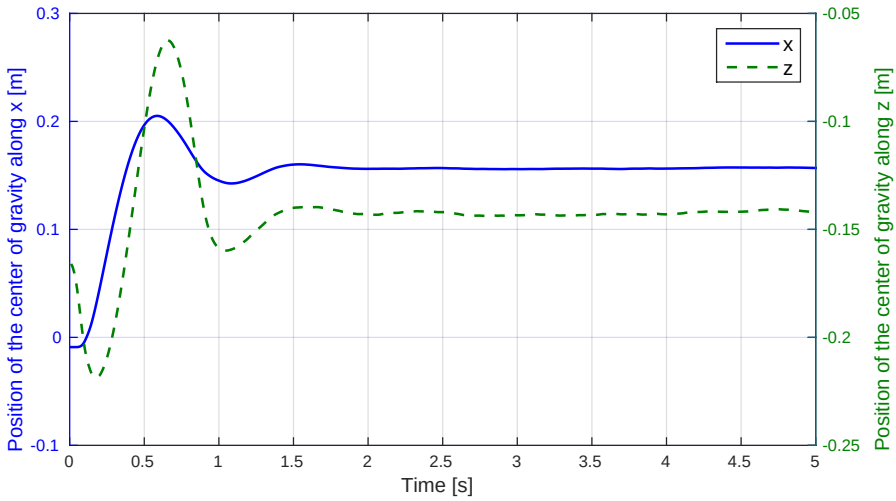

Figure 2.26: Position of the center of gravity of the balls during the first 5 s of the simulation. After around 2.5 s, the pseudo steady state seems to have been reached.

from 2.5 s to 5 s: $P_{\text{rot}} = 1398.8$ W and $P_{\text{dissip}} = 1390.2$ W. Since the relative difference between the different averages from 2.5 s to 5 s, and from 7.5 s to 10 s remains below 1%, it seems reasonable to reduced the total simulated time to 5 s. Therefore, *the characteristics of the pseudo steady state will be determined by averages over the period from 2.5 to 5 s.*

Finally, the figure 2.28 gives an idea about the importance of the mechanisms by which power is dissipated in the ball mill[30]. On average, the *sliding power accounts for 52%, while the normal and tangential power only account for 40% and 8%.* This power distribution emphasizes why the major comminution mechanism in ball mills is the abrasion of a relatively soft feed material by harder steel balls.

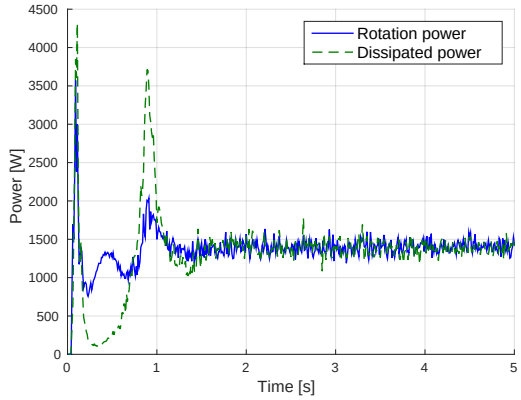

Figure 2.27: Rotation power P_{rot} and the dissipated power in collisions $P_{\text{dissip}} = P_{\text{normal}} + P_{\text{tangential}} + P_{\text{sliding}}$ during the first 5 s of the simulation.

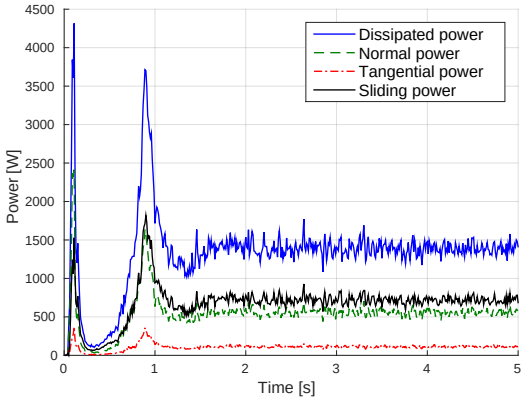

Figure 2.28: Dissipated power in the collisions P_{dissip} and its components, the power dissipated by normal damping P_{normal}, by tangential damping $P_{\text{tangential}}$ and by sliding P_{sliding} during the first 5 s of the simulation.

Experimental calibration

To predict the reality, the parameters of a model are *calibrated* on the basis of experimental data. In this section, the parameters of the charge motion simulation will be adjusted by means of the first experimental data set described previously (case 1, section 2.1.2).

In order to choose the appropriate simulation parameters, it is essential to understand which is their influence on the results. For this reason, the effect of the *geometry* on the results will first be analyzed by focusing on the mesh refinement. Afterwards, we will try to comprehend how the *material* (contact) parameters affect the charge motion and the power draw of the mill. Finally, the material parameters, which best fit the experimental observations, will be determined.

[30]The following percentages will change after the calibration of the contact parameters. The sliding dissipation will, however, remain the major dissipation mechanism.

The parameters of the simulation[31] used throughout this section are identical to those used in the previous section except for the meshes of the geometry and the material (contact) parameters in the subsections related to their respective study.

Influence of the mesh refinement The influence of the *mesh refinement* was studied for the coarse, medium and fine meshes illustrated previously by the discretization of their profile curve in the figure 2.8. The charge motion was analyzed by plotting the *position density limit* (similar to the red curve in the figure 2.16) of the charge for each mesh. Due to the almost exact superposition of theses curves in the same plot, their representation was not included here. The conclusion is that the mesh refinement has no apparent influence on the average charge motion (at the considered level of the facet element size).

The average rotation power for the coarse, medium and fine meshes were respectively equal to 1388.1 W, 1392.3 W and 1394.4 W. This increasing power with the refinement could be the consequence of the increasing average *roughness* (integral of the squared distance between the discretized profile and the circle with the mean profile diameter) of the meshes. In other words, the geometrical approximation by the coarser meshes are less accurate with respect to the real profile curve of the liner. Nevertheless, the power obtained by the different meshes are roughly identical, which leads to the conclusion that the simplified regularization strategy (stiffening effect due to multiple collisions on edges) has no visible kinematic influence. Further studies would, however, be required to check if the change in the geometry approximation is the predominant factor leading to the change in power instead of the simplified regularization strategy; such a study seems, however, not to be necessary in the framework of this analysis due to the *negligible* difference between the different power predictions.

It is also interesting to notice that the average rotation power obtained with the medium mesh is 6 W lower than the average rotation power obtained in the previous section for the exact same simulation input and averaging period. This difference illustrates the *non-determinism* of DEM simulations, which are run in parallel on several processors. Fortunately, the difference is insignificant. Moreover, this illustrates that the ascending order of the previous power predictions might only be caused by chance, or more precisely, the pseudo-random combination of numbers with a finite precision on multiple cores.

In conclusion, the *mesh refinement has essentially no influence on the results* if the geometry of the liner is sufficiently well approximated. Due to the better approximation of the geometry

[31] In short (recapitulation), the mill is filled up to 30% by 15 mm diameter spherical balls having a density equal to 7640 kg/m^3. The medium *Perfecto ABAB* liner mesh (except for the study of the refinement) rotates at 70% of its critical speed. The material contact parameters are the following (except for the material study): equivalent normal stiffness $k_n = 10^5$ N/m, equivalent tangential stiffness $k_t = 10^5$ N/m, (theoretical) coefficient of normal restitution $\varepsilon_n = 0.3$ (with respect to the sphere/sphere collision, hence the equivalent normal damping coefficient $c_n \approx 18.6$ Ns/m), equivalent tangential damping coefficient $c_t = c_n$ and the coefficient of friction $\mu = 0.75$. In this case, the time step is equal to $\Delta t = 10^{-5}$ s. In all cases, the total simulated time is equal to 5 s and the pseudo steady state characteristics are averaged over the period from 2.5 to 5 s. The sampling period of the post-processing data is equal to $\Delta t_{\text{rec}} = 0.01$ s.

(with respect to the coarse mesh) and the smaller computation overhead (with respect to the fine mesh), the *medium* mesh will be used in the following analysis.

Influence of the material While the density of the balls is a material property, which is easily quantifiable, the contact parameters are far more difficult to determine either because of their intrinsic variability (e.g. coefficient of friction) or the complexity of the experimental measurements (e.g. by strain waves [Mishra & Rajamani, 1992] or high-speed photography [Thornton et al., 2013]). Therefore, these parameters are commonly calibrated by means of global results, like the average charge motion or the power draw of the ball mill.

In this section, the importance of the *tangential component* of the contact law and the influence of the different contact mechanisms, i.e. the *spring*, *damping* and *sliding* mechanisms, will be studied.

Tangential component Using different values for the normal and tangential stiffness and damping coefficients, i.e. $k_n \neq k_t$ and $c_n \neq c_t$, requires a very detailed validation study due to the large number of parameters: k_n, k_t, c_n, c_t and μ. In the previous study of the laboratory mill [Sawley, 2003], as well as in Cleary's significant work in this field, i.a. [Cleary, 2009], identical values for the stiffness and the damping coefficients along the normal and tangential directions were used, probably for this reason. Therefore, it seems unreasonable to try calibrating these parameters independently in this study. Nevertheless, we will attempt to understand their influence on the results, first by eliminating the *sliding* mechanism and then by adjusting the *relative importance of the tangential spring and damper with respect to the normal components*.

The figure 2.29 and the table 2.3 respectively show the position density limit and the power draw for the contact law *with and without Coulomb sliding*. The simulation parameters are identical to those used previously except for the friction coefficient of the model without sliding, which was set equal to 1000, thus preventing almost any sliding motion. As expected, the shoulder of the charge rises since it can not slide anymore. The global power draw is almost unchanged but increases slightly due to the increased lifting of the charge (without sliding). Moreover, the dissipation by sliding has roughly been replaced by the tangential dissipation.

Notice that the sum of the *power percentages is not necessarily equal to 100%* for three reasons. First, the percentages of dissipated power are calculated with respect to the rotation power and rounded half down. Second, energy might be created or destroyed artificially mainly due to the explicit integration with a finite time step and the approximate rotation of the tangential spring force. Third, the power estimations are averages over a finite sample of stochastic data. As long as the difference between the rotation power and the dissipated power remains as small as a few percents, the results seem to be acceptable from a numerical point of view.

Concerning the *relative importance of the normal component with respect to the tangential component*, we explained earlier that different parameter values for each direction were only used very rarely in the literature. For instance, [Kalala, 2008] used a tangential stiffness which is 1/4 smaller than the normal stiffness. Similarly, [Mishra, 2003a] explains that the tangential

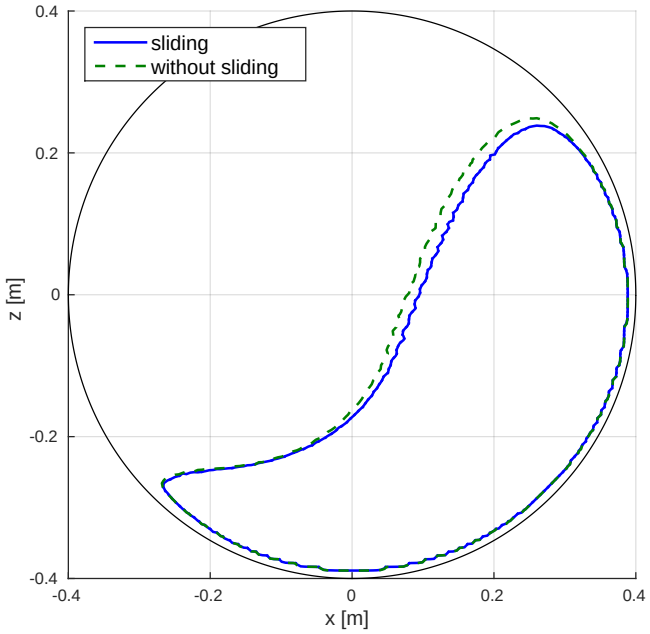

Figure 2.29: Increased shoulder angle when the sliding mechanism is virtually removed from the contact law illustrated on the basis of the position density limit plot. The conditions of the simulations are defined at the beginning of this section except for the coefficient of friction μ, which is equal to 0.75 and 1000 in the cases with and without sliding, respectively.

Coefficient of friction [-]	Rotation power [W]	Percentage of normal damping dissipation [%]	Percentage of tangential dissipation [%]	Percentage of sliding dissipation [%]
0.75	1395	40	8	51
1000	1389	47	54	0

Table 2.3: Influence of the sliding component of the contact law on the power dissipation. The conditions of the simulations are defined at the beginning of this section except for the coefficient of friction μ, which is defined in this table.

stiffness should have a value between 2/3 and 1 of the normal stiffness according to the Hertz-Mindlin contact theory. To determine whether this difference actually has an influence on the global charge motion and the power draw, the ball mill was simulated for different normal and tangential stiffness and damping values, i.e the combinations of $k_t = 2/3\ k_n$, k_n and $4/3\ k_n$, and $c_t = 2/3\ c_n$, c_n and $4/3\ c_n$.

The resulting position density limit curves were not represented since they are completely superposed. Hence, the change in the importance of the tangential stiffness and damping has no significant influence on the global charge motion[32]. The power draw and its components are summarized in the table 2.4. The most important consequence is certainly that the difference of the global power draw remains below 1% for the different cases. Consequently, *it seems reasonable to use the same stiffness and damping coefficient along the normal and tangential direction*. Moreover, it can be concluded that the percentage of power dissipated by normal damping is almost insensitive to the change in the importance of the tangential component, i.e. it increases very slightly with the tangential stiffness, while the percentage of power dissipated by sliding increases with k_t and c_t, at the disadvantage for the tangential dissipation. In simple words, this response of the model can be explained by noticing that the friction limit is reached quicker for higher values of k_t and c_t.

Stiffness k_t [N/m]	Tangential damping coefficient c_t [Ns/m]	Rotation power [W]	Percentage of normal damping dissipation [%]	Percentage of tangential dissipation [%]	Percentage of sliding dissipation [%]
$2/3\ k_n$	$2/3\ c_n$	1392	39	13	48
k_n	$2/3\ c_n$	1398	40	9	51
$4/3\ k_n$	$2/3\ c_n$	1397	41	6	53
$2/3\ k_n$	c_n	1393	39	11	50
k_n	c_n	1395	40	8	51
$4/3\ k_n$	c_n	1393	41	6	53
$2/3\ k_n$	$4/3\ c_n$	1394	39	10	52
k_n	$4/3\ c_n$	1397	40	6	54
$4/3\ k_n$	$4/3\ c_n$	1397	40	6	54

Table 2.4: Influence of the tangential stiffness and damping on the estimated average power draw of the mill. The simulation conditions are defined at the beginning of this section except for the tangential stiffness and the tangential damping coefficient, which are defined in this table. The power percentages are calculated with respect to the rotation power and rounded half down.

Stiffness, damping and friction If identical values are chosen for the normal and tangential stiffness and damping coefficients, i.e. $k_t = k_n$ and $c_t = c_c$, three independent contact param-

[32] It might for instance have some influence on the spin of the particles. Nevertheless, only the average contour of the ball charge can be experimentally validated by the photographs.

eters remain: the normal stiffness k_n, the normal coefficient of restitution ε_n (with regard to the sphere/sphere collision) and the coefficient of friction μ. In this section, their influence on the charge motion and the power draw will be analyzed by a parameter study. First, the *choice of the values of theses parameters* will be explained and then their *results* will be examined carefully.

According to the figure 2.18, the *normal stiffness* k_n should be greater than 10^5 N/m and smaller than 10^7 N/m in order to limit the overlap during a collision roughly from 1 to 10 % with respect to the diameter of a ball for an impact velocity equal to 4 m/s. Such percentages of overlap are certainly unrealistic but necessary to keep the computation time small enough. Moreover, this interval corresponds to the interval of the typical values of the stiffness used in the literature as mentioned earlier (section 1.2.2). Hence, the charge motion and the power draw will be determined for $k_n = 10^5$ N/m, 10^6 N/m and 10^7 N/m.

With regard to the *normal coefficient of restitution*, which is required to determine the normal damping coefficient c_n (sphere/sphere collision), three different values were chosen, too: $\varepsilon_n =$ 0.3, 0.6 and 0.9. The first value was used in the previous validation study of the charge motion in the laboratory mill [Sawley, 2003], as well as in almost any simulation published by Cleary[33], i.a. [Cleary, 1998]. Since the coefficient of restitution takes a value between 0 and 1, the choice of these three values seems to be sufficient to draw a conclusion for the entire interval.

Three different values were also chosen for the *coefficient of friction*. Considering that this coefficient varies between 0 and 1 (except for some particular materials, like rubber), too, we could use the same values as for the normal coefficient of restitution. Nonetheless, the values $\mu = 0.25$, 0.5 and 0.75 were chosen since Cleary and Sawley mainly used the last value, i.e. 0.75, in their studies.

Finally, the time step, which is necessary to accurately integrate the collisions, was determined based on the explanation in the section 2.4.1 by limiting the creation of numerical energy to 1%. The table 2.5 gives some indications about how the time step can be calculated. Despite the generally larger admissible time step in this table, we decided to use the same time step for the same normal stiffness to standardize our approach. Hence, the time steps are equal to $\Delta t = 10^{-5}$, $2.5 \cdot 10^{-6}$ and 10^{-6} s respectively for $k_n = 10^5$, 10^6 and 10^7 N/m. In other words, the simulations take about 4 and 10 times more time for the higher values of stiffness with respect to the smallest stiffness. Altogether, the 27 simulations resulting from the combination of the different parameters took around 5 full days of computation time.

The *results* of the parametric study are shown in the figures 2.30, 2.31 and 2.32 as well as in the table 2.6.

Concerning the *stiffness* of the normal and tangential springs, the global charge motion in the pseudo steady state is almost *independent* of this parameter as shown in the figure 2.30; only the toe angle slightly decreases when the stiffness increases[34]. As a consequence, the power

[33] Cleary, however, uses this value only in simulations of comminution devices containing also a feed material (usually rocks). Therefore, it is questionable why Sawley used this value to model the laboratory mill, which contained only steel balls.

[34] We could not explain why the increase in stiffness actually results in this response of the charge motion. In fact,

k_n [N/m]	ε_n [-]	$\overline{\varepsilon}_n$ [-]	p_n [%]	n [-]	t_c [s]	Δt [s]
10^5	0.3	0.4	5.2	28	$10^{-3.06}$	$3.1 \cdot 10^{-5}$
10^5	0.6	0.63	1.5	52	$10^{-3.08}$	$1.6 \cdot 10^{-5}$
10^5	0.9	0.9	0.23	85	$10^{-3.09}$	$9.6 \cdot 10^{-6}$
10^6	0.3	0.4	5.2	28	$10^{-3.56}$	$9.8 \cdot 10^{-6}$
10^6	0.6	0.63	1.5	52	$10^{-3.59}$	$4.9 \cdot 10^{-6}$
10^6	0.9	0.9	0.23	85	$10^{-3.59}$	$3.0 \cdot 10^{-6}$
10^7	0.3	0.4	5.2	28	$10^{-4.06}$	$3.0 \cdot 10^{-6}$
10^7	0.6	0.63	1.5	52	$10^{-4.09}$	$1.6 \cdot 10^{-6}$
10^7	0.9	0.9	0.23	85	$10^{-3.1}$	$9.3 \cdot 10^{-7}$

Table 2.5: Detailed calculation of the time step on the basis of the strategy explained in the section 2.4.1. The variables k_n, ε_n, $\overline{\varepsilon}_n$, p_n, n, t_c and Δt respectively represent the normal stiffness, the theoretical coefficient of normal restitution (sphere/sphere collision), the effective coefficient of normal restitution, the percentage of numerical energy created during one collision with respect to the non-numerical energy after the collision, the number of time steps per collision, the contact time and the resulting time step.

draw increases in general for greater values of the stiffness (and identical values of ε_n and μ). Nevertheless, the maximum power variation (for identical values of ε_n and μ) is smaller than 3%, which illustrates again the relative independence of the results from the stiffness. This conclusion is very important due to the strong connection between the time step and the stiffness. Hence, choosing a lower stiffness has no significant impact on the results but considerably decreases the computation time. With respect to the dissipation mechanisms, it can be stated that they are also rather independent of the stiffness; on average, the normal damping dissipation increases very slightly, while the tangential dissipation decrease. The reason behind this observation is probably the reduction of the contact time with the increasing stiffness, which in turn reduces the importance of tangential interactions.

The figure 2.31 illustrates that the *coefficient of restitution* becomes important for high values, i.e. close to 1. This behavior can simply be explained by the fact that if a ball loses less energy in a collision, it is able to rebound more powerfully. Therefore, the charge cloud *expands* with the coefficient of restitution. This expansion is particularly important in the toe region, where the liner profile reenters into the charge and thus transfers a significant amount of energy to it. Since the charge is on average displaced to the left, when the coefficient of restitution increases, its center of gravity comes closer to the horizontal center of the mill. Thus, the power draw decreases with ε_n. With regard to the power dissipation mechanisms[35], the normal damping

the opposite change seems to be more realistic since the overlap increases when the stiffness decreases; hence, the size of the charge cloud would be reduced. The variation remains, however, relatively negligible, which is why this phenomenon was not further investigated.

[35] As explained earlier, the sum of the different dissipation percentages might be a few percentages smaller or greater than 100%. In particular, the sum of these percentage, i.e. the power created artificially, increases with ε_n. This strong dependence in the coefficient of restitution is a clear evidence of the artificial creation of energy by the rotation of the tangential spring force. In fact, the greater the coefficient of restitution, the greater the amount of energy which has to be stored during the interaction. Since this energy is stored under the form of a force, which is

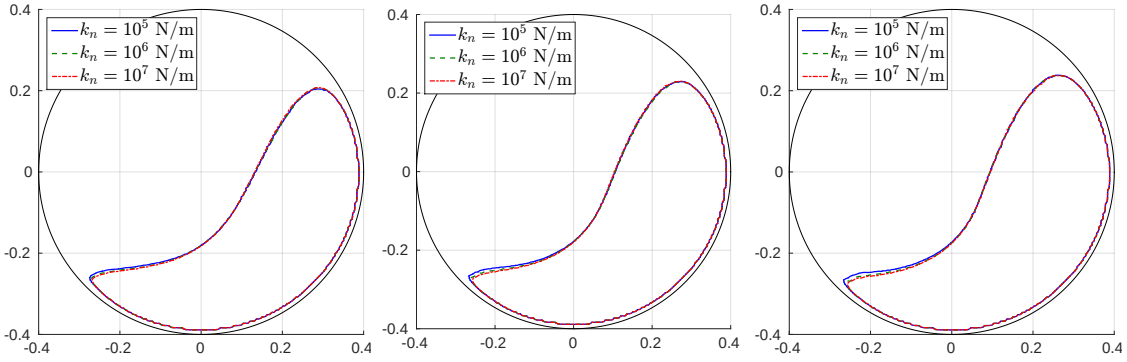

(a) $\varepsilon_n = 0.3$, $\mu = 0.25$. **(b)** $\varepsilon_n = 0.3$, $\mu = 0.5$. **(c)** $\varepsilon_n = 0.3$, $\mu = 0.75$.

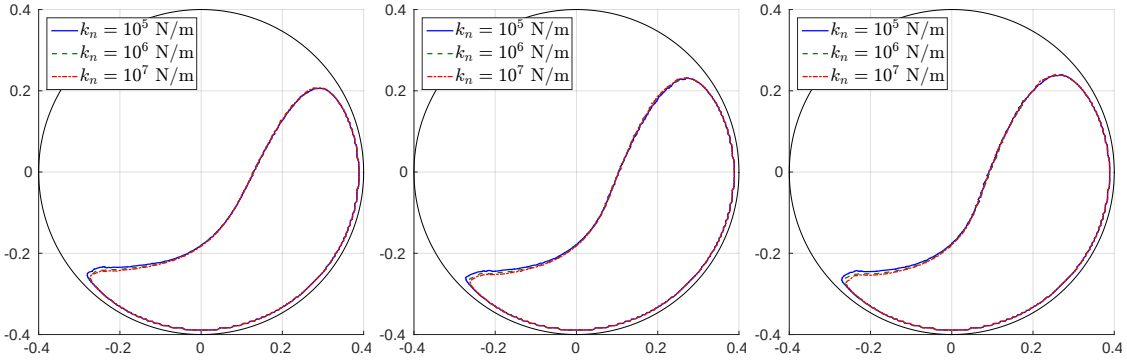

(d) $\varepsilon_n = 0.6$, $\mu = 0.25$. **(e)** $\varepsilon_n = 0.6$, $\mu = 0.5$. **(f)** $\varepsilon_n = 0.6$, $\mu = 0.75$.

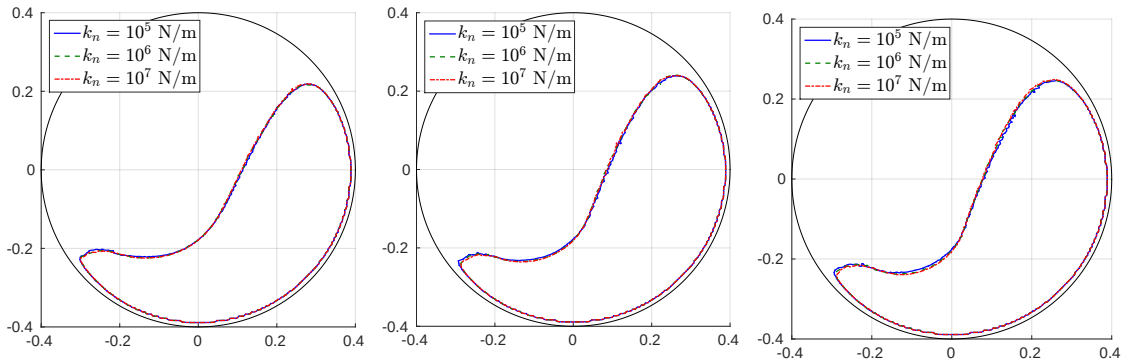

(g) $\varepsilon_n = 0.9$, $\mu = 0.25$. **(h)** $\varepsilon_n = 0.9$, $\mu = 0.5$. **(i)** $\varepsilon_n = 0.9$, $\mu = 0.75$.

Figure 2.30: Influence of the stiffness k_n on the global charge motion, for $k_n = 10^5$ N/m, 10^6 N/m and 10^7 N/m. This figure shows the outline of the mill shell (diameter 0.8 m) and the position density limits for different values of the stiffness and identical values of the coefficient of normal restitution ε_n and the friction coefficient μ for each plot. The simulation parameters are defined at the beginning of this section, except for the contact parameters k_n, k_t, c_n, c_t, μ, which are defined in the labels and legends of the figures ($k_t = k_n$, c_n is deduced from ε_n for a sphere/sphere collision, $c_t = c_n$) and the time step Δt, which was defined in the text section.

dissipation logically decreases considerably while the sliding dissipation increases, when the coefficient of restitution increases. The maximum power variation for a specific stiffness and a specific coefficient of friction, however, remains still quite low, i.e. below 3%, even though the coefficient of restitution almost takes its extremal values.

While the stiffness and the coefficient of restitution only had a relatively small impact on the rotation power, it varies strongly with the *coefficient of friction* (the stiffness and the coefficient of restitution being constant), i.e. at most by 7.7%. The reason behind this important influence is simply the supplementary sliding and the resultant reduction of the lifting of the charge, when the friction coefficient decreases. Hence, the shoulder angle decreases and the toe angle increases at the same time (figure 2.32). In terms of the power dissipation mechanisms, the tangential dissipation obviously rises while the sliding is reduced, when μ increases.

Comparison with the experimental data In this section, the DEM model will finally be *calibrated* on the basis of the experimental data (case 1, section 2.1.2). First, it is inefficient and unnecessary to use unreasonably large values of the stiffness, like 10^6 N/m and 10^7 N/m, even though the predicted power might be slightly lower. Simultaneously, choosing a low stiffness does not mean choosing a very low stiffness. The figure 2.18 showed that when the stiffness k_n drops below 10^5 N/m, the overlap quickly rises to non negligible values. Hence, $k_n = 10^5$ N/m is an acceptable limit, which minimizes the computation time.

In terms of the power draw, the laboratory mill consumes approximately 1,449 W. Since the ball charge weights around 250 kg, it can be expected that around 1 to 5% of this power are dissipated by the bearings of the mill, by damped vibrations, ..., which are obviously inexistent in the simulation. Therefore, the predicted rotation power should have a value between 1376 W and 1434 W. In consequence, the table 2.6 shows that the coefficient of friction should at least be equal to roughly 0.75 so that the rotation power is inside of this interval. It is interesting to notice that the previous DEM results concerning the laboratory mill [Sawley, 2003], are very close to our results. For instance, Sawley predicted 1,401 W and 1,314 W, if $k_n = 10^5$, $\varepsilon_n = 0.3$ and $\mu = 0.75$ or $\mu = 0.25$ respectively[36], while we found 1,394 W and 1,312 W. Consequently, the influence of the implementation of the DEM solver remains negligible (at least from this point of view).

To select a set of material parameter with $k_n = 10^5$ N/m and at least $\mu = 0.75$, we superimposed the position density limits for these parameters (obtained in the previous section, except for $\varepsilon_n = 0.8$) on the photograph of the charge in the figure 2.33. Due to the pronounced perspective of the picture and the parallel projection of the charge in the position density plot, it is necessary that the contour only delimits the charge in contact with the transparent end wall. Since the camera focuses mainly on this area, the picture taken with the higher shutter speed was also represented to distinguish more clearly the depth of the balls in this picture.

rotated by an approximate transformation, the amount of energy created during the rotation increases. More details can be found in [Šmilauer et al., 2014].

[36]The only major difference between Sawley's and our model are the density of the balls (here, 7640 kg/m^3, instead of 7611 kg/m^3, but the total mass of balls is the same) and the surface mesh of the liner.

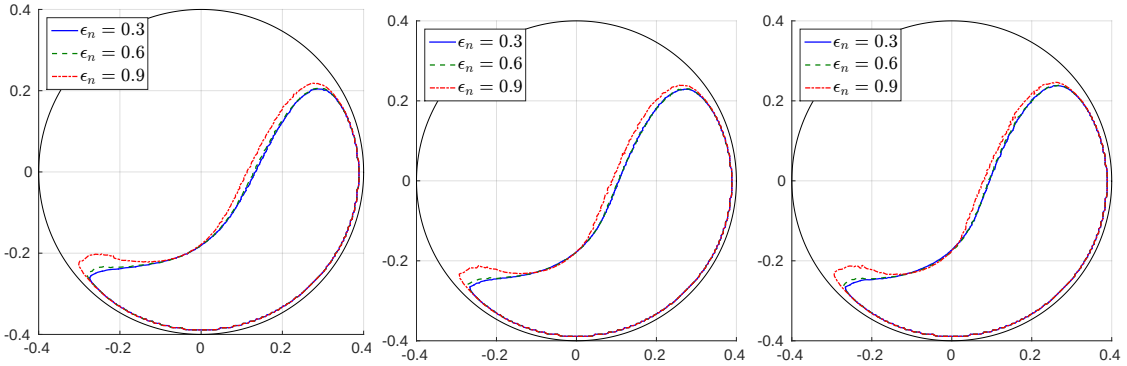

(a) $k_n = 10^5$ N/m, $\mu = 0.25$. **(b)** $k_n = 10^5$ N/m, $\mu = 0.5$. **(c)** $k_n = 10^5$ N/m, $\mu = 0.75$.

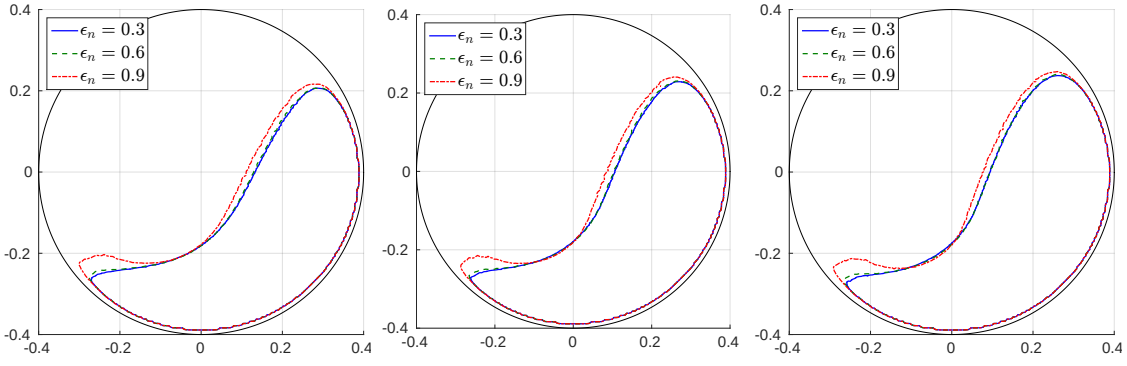

(d) $k_n = 10^6$ N/m, $\mu = 0.25$. **(e)** $k_n = 10^6$ N/m, $\mu = 0.5$. **(f)** $k_n = 10^6$ N/m, $\mu = 0.75$.

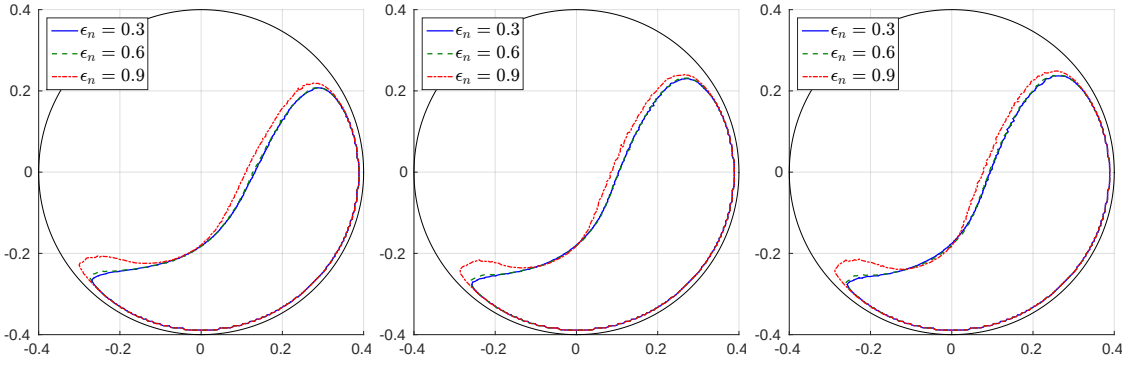

(g) $k_n = 10^7$ N/m, $\mu = 0.25$. **(h)** $k_n = 10^7$ N/m, $\mu = 0.5$. **(i)** $k_n = 10^7$ N/m, $\mu = 0.75$

Figure 2.31: Influence of the restitution ε_n on the global charge motion, for $\varepsilon_n = 0.3$, 0.6 and 0.9. This figure shows the outline of the mill shell (diameter 0.8 m) and the position density limits for different values of the coefficient of restitution and identical values of the normal stiffness k_n and the friction coefficient μ for each plot. The simulation parameters are defined at the beginning of this section, except for the contact parameters k_n, k_t, c_n, c_t, μ, which are defined in the labels and legends of the figures ($k_t = k_n$, c_n is deduced from ε_n for a sphere/sphere collision, $c_t = c_n$) and the time step Δt, which was defined in the text section.

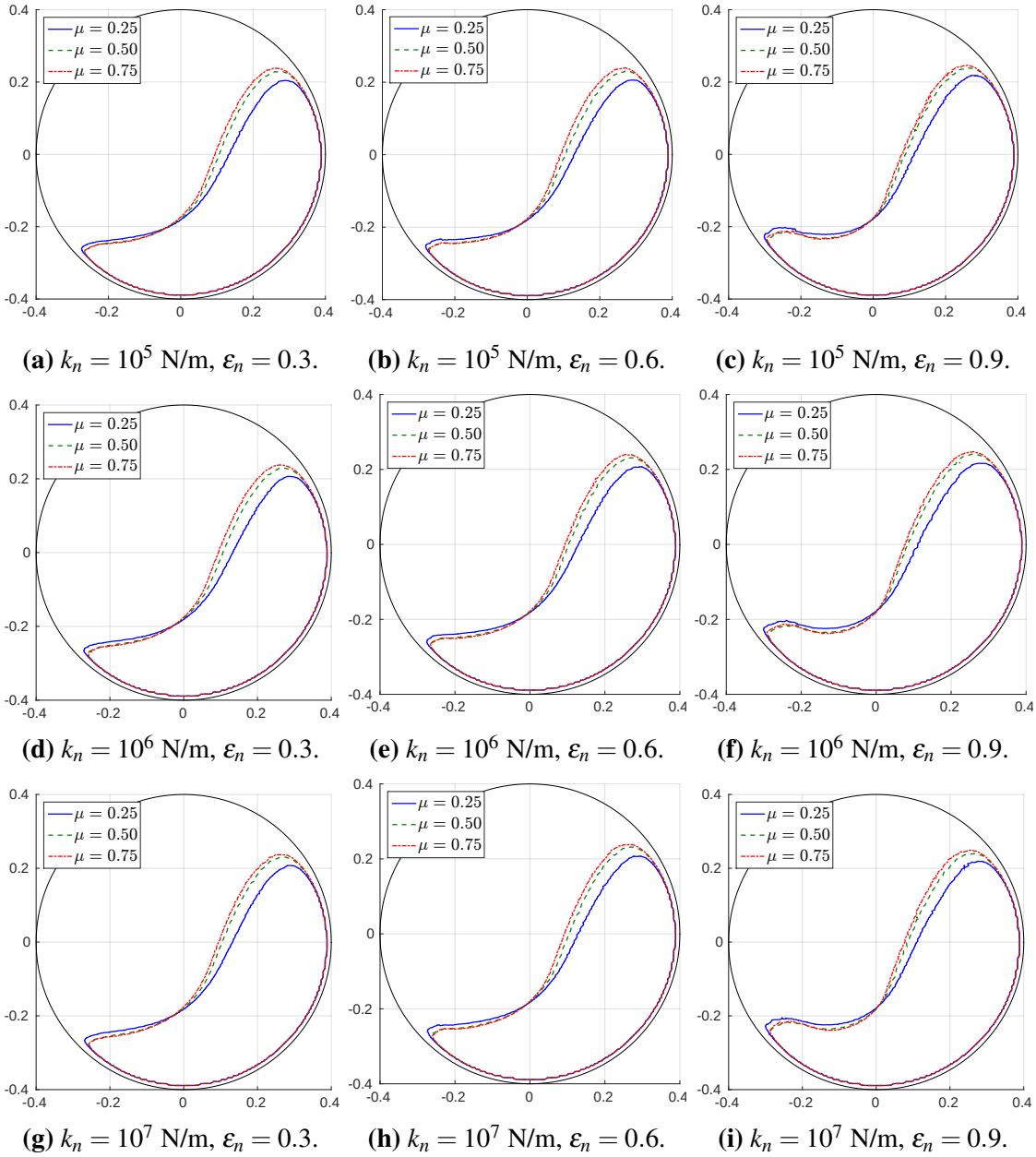

(a) $k_n = 10^5$ N/m, $\varepsilon_n = 0.3$. **(b)** $k_n = 10^5$ N/m, $\varepsilon_n = 0.6$. **(c)** $k_n = 10^5$ N/m, $\varepsilon_n = 0.9$.

(d) $k_n = 10^6$ N/m, $\varepsilon_n = 0.3$. **(e)** $k_n = 10^6$ N/m, $\varepsilon_n = 0.6$. **(f)** $k_n = 10^6$ N/m, $\varepsilon_n = 0.9$.

(g) $k_n = 10^7$ N/m, $\varepsilon_n = 0.3$. **(h)** $k_n = 10^7$ N/m, $\varepsilon_n = 0.6$. **(i)** $k_n = 10^7$ N/m, $\varepsilon_n = 0.9$.

Figure 2.32: Influence of the friction coefficient μ on the global charge motion, for $\mu = 0.25$, 0.5 and 0.75. This figure shows the outline of the mill shell (diameter 0.8 m) and the position density limits for different values of the friction coefficient and identical values of the normal stiffness k_n and the coefficient of normal restitution ε_n for each plot. The simulation parameters are defined at the beginning of this section, except for the contact parameters k_n, k_t, c_n, c_t, μ, which are defined in the labels and legends of the figures ($k_t = k_n$, c_n is deduced from ε_n for a sphere/sphere collision, $c_t = c_n$) and the time step Δt, which was defined in the text section.

Stiffness [N/m]	Normal coefficient of restitution [-]	Coefficient of friction [-]	Rotation power [W]	Percentage of normal power [%]	Percentage of tangential power [%]	Percentage of sliding power [%]
10^5	0.3	0.25	1311	38	1	60
10^5	0.3	0.50	1382	38	4	58
10^5	0.3	0.75	1391	40	8	52
10^5	0.6	0.25	1300	34	1	65
10^5	0.6	0.50	1373	33	4	64
10^5	0.6	0.75	1393	34	9	57
10^5	0.9	0.25	1281	20	0	82
10^5	0.9	0.50	1365	17	0	84
10^5	0.9	0.75	1379	18	5	81
10^6	0.3	0.25	1322	39	1	60
10^6	0.3	0.50	1394	38	3	58
10^6	0.3	0.75	1414	40	7	53
10^6	0.6	0.25	1336	35	1	62
10^6	0.6	0.50	1386	34	3	63
10^6	0.6	0.75	1417	35	8	58
10^6	0.9	0.25	1299	22	-1	79
10^6	0.9	0.50	1382	19	-1	84
10^6	0.9	0.75	1396	20	4	80
10^7	0.3	0.25	1327	39	1	59
10^7	0.3	0.50	1391	39	3	60
10^7	0.3	0.75	1410	40	6	54
10^7	0.6	0.25	1329	37	0	62
10^7	0.6	0.50	1396	34	3	63
10^7	0.6	0.75	1416	35	7	59
10^7	0.9	0.25	1302	23	-1	78
10^7	0.9	0.50	1373	20	-1	83
10^7	0.9	0.75	1388	21	4	81

Table 2.6: Average power draw of the laboratory mill and the percentages of power dissipated by the specific mechanisms (with respect to the rotation power, rounded half down) calculated for the 27 combinations of the material parameters in the parametric study. The simulation parameters are defined at the beginning of this section, except for the contact parameters k_n, k_t, c_n, c_t, μ, which are defined in this table ($k_t = k_n$, c_n is deduced from ε_n for a sphere/sphere collision, $c_t = c_n$) and the time step Δt, which was defined in the text section.

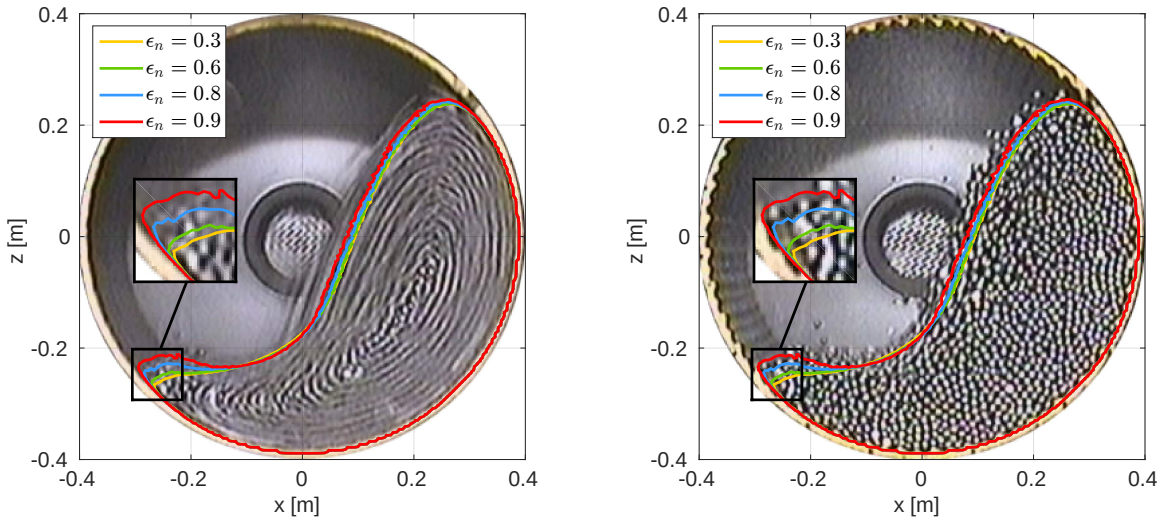

(a) Shutter speed equal to 1/12 s - trajectories.

(b) High shutter speed - instantaneous position.

Figure 2.33: Ball charge photograph with the superimposed position density limit curves for different coefficients of normal restitution ε_n (sphere/sphere collision). The simulation parameters are defined at the beginning of this section, except for the contact parameters k_n, k_t, c_n, c_t, μ. The normal stiffness k_n and the coefficient of friction μ are equal to 10^5 N/m and 0.75, respectively. The other parameter values can be deduced from these values ($k_t = k_n$, c_n is deduced from ε_n for a sphere/sphere collision, $c_t = c_n$ and $\Delta t = 10^{-5}$ s).

For all four coefficients of restitution, the figure 2.33 shows a very good correlation between the experimental and the numerical charge motions. For $\varepsilon_n = 0.3$ and 0.6, the toe angle seems, however, to be slightly too small, while it is too high for $\varepsilon_n = 0.9$. At the same time, the charge cloud is not expanded enough for $\varepsilon_n = 0.3$ and 0.6. Hence, the contour curve for $\varepsilon_n = 0.8$ was added to find a better compromise. The same coefficient of restitution was used by Cleary to simulate the balls in a cement tube mill without feed material [Cleary, 2009]. This choice is also more reasonable than $\varepsilon_n = 0.3$ (used in the previous study) for balls and liner plates made from steel, which probably remain fairly elastic and thus energy-preserving during a collision. The predicted power draw in this case is equal to 1,384 W. Hence, the predicted power is 4.5% lower than the real power, which might be explained by the non-existence of some real dissipation mechanisms in the model, like the viscous dissipation in the bearings or damped vibrations of the structure. Since determining this power loss accurately is quite complex and since a 4.5% error remains negligible with respect to the stochastic fluctuations of the power draw in the pseudo steady state, this last set of material parameters is as close as we can get to the precise prediction of the charge motion and the power draw in the laboratory mill.

Experimental validation

To prove that the model is truly *predictive*, our choice of the simulation parameters will first be summarized in this section. Then, this model will be used to predict the general charge motion and the power draw of the different experimental scenarios presented in the section 2.1.2.

The mill is filled with 15 mm diameter spherical balls having a material density equal to 7640 kg/m^3. The medium *Perfecto ABAB* and the *Duolift* meshes geometrically approximate the shell liner. The material contact parameters are the following:

- equivalent normal stiffness: $k_n = 10^5$ N/m
- equivalent tangential stiffness: $k_t = 10^5$ N/m
- theoretical coefficient of normal restitution $\varepsilon_n = 0.8$ (with respect to the sphere/sphere collision, to deduce the equivalent normal damping coefficient c_n)
- equivalent tangential damping coefficient $c_t = c_n$
- coefficient of friction $\mu = 0.75$

The time step is equal to $\Delta t = 10^{-5}$ s. The total simulated time is equal to 5 s and the pseudo steady state characteristics are averaged over the period[37] from 2.5 s to 5 s. The sampling period of the post-processing data is equal to $\Delta t_{\text{rec}} = 0.01$ s. To create the position density plots and its contour curves the space (0.8 m $\times$ 0.8 m) was divided into 150×150 cells.

The results are finally summarized in the figures 2.34 and 2.35, as well as in the table 2.7. The first figure shows the real trajectories of the charge (low shutter speed) and the position density plots for each validation case. The position density limits (based on the respective simulations) were also added in the sub-figures in order to simplify their comparison; it is obviously the same in the two respective figures since it was determined by the simulation. Two conclusions can be drawn. The most important conclusion is certainly that the DEM model is truly *predictive* with respect to the global charge motion. It is difficult to see any systematic difference between the ball charge and the position density limit. One may think that the balls move into the liner for the *Duolift* profile. Nevertheless, this is only due to the large average roughness (distance between peaks and valleys) of this profile and the long exposure time. The second conclusion is that the *position density limit* is a perfect tool to determine the global charge motion and in particular, the shoulder and toe angles based on the DEM model.

To emphasis how accurate the predictions of the charge motion are, the figure 2.35 illustrates the real and simulated positions of the charge. Since the perspective is included in both representations (real and numerical), i.e. it is not a parallel projection, a clear agreement between the reality and the simulation can also be observed more deeply inside of the mill.

[37] It was checked if the pseudo steady state was reached after 2.5 s for the different filling ratios and percentages of critical velocity. Mainly for the case 3 (greater filling ratio), the transient response is still visible after 2.5 s. The averaging period was, however, not adapted since its seems reasonable that the influence of the oscillations is annihilated after calculating the average, i.e. the influence of the transient state is assumed to be negligible.

Concerning the average power draw, the table 2.7 shows that the real power draw is very close to the predicted rotation power. This latter power is, however, systematically lower than the real power by 1.6 to 4.9 %. This difference seems to be acceptable since the increased friction losses in the bearings due to the additional mass and the damped vibrations of the structure were not quantified in the simulation. In terms of the dissipation mechanisms, at most 3% of artificial power are created by the explicit integration and the approximate rotation of the tangential spring force, while the sliding of the charge remains the major dissipation mechanism accounting for around 70%.

In conclusion, the *DEM model is able to predict the global charge motion and the power draw* of the laboratory mill for different filling ratios, percentages of critical velocity and liner profiles within the limits of their validity (photographs of the charge motion and variation of the power draw by around 5 %). Hence, the DEM model renders future experimental tests unnecessary.

Name	Real power draw [W]	Rotation power [W]	Percentage of normal power [%]	Percentage of tangential power [%]	Percentage of sliding power [%]
Case 1	1,449	1,394	26	7	68
Case 2	1,656	1,630	28	8	67
Case 3	1,893	1,864	27	8	68
Case 4	1,429	1,365	26	7	69

Table 2.7: Average power draw of the laboratory mill and the percentages of power dissipated by the specific mechanisms (with respect to the rotation power, rounded half down) calculated for the 4 calibration and validation cases.

2.4.3 Extension to the industrial mill

While the DEM model provides quite accurate predictions of the charge motion and the power draw of the laboratory mill, the question arises whether this model is also able to directly estimate these characteristics for an *industrial mill*. In this section, we will try to answer this question by rescaling the DEM model of the laboratory mill to the equivalent full-scale mill and by comparing the charge motion and the power draw in both cases.

In terms of the *geometry*, the laboratory mill is the spatial reduction of a 4 m diameter ball mill. Hence, the dimensions of the shell liner mesh and the diameter of the balls simply have to be multiplied by 5 in order to obtain their real sizes in the industrial mill. In consequence, the rotation speed has to be reduced to keep the percentage of critical velocity unchanged. Hence, the total ball charge weights 32,156 kg and the mill rotates at 15.07 rpm in the first scenario (case 1, section 2.1.2).

In contrast to the geometry, it is less obvious to determine the *material* parameters. First, the stiffness has to be increased due to the increased mass and the increased velocity of the balls in order to limit the percentage of overlap. If the drop height of a ball is equal to the

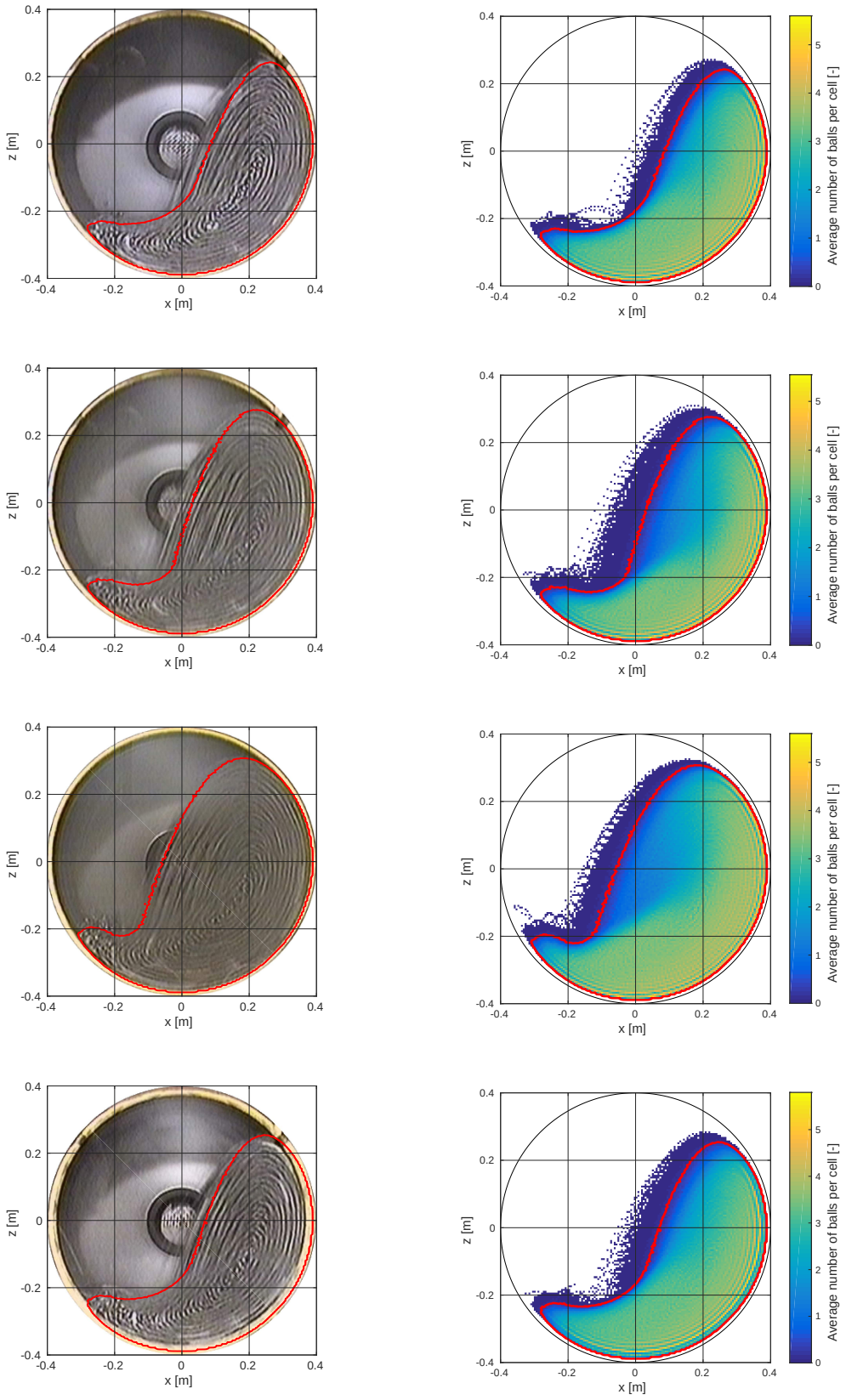

Figure 2.34: Trajectories of the real charge motion (shutter speed equal to 1/12 s) with their respective position density plots. The position density limits were also represented for each case in both figures (based on the respective simulation). Cases 1 to 4 from the top to the bottom.

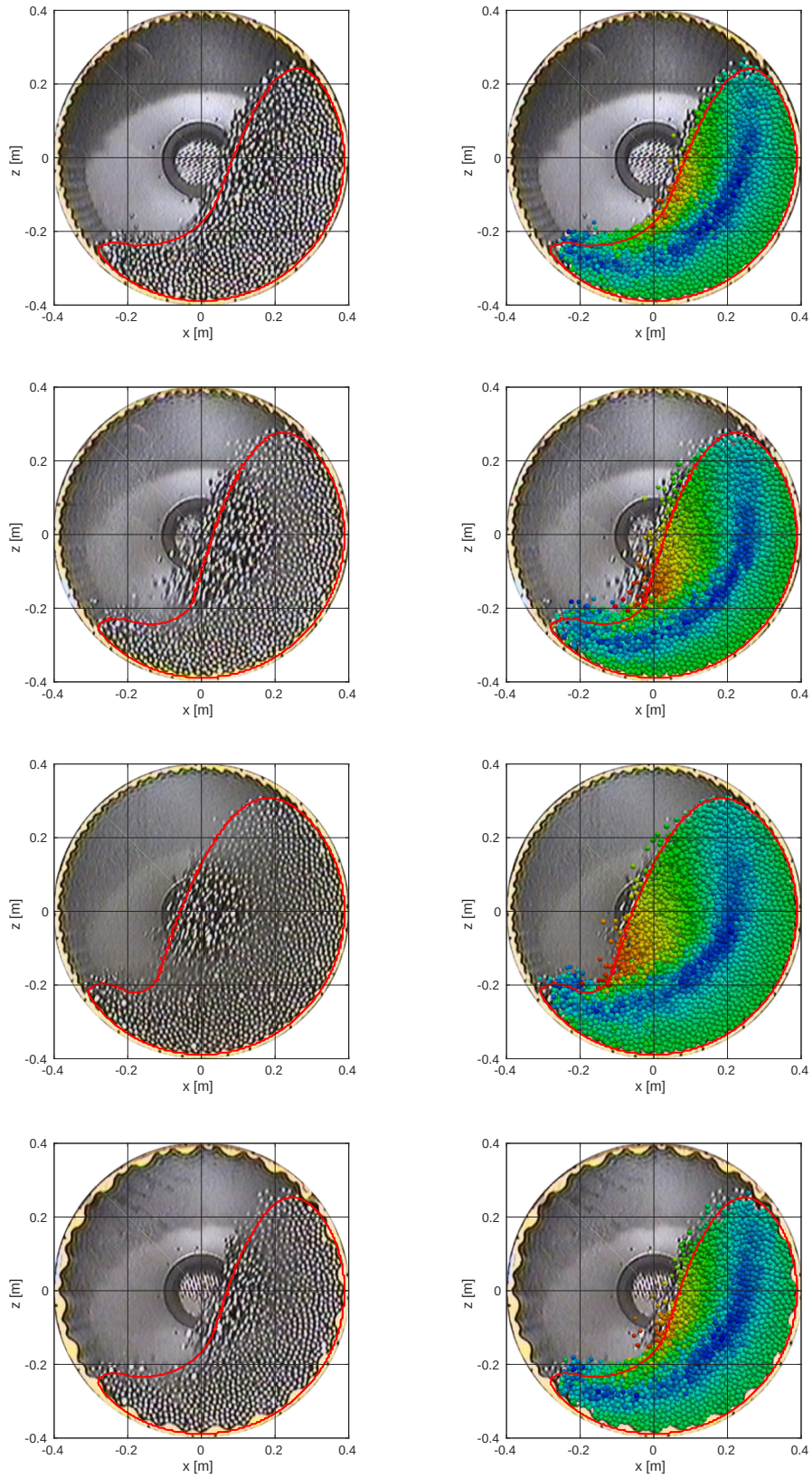

Figure 2.35: Position of the real charge (high shutter speed) on the left and right with the superposed simulated charge after 5 s of simulated time on the right. The position density limits were also represented for each case in the two corresponding figures (based on the simulation). The color code represents the amplitude of the translation velocity, i.e. blue (at rest) to red (3, 3.2, 3.4 and 3.15 m/s in the cases 1 to 4, respectively). Cases 1 to 4 from the top to the bottom.

diameter of the mill, its maximum velocity is almost equal to 9 m/s. In the laboratory mill ($k_n = 10^5$ N/m and $\varepsilon_n = 0.8$), the maximum percentage of overlap (with respect to the diameter of the ball) during a ball/ball collision at 4 m/s was equal to 6.23%, which corresponds to 0.934 mm. The same percentage of overlap and the same absolute overlap are approximately reached for $k_n = 2.5 \cdot 10^6$ N/m and $k_n = 6 \cdot 10^7$ N/m in the full-scale model at 9 m/s (with $\varepsilon_n = 0.8$). Notice that this strategy, which is used to determine the normal stiffness of the balls in the full-scale mill, is totally *heuristic*. In fact, choosing a stiffness, which is based on the physical characteristics of the balls, would only significantly increase the computation time, while the results[38] are almost independent of this parameter as mentioned above.

With regard to the *coefficient of restitution*, it seems likely that the percentage of energy dissipated during a collision in the industrial mill with respect to the energy before the collision is greater than the respective percentage in the laboratory mill because of the greater impact forces. In fact, if the forces are higher, it can be expected that the material is stressed increasingly in its plastic zone, which is responsible for the energy dissipation. Moreover, the industrial mill contains a feed material in contrast to the laboratory mill. Even though the volume occupied by this material is relatively low in the first chamber of a cement grinding mill (volume of the interstices between the balls), it might have an influence on the coefficient of restitution. Considering that no validation data of the charge motion in an industrial mill is available, only the influence of the contact parameters on this charge motion and the power draw can be determined. Hence, it would be interesting to compare these characteristics for $\varepsilon_n = 0.3$, i.e. the value which was extensively used by Cleary and Sawley [Cleary, 1998, Sawley, 2003], and $\varepsilon_n = 0.8$, i.e. the value which we determined previously for the laboratory mill.

Finally, the *coefficient of friction* is in general a parameter, which is independent of the size of the mill according to its definition in the Coulomb model, e.g. in [Rabinowicz, 1995]. For this reason, it is supposed that this value is the same for the laboratory and the industrial mills. It might be criticized that the feed material would change this value. Nonetheless, Cleary used the same value, which we used without a feed material, i.e. $\mu = 0.75$, to analyze the charge motion of comminution devices filled with a feed material. Since no additional information is known about this parameter, it seems reasonable to suppose that it does not change with the size of the mill.

In a nutshell, it would be interesting to study the charge motion and the power draw in the full-scale mill for $k_n = 2.5 \cdot 10^6$, $5 \cdot 10^7$ N/m (instead of $6 \cdot 10^7$ N/m, which is almost identical to this value), $\varepsilon_n = 0.3$, 0.8 and $\mu = 0.75$. As explained earlier, we assume that the tangential parameters of the contact model are equal to the normal parameters, i.e. $k_n = k_t$ and $c_n = c_t$. The table 2.8 summarizes the simulated cases and their *times steps*, which were calculated according the guidelines in the section 2.4.1; since the mass of the balls is larger than in the laboratory mill, the time step has the same order of magnitude than before despite the larger values of the

[38] Here the results are only the global charge motion and the power draw. Maybe, the stiffness has a significant impact on other characteristics, like the individual ball trajectories or the forces. Nevertheless, these characteristics can not be validated in this thesis since the corresponding experimental data is not available and usually very difficult to obtain (e.g. instrumenting a lifter with strain gauges and/or radioactive tracing of the balls).

stiffness. Because the rotation speed has been divided by 2 with respect to the laboratory mill, the pseudo steady state starts only after 5 s instead of 2.5 s according to the evolution of the center of gravity of the charge. Hence, the charge motion and the power draw will be averaged from 5 to 10 s in order to obtain their mean values.

Name	k_n [N/m]	ε_n [-]	μ [-]	Δt [s]
Case 1	$2.5 \cdot 10^6$	0.3	0.75	$5 \cdot 10^{-5}$
Case 2	$2.5 \cdot 10^6$	0.8	0.75	$2.5 \cdot 10^{-5}$
Case 3	$5 \cdot 10^7$	0.3	0.75	10^{-5}
Case 4	$5 \cdot 10^7$	0.8	0.75	$5 \cdot 10^{-6}$

Table 2.8: Contact parameters (normal stiffness, normal coefficient of restitution with respect to the sphere/sphere collision and the coefficient of friction) and time steps used to predict the charge motion and the power draw in the industrial mill.

The figure 2.36 shows the position density limits for the industrial mill but also the limit obtained for the laboratory mill ($k_n = 10^5$ N/m, $\varepsilon_n = 0.8$ and $\mu = 0.75$), which has been *rescaled*. As expected the general charge motion (with regard to the space occupied by the balls) in the laboratory mill is *virtually identical* to the charge motion in the full-scale mill for $k_n = 2.5 \cdot 10^6$ N/m and $\varepsilon_n = 0.8$ because of three reasons: the definition of the velocity with respect to the critical velocity, the geometric similarity of the reduced mill and its charge with respect to the full-scale mill, as well as the adapted contact parameters.

More precisely, if these three hypotheses are satisfied and if a ball is located at a geometrically similar position in the laboratory mill or the industrial mill, the motion of this ball is defined by exactly the *same equilibrium equation*. This statement can be illustrated by writing the equilibrium equation[39] of this ball along the x-axis, which is independent of the size of the mill since the mass m can be simplified:

$$m\,\ddot{x} = c_1\,m\,r\,\omega^2 + c_2\,m\,g \quad \Rightarrow \quad \ddot{x} = c_1\,r\,\omega^2 + c_2\,g \tag{2.14}$$

where x, r, ω and g are the position of the ball along the x-axis, the radial distance between its center and the rotation axis, the angular speed of the mill and the gravitational acceleration, respectively. The non-dimensional constants c_1 and c_2 depend on the specific position of the ball (i.e. sines and cosines to project the forces along the x-axis) in the mill and the friction coefficient. Hence, if a ball is located at a *similar* position in both mills (importance of the same filling ratio) and if the percentages of critical velocity (i.e. $r\,\omega^2$ is constant) and the friction coefficients are identical (in both mills), the motion of this ball is governed by the same equation. For instance, this is the reason why the balls diverge from the liner at the same shoulder angle in the reduced and the full-scale mill.

To obtain numerically the same average charge motion[40] in both mills, it is also important to

[39] The contact with other balls or the liner is implicitly represented by the centrifugal term in this equation, which is not entirely correct but the only simple explanation of the similarity of the results.

[40] The charge motion denotes here the place occupied by the balls in the mill. Their velocity is obviously different in similar regions of both mills due to their different size.

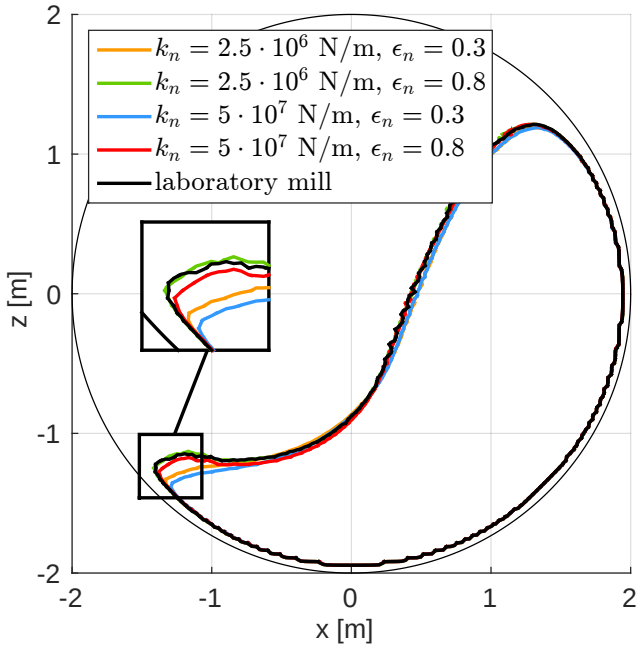

Figure 2.36: Position density limits of the charge in the industrial mill and the rescaled limit of the charge in the laboratory mill for the first experimental data set (case 1, section 2.1.2). The simulation and averaging parameters were explained in this section for the industrial mill and in the section 2.4.2 for the laboratory mill. The grid used to determine the position density is still composed of 150 horizontal and 150 vertical divisions.

use the same value of coefficient of restitution, since this factor is by definition independent of the mill size. In reality, it depends, however, on the ball size, as explained earlier. Finally, choosing the normal stiffness based on the percentage of overlap ensures that the overlap in the full-scale mill is approximately equal to the overlap in the reduced mill multiplied by the scale factor, such as any other geometrical characteristic. In conclusion, these reasons give some indications about why geometrically similar results of the charge motion were found for the laboratory and the industrial mill.

Concerning the influence of the stiffness and the coefficient of restitution, the charge position remains *almost unchanged* (figure 2.36), i.e. the toe angle decreases slightly with the stiffness and more significantly with the coefficient of restitution. The table 2.9 confirms this observation by means of the maximum relative power difference, which is equal to only 2.2%. It is interesting to notice that the power draw of the laboratory mill is not simply multiplied by the scale factor to obtain the power draw of the industrial mill; in fact, it is rather multiplied by the *scale factor to the power of 3.5*, e.g. $1.394 \cdot 5^{3.5} = 389.6$ kW. The power draw can actually be calculated by

the following formula in the pseudo steady state:

$$P_{\text{rot}} = m\, g\, x_{\text{COG}}\, \omega \tag{2.15}$$

where m, g, x_{COG} and ω are the mass of the charge, the gravitational acceleration, the horizontal distance of the center of gravity of the mill charge with respect to the rotation axis and the rotation speed, respectively. Since the average relative position of the charge is almost unchanged by the scaling of the mill,

$$P_{\text{rot}} \propto D^3\, g\, D \sqrt{\frac{g}{D}} \quad \Rightarrow \quad P_{\text{rot}} \propto D^{3.5} \tag{2.16}$$

where D is the diameter of the mill[41].

Name	Rotation power [kW]	Percentage of normal power [%]	Percentage of tangential power [%]	Percentage of sliding power [%]
Case 1	390.0	41	7	52
Case 2	387.0	26	7	66
Case 3	395.4	40	5	54
Case 4	393.3	28	6	65

Table 2.9: Average power draw of the industrial mill and the percentages of power dissipated by the specific mechanisms (with respect to the rotation power, rounded half down) calculated for the experimental validation case 1 (section 2.1.2) and the 4 material sets summarized in the table 2.8.

In conclusion, it is impossible to prove that the average charge motion and the power draw of the industrial mill are accurately estimated by the DEM model of the full-scale mill because no experimental validation data is available. Nevertheless, there is *strong evidence that this prediction strategy actually delivers accurate results* provided that the material parameters do not change significantly (except for the stiffness).

[41] In practice, the power scaling is rather written as a function of the diameter scale factor s_{dia} and the length scale factor s_{length}. Hence, the power of the laboratory mill is theoretically multiplied by $s_{\text{dia}}^{2.5}\, s_{\text{length}}$. A better empirical approximation is, however, $s_{\text{dia}}^{2.7}\, s_{\text{length}}$ according to [Prignon & Lepoint, 2001].

Chapter 3

Liner Wear Simulation

Wear is one of the reasons why material objects loose their usefulness over time. In the case of ball mills, the liner profile becomes smoother after each working hour and hence the energy available for comminution is reduced. Simultaneously, the protection of the mill shell by the liner decreases. In order to enhance its lifespan, it is necessary to understand how the material is worn away from the liner. In consequence, a *general method to predict the spatial wear distribution but also the resulting change in the geometry* of the mill liner will be explained in this chapter. The wear distribution could for instance give some advice about where a more abrasion-resistant insert would be required in the structure while the predicted geometry modification could be used to develop a shape-preserving liner profile. It is important to notice that the procedure, which will be explained hereinafter, can also be applied to other systems subjected to stresses by granular materials, such as vertical shaft impactor mills.

First, *experimental data*, which consists of several wear profiles measured in a full-scale industrial mill, will be described. In the same way as in the second chapter, this data will later be used to calibrate and validate the wear model. Based on the guidelines of the second chapter, the *charge motion simulation*, which is necessary to sample the load leading to wear, will then be specified. Finally, by combining the charge motion simulation with the wear model, we will *simulate the wear evolution* of the mill liner in the third part of this chapter. In contrast to the second chapter, the explanation of the method will be less separated from the numerical results in order to use these results directly as an illustration of the theoretical principles.

3.1 Experimental Data

As explained earlier, *experimental data* is necessary to build the bridge between computational engineering and the reality. In the case of liner wear simulations, detailed experimental data is usually *rare* because of the preponderant complexity of the measurements (mechanical profiling gauge, section 1.4.2) with respect to the little need of such measurements in the past. Only

recently, more sophisticated devices, like the Outotec®-MillMapper[1], a 3D laser scanner connected to a specific post-processing program, have become available.

In this study, we will analyze the liner wear evolution of *Magotteaux's Duolift liner* in the first compartment of a 5.8 m diameter cement tube mill. The total length of the mill is equal to 17.14 m, while the length of the first compartment is only equal to 5.1 m.

In terms of the *operating conditions*, the mill rotates at 13.48 rpm, which is equivalent to 76.75% of its critical speed. The ball charge distribution in the first compartment is provided in the table 3.1.

Average diameter [mm]	Mass [t]	Number
82.3	22.7	10180
79.0	27.2	13761
72.4	44.3	29181
63.0	51.0	50987

Table 3.1: Ball charge distribution in the first compartment. The density used to calculate the number of balls is equal to 7640 kg/m^3.

The *Duolift* liner plate spans a 500 mm arc of the shell circle and it has an axial width equal to 250 mm. In consequence, the entire liner is assembled of 20 rows of which each is composed of 36 liner plates. A new liner plate weights around 85 kg and is made of 12% chromium cast iron, which is a popular abrasion-resistant alloy reaching a hardness of around 50 HRC, i.e. 500 HV. The liner profile curve consists of a smaller and a larger wave as illustrated in the figure 3.1. This design is known for its shape-preserving profile over time. In fact, to obtain some tangible evidence of this characteristic, the wear evolution of this liner was monitored carefully during a decade. Hence, the figure 3.1 also shows a limited number of its *wear profiles* measured on a plate of the fourth row (with respect to the head liner) from 1996 to 2006. The full data set can be found in the appendix D.

Even though the liner is a 1D liner, i.e. its height does initially not change along the axial direction, it is characterized by a significant difference between the maximum and minimum height after several thousand operating hours. The reason behind this difference is the creation of *grooves* in the liner due to the organized flow patter of the balls. The figure 3.2 illustrates this phenomenon. Next to the head liner, the grooves seem to follow a helicoidal trajectory while the trajectories further away seem to be located in vertical planes having a constant axial offset. This offset was measured for a plate of the fifth row (figure 3.3). Unfortunately, the exact azimuthal position of the measurement and the respective number of operating hours are not known. The offset is on average equal to 62.5 mm (four grooves per plate), which is slightly smaller than the weighted[2] average diameter of the balls (around 70 mm).

[1] http://www.outotec.com/en/Products--services/Process-equipment/Grinding-mills/Liner-condition-monitoring/MillMapper/

[2] The weight is the number of balls.

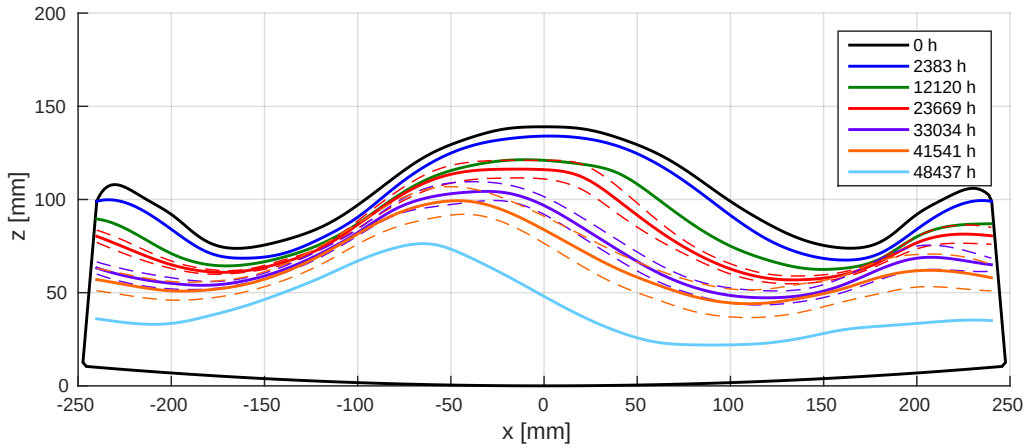

Figure 3.1: Outline of the *Duolift* liner plate with a limited number of its wear profiles measured on a plate of the fourth row (with respect to the head liner) from 1996 to 2006. The full data set is provided in the appendix D. The solid lines represent the average height while the dashed lines represent the respective minimum and maximum height of the plate, if these are known. The last line is, however, not the average but the minimum height of the profile, when it was changed. The mill rotates (negatively) around the *y*-axis, i.e. from the left to the right with respect to the pictured plate. The legend indicates the number of operating hours after which the profiles were measured.

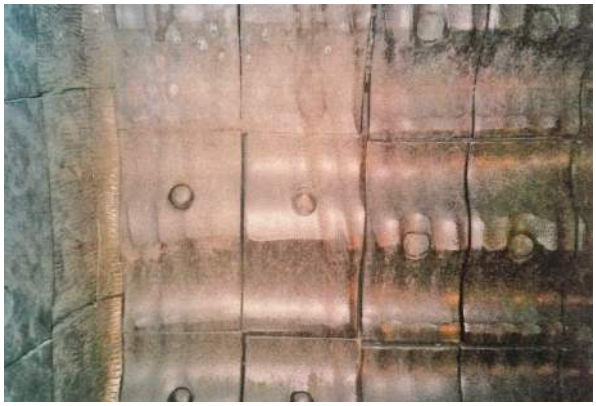

(a) Liner plates with grooves next to the head liner. The fourth row is the last visible row in this picture.

(b) Liner plates along the first compartment.

Figure 3.2: Worn liner plates after around 20,000 h [Magotteaux S.A., 2015].

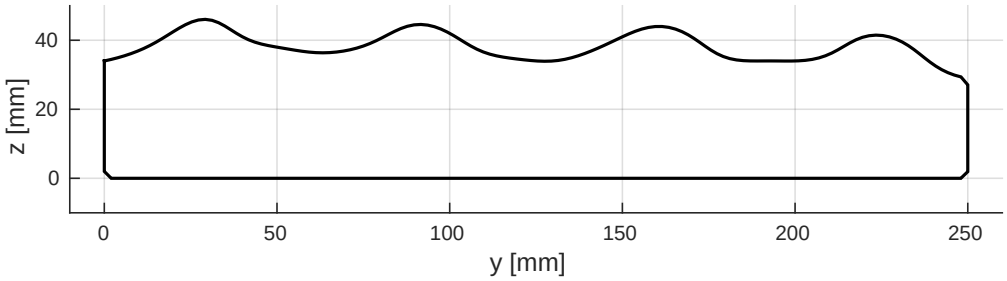

Figure 3.3: Axial profile of a liner plate of the fifth row. The corresponding azimuthal position and the number of operating hours, after which the measurements were taken, are not known. According to the height, this measurement seems, however, to have been taken, when the liner was changed.

Supposing that the radial segregation of the balls due to their different diameters remains non-discernible for a percentage of critical velocity close to 70% [Cleary, 1998], the smaller offset of the grooves with respect to the weighted average diameter of the balls can be explained by taking into account the structural organization of the balls, which is illustrated in the figure 3.4. In this case, the offset would be equal to about 61 mm. Since the heavier balls are located more at the outside of the charge (radial segregation by the centrifugal force), its is understandable why the offset between the grooves is a little larger than 61 mm in the reality, i.e. around 62.5 mm.

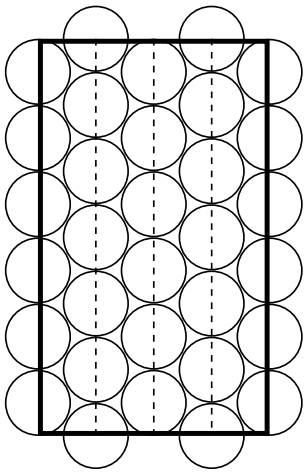

Figure 3.4: Simplified structural organization of the balls, which is the reason for the offset between the grooves being smaller than the weighted average diameter of the balls. The bold rectangle and the dashed lines represent the plate (viewed from above) and the valleys of the grooves, respectively.

The experimental data described in this section will be used in order to calibrate and validate the wear model in the third section of this chapter (section 3.3). Notice that calibrating

and validating a model with the same data obviously begs the question (circular reasoning). In consequence, further studies will be necessary to clearly assess the predictive capabilities of the model for different operating conditions, materials and geometries.

3.2 Charge Motion Simulation

Since wear in dry ball milling is the consequence of mechanical interactions between the balls and the liner, it is essential to *determine the characteristic values of these interactions*, like the normal forces or sliding distances, before deducing the resulting wear from them. According to the findings in the previous chapter, the discrete element method is the most promising method to predict the interactions between the balls and the liner despite the idealized contact model.

For this reason, we will explain the different *DEM models*, which will be used to compute the interaction data, in this section. In a similar way than in the previous chapters, the explanation will be divided into three sections: the *material*, the *geometry and boundary conditions*, and the *simulation* as such.

3.2.1 Material

Concerning the material, the *linear spring-slider-damper contact law* will obviously be used with the following parameters as a result of the previous chapter (section 2.4.3):

- density: $\rho = 7640$ kg/m^3
- normal stiffness: $k_n = 2.5 \cdot 10^6$ N/m.
- coefficient of normal damping c_n derived from the coefficient of normal restitution $\varepsilon_n = 0.3$ for the collision of two spheres with the same diameter.
- tangential stiffness: $k_t = k_n$.
- coefficient of tangential damping: $c_t = c_n$.
- coefficient of friction: $\mu = 0.75$.

Even though the normal stiffness could be slightly greater than $2.5 \cdot 10^6$ N/m, since the mill diameter is slightly larger than the diameter of the full-scale laboratory mill (in the section 2.4.3), i.e. 5.8 m vs. 4 m, we will continue to use the previous value since it has a negligible influence on the charge motion as well as on the power draw[3]. At the same time, it renders possible to use a larger time step. Notice also, that the lower coefficient of restitution was used, i.e. 0.3 instead of 0.8, to account for the seemingly higher dissipation of collisions in the presence of the clinker in the cement mill.

The previous material parameters will be used throughout the whole third chapter. Changing them or trying to study their influence on the wear is relatively difficult because it would add an important number of degrees of freedom to the study.

[3]This material parameter might have an influence on other characteristics of the interactions, like the impact time. Nevertheless, these characteristics are very difficult to validate on the basis of experimental results. Hence, we have no argument in favor or against the change in the stiffness except for the charge motion (outline of the charge cloud) and the power draw.

3.2.2 Geometry and boundary conditions

As mentioned previously, the geometry modification by wear in ball mills is essentially a *3D phenomenon* since grooves are created in a liner, which initially had no height variation along the axial direction. To fully capture the wear data in the charge motion simulation, the underlying binning structure (section 1.4.1), which accumulates the local wear data, has therefore not only to be discretized along the azimuthal direction but also along the axial direction. In DEM simulations, the most direct definition of a binning structure of the liner is obviously the surface mesh, which represents this liner. The previous reasoning therefore implies that a surface mesh similar to the one used in the previous chapter (for instance, in figure 2.10) is not sufficient anymore to predict the full geometry modification of the liner. In fact, the surface mesh has to be much finer.

Since the axial length of the grooves is on average equal to 62.5 mm, a good estimate of the average element size in the triangular surface mesh seems to be 15 mm. Hence, each groove could be geometrically approximated by 4 segments along the axial direction. One plate would then require around 1,200 elements, which would lead to almost 900,000 facet elements in addition to around 100,000 spherical elements, if the entire first compartment of the mill was simulated. This number of elements is obviously far too large considering that the simulations in the second chapter took already around 2 h for a total of almost 22,000 elements and a simulated time of 5 s. Instead of simulating the entire first compartment, it is therefore more reasonable to simulate only an *axial slice* of the mill (figure 3.5). Here, we will focus on a *250 mm and a 500 mm slice*, which are equivalent to 1 or 2 rows, in order to understand the influence of their length on the results.

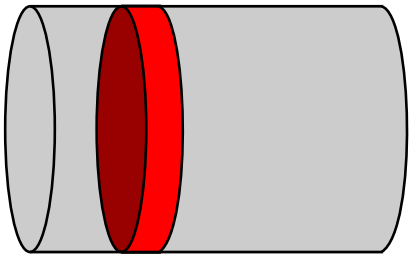

Figure 3.5: Axial slice of the mill.

Simulating only a slice of the mill brings up the question of how to *axially close this slice* so that the balls do not simply fall out of the liner. One answer to this question is to define a *periodic boundary condition*, i.e. the balls leaving the slice on one side reenter it from the other side (figure 3.6a). Because of the relatively long distance between the analyzed plate (forth row) and the head liner, the influence of this head liner seems to be negligible at the forth row. Hence, this boundary condition seems to be consistent with the reality. It has, however, the serious drawback of not axially restraining the charge motion. Theoretically, grooves can therefore not be created with the periodic boundary condition. This is why a second answer to the previous question can be considered.

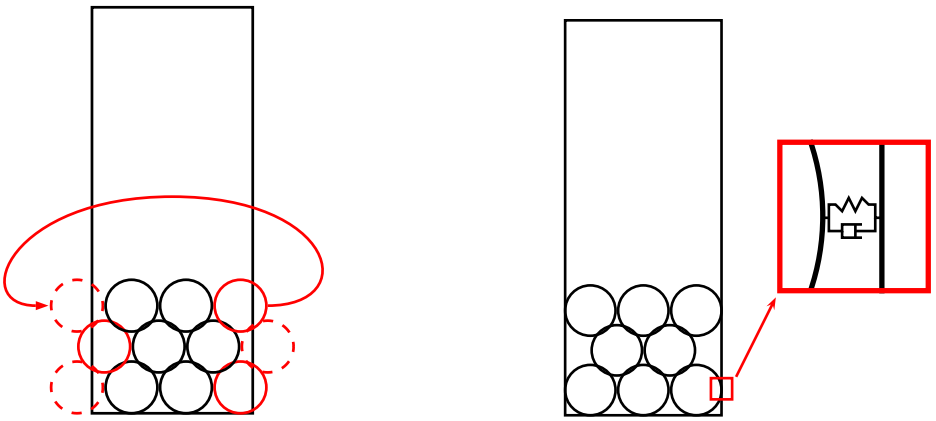

(a) Periodic boundary condition, i.e. a ball, which leaves the slice on one side, reenters by the other side.

(b) Wall without tangential interaction, i.e. only the normal spring and damper remain.

Figure 3.6: Schematic representation of the boundary conditions applied to the slice of the mill.

In fact, at the fourth row of the shell liner, it is reasonable to suppose that the influence of the lifting of the charge by the tangential interaction with the end wall is negligible. Nevertheless, the axial motion near the shell liner is restrained by the head liners and the important weight of the balls, which forces them to take up as little space as possible. For these reasons, the intermediate boundary condition between the periodic boundary condition and the solid wall condition, are two *walls without tangential interaction* on both sides of the slice (figure 3.6b). These walls thus simply prevent the balls from leaving the slice while inducing no additional lifting. Such a wall can be created in the simulation by setting the tangential stiffness and damping coefficient of a ball/wall interaction equal to 0. This second solution, however, has the drawback of increasing the wear near the end walls of the slice for two reasons. First, the balls in contact with the end walls will most likely always stress the shell liner at the same offset with respect to the wall[4]. This reason is absolutely no problem in the case of a mill with real walls, i.e. walls, which tangentially interact with the balls. More precisely, in the case of a mill with real walls, the balls near the wall slide less due to their interaction with the wall. This is obviously not true for the simulated mill with frictionless[5] walls, where the wear near the walls can be supposed to be relatively high. Other boundary conditions can certainly be considered but in this study, we will limit the analysis to the previous conditions since these seem to be the best compromise between the computation time and the representation of the reality by the model.

Having already introduced a 250 mm and a 500 mm slice as well as a periodic boundary condition and walls without tangential interaction, we will introduce an additional geometrical

[4]This argument is only valid, if the balls in contact with the shell liner and the end walls have the same diameter. Hereinafter, we will explain why balls with the same diameter were chosen in this study.

[5]The term *frictionless* might be a little ambiguous since the whole tangential interaction is nonexistent for these walls, i.e. the Coulomb friction as well as the tangential spring and damper.

feature. The figures 3.1 and 3.3 previously showed that the height of the grooves is relatively small with respect to the average height of the profile after a given number of operating hours. Thus, before trying to simulate the more complex phenomenon, i.e. the grooves, it would be interesting to predict the predominant geometrical modification, i.e. the average azimuthal height loss, first. For this reason, we will try to develop an algorithm which is sufficiently general to estimate the wear of 1D and 2D liners. Hence, we will have to use a *fine 2D surface mesh and a rather coarse 1D extruded mesh*[6] similar to the one used in the previous chapter.

More precisely, the height of 1D liners initially changes only along the azimuthal direction. Neglecting any variation of the profile due to wear along the axial direction, therefore implies that a discretization along this specific direction is sufficient to capture the average height loss. While the surface mesh in the second chapter had only the function of simulating the interactions with the balls, it has the additional function of being able to record the local wear data in this chapter. Thus, instead of discretizing the liner profile curve based on its curvature, it is more reasonable to discretize it into elements having the same size. Setting the average size equal to 15 mm, as explained earlier, for the fine and the coarse mesh, we obtain the profile curve discretization[7] of the coarse 1D mesh as shown in the figure 3.7.

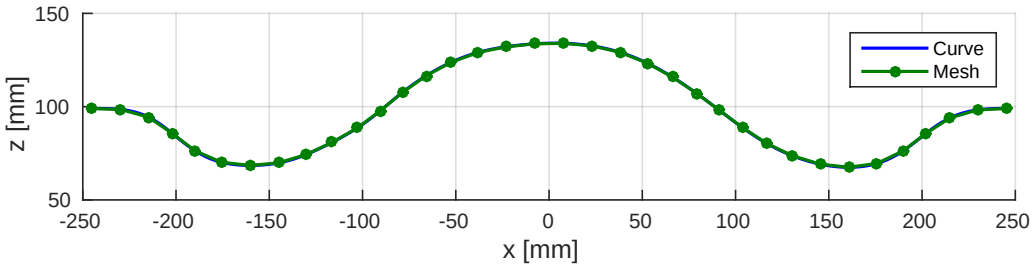

Figure 3.7: Profile curve discretization of a *Duolift* liner plate in the 5.8 m diameter ball mill (forth row, after 2383 h). Each element has an average size of 15 mm, which results in 36 vertices.

The previous profile curve discretization could then be extruded along the axial direction as shown in the second chapter (figure 2.10) in order to obtain the mesh of a liner plate. Unfortunately, the periodic boundary condition in YADE, and in particular, the implementation of its collision detection algorithm, does not allow discrete elements to have their size being equal to half of the periodic length. In fact, if their size would be greater than half of the periodic length, two bodies could interact multiple times. And since YADE identifies the contact by the identifiers of the contacting bodies, these different contacts would not be distinguishable. For this reason,

[6]While a *1D liner* was previously defined as a liner without variation of its height along the axial direction, we will continue to use this attribute for liner meshes which can not represent a height variation along the axial direction due to the volume loss by wear. By analogy, a *2D liner mesh* can represent this variation, i.e. for instance the creation of grooves.

[7]The profile was first drawn with the spline tool in CATIA. It was then discretized in GMSH. And finally, the specific vertices of the curve discretization were selected in MATLAB.

the 250 mm and the 500 mm *1D meshes* were divided into 3 rows[8] along the axial direction as illustrated in the figure 3.8a, instead of one row.

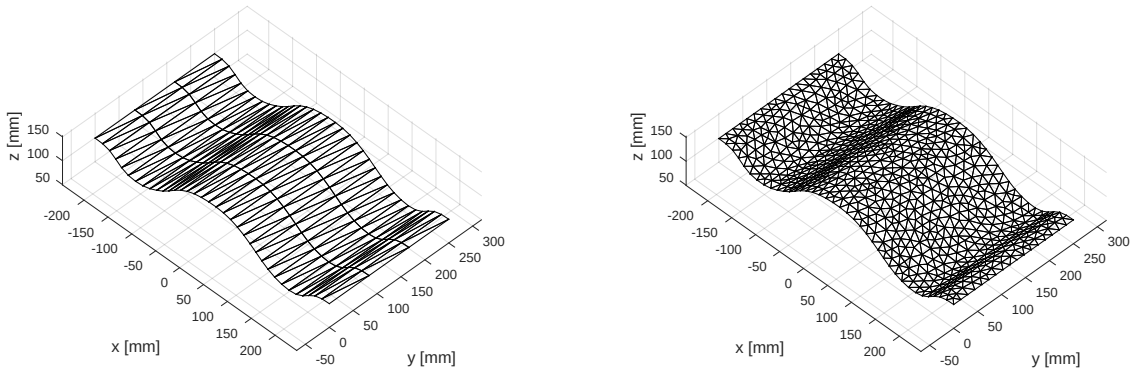

(a) Coarse 1D mesh. **(b)** Fine 2D mesh.

Figure 3.8: Surface meshes of the *Duolift* liner plate in the 5.8 m diameter ball mill (forth row, after 2383 h).

In contrast to the 1D plate mesh, the *2D mesh* is a usual unstructured surface mesh with triangular elements (figure 3.8b). The average element size is still equal to 15 mm. Consequently, it contains 1408 triangles while the 1D mesh of the plate contains only 210 elements. An important characteristic of these meshes is that the *distribution of the vertices is identical on each opposite edge* of the surface. This feature will be important for calculating the normals of the surface at the vertices (section 3.3.3) and for regularizing the surface during the geometry modification (section 3.3.5).

The *entire shell liner mesh* of the slice is then assembled after duplicating and rotating the mesh of one plate. While this technique had no advantage in the previous chapter, it will decisively increase the representativity of the wear data in this chapter. In fact, because of the periodicity of each elementary facet, the wear data accumulated on this facet (section 3.3.2) can be averaged over all the similar facets. This *master lifter mapping technique* was previously explained in the section 1.4.1. Moreover, the wear data can also be averaged axially over the 6 facets, which correspond to the extrusion of a segment in the discretized profile curve, of the coarse 1D meshes. Hence, the data is not only *averaged along the azimuthal direction but also along the axial direction*[9].

[8] We also tried to use only two axial divisions and to slightly increase the length of the periodic slice, for instance, 251 mm instead of 250 mm. The software, however, still ran into a problem, i.e. some spheres simply left the liner as if it would not exist. To fix this bug, it is necessary to analyze the implementation of the periodic insertion sort collision detection algorithm more in detail. Since the problem could be bypassed by adding an additional axial division, which did not excessively increase the number of elements, this problem was not further examined.

[9] Axial averaging is also possible for 2D liners if they are axially periodic, like the *New Duostep* liner produced by Magotteaux S.A. (wave along the azimuthal and axial direction), and if the charge motion is also periodic (or

In conclusion, 4 different *liner mesh* types (combinations of coarse 1D, fine 2D, 250 mm length and 500 mm length), as well as two different boundary conditions (periodic and walls without tangential interaction) were introduced.

Finally, the geometrical approximation of the *balls* remains to be defined. Despite their progressive grinding, they will be represented by *spheres with a constant 70 mm diameter*, which is almost equal to the weighted average diameter of the balls. In order to keep the total mass of the balls constant, 5187 and 10375 spheres are simulated in the 250 mm slice and the 500 mm slice, respectively. Alternatively, it is obviously possible to use a more realistic diameter distribution based on the data provided in the table 3.1. Reaching the pseudo steady state would then, however, be far more complex since the segregation of the balls, i.e. the distribution of balls as a function of their diameter in the mill, would have to be studied[10]. Because of the chaotic motion and the relatively small difference in diameter of the real ball charge, it seems, therefore, to be reasonable to simply neglect the segregation by using only balls with an identical diameter.

3.2.3 Simulation

The simulation as such is very similar to the simulation in the previous chapter. Hence, the liner *rotates* at 13.48 rpm (negatively around the y-axis) and the *gravitational acceleration* is applied along the vertical z-axis. Moreover, the *time step* is equal to $5 \cdot 10^{-5}$ s (section 2.4.3).

There are, however, two major differences with respect to the previous chapter. On the one hand, the *total simulated time will usually be much longer* since it takes more time to record sufficiently representative data of the wear than of the charge motion or of the power draw. This characteristic will be studied rigorously in the section 3.3.2.

On the other hand, the implementation of a multi-step procedure will be studied in the section 3.3.7. As explained in the section 1.4.3, it consists in a progressive update of the geometry in order to account for the changing load on the liner during its wear. The iterative process therefore consists in a simulation, which is followed by the modification of the geometry. This modification is then again followed by a simulation with the updated liner and so on. In order to decrease the total computation time, it would thus be beneficial to *restart a simulation with the state of the balls from the previous simulation* but with the updated liner geometry. Hence, this procedure would not require to restart the simulation from the initial position of the balls (similar to figure 2.12). Consequently, the subsequent pseudo steady state could be reached quicker. Except for the first simulation of the multi-step procedure, the position, the translation velocity and the angular velocity will therefore be loaded from the previous iteration of the multi-step procedure.

unchanged) along the axial direction, which is only true for the periodic boundary condition. In the case of the 2D mesh of the *Duolift* liner, it makes, however, no sense to create an axially periodic mesh since the liner has initially no variation of its height along the axial direction. Hence, the 1D coarse mesh is already sufficient.

[10]More specifically, it is possible that the pseudo steady state would be reached only after a relatively long time. This time would be the time necessary for the balls to organize themselves in the mill. For instance, the balls with a greater diameter would preferentially be in contact with the liner due to their higher mass and the centrifugal force.

3.3 Wear Simulation

Having defined the charge motion model in the previous section and even more extensively in the second chapter, we will finally combine this model with a wear model and a geometry modification strategy in order to *predict the wear distribution but also the resulting change in the geometry of the shell liner due to wear*.

In this section, *seven stages*, which are necessary to achieve the previous objective, will be defined. To understand why these stages are necessary, we will briefly sketch out the general method from a bird's eye perspective.

While DEM simulations usually start with their ball charge at rest, industrial mills rotate at a constant angular speed during several ten thousand hours before changing the liner. The initial step in wear modeling is therefore to determine when starts the *first pseudo steady state*. Once this state has been reached, sufficiently *representative wear data*, like the tangential damping energy, has to be recorded for each facet during the following rotations. This data indicates the relative wear level of each facet after the simulation. The relative wear rate is then determined by dividing the accumulated wear data by the time during which it was recorded. In order to transform the numerical result into a real absolute volume loss rate, the *real wear data* has to be extracted from the measured wear profiles. The correlation of the relative and absolute wear rates finally provides the *wear constant*, which is the connection between the model and the reality. On the basis of the wear constant and the relative wear rate, the absolute wear rate can be calculated. The absolute volume loss of each element of the liner mesh after a specific number of operating hours is then predicted by multiplying the wear rate by this number of operating hours. Since the average volume loss of each facet is known, the *geometry of the liner can be modified* to account for this volume loss. As explained earlier, one single update of this geometry is generally not accurate enough because it neglects the variation of the liner load due to the transformation of the geometry. Thus, a charge motion simulation has to be executed with the updated liner. To reduce the computation the final state of the balls in the previous simulation is used as the initial state in the new simulation. Therefore, it is necessary to determine when the *second pseudo steady state* is reached. Finally, in the last section, we will study the *multi-step procedure* more in detail to determine how many steps are usually necessary with or without spatial smoothing to predict the liner wear evolution.

3.3.1 First pseudo steady state

Sampling the wear data in the transient state would make no sense since ball mills essentially always rotate at a constant angular speed. Starting from an initial state similar to the one depicted in the figure 2.12, the *pseudo steady state can be reached after around one to two rotations* as shown in the figure 3.9. Two rotations are a more conservative limit, which is why this number of rotations will be used in all the following simulations.

In the section 3.2.2, 8 different scenarios were defined, i.e. the combinations of a periodic

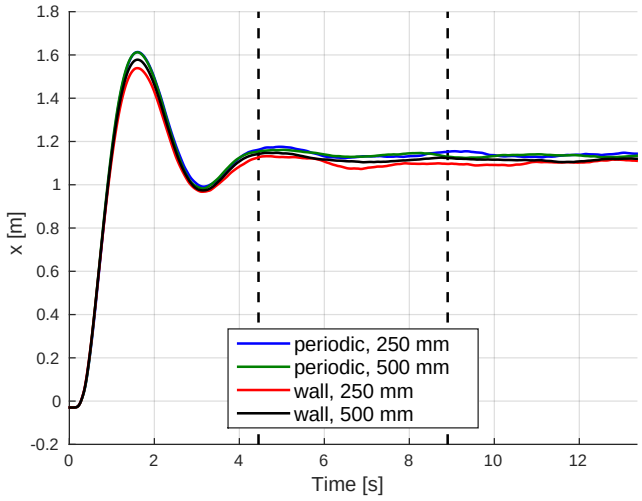

Figure 3.9: Horizontal position of the center of gravity as a function of time for the four scenarios defined in the section 3.2.2 with the coarse 1D meshes. The horizontal dashed lines indicate when a full rotation has been completed.

boundary condition or walls without tangential interaction, a 250 mm axial slice or a 500 mm axial slice and a coarse 1D mesh or a fine 2D mesh. Having represented only the cases with the coarse 1D meshes in the figure 3.9 means that we obtained identical results with the fine 2D meshes. Hence, no influence of the additional stiffening (section 2.4.2) due to the increased edge collisions with the fine mesh was observed. Using a coarse 1D and a fine 2D mesh, which almost equally well approximate the geometry, has therefore no influence on the charge motion.

Concerning the length of the slice and the axial boundary condition, very interesting observations can be made. For instance, the power draw of the scenario with the periodic boundary condition is higher than with the frictionless walls as shown in the table 3.2. The difference, however, decreases with the length of the slice. The same conclusion can be drawn from the position density limits in the figure 3.10, where the toe is slightly higher for the simulations with (frictionless) walls. Moreover, its height decreases with the length of the slice. Since the shoulder angle is almost identical in the different scenarios, the power draw should be higher for the simulations with the frictionless walls.

The difference in power can finally be explained by the position density plots of the mill viewed from above as shown in the figure 3.11. In fact, the increased interlocking of the balls (by the periodicity) in the scenario with the periodic boundary condition allows them to be lifted higher, i.e. the toe decreases. Hence, the center of gravity of the balls is further away from the rotation axis and the power increases. An additional argument confirming this explanation is probably the fact that the percentage of sliding power is slightly higher for the cases with the periodic boundary condition since in the case with the frictionless walls, the balls can neither dissipate their energy by sliding on the walls, nor on their periodic counterpart.

Case	Rotation power [kW]	Percentage of normal damping dissipation [%]	Percentage of tangential dissipation [%]	Percentage of sliding dissipation [%]
250 mm, 1D mesh, periodic	112.2	38	8	56
250 mm, 1D mesh, wall	109.3	42	7	53
250 mm, 2D mesh, periodic	111.9	38	8	57
250 mm, 2D mesh, wall	108.0	42	7	53
500 mm, 1D mesh, periodic	224.1	38	8	57
500 mm, 1D mesh, wall	220.6	40	8	54
500 mm, 2D mesh, periodic	223.7	39	8	57
500 mm, 2D mesh, wall	220.1	40	8	55

Table 3.2: Influence of the length of the slice, the mesh, and the boundary condition on the estimated average power draw of the mill. The power values were calculated by averaging the post-processing data (sampling period: 0.01 s) over the third rotation of the mill. The power percentages are calculated with respect to the rotation power and rounded half down.

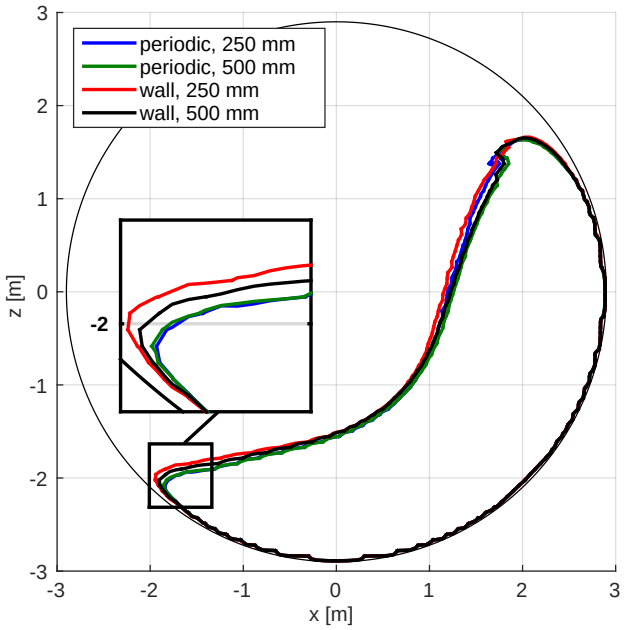

Figure 3.10: Position density limits of the four scenarios defined in the section 3.2.2 with the coarse 1D meshes. The density limits were calculated according to the explanation in the section 2.3.4 with a 100×100 binning grid on the basis of the post-processing data (sampling period: 0.01 s) of the third rotation of the mill.

Moreover, the figure 3.11 clearly illustrates that a periodic boundary condition is not able to induce the creation of grooves if the liner initially has not geometrical feature which restrains the axial displacement of the balls. The boundary condition with frictionless walls, however, has the drawback of limiting the motion of the balls at a constant offset with respect to the wall; this offset is obviously equal to the radius of the balls. To enhance the visibility of the organization of the charge motion, the color legend was rescaled by setting its maximum value equal to 4 instead of 18. As expected, the number of (potential) grooves per plate is identical to the one found in the reality for the scenario with the frictionless walls. Since the organization of the balls decreases with the length of the slice, the charge motion of the previous scenario converges to the one with the periodic boundary condition. This eventually explains why the relative difference of the power draw for the two boundary conditions is lower for the 500 mm slice than for the 250 mm slice.

3.3.2 Representative wear data

Once the first pseudo steady state has been reached after around two rotations, the data, which represents the relative wear level, has to be recorded during several rotations of the mill. In this section, we will define the *wear models* and the *data extraction technique* in order to determine the relative wear rate on the basis of the simulation. Moreover, we will find out how many rotations are necessary to sample sufficiently representative wear data and what influence the boundary conditions and the length of the slice have on the *numerical results*.

Wear models

In the section 1.3, a detailed overview of different wear models was provided. Instead of choosing one of these models without any prior knowledge about its accordance with the reality, we will rather *implement the most promising wear models in the field of ball mill liner wear and choose the best fitting model a posteriori*.

An alternative approach would be to record the *components* of the wear models, like the sliding distance or the normal force, individually and to try to *combine* these components on the basis of the real wear data in order to obtain the best fitting model. This strategy, however, has two major drawbacks, which render it virtually impossible. On the one hand, each component would add an additional degree of freedom to a study, which in any case has already a large number of degrees of freedom (in terms of parameters). To keep the wear model as simple as possible, it thus seems to be more reasonable to choose only one or two combinations of (entire) wear models, which have already delivered accurate results in previous studies. On the other hand, a synthetic data extraction technique (section 1.4.1) is absolutely needed to keep the data creation during DEM simulations sufficiently low while maintaining a high degree of representativity of the variables causing wear. Hence, it would be necessary to accumulate the individual wear components over time, which rises the question about the form of the accumulation, i.e. moving average, moving squared average, ... Due to this short-coming, the wear components could loose

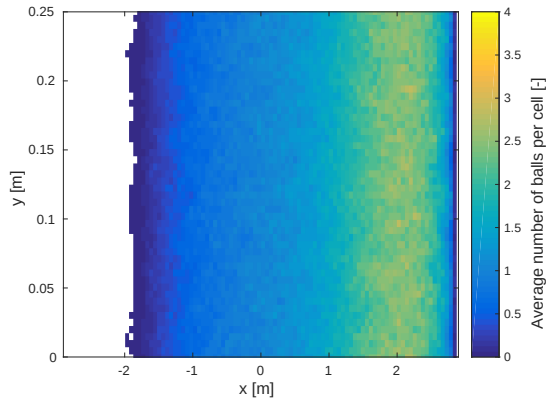

(a) Periodic boundary condition, 250 mm slice (coarse mesh).

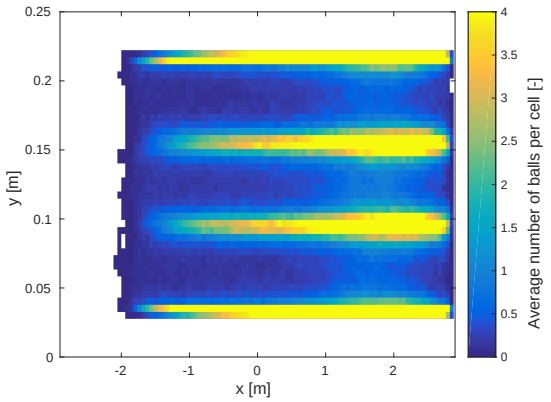

(b) Walls without tangential interaction, 250 mm slice (coarse mesh).

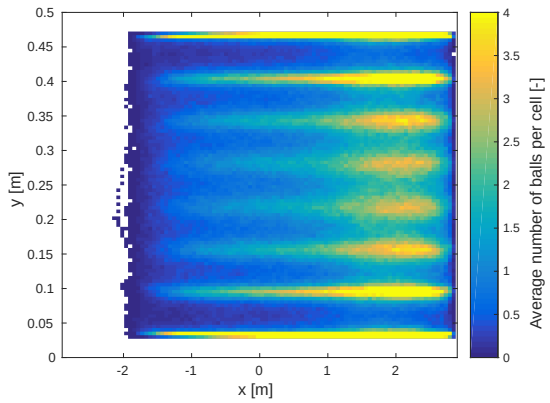

(c) Walls without tangential interaction, 500 mm slice (coarse mesh).

Figure 3.11: Position density plots of the mill viewed from above with a 100×50 (resp. 100×100) binning grid for the 250 mm (resp. 500 mm) slice created on the basis of the post-processing data (sampling period: 0.01 s) of the third rotation of the mill. The color legend was rescaled to enhance the visibility of the organization of the charge motion. In fact, the maximum average value of balls per cell reaches 18 in the cases with frictionless end walls next to these walls.

any meaning. For instance, the Archard wear is essentially equal to the normal force multiplied by the sliding distance. If the normal force would be always equal to zero, when the body slides, no wear would be accumulated by the model while the combination of the average normal force and the average sliding distance could not reproduce this result.

Therefore, we will define the *most promising wear models* in the following paragraphs. As will be explained in the next section, the relative wear data calculated by these models is accumulated for each facet and each time step dt, i.e. a variable will be created for each facet and for each wear model. At every time step, the relative wear is calculated and added to this variable. After the simulation, the variable will thus quantify the relative wear of the facet according to a specific wear model. To post-process the wear data more easily, the wear models will only be composed of actual *variables* of the simulation. In other words, the wear constant and the hardness have been removed from the models but will be added later on. To leave no place for ambiguities, the actual implementation[11] of the wear models can be found in the appendix B. The different models were in general already explicitly described in the section 1.3.

Energy dissipated by normal damping The energy dissipated by the normal damper of the contact law measures the energy dissipated by the normal impact of discrete elements. It is defined as follows in incremental form:

$$W_{\text{normal}} = W_{\text{normal}} + c_n \, v_n^2 \, dt \tag{3.1}$$

where c_n, v_n and dt are the normal damping coefficient, the norm of the normal velocity and the time step, respectively. The product $c_n \, v_n$ is the force created by the damper, which is multiplied by the incremental normal displacement $v_n \, dt$.

Energy dissipated by tangential damping The energy dissipated by the tangential damper of the contact law quantifies the energy dissipated by a tangential collision of discrete elements, without sliding. This wear model puts more emphasis on the energy dissipated by a tangential collision (a phenomenon with a rather short time scale) while the following wear model focuses on the sliding (a phenomenon with a rather long time scale). The model is defined in a similar way to the energy dissipated by normal damping:

$$W_{\text{tangential}} = W_{\text{tangential}} + c_t \, v_t^2 \, dt \quad \text{if} \quad F_t < \mu \, F_n \tag{3.2}$$

where c_t, v_t, dt, F_t, μ and F_n are the tangential damping coefficient, the norm of the tangential velocity, the time step, the norm of the tangential interaction force, the coefficient of friction and the norm of the normal interaction force, respectively.

[11] In the implementation, the wear is divided by the area of the facet element in order to create consistent results for the VTK output. Here, the wear model will, however, be defined without dividing the relative wear volume by this area.

Energy dissipated by sliding The energy dissipated by sliding quantifies the energy dissipated along the tangential direction of the collision, when the friction limit has been exceeded:

$$W_{\text{sliding}} = W_{\text{sliding}} + \mathbf{F}_t \cdot \mathbf{v}_t \, dt \quad \text{if} \quad F_t \geq \mu \, F_n \tag{3.3}$$

where $\mathbf{F}_t$, $\mathbf{v}_t$, dt, F_t, μ and F_n are the tangential interaction force, the tangential velocity, the time step, the norm of the tangential interaction force, the coefficient of friction and the norm of the normal interaction force, respectively. The dot product is necessary because the sliding force and the tangential velocity are not necessarily aligned due to the history of the tangential spring force.

Archard wear The Archard wear equation quantifies the wear created when two objects slide over each other since it is proportional to the normal contact force and the sliding distance:

$$W_{\text{Archard}} = W_{\text{Archard}} + F_n \, v_t \, dt \tag{3.4}$$

where F_n, v_t and dt are the norm of the normal interaction force, the norm of the tangential velocity and the time step.

Finnie wear In contrast to the previous wear models, the wear created according to the model of Finnie is only calculated when a new interaction is created, i.e. not during the interaction. Hence, if the interaction is new, the Finnie wear is defined as follows:

$$W_{\text{Finnie}} = W_{\text{Finnie}} + f(\alpha) \, m \, v^2 \quad \text{with} \quad f(\alpha) = \begin{cases} 1/3 \, \cos(\alpha)^2 & \text{, if } \tan(\alpha) > 1/3 \\ \sin(2\alpha) - 3\sin(\alpha)^2 & \text{, otherwise.} \end{cases} \tag{3.5}$$

where α is the collision angle defined in the figure 1.20, and where m and v are the mass of the ball, which collides with a facet, and the norm of the relative collision velocity, respectively.

Excess kinetic energy In the same way as for the Finnie wear, the excess kinetic energy is only calculated when a new interaction is created. It represents the kinetic impact energy of the balls, which have a normal velocity greater than 0.1 m/s:

$$W_{\text{kinetic}} = W_{\text{kinetic}} + m \, v_n^2 \quad \text{if} \quad v_n > 0.1 \tag{3.6}$$

where m and v_n are the mass of the ball, which collides with a facet, and the norm of the normal (impact) velocity, respectively.

Data extraction technique

The next step of the wear simulation is to *extract the data*, which has been defined by the wear model, from the DEM solver. In the section 1.4.1, two solutions to this problem were defined:

the explicit and the synthesized data extraction. To reduced the data creation by the software and to increase the representativity of the wear data, the *synthesized data extraction strategy* was chosen. In contrast to the other strategy, it required, however, to modify the source code of YADE. The following list, summarizes the changes in the software:

- new linear spring-slider-damper contact model implemented in `SprSldDmp.hpp` and `SprSldDmp.cpp`[12]. During an interaction, the new spring-slider-damper contact law calculates not only the interaction forces, but also the wear created during this interaction.
- new state properties of the elements implemented[13] in `State.hpp`. A variable for each wear model was added to the state of the elements in order to account for their progressive wear. To retrieve the values of the new variables in the PYTHON control script, the wrapper implemented in `yadeWrapper.cpp` was also enriched.
- new global scene flag `O.trackWear` implemented in `Scene.hpp` similar to the `O.trackEnergy` flag. Only if this flag is true, the wear will actually be calculated.
- new global timing variable `O.recordingStartTime` implemented in `Scene.hpp`, which allows to start the recording of the wear only after a given time. This feature makes it possible to start the recording once the pseudo steady state has been reached, in the same simulation.
- new `wear` output recorder in the `VTKRecorder` class implemented in `VTKRecorder.hpp`. This recorder enables the output of the wear data in the `.vtu` VTK file format, which can be visualized in the PARAVIEW software. This feature is also the reason why the wear data is divided by the facet area in YADE. Hence, its representation is independent of the size of the facet.

These new components of the DEM solver render it possible to accumulate the wear of each facet for each time step in the pseudo steady state over the whole simulation, and to finally retrieve and save this data by the PYTHON control script at the end of the simulation. For instance, the figure 3.12 illustrates the energy dissipated by tangential damping on each facet divided by the area of this facet, accumulated on the coarse 1D (resp. fine 2D) mesh of the 250 mm long slice with frictionless walls during 4 rotations (resp. 8 rotations) in the pseudo steady state.

This figure also shows that the corresponding number of rotations is clearly not enough to obtain sufficiently representative wear data; facets, which should have the same wear level because of their geometrical symmetry, have different values. This is the consequence of the chaotic charge motion and the reduced sampling time, i.e. around 18 s for the coarse 1D mesh and around 36 s for the fine 2D mesh versus several ten thousand hours in the reality. For this reason, the *master lifter mapping procedure* was explained in the section 3.2.2. Because of the azimuthal

[12]The source code can be found in the appendix C.

[13]In the future, the additional properties should better be implemented in a class that inherits from the `State` class, like the `CpmState` class of the concrete particle model in the `ConcretePM.hpp` file.

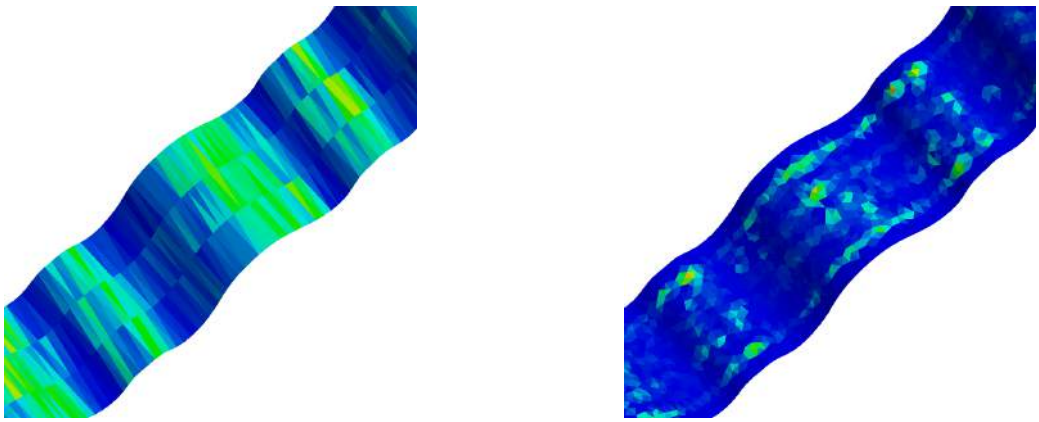

(a) Coarse 1D mesh. **(b)** Fine 2D mesh.

Figure 3.12: Energy dissipated by tangential damping on each facet divided by the area of this facet, accumulated on the coarse 1D (resp. fine 2D) mesh of the 250 mm long slice with frictionless walls during 4 rotations (resp. 8 rotations) in the pseudo steady state. The color legend was not represented, since the absolute values have no importance here. The color varies, however, from blue to red (rainbow) and has been scaled from the minimum to the maximum value. The pictures were created in PARAVIEW.

periodicity and the axial periodicity (for the 1D mesh), it is possible to increase the statistical representativity of the sampled data by 36 for the fine 2D mesh and by 216, i.e. $36 \cdot 6$, for the coarse 1D mesh, if the data of the facets is mapped on one representative master plate.

Numerical results

By means of the previous explanation, it is now possible to extract the data from YADE and to map it on a representative master plate in MATLAB. In this section, we will analyze the *numerical results* in order to determine the *number of rotations*, which is necessary to obtain sufficiently representative wear data, and to understand the *influence of the boundary condition and the length of the slice on the wear distribution*.

In the section 3.3.4, it will be demonstrated that the energy dissipated by tangential damping is the most accurate single wear model of the liner wear with respect to the reality. To simplify this study, the following explanation will therefore be based entirely on this specific wear model. Nevertheless, it would be surprising to find significantly different results in terms of the number or rotations and the influence of the boundary conditions for the other models. To obtain results, which are independent of the area of the facet in the surface mesh and the simulated time, the energy of the wear model will be divided by the area of the facet and the simulated time. Consequently, it represents the *relative height*[14] *loss rate of the facet* in [J/(s.m^2)].

[14]It is the relative height loss rate, since an energy per area per time divided by a hardness gives the units [m/s]. The attribute *relative* is used to account for the fact that the data has not yet been multiplied by the wear constant and divided by the hardness.

Number of rotations In the case of the *coarse 1D mesh*, the figure 3.13 shows the relative height loss rate along the liner plate for each segment of the discretized liner profile curve (figure 3.7) after a given number of rotations of the 250 mm slice with frictionless walls. The profile curve was discretized by 35 segments. Hence, the figure shows the relative height loss rate of each segment from the left to the right. The greatest height losses are therefore expected to be on the right side of the small and the big waves of the profile[15]. The wear distribution will be explained in more detail in the section 3.3.4.

According to the figure 3.13, the wear distribution converges relatively quickly so that almost no difference between the curves can be observed after two rotations. Mathematically, this means that the difference of the wear data of two successive rotations converges to 0 (figure 3.14a) since more and more wear data is accumulated, which leads to a more representative sampling of the variables causing wear. In conclusion, we will use a conservative number of *three rotations to record the wear data*[16] with a coarse 1D mesh. Two or even one rotation would, however, not significantly change the results. The previous conclusion is also true for the periodic boundary condition with a coarse 1D mesh in agreement to the results in the figure 3.14a.

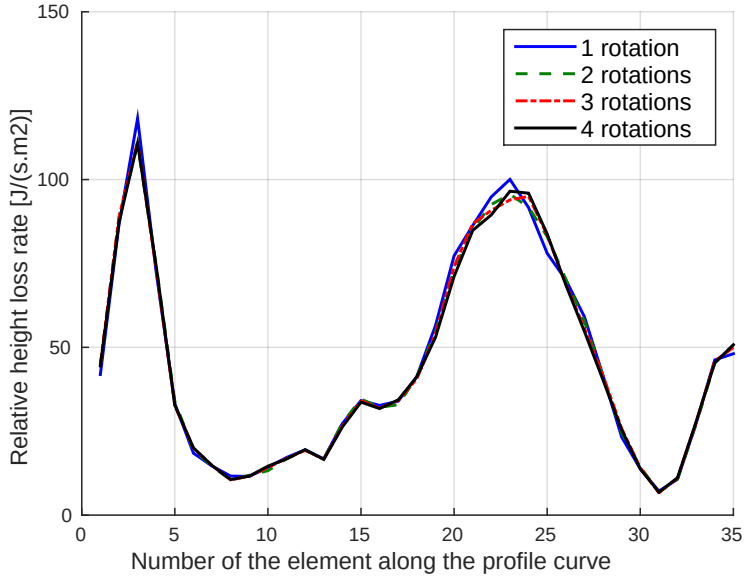

Figure 3.13: Relative height loss rate along the liner plate for each segment of the discretized liner profile curve. The results were obtained with the 1D coarse mesh of the 250 mm slice and the end walls without tangential interaction. Each additional rotation of the slice in the pseudo steady state leads to a better convergence of the wear distribution.

[15]The mill rotates from the left to the right with respect to the plate, which is located at the bottom of the mill.

[16]Three rotations might seem to be a very conservative number of rotations. We want, however, to make sure to reduce any disturbing factor in the development of the method. Once, the method proves to be sufficiently accurate, less precautions might be taken to accelerate the computation of the wear evolution of a new liner profile.

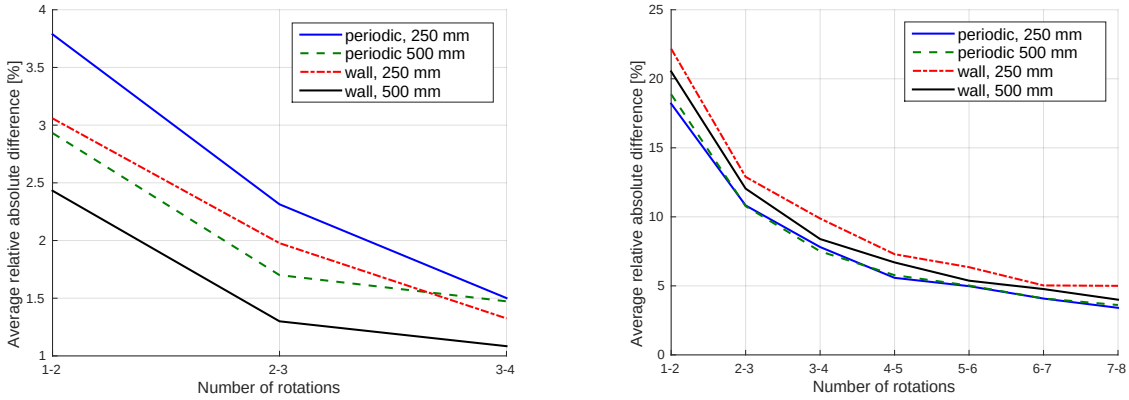

(a) Coarse 1D mesh.

(b) Fine 2D mesh.

Figure 3.14: Convergence of the average relative absolute difference of the relative height loss rate with the number of rotations. The relative height loss rate can be calculated for each facet after each rotation. By computing the absolute difference between the relative height loss rates of the current and the previous rotation and dividing this difference by the relative height loss rates of the current rotation, we obtain the relative change of the height loss rate for each facet. The average of these values over all the facets then illustrates the convergence of the wear data with the number of rotations. In simple terms, the representativity of the wear sample increases with the number of rotations, i.e. the average absolute difference of the wear level decreases.

Concerning the *fine 2D meshes*, the absolute difference of the relative height loss rate between two rotations following each other is much higher, as shown in the figure 3.14b, due to the large number of facets. For instance, one facet could be impacted several times in a row, while another facet is not touched at all during the simulation. Even though the *average* absolute relative difference becomes smaller than 5% after 7 rotations (with respect to the 8th rotation), the *individual* relative absolute differences at the level of the facets still attain 22% at their maximum levels (figure 3.15b). This result is, however, far more accurate than the one obtained after the first two rotations, were the variation of a value of one facet occasionally gets close to 80% (figure 3.15a). Interestingly, these large variations logically occur in regions, where usually few collisions take place, i.e. immediately behind the small and the big waves. In the same way as for the coarse 1D meshes, similar results were found for the scenarios with the periodic boundary condition and the walls without tangential interaction, in terms of the convergence of the wear data. Due to the 22% maximum relative difference and the long computation time with the fine 2D meshes (around 10 h for the 250 mm slice and 30 h for the 500 mm slice, depending on the workload of the processor), *8 rotations* seem to be an acceptable compromise to sample the representative wear data with a *fine 2D mesh*.

Boundary condition and length of the slice Based on the figures 3.16a and 3.16b, the *boundary condition and the length of the slice have a negligible influence on the wear distribution,*

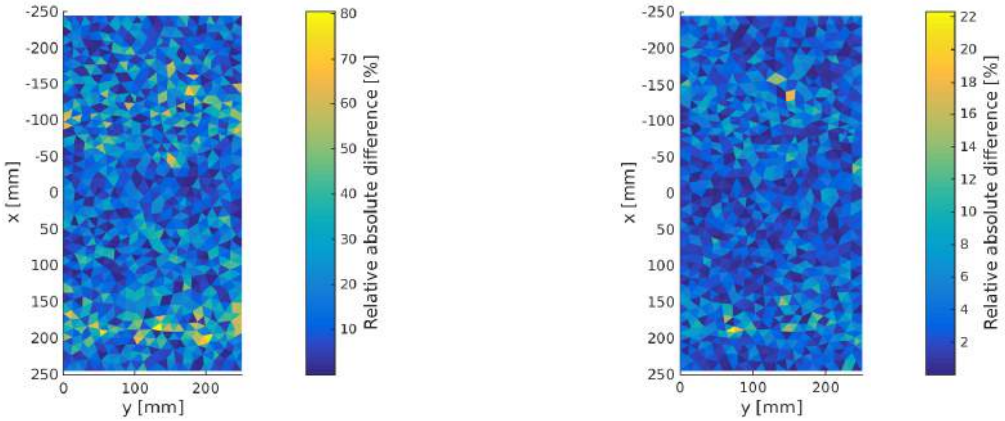

(a) Rotations 1-2.

(b) Rotations 7-8.

Figure 3.15: Convergence of the relative absolute difference of the relative height loss rate with the number of rotations at the level of the facets. The relative height loss rate can be calculated for each facet after each rotation. By computing the absolute difference between the relative height loss rates of the current and the previous rotation and dividing this difference by the relative height loss rates of the current rotation, we obtain the relative change of the height loss rate for each facet. The results were obtained with the fine 2D mesh of the 250 mm slice and the periodic boundary condition.

which has been accumulated on a coarse 1D mesh. Since the wear data is averaged along the axial direction for the coarse 1D meshes, these meshes are not able to reproduce the real axial wear patters, which are much more complex as shown in the figure 3.17 for the fine 2D meshes. The wear distribution is thus clearly the natural consequence of the organization of the charge motion as shown in the figure 3.11, i.e. that grooves can only be created if the charge motion is axially restrained, like in the scenario with the frictionless end walls. In consequence, the length of the slice has no real influence on the wear calculated with the periodic boundary condition.

As a result of the previous conclusions and due to the extremely long computation time of simulations containing the fine 2D meshes of a 500 mm slice (30 h versus 10 h for the fine 2D meshes of the 250 mm slice and around 2 h for the coarse 1D meshes[17], depending on the workload of the processor), only the following scenarios will be studied in the next sections:

- coarse 1D mesh, walls without tangential interaction, 250 mm slice
- fine 2D mesh, walls without tangential interaction, 250 mm slice

[17]Moreover, the periodic insertion sort algorithm in YADE has not yet been parallelized. Choosing the scenario without the periodic boundary condition therefore reduces the computation time even more.

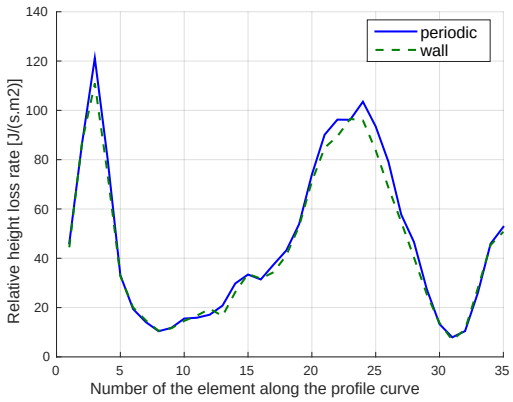

(a) Influence of the boundary condition for the 250 mm slice.

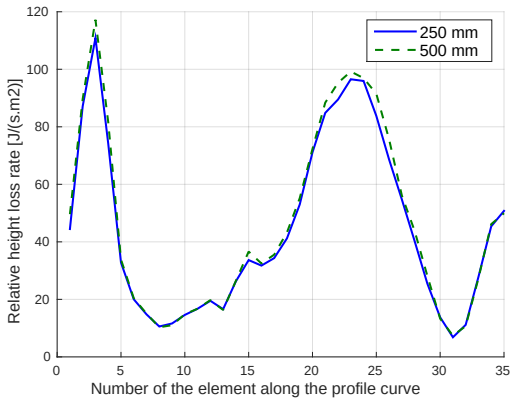

(b) Influence of the length of the slice for the scenario with frictionless walls.

Figure 3.16: Influence of the boundary condition and the length of the slice on the relative height loss rate computed along the coarse 1D meshes after 4 rotations of the mill.

3.3.3 Real wear data

Before transforming the predicted relative wear into an absolute volume loss for each facet, it is necessary to determine the *real wear data*. This data will be correlated with the relative wear in the next section (section 3.3.4) to determine the best fitting wear model and the corresponding wear constant. Since the relative wear was previously estimated for each facet, it would be interesting to extrapolate the real wear data of the wear profiles (figure 3.1 and appendix D) to each individual facet of the liner mesh, too. In this section, we will therefore explain the *volume extraction technique* based on the wear profiles and criticize the *evolution of the real liner wear*.

In total, measurements of the *Duolift* liner plate along the azimuthal direction and the radial direction were taken 11 times in order to determine its maximum and minimum height due to the creation of grooves over time (appendix D). In the following analysis, we will, however, only focus on 9 of these measurements because of the following reasons. On the one hand, the *wear from 0 to 2383 operating hours is too uniform* to be predicted by a wear model, which assumes that the material properties of the liner plate are homogeneous[18] (see figure 3.1). In fact, the uniform height loss along the profile from 0 h to 2383 h might be caused by the softening of the plate, when the carbon in the material leaves the plate at its surface during the cooling phase after its casting. Hence, the soft surface layer is quickly worn away until reaching the harder core material. On the other hand, we will only calculate the wear data based on the *average wear profiles*, which are equal to the average of the maximum and minimum profile height, for each of the 9 measurements. Taking into account the grooves would only make the analysis

[18]It would be relatively easy to take the variation of the hardness (according to the position inside of the plate) into account at the level of the model. Nevertheless, measuring this variation and calibrating the wear constants would certainly be extremely complex.

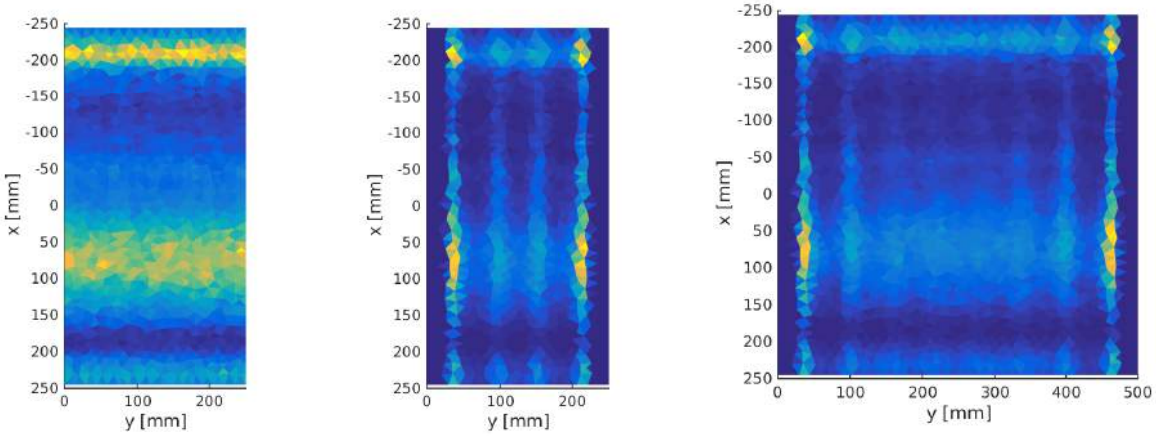

(a) Periodic boundary condition, 250 mm slice. Identical results were obtained for the 500 mm slice with this boundary condition.

(b) Walls without tangential interaction, 250 mm slice.

(c) Walls without tangential interaction, 500 mm slice.

Figure 3.17: Influence of the boundary condition and the length of the slice on the relative height loss rate computed for each facet of the fine 2D meshes after 8 rotations of the mill. The color legend was not represented, since the absolute values have no importance here. The color varies, however, from dark blue to yellow and has been scaled from the minimum to the maximum value for each figure individually.

more complicated and not really improve the results. Because the last wear profile, i.e. after 48437 h, was only measured in the valley of the groove, it will not be considered in the analysis. In conclusion, the *9 average wear profiles*[19] from 2383 to 41541 operating hours will be used to determine the real wear data.

Having 9 average wear profiles at one's disposal renders it possible to define 8 sets of wear data, i.e. from 2383 h to 7060 h, from 7060 h to 12120 h and so on. Consequently, we can approximate the volume loss for each of the 8 steps. Since a *material body looses its material by wear normally to its surface*, the *lost volume related to each facet* can be approximated as illustrated in the figures 3.18 and 3.19. More precisely, the vertices of the current wear profile mesh are normally projected on the following mesh. In particular, the *vertex normals* are calculated by averaging the normals of the neighboring facets of a vertex as explained in [Jin et al., 2005]. Moreover, the plate is repeated in space around the master plate to increase the independence of the normals from the mesh at its edges. This explains why the vertices on the edges of the plate had to be distributed identically on opposite edges (section 3.2.2). Once the projection of each vertex is known, the volume loss below every facet can be calculated by computing the volume of each polyhedron, which is delimited by the initial and the projected vertices. The *wear rate*

[19] Precisely, the average profiles after 2383 h, 7060 h, 12012 h, 16680 h, 23669 h, 28668 h, 33034 h, 37020 h and 41541 h in the appendix D will be used.

or the volume loss rate at each facet is then obtained by dividing the volume loss below each facet by the operating hours separating the current profile from the following profile of the liner plate in time. The result is represented in the figure 3.20. The previous procedure can finally be applied to the 9 selected wear profiles in order to extract the 8 real wear rates at each facet.

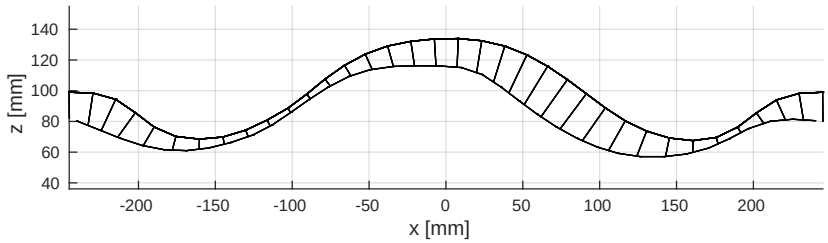

Figure 3.18: Normal projection of the vertices of the current wear profile mesh onto the mesh of the following wear profile. This figure shows the side view of the figure 3.19.

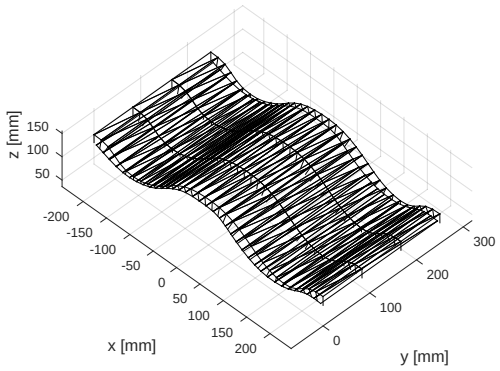

Figure 3.19: Normal projection of the vertices of the current wear profile mesh onto the mesh of the following wear profile. The side view of this figure is represented in the figure 3.18. The initial vertices of the facet and their projection can be used to calculate the volume loss below this facet.

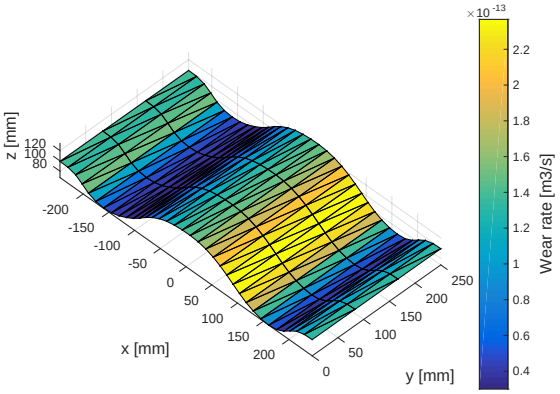

Figure 3.20: Illustration of the real wear rate which can be calculated on the basis of the results in the figure 3.19 and the corresponding operating duration.

Before correlating this data with the predicted relative wear rates in the following section (section 3.3.4) in order to determine the wear constant, the wear data has to be *criticized*. In fact, by computing the sum of the volume loss rate of each facet, it is possible to determine the total volume loss rate for each of the 8 wear steps. This rate has been plotted in the figure 3.21 to show the *evolution of the wear rate over time*. Theoretically, the wear rate should be strictly decreasing since the liner profile looses its aggressiveness with an increasing level of wear. Hence, less energy is transferred to the charge, which in turn wears less the liner. The figure 3.21 thus implies

that one of the modeling hypothesis has been violated. The only reasonable explanation[20] is that the rotation speed of the mill was increased after the first half of the lifespan of the liner to compensate for the decreasing mill throughput due to the worn profile. Increasing the rotation speed of the mill is usually not possible but the wear profiles were actually measured in a mill which can rotate at different speeds. Nevertheless, it was impossible to find the data, which proves or denies the increase of the rotation speed. Despite this incongruence between the real wear data and the simulation, it should, however, be possible to determine the best fitting wear model and its average wear constant. How to reach these objectives will be explained in the next section.

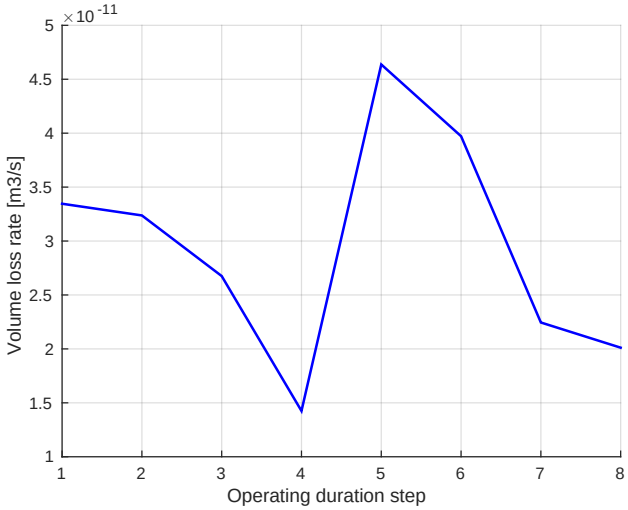

Figure 3.21: Wear rate evolution of the *Duolift* liner plate over time. The time was substituted by the number of the operating duration step since the measurements are almost equally separated in time by 5000 h. These steps correspond to the profiles from 2383 h to 7060 h, 7060 h to 12120 h and so on.

3.3.4 Wear constant

In this section, we will combine the relative wear data calculated in YADE (section 3.3.2) and the real wear data of the wear profile measurements (section 3.3.3) in order to *choose the most promising wear model* and to *calibrate its wear constant*.

[20] We found mainly four alternative explanations, which are, however, less likely because of the strong first order discontinuity of the wear rate. First, the hardness of the plate might be very non-homogeneous such that the wear rate increases strongly once a specific depth of the plate has been reached. Second, the wear rate might first decrease and then increase because initially the profile becomes less aggressive and less energy is available to erode the plates. Once a certain threshold has been reached, the charge slides more and more and this increased sliding might increase the wear rate again. The third explanation is that a different clinker type, which is harder, was ground after around 23000 operating hours. The final explanation is the progressive grinding of the balls and the very infrequent refilling with new balls.

In the section 3.3.2, it was explained why only the scenarios with the coarse 1D mesh and the fine 2D mesh of the 250 mm slice with frictionless walls will be further analyzed. Correlating the relative wear data of the 2D mesh scenario with its real wear data, would, however, not make much sense because we did not take into account the grooves in the real wear data. Moreover, if the wear constant can be determined with the wear data of the coarse 1D mesh, it should by definition be the same for the simulation with the 2D mesh. Hence, the following results were obtained with the *1D mesh of the 250 mm slice closed by walls without tangential interaction*.

Instead of trying to combine multiple wear models, like it has extensively been done in the literature (section 1.4.4), we will rather check if *one model* is not sufficient, and only enrich the solution by another model, if this seems to be necessary. The figure 3.22 shows the predicted and the real wear rates along the profile curve for each axial stripe defined by the segments in the figure 3.7. The *global wear constant*[21], $\overline{K} = K/H$, which was required to rescale the relative wear data in this figure, was determined by *liner regression* using a least-squares approach, independently for each model (obviously), i.e. $\overline{K}$ is the solution of the following problem:

$$\overline{K} = \underset{\overline{K}^*}{\arg\min} \left(\sum_{i=1}^{n_f} \left(\overline{K}^* \, \dot{W}_{\mathrm{rel}_i} - \dot{W}_{\mathrm{real}_i} \right)^2 \right) \tag{3.7}$$

where n_f, $\dot{W}_{\mathrm{rel}_i}$ and $\dot{W}_{\mathrm{real}_i}$ are the number of facets, the relative wear rate of the facet i (for a given wear model) and the real wear rate of the facet i.

In general, the *energy dissipated by normal damping*, the *energy dissipated by tangential damping* and *Archard's wear model* are the best fitting wear models despite the peak on the leading edge of the small wave according to the figure 3.22. The energy dissipated by sliding is distributed too evenly over the profile and the highest wear rate is rather located on top of the wave instead of on its leading edge. Finnie's wear model provides almost identical values for the maxima and minima but they seem to be phase-delayed along the profile. This delay might be due to the influence of the factor 1/3 in the definition of the model (equation 3.5). This factor depends on the boundary condition of the body during its collision with the facet, i.e. either its velocity is zero after the impact or it leaves the surface while its tip is still scratching this surface, as explained in the section 1.3. Adjusting this parameter seemed not to be necessary because the other wear models already provided relatively accurate data. It is also important to notice that we did *not smooth* the wear data in spite of its sometimes strong first order discontinuity[22]. Smoothing the data at this stage would only introduce an additional parameter in this study without changing significantly its outcome due to the overall variation of the wear constant, as explained in the next paragraph.

Since our objective is to find the *best fitting wear model with a wear constant, which is actually constant*, we have to calculate the average wear constant over the whole life of the liner for each model before choosing the wear model. Hence, the least-squares problem described by

[21] The wear constant is usually the variable K (section 1.3) but since the hardness H is also assumed to be constant, we can define a global wear constant $\overline{K} = K/H$.

[22] This statement is only valid because the facets have almost the same size. Otherwise, the volume loss rates of the different facets could not be compared that easily.

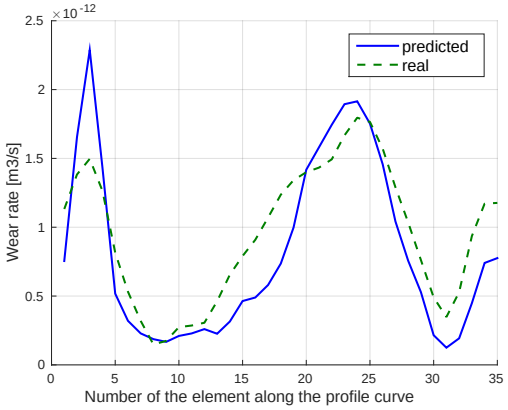

(a) Energy dissipated by normal damping.

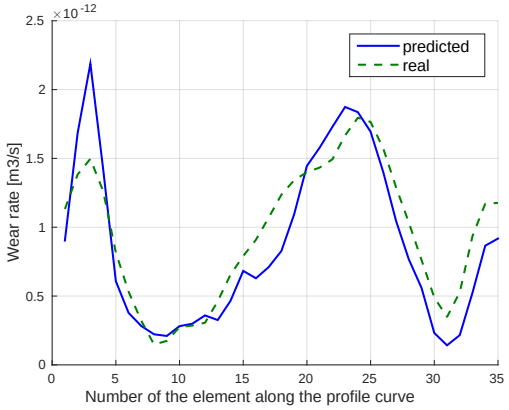

(b) Energy dissipated by tangential damping.

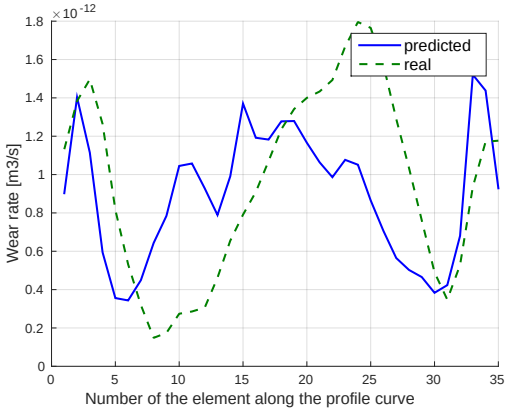

(c) Energy dissipated by sliding.

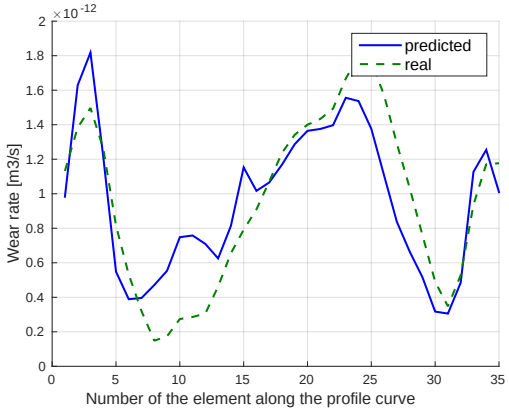

(d) Archard's wear model.

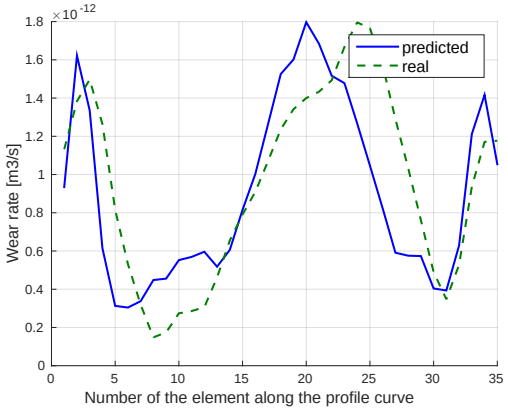

(e) Finnie's wear model.

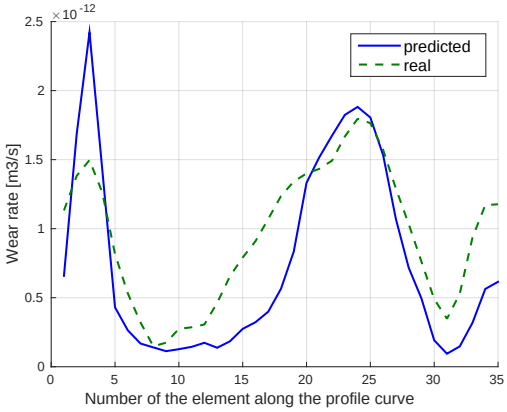

(f) Excess kinetic energy.

Figure 3.22: Numerically predicted wear rate vs. the real wear rate for each of the 35 axial stripes of the coarse 1D mesh. Each stripe is approximated by 6 facets in the mesh due to the axial extrusion of the 35 segments of the liner profile discretization in the figure 3.7. The real wear rate was calculated based on the profile curves after 2383 h and 7060 h, while the predicted relative wear rate was determined based on the coarse 1D mesh of the profile curve after 2383 h. The predicted wear rate was then obtained by multiplying the predicted relative wear rate by the corresponding global wear constant $\overline{K}$, which is the solution of the least-squares problem in the equation 3.7.

the equation 3.7 is solved for each of the 6 wear models and for each of the 8 operating duration steps (from 2383 h to 7060 h, from 7060 h to 12120 h and so on). This means, that we also created the 1D coarse meshes of the profile after 7060 h, 12120 h, ... and that a simulation was executed for each of these meshes to accumulate their wear data. Then, the weighted average of the wear constants over the 8 steps is determined for each model. The weighting coefficients used to calculate these averages are the number of operating hours of the specific operating duration step (e.g. 7060 - 2383 = 4677 h for the first step, and so on) since wear constants, which are determined over a longer time scale, seem to be more representative of the *real* wear constant; calculating a non-weighted average would, however, not have changed the results significantly. In fact, the wear constants of each individual step are fluctuating by about $\pm 50\%$ around their average values as shown in the figure 3.23. Interestingly, the variation of the wear constant is very similar to the variation of the real wear rate shown in the figure 3.18. This behavior therefore implies that the load on the liner is first reduced, then increased and finally reduced again in the real mill. Hence, this behavior is an additional argument for the *increase of the rotation speed after around 23669 operating hours* in the real mill, as mentioned earlier.

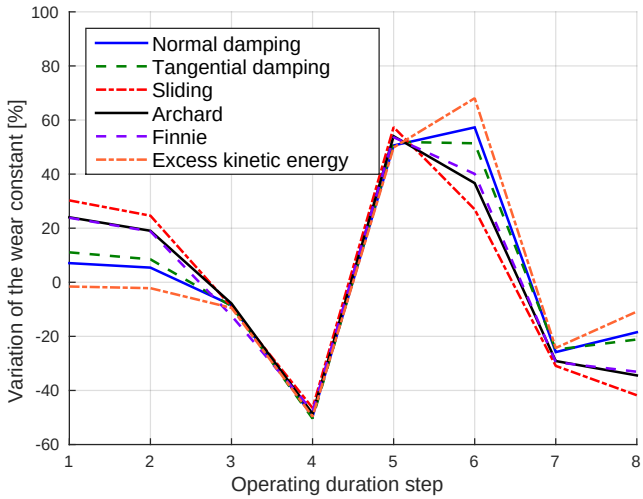

Figure 3.23: Fluctuation of the wear constants at each operating duration step around the average wear constant of the specific wear model.

Changing the rotation speed of the mill in the model is certainly possible but relatively complex because of the limited experimental data. This is why, we will only determine the *best fitting wear model with its average wear constant*. More precisely, we calculated the predicted wear rate for each of the 8 operating duration steps, for each wear model with the average wear constant of the model and for each facet. Then, the mean[23] squared errors between the real wear rates and the corresponding predicted wear rates were computed. Finally, after dividing the mean square errors of the 6 wear models at each operating duration step by the largest mean

[23] It is the average over all the facets for a given operating duration step and a given wear model.

square error at the specific step, we get the *error percentages of the models with respect to the worst fitting model at the current step, i.e. the lower the percentage, the better the fitting of the model with the reality*. On average, the *energy dissipated by tangential damping* is therefore the best[24] fitting wear model according to the figure 3.24. The corresponding average global wear constant is equal to $\overline{K} = 4.6 \cdot 10^{-12}$ m^2/N. Since the hardness of the liner is equal to 50 HRC, i.e. 500HV $\approx$ 500 MPa, the wear constant is equal to $K = 2.3 \cdot 10^3$. This value falls within the interval of the abrasion wear constant provided in the section 1.3.1. The numerical results thus seem to be coherent with the real wear phenomenon. In the next section, we will try to push things a little further by estimating the modification of the geometry due to wear.

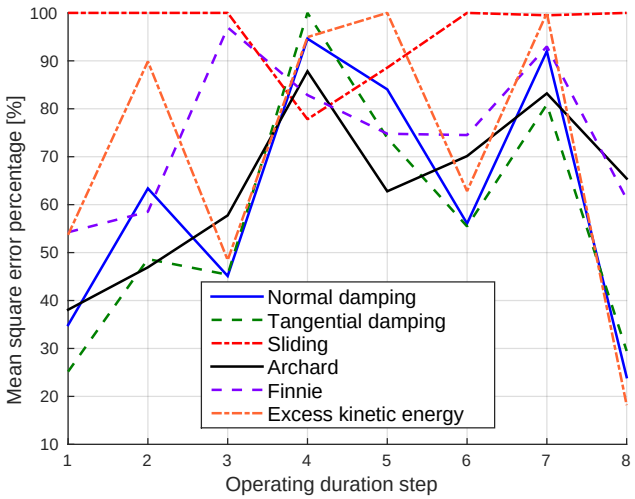

Figure 3.24: Error percentage of the wear model with respect to the worst fitting model at the specific operating duration step, i.e. the lower the percentage, the better the fitting of the model with the reality. The error is equal to the mean square error of the predicted wear data (on the basis of the simulation and the average wear constant of the specific wear model) and the real wear data of the given operating duration step.

3.3.5 Geometry modification

The best shell liner profiles in balls mills have low wear rates and preserve their shape during their whole operating duration. In order to compare these characteristics for different liner profiles, a simple but sufficient *geometry modification strategy* will be introduced in this section. More precisely, this section will be divided into three parts: the *displacement of the vertices* (of the mesh) due to wear, the *smoothing* of the resulting surface and its *regularization*.

[24]The energy dissipated by normal damping and the Archard wear model also deliver relatively good results but by summing the error percentages in the figure 3.24 over all the operating duration steps separately for each model, the energy dissipated by tangential damping has the smallest value, i.e. it is the best fitting model in agreement with this criteria.

Displacement of the vertices

The starting point of such a strategy is a *liner profile mesh*, in our case, the coarse 1D and the fine 2D meshes of the 250 mm slice after 2383 operating hours, and the *predicted wear rates of each facet*, which were determined according to the explanations in the previous sections. The liner profile after 12120 h can then be determined as follows. Since the liner mesh is initially assembled from the meshes of each plate, modifying the geometry of one plate is equivalent to modifying the entire liner. This is why, we will focus only on the geometry modification of *one plate*.

First, the *directions*, along which the vertices of the initial mesh (here the mesh after 2383 h) will be displaced, have to be chosen. Since a material body looses its material by wear normally to its surface, these directions are provided be the *normals of the surface*. These normals can be approximated at the vertices of the mesh by the average normal of the neighboring facets [Jin et al., 2005]. In order to obtain a better approximation of the normals at the edges and the corners of the plate, this plate is virtually reproduced in space and translated or rotated as illustrated in the figure 3.25. Hence, the normals at the edges and the corners are not only calculated by means of the neighboring facets of the vertex within the current plate but also by means of the neighboring facets within the bordering plates.

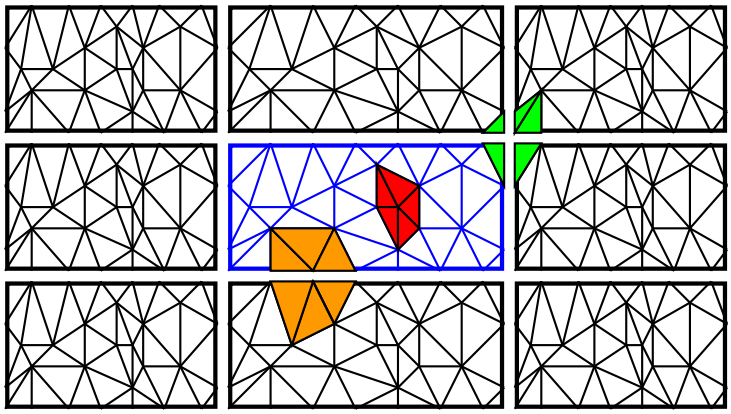

Figure 3.25: Illustration of the neighboring facets of a vertex, which are used to calculate the normal of the surface at this vertex. The master plate is translated axially and rotated azimuthally in order to reproduce the bordering plates. The colored patches around a vertex show which facets are included in the calculation of the normal at a vertex inside of the master plate, on an edge or at a corner. The shrinking of the plates on the left and on the right represents the rotation of those plates, which thus become shorter, if viewed from above.

Once the direction is known for each vertex, the *amplitude of the displacement along this direction* is determined on the basis of the predicted wear rate. For this reason, the predicted wear rate of each facet is multiplied by the operating duration, which separates the current liner profile from the new predicted profile in time. Consequently, the predicted volume loss below each facet is known. Choosing the operating duration step means that the geometry modification

strategy is *explicit*. Therefore, this step has to be chosen carefully. In our case, we want to predict the liner profile after 12120 h, i.e. after 12120 - 2383 = 9737 h with respect to the profile at 2383 h. How many steps are needed in practice to simulate the whole liner life will be explained in the section 3.3.7. By means of the predicted volume loss of each facet, their height loss can then be determined because it is equal to the volume loss divided by the area of the facet. The displacement of each vertex along its normal is then equal to the *average height loss of the neighboring facets*. Such a strategy is certainly an approximation but it has the benefit of already smoothing the profile without having to specify any additional parameter.

The last two steps of the geometry modification strategy are the *smoothing* of the new liner profile and its *regularization*. To understand why the smoothing might be necessary in some cases, the figure 3.26 shows the unsmoothed predicted liner profile after 12120 h based on the fine 2D mesh. Hence, the vertices on the leading edge of the small wave are displaced too far, which is clearly non physical. In the reality, wear is self-smoothing in the sense that, if the height loss at a given location would be greater than at the immediate neighboring locations, these neighboring locations would be worn away until reaching the same height as at the given location, i.e. the wear profile can only be smooth in the reality. For this reason, *mathematical smoothing can be seen as the numerical equivalent of this process* if the operating duration time step is too large to capture this effect. For this reason, we will show in the section 3.3.7, that smoothing allows to accelerate the analysis of a profile over its entire life while it is also possible to simulate the wear without any smoothing at all, if the number of operating duration steps is large enough.

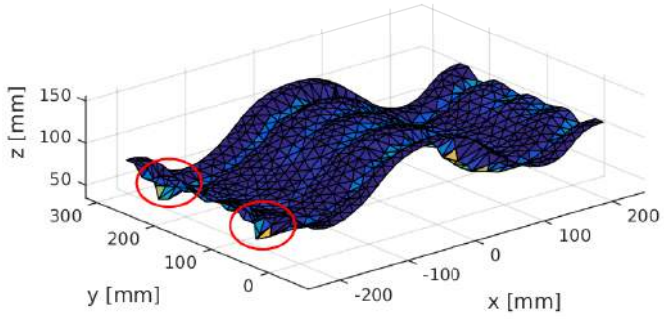

Figure 3.26: Predicted liner profile after 12120 h based on the fine 2D mesh of the 250 mm slice with frictionless walls after 2383 h. The red ellipses encircle the reason why the smoothing of the surface mesh is necessary, i.e. the displacement of the vertices on the leading edge of the small wave is too large in comparison to the real displacement. The color code represents the volume loss of each facet (dark blue to yellow). The problem is also highlighted in the figure 3.27.

Due to the ambiguity of 2D representations of 3D surfaces, we will introduce a method, which simplifies the analysis of 3D surfaces and their smoothing. More precisely the figure 3.27 shows the normal projection of the vertices on the *xz*-plane as well as the *alpha shape boundary* of these points [Edelsbrunner et al., 1983]. This boundary is a very convenient way to determine

the valley of the grooves. The upper region of the contour has, however, less significance as it is the profile curve of the liner after 2383 h with frictionless end walls, which prohibit any contact between the balls and the facets next to the walls. The boundary thus shows that the leading edge of the small wave is unrealistically flattened. For this reason, we will introduce *two smoothing algorithms*.

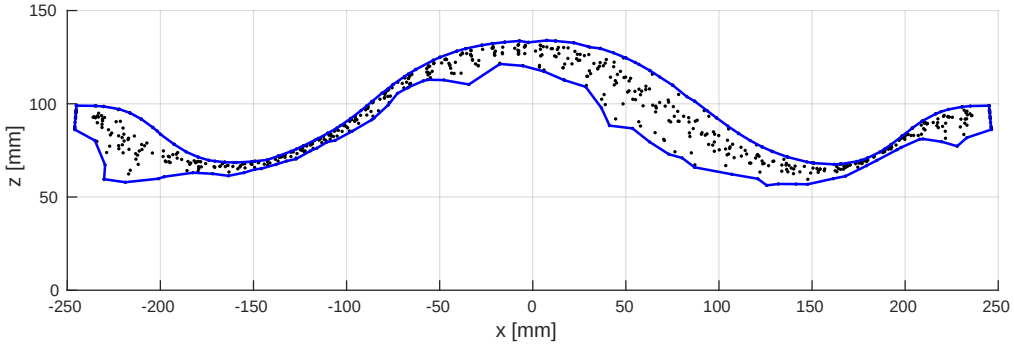

Figure 3.27: Projection of the vertices of the predicted liner profile on the xz-plane with their alpha shape boundary. The excessively large displacement of the vertices on the leading edge of the small wave can be seen in the region from -250 mm to -200 mm along the x-axis.

Smoothing

A vast number of surface smoothing algorithms can be found in the field of *surface reconstruction from noisy point clouds*. For this reason, we limited the scope of the research to simple algorithms, which are easy to implement or have already been implemented in MATLAB and which proved successful in previous studies. One technique, which has extensively been used, at least for the smoothing of 1D liner profiles, are *smoothing splines* (section 1.4.4). In particular, we first used the *thin-plate smoothing spline algorithm* to smooth the wear profiles. This algorithm is described in [Wahba, 1990, p. 10-14] and implemented in the `tpaps` MATLAB function. It has the advantage to take scattered data as input and to depend only on one smoothing parameter p, which quantifies the *compromise between the interpolation and the smoothing*. More precisely, the coefficients c_i and the control points $\mathbf{w}_i$ of the radial basis functions ϕ_i of the thin plate spline f,

$$f(x,y) = \sum_i c_i \, \phi_i((x,y)) \quad \text{with} \quad \phi_i((x,y)) = \|(x,y)\|^2 \, \log\|(x,y) - \mathbf{w}_i\|^2 \tag{3.8}$$

are determined by solving the following problem:

$$\min_{c_i, \mathbf{w}_i} \left(p \sum_{j=1}^{n} \left(z_j - f(x_j, y_j)\right)^2 + (1-p) \iint \left[\left(\frac{\partial^2 f}{\partial x^2}\right)^2 + 2 \left(\frac{\partial^2 f}{\partial x \, \partial y}\right)^2 + \left(\frac{\partial^2 f}{\partial y^2}\right)^2 \right] dx \, dy \right) \tag{3.9}$$

where (x_i, y_i, z_i) are the coordinates of the vertices before the smoothing of the liner surface. The first term in the optimization problem is related to the interpolation while the second term is related to the curvature. Once the coefficients of the spline have been computed, it can be evaluated at (x_i, y_i) to get the new z_i values. It becomes clear that the weakness of this strategy is that the thin-plate spline algorithm in MATLAB only takes bivariate data as input. If the xy-plane can, however, not be used as the *basis of the parameterization*, finding another basis becomes much more difficult. For instance, the vertical line between the plates in the *Perfecto ABAB* liner (section 2.1.2) could not be (easily) parameterized by a point in the xy-plane; in fact, multiple z coordinates of the liner would correspond to one (x, y) coordinate.

The previous problem can be solved by the second smoothing algorithm, i.e. the *surface relaxation by a 2D moving average*. This algorithm simply consists in substituting the position of a vertex by the average position of its neighboring vertices. For instance, if the coordinates of the vertices in the figure 3.28 are denoted by P_i, the new position of the vertex P_0 is determined by the following equation:

$$P_0^* = \frac{1}{5} \sum_{i=1}^{5} P_i \tag{3.10}$$

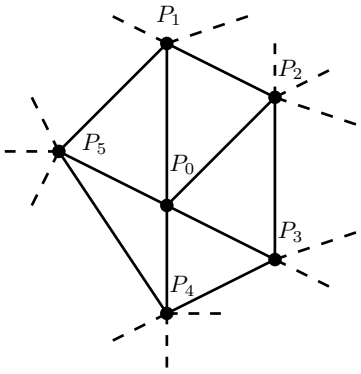

Figure 3.28: Illustration of the surface relaxation by a 2D moving average.

While this algorithm can be applied to any kind of mesh in contrast to the thin plate spline smoothing algorithm, it has mainly two drawbacks. On the one hand, the *smoothing can not be adjusted continuously*. It is, however, possible to apply the algorithm several times to the surface mesh. Ultimately, it would also be possible to introduce weighting coefficients for the neighboring nodes. Trying to keep the model as simple as possible, we will, however, only study the multiple application of the algorithm without weighting coefficients. On the other hand, the surface relaxation is *mesh-dependent*, i.e. the larger the elements (with respect to the characteristic size of the liner), the faster the curvature will vanish.

Before analyzing the results obtained by applying each algorithm, it has to be mentioned that the plate was again reproduced in space to account for the axial and azimuthal periodicity (similar to the figure 3.25). This means that the vertices of the nine plates were used in the thin

plate spline smoothing method. Similarly, the neighboring nodes of the bordering plates were used to calculate the average of the nodes on the edges and at the corners of the master plate in the surface relaxation method.

The influence of the smoothing on the liner shape is shown in the figure 3.29. In general, the results are almost identical for both smoothing algorithms, which is partially due to the values of the smoothing parameter p. Most interesting is, however, that both algorithms almost equally well interpolate the initial point cloud while loosing a matching amount of curvature. Since both algorithms lead to similar results and since the surface relaxation algorithm is much simpler and more versatile than the thin plate spline smoothing algorithm, we will focus exclusively on this algorithm in the next sections (esp. in section 3.3.7). It is also interesting to see that the smoothing by relaxation converges relatively quickly, i.e. after one or two relaxations, no significant change of the alpha shape boundary can be observed. In the case of the coarse 1D mesh, the smoothing seems almost not necessary. Nevertheless, we will show that this small amount of smoothing is necessary to keep the wear profiles coherent when the entire liner life is simulated with a large operating duration step in the section 3.3.7.

Regularization

The last step of the geometry modification method is the surface *regularization*. Since only the vertices of one plate were displaced and smoothed, it might happen that small *gaps or overlaps* (characteristic scale of about 1 mm) exist if the entire liner is assembled of the plates. These small imperfections can quickly increase the local wear rate in the simulation. This is why they have to be eliminated. First, the vertices of the edges are averaged with the vertices of the bordering plates as illustrated in the figure 3.30 for the rear and front edges of the plate. In addition to the averaging, the vertices of the lateral edges are projected on the xz-planes in $y = 0$ and $y = 250$ mm, to reestablish the full 250 mm slice.

3.3.6 Second pseudo steady state

The comparison of the results with the real wear profile will be described in the section 3.3.7 for the whole liner life. Simulating this evolution, however, requires to restart a simulation starting from the modified geometry in order to account for the variation of the load on the liner due to its shape modification. In consequence, it is necessary to determine when starts the (second) pseudo steady state after starting from the previous state. This question will be answered in this section.

As mentioned in the section 3.2.3, we will use the *final state (positions and velocities) of the balls in the previous simulation as the initial state in the following simulation* to reach more quickly the pseudo steady state. This is also one of the reasons why the total simulated time in the previous simulations was always equal to a multiple of the time necessary for one rotation. Hence, the small and large waves of the profile are located at almost the same positions (at the end of the previous simulation and the start of the new simulation) and no undesired interactions

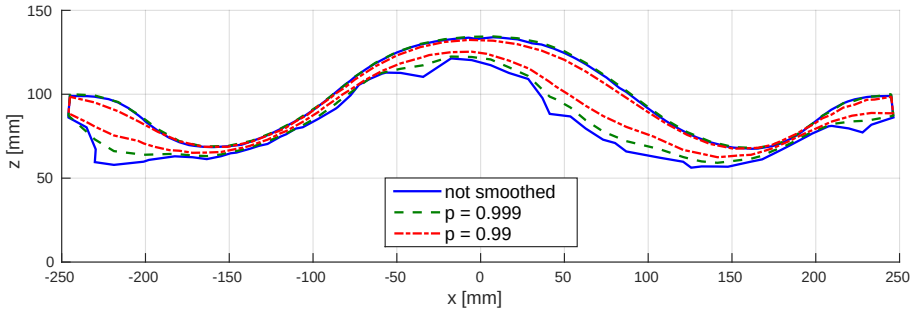

(a) Thin plate spline smoothing of the fine 2D mesh.

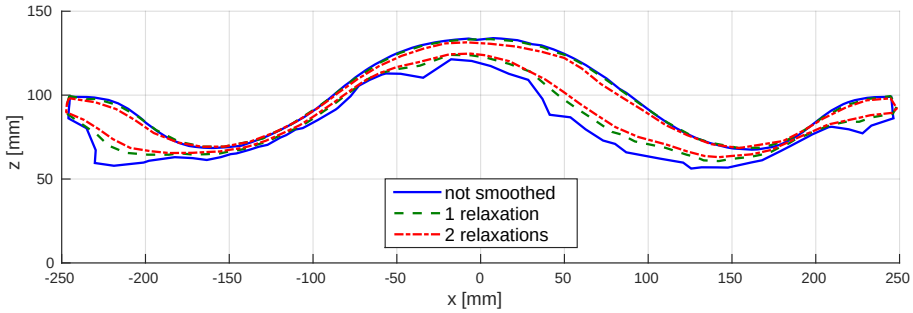

(b) Relaxation of the fine 2D mesh.

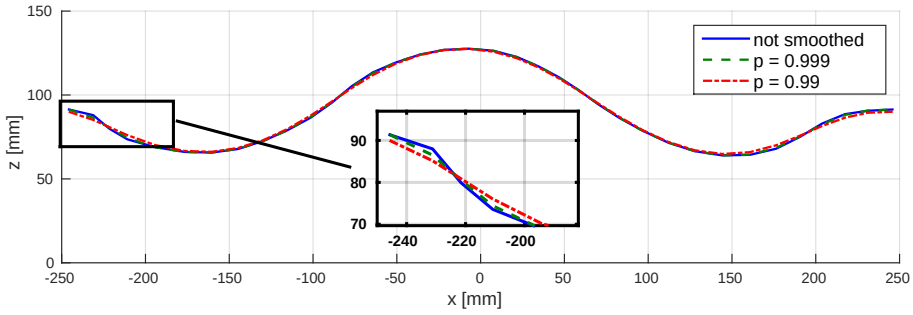

(c) Thin plate spline smoothing of the coarse 1D mesh.

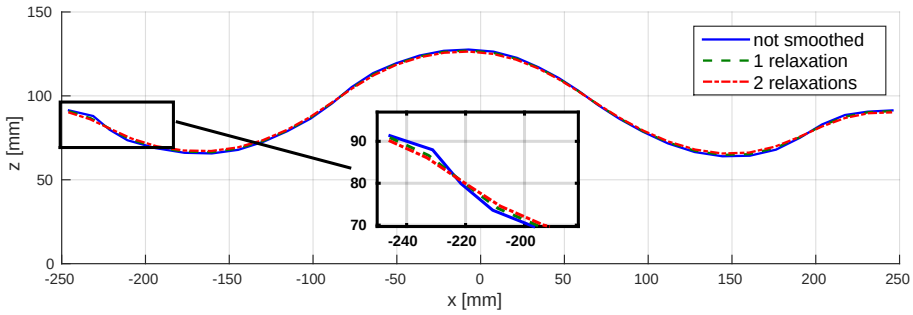

(d) Relaxation of the coarse 1D mesh.

Figure 3.29: Influence of the smoothing algorithms on the predicted profile after 12120 h starting from the profile at 2383 h. The alpha shape boundaries are represented for the 2D meshes and the profile curves for the 1D meshes. These results were obtained with the 250 mm slice, two end walls without friction, the energy dissipated by tangential damping as wear model, and the global wear constant $4.6 \cdot 10^{-12}$ m^2/N. The wear data was accumulated over 4 rotations in the pseudo steady state for the coarse 1D mesh and over 8 rotations for the fine 2D mesh, as the results of the previous section were reused.

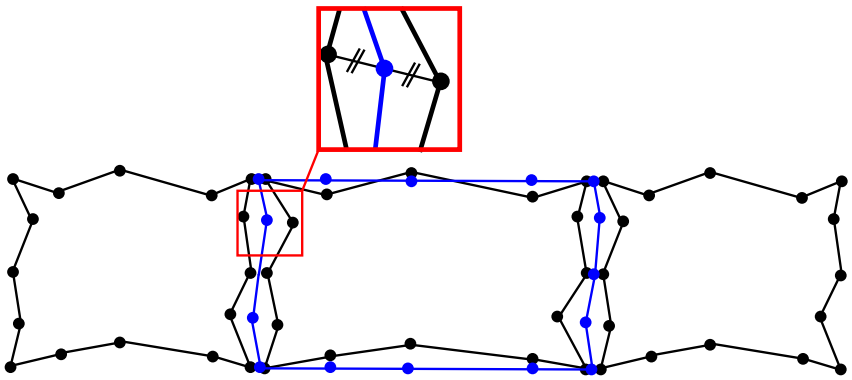

Figure 3.30: Illustration of the surface regularization, which is necessary to eliminate any gap or overlap after the assembly of the liner plates. The figure shows only three plates and the resulting regularized plate in blue. The zoom focuses on the average position of matching vertices.

between the balls and the liner can exist; this is also true because the mean diameter of the liner increases with its level of wear.

Based on the data of the previous section, it is possible to determine the profiles at 7060 h and 12120 h starting from the profile at 2383 h. Consequently, the coarse 1D meshes were created at 7060 h and 12120 h. The fine 2D mesh was, however, only determined at 12120 h. In fact, the small operating duration step (around 5000 h) will be impracticable with the fine 2D mesh because of the long computation time (around 10 h per simulation), which is why the corresponding mesh was not created.

The ball charge motion simulation was then restarted for these three meshes starting from the final state of the previous simulation. The resulting vertical position of the center of gravity (of the balls) is represented in the figure 3.31. To highlight the change of its position, the last rotation with the mesh after 2383 h was also represented.

Because of the small periodic fluctuations, which are certainly a remnant of the initial transient state, it is difficult to say when the second pseudo steady state starts, especially for the small liner modification after 7060 h. For the larger modifications after 12120 h, it is, however, clearly visible that the lifting capability of the liner decreases, since the average position of the center of gravity drops. Due to the evolution of this average position, *one rotation* seems to be a reasonable amount of time necessary to reach the second pseudo steady state.

3.3.7 Multi-step procedure

In this last section, we will combine the methods of the six preceding sections in order to predict the entire *liner wear evolution* by introducing the multi-step procedure. In the first part of this section, we will therefore explain the *antagonism between the operating duration step and the smoothing of the mesh*. In the second part, the *numerical results will finally be compared with*

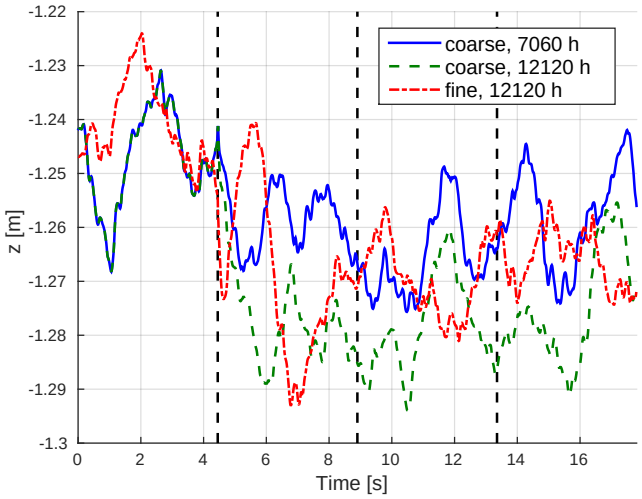

Figure 3.31: Vertical position of the center of gravity (of the balls) over time for the coarse 1D mesh as well as for the fine 2D mesh. The dashed vertical lines indicate the end of a full rotation. During the first rotation, the meshes after 2383 h were used. The continuity of the curves between the first and the second rotation indicates that the final state of the simulation with the 2383 h meshes was used as the initial state of the following 3 rotations. These 3 following rotations were created with the coarse 1D meshes after 7060 h and 12120 h, and the fine 2D mesh after 12120 h.

the real measurements in order to judge the predictive capability of the model.

Operating duration steps vs. smoothing

As mentioned earlier, the *multi-step procedure* consists in progressively updating the geometry of the liner in order to capture the variation of the load, to which it is subjected, due to the modification of its geometry. Since the procedure is completely explicit, i.e. based only on the current shape of the liner to determine its future shape, it is important to carefully choose the *operating duration step*. This step is the amount of real operating time, which separates two successive updates of the geometry.

In the following lines, we will illustrate the importance of the operating duration step and the smoothing on the basis of the *coarse 1D* and the *fine 2D meshes* of the 250 mm slice at 2383 h closed by end walls without tangential interaction (section 3.2). Initially, the simulations start with the balls at rest. The first pseudo steady state is supposed to be reached after two rotations of the mill (section 3.3.1). The wear data is then recorded during 3 and 8 rotations respectively for the 1D and the 2D meshes (section 3.3.2). By means of the relative wear data, the energy dissipated by tangential damping and the corresponding wear constant (section 3.3.4), the new geometry of the liner after a specified operating duration is predicted (section 3.3.5). Starting from the previous final state, one rotation is supposed to be sufficient in order to reach the second

pseudo state (section 3.3.6). Afterwards, the wear data is again recorded and the iterative process continues until reaching the required total operating duration.

Since we will only use the experimental wear profiles from 2383 h to 41541 h (section 3.3.3) in order to validate the model in the next section, a good choice of the operating duration steps seems to be the time between the measurements. These measurements were taken after 2383 h, 7060 h, 12120 h, 16680 h, 23669 h, 28668 h, 33034 h, 37020 h and 41541 h, i.e. the average operating duration steps is equal to 5000 h, if the profile evolution is simulated in 8 steps starting from the liner after 2383 h.

Coarse 1D mesh In the section 3.3.5, it was shown that the smoothing of the liner mesh seemed not to be necessary for the coarse 1D mesh (see figure 3.29d). This observations rises the question whether the smoothing is actually needed for this kind of meshes. To answer this question, the figure 3.32 shows the evolution of the liner profile over time in 4 steps with an increasing level of smoothing. In consequence, the *smoothing is necessary in the case of a 4 step liner modification* in order to not amplify a small error during the progressive evolution of the liner. Interestingly, a facet, which protruded from the average profile at the previous iteration, lies below this profile at the next iteration. This characteristic is clearly visible in the region of the small wave on the left. Previously, this phenomenon was described as the self-smoothing feature of wear (section 3.3.5), i.e. if a zone of the liner can not be touched by the balls, the immediate neighboring region is worn away until the balls can again touch that zone. According to the figure 3.32, the numerical smoothing successfully models this feature with *only one surface relaxation*; any additional relaxation would only reduce the global curvature of the profile without significantly improving its smoothness.

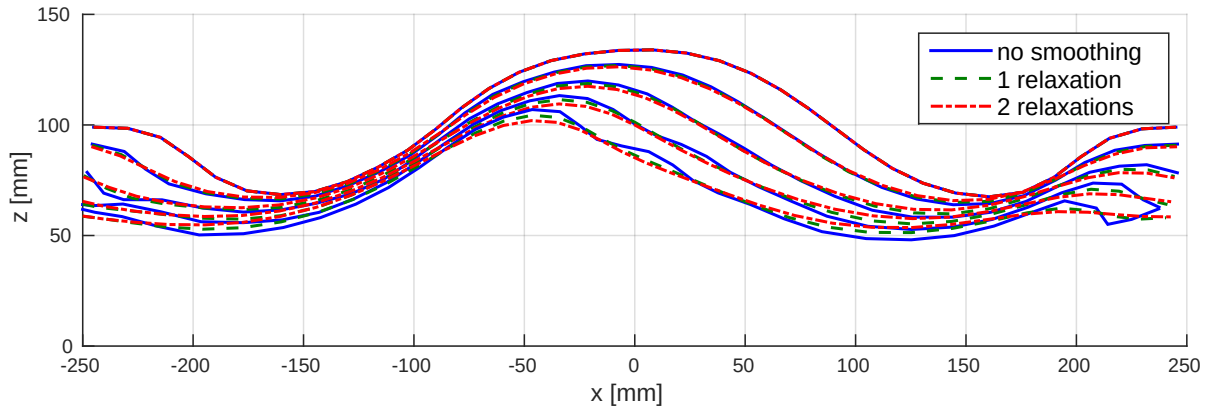

Figure 3.32: Influence of the smoothing on the coarse 1D liner mesh. Liner wear evolution in 4 steps with the surface relaxation smoothing method: 2383 h, 12120 h, 23669 h, 33034 h, 41541 h. The blue profile curve was obtained without any smoothing at all, while the other profiles were relaxed either one or two times at each iteration.

While the liner evolution in 4 steps requires smoothing, a second questions rises: is it possible to predict the liner evolution without any smoothing method but with more operating duration steps? The answer to this question is given in the figure 3.33. Since the results are globally overlapping, it is also *possible to simulate the liner wear without smoothing but the number of operating duration steps has to be increased*; hence, the computation time is also increased.

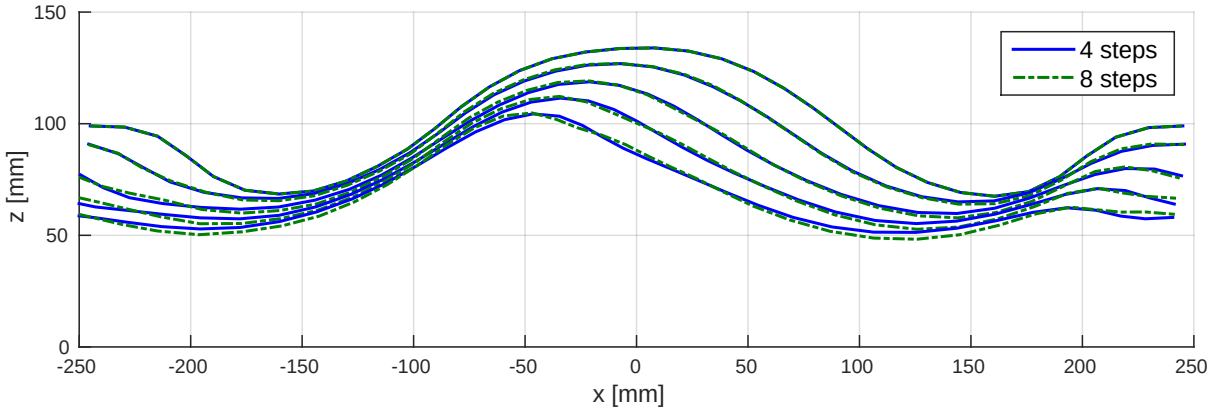

Figure 3.33: Number of operating duration steps vs. smoothing for the coarse 1D liner mesh. Liner wear evolution in 4 steps with one surface relaxation at each step (2383 h, 12120 h, 23669 h, 33034 h, 41541 h) and in 8 steps without any smoothing (2383 h, 7060 h, 12120 h, 16680 h, 23669 h, 28669 h, 33034 h, 37020 h, 41541 h). The intermediate steps of the 8 step procedure were not represented to keep the figure readable.

Fine 2D mesh In a similar way as for the coarse 1D mesh, the importance of the smoothing can be studied for the fine 2D mesh. The only major difference with respect to the previous study is that a single 4 step procedures takes *about 48 h of computation time instead of 8 h*. On this account, only the influence of the relaxation during the liner evolution was studied as shown in the figures 3.34 and 3.35, i.e. the liner evolution in 8 steps without smoothing was not simulated. The figure 3.34 shows that only one relaxation is in general not sufficient to obtain a smooth profile with a 4 step procedure. In fact, the spike on the right side of the figure comes from a collection of facets, which were in the optimal position to be hit strongly by the balls. In reality, this zone would be quickly worn away so that the material in the neighboring region would also erode at a similar rate. Because of the reduced number of operating duration steps, the response time of the model is, however, too long to correct the errors, which is why they are amplified.

This problem has two solutions: either the smoothing is increased or the operating duration step length reduced. On the one hand, the first solution has the drawback of eliminating more and more the characteristic information of the geometry since it reduces the global curvature, i.e. the curvature due to the errors but also the natural curvature of the liner profile. For instance, the creation of grooves at the center of the profile can be observed in the figure 3.35 for the

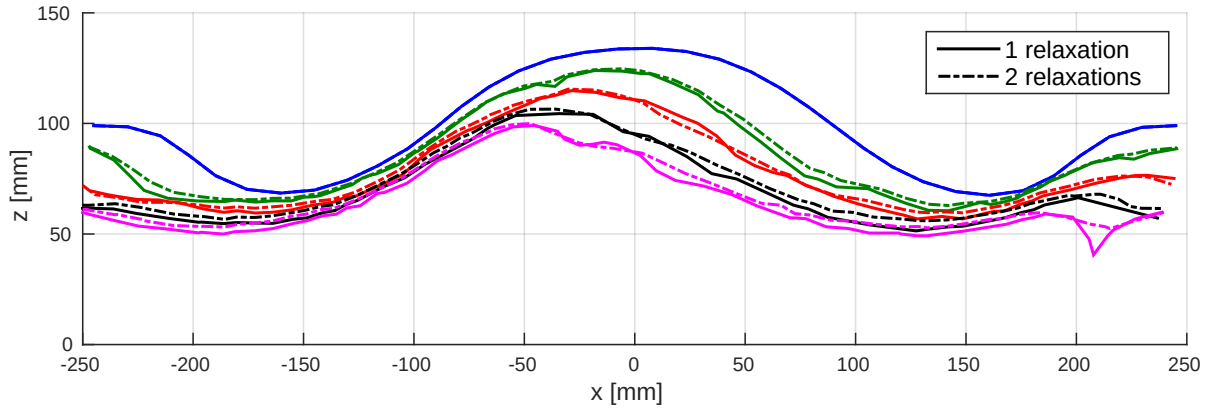

Figure 3.34: Influence of the smoothing on the fine 2D liner mesh along the azimuthal direction. Liner wear evolution in 4 steps with the surface relaxation smoothing method: 2383 h, 12120 h, 23669 h, 33034 h, 41541 h. The figure shows the valley of the grooves since the lower part of the alpha shape boundary was represented.

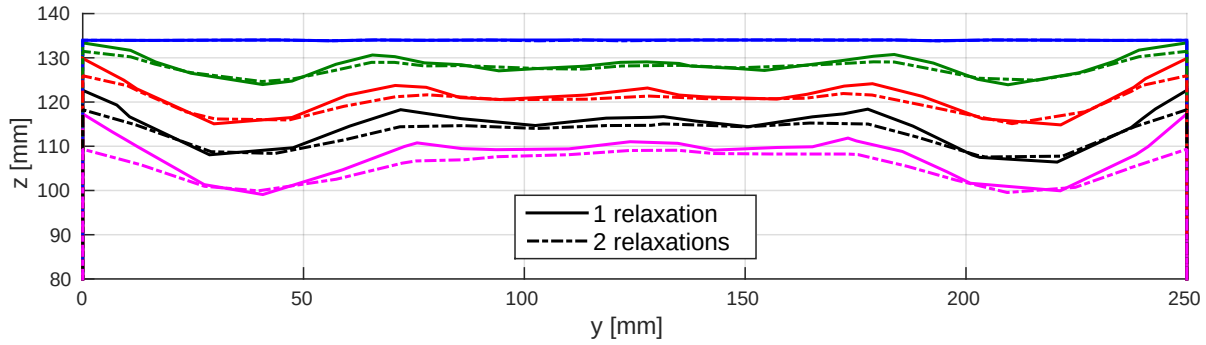

Figure 3.35: Influence of the smoothing on the fine 2D liner mesh along the axial direction. Liner wear evolution in 4 steps with the surface relaxation smoothing method: 2383 h, 12120 h, 23669 h, 33034 h, 41541 h. The figure shows the alpha shape boundary of the plate along its axial direction (top of the big wave), i.e. the boundary of its projection onto the *yz*-plane.

curves obtained with one relaxation, while two relaxations completely remove this information. On the other hand, reducing the operating duration step length increases the computation time considerably. Hence, the only acceptable solution at the current state is to *smooth the profile by two relaxations*. In the future, it would be very interesting to simulate the entire liner evolution in 8 steps, once without smoothing, and once with one surface relaxation in order determine whether the response time is sufficient to obtain smoother wear profiles with an adequate content of curvature. If these simulations are not conclusive, a more powerful smoothing algorithm should be implemented and the influence of the average element size on the liner evolution should be studied.

Prediction vs. reality

In this section, we will finally compare the predicted wear profiles with the real wear profiles in order to evaluate the predictive capability of the model. The results are shown in the figures 3.36 and 3.37 respectively for the coarse 1D mesh and the fine 2D mesh.

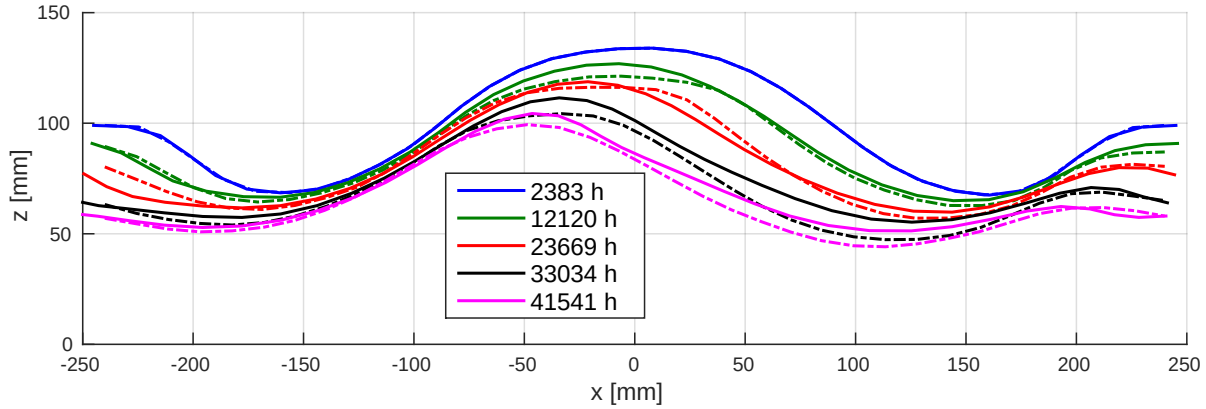

Figure 3.36: Comparison of the predicted wear profiles (solid lines) with the real wear profiles (dashed lines) for the coarse 1D mesh. The predicted wear profiles were obtained by a 4 step procedure with one relaxation smoothing pass. The other parameters are summarized at the beginning of this section (section 3.3.7). The real wear profiles are the average values of the minimum and maximum height measured at the specified moments in time.

Concerning the coarse 1D mesh, the *correlation between the real wear and the prediction is relatively good*. Only after 23669 h, the difference on the leading edge of the big wave becomes a little more significant. This difference can be explained by the increased rotation speed of the real mill after half of its lifespan in order to keep the throughput constant with a more and more worn out liner as explained in the section 3.3.4. Obtaining a better correspondence between the real wear profiles and their predicted counterparts would therefore only be possible by monitoring

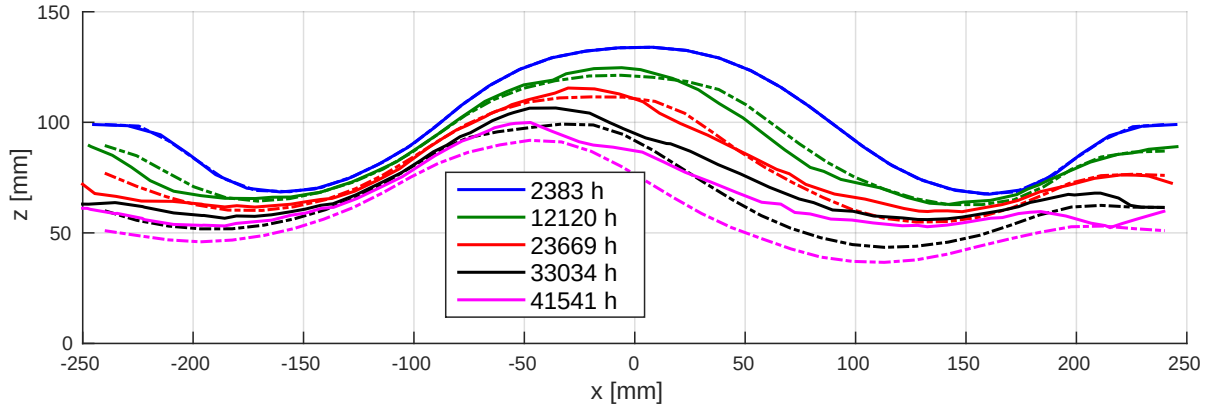

Figure 3.37: Comparison of the predicted wear profiles (solid lines) with the real wear profiles (dashed lines) for the fine 2D mesh. The predicted wear profiles were obtained by a 4 step procedure with two relaxation smoothing passes; these profiles represent the lower part of the corresponding alpha shape boundary, i.e. the contour of the projected points onto the *xz*-plane. The other parameters are summarized at the beginning of this section (section 3.3.7). The real wear profiles are the minimum height measured at the specified moments in time, if a minimum height was available. Otherwise, i.e. at 12120 h, it is the average profile height.

more carefully the operating conditions of the real mill and by modeling second order phenomena like the progressive grinding of the balls and their radial segregation.

It is important to notice that the liner evolution was predicted with *one single global wear constant*, i.e. $\overline{K} = K/H = 4.6 \cdot 10^{-12}$ m^2/N (section 3.3.4). If the number of operating duration steps is sufficiently large, the profile height is linear in this constant. Increasing the hardness of the plate or the ground clinker by a certain factor would thus divided the life expectancy of this plate by the same factor. The evolution of the geometry would, however, spatially be the same for different values of the hardness (except for their time scale).

With regard to the fine 2D mesh, more significant differences than for the coarse 1D mesh can be observed in the figure 3.37. In the same way as for the coarse 1D mesh, the correlation is relatively good for the first three profiles. After 23669 h, the difference increases again due to the increased rotation speed of the real mill. In contrast to the 1D mesh, the disagreement between the curves is more important, though. Essentially two reasons might explain this larger disagreement; further subsidiary reasons certainly also exist: the *operating duration step* or the *enrichment of the solution space*.

On the one hand, we stated earlier that at least two relaxations were required for a 4 step simulation in order to obtain a sufficiently smooth profile. Each of these *relaxations eliminates some of the useful geometrical information* while also removing the spurious first order discontinuities. Hence, the profile might be numerically worn a little less than it should be. According to the figure 3.35, the importance of this first reason is, however, rather low since the corresponding

curves are relatively close. As pointed out previously, an 8 step simulation with and without one relaxation should give more conclusive results with respect to this phenomenon in the future.

On the other hand, by allowing the axial modification of the fine 2D mesh, we enrich the solution space. From the perspective of the balls, wear can be seen as an optimization process because these *balls try to find their optimal trajectory*. This optimal trajectory is the path where the balls encounter the least obstacles. Otherwise, these obstacles are little by little worn away. Allowing the axial alteration of the profile renders is possible to create ball trajectories which are better, i.e. with less obstacles, than those of a 1D mesh. Therefore, the average wear rate is lower for 2D meshes than for 1D meshes (with the same initial profile), provided that the liner evolution was predicted with the same wear constant. This reasoning is a *strong argument for designing ball mill liner plates with initial grooves* similar to those of the worn liner. The figure 3.38 illustrates this phenomenon on the basis of the wear distribution accumulated on the initial liner and the worn liner. Thus, the predicted height loss rate is very concentrated in some regions of the initial liner while it is more uniformly distributed and lower on the worn liner. For this reason, the wear constant should be adjusted for the 2D meshes. If the facet size decreases, the adjusted wear constant increases until converging to the *real* wear constant since the solution space in the model is likely to converge to the solution space of the real liner. As mentioned earlier, adjusting the wear constant should, however, have no influence of the geometry modification from a spatial point of view since the model is linear in this constant, i.e. only the time scale is rescaled.

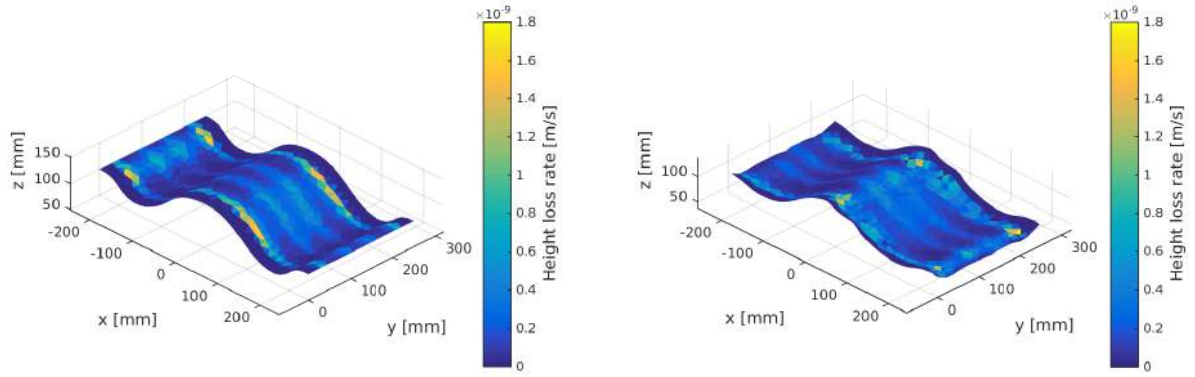

(a) Geometry and wear distribution after 2383 h. **(b)** Geometry and wear distribution after 33034 h.

Figure 3.38: Geometry and wear distribution accumulated on the initial liner plate and the worn liner plate (2D mesh). The profiles were obtained by a 4 step procedure with two relaxations.

One important question remains: why are the grooves at the center of plate not as deep as in the reality (figure 3.35)? First, the smoothing algorithm might be too strong and the element size to large so that the smoothing simply removes the axial curvature, which leads to the creation of the grooves. Second, the slice might be too short to create 4 grooves but too long to create 3 grooves, which means that the grooves at the center annihilate themselves. Moreover, the

particular boundary condition, i.e. flat end walls without tangential interaction, overestimates the outer grooves, which reduces the space available for the creation of the central grooves.

In conclusion, relatively good predictions of the liner wear evolution can be obtained for 1D meshes. Their accuracy is mainly limited by the explicitness of the experimental reference data and the modeling of second order phenomena. Almost satisfactory results can be obtained for 2D meshes but the influence of the boundary condition, the facet size and the smoothing algorithm in combination with the number of operating duration steps has to be studied in more detail in the future. This study is mainly limited by the long computation time with 2D meshes. Concerning the predictive capability of the model in scenarios with different liner geometries and different operating conditions, no definite conclusion can obviously be draw from this study but there is strong evidence that at least the 1D model will deliver quite satisfactory estimates of the liner evolution in those scenarios.

Conclusion

In this thesis, a DEM-based method to predict the *charge motion* and the *power draw* of a ball mill has been calibrated and validated by means of photographs of the charge motion, and power draw measurements of a 1:5-scale laboratory mill (chapter 2). This computational method essentially renders future *experimental testing unnecessary* in order to quantify the previous characteristics of the mill. Based on this first method, we have developed, implemented and tested a generic procedure for predicting the *wear distribution* and the *progressive shape evolution of liner surfaces*, here the shell liner in the first compartment of a clinker grinding 5.8 m diameter cement tube mill (chapter 3). The liner wear evolution of profiles with no axial variation can be predicted with confidence while the study of this evolution for fully variable geometries is still limited by the significant computation time. Moreover, additional validation studies of the wear prediction are required but usually difficult to realize because of the rare and incomplete experimental data commonly available in this field.

In the next section, these general conclusions will be described more explicitly to *summarize* the most important results of the previous chapters. Finally, in the last section, we will put emphasis on possible *improvements and future applications* of these results.

Summary and main contributions

The content of the thesis and the main contributions will be summarized by following the structure of this document.

First chapter - Theoretical background

In the *first chapter*, basically no new contributions to the fields of DEM ball mill modeling and wear prediction are introduced. Its objective is rather to build a solid *theoretical foundation* for the models of the following chapters by reviewing the current state of the art.

In summary, the grinding process in *ball mills* is highly energy-intensive and aggressive in terms of wear. This process can be improved by the design of a wear-resistant liner, which enhances the energy transfer to the charge.

The most promising method to simulate the ball mill and its charge is the 3D *discrete element method*. In this method, the balls are represented by spherical particles and the liner by a surface mesh assembled of triangular facets. The bottleneck of DEM simulations with respect to the computation time is the collision detection between the bodies. The linear spring-slider-damper contact law, which is based on a soft representation of the contact, i.e. with overlapping, is a sufficient and necessary but idealized model to predict the forces between the particles. Once these forces are known, the equations of motion are integrated explicitly with a constant time step. Ball mills have already been simulated in the literature by this method but no general agreement about the values of the contact parameters seems to exist. This is why an extensive parameter validation study was carried out in the second chapter.

To predict the wear, the major *wear mechanisms and wear models* were introduced in the third section of the first chapter, but no single wear model was found to be valid in general. For this reason, the best fitting wear model with the real wear was determined a posteriori in the third chapter.

In the last section of the first chapter, the current state of the art in *ball mill liner wear modeling* was summarized by combining the results of the previous sections. Hence, the best way of modeling the wear of a liner in a ball mill is as follows: first, sufficiently representative numerical wear data has to be synthetically accumulated on the surface mesh of the liner, which plays the role of a binning structure, during a DEM charge motion simulation. The numerical wear data, which is defined by the best fitting wear model and the simulation, is then converted into a real volume loss by the wear constant and the specified operating duration. Since the volume loss of the material immediately below each facet is known, the surface of the mesh can be displaced to account for the respective volume loss after the corresponding duration; a smoothing technique might be necessary to obtain realistic wear profiles. Finally, this process should be repeated several times in order to capture the variation of the load on the liner due to the modified particle flow pattern after the update of the geometry; this process is called a multi-step procedure.

Second chapter - DEM ball mill simulation

In the *second chapter*, a *DEM model of a laboratory ball mill* is calibrated and validated on the basis of experimental data. This *data* consists of photographs of the charge motion and power draw measurements of a Ø 800 mm $\times$ 400 mm laboratory mill with different 1:5-scale shell liner plates (of the first chamber of a clinker grinding cement tube mills) provided by the company Magotteaux International S.A. .

The *open-source DEM solver* YADE was selected to create the simulations because of its versatility and reduced size in contrast to the software LIGGGHTS, which is, however, on average 2.5 times faster than YADE.

Concerning the *DEM model*, the linear spring-slider-damper contact law was implemented in YADE with some additional features, like the possibility of calculating the different power

components, by which energy is dissipated during collisions. The geometry of the mill is then represented by an extruded surface mesh of the liner profile curve, which has been discretized on the basis of its curvature in order to reduce the number of elements. Concerning the evaluation of the model, it was interesting to notice that DEM simulations lead to results, which are on average equal, but non-deterministic, when they are run in parallel on multiple processors. In the last section about the DEM model, the position density limit was introduced as a new and efficient post-processing tool to characterize easily the global charge motion in the pseudo steady state.

The essential conclusion in the section about the *numerical results* is that the DEM model can predict the charge motion and the power draw with accuracy, i.e. the representations of the predicted and the real charge motion overlap almost exactly, when they are superposed. Moreover, the power draw prediction is systematically lower than the real power draw (at maximum by 5%), which can be explained by additional dissipative mechanisms in the reality. In general, the charge motion and the power draw of the mill are relatively insensitive to the material parameters. Choosing the normal stiffness such that the maximum overlap between two colliding balls is equal to about 5% minimizes the computation time and has a negligible influence on the results of the simulation. Moreover, the coefficient of normal damping should be deduced from the coefficient of normal restitution. This coefficient leads to realistic results, when it is equal to around 0.3 and 0.8 respectively for a mill containing metal balls and a feed material, and for a mill containing only metal balls. A realistic value of the coefficient of friction is 0.75. At the same time, the tangential stiffness and the tangential damping coefficient should be equal to their normal counterparts. Moderately different values deliver, however, nearly identical results in terms of the average charge motion and the power draw. Interestingly, the energy in the model is mainly dissipated by the sliding of the charge. Finally, it was shown that there is strong evidence that the discrete element method is also able to predict the charge motion and the power draw of full-scale industrial ball mills.

Third chapter - Liner wear simulation

In the *third chapter*, a DEM-based generic procedure was developed to *simulate the wear*, i.e. the spatial distribution of the wear and the progressive change in the geometry due to wear, of lining surfaces. This procedure was illustrated, calibrated and validated on the basis of experimental data measured during one decade in the first chamber of a cement tube mill. More precisely, the *experimental reference data* consisted of the wear profiles of a *Duolift* liner plate kindly provided by Magotteaux International S.A. .

The fundamental requirement of the wear simulation is a *DEM charge motion model* in order to predict the numerical wear data. While the material parameters were easily determined on the basis of the previous chapter, defining the geometry and the boundary conditions was more complex since simulating the entire first chamber of the mill was impossible within the time frame of the thesis, and also unnecessary at the current stage of development. Hence, 8 different scenarios were defined by combining the following conditions: 250 mm or 500 mm axial slice of

the mill, periodic boundary condition or end walls without tangential interaction, 1D liner mesh or 2D liner mesh, where the first mesh category only allows modifications of the liner along the radial direction (axial extrusion of the liner profile curve) while the second category also allows modifications along the axial direction (average triangular facet size: 15 mm). These 8 scenarios were then studied by a *wear simulation* strategy in 7 stages.

First, it was shown that the *pseudo steady state* of the mill is reached after 1 to 2 rotations starting from rest.

The *representative wear data* for 6 different wear model was then accumulated by a synthetic data extraction strategy on each facet during 2 to 3 and at least 8 rotations in the pseudo steady state for the 1D and 2D meshes, respectively. To obtain sufficiently representative wear data, a master lifter mapping scheme, was absolutely necessary. This scheme consists in mapping the wear data accumulated on all the plates, on one single plate thanks to the azimuthal periodicity. Axial averaging is also possible for axially periodic plates and an axially periodic charge motion, like the one obtained with a periodic boundary condition. Based on the relative wear distribution, it was concluded that only the scenarios with the 250 mm slice and frictionless end walls are realistic (grooves can not be created with a periodic boundary condition and a shell liner, which initially has no height variation along the axial direction) and computationally feasible.

The third step of the wear simulation is the extraction of the *real wear data* from the experimental wear profiles for each facet of the liner mesh to correlate it with the predicted relative wear. Interestingly, the real wear rate increased strongly after half the lifespan of the liner. This phenomenon was explained by the increase in the rotation speed of the real mill in order to keep the throughput constant with a more and more worn out liner.

In the next section, its was shown that the energy dissipated by tangential damping is the best fitting *wear model*. Its *wear constant* was also determined.

On the basis of the predicted wear rate, the *geometry* of the liner mesh was then *modified* by displacing each vertex normally to the surface by a distance equal to the average height loss of the neighboring facets due to wear. As a result of the scattering of the wear data and the relatively large operating duration between the initial and the modified liner mesh, it was concluded that smoothing is required for 2D meshes but not necessarily for 1D meshes. Therefore, a thin-plate spline smoothing algorithm and a surface relaxation algorithm were introduced. Because of the similar compromise between the curvature loss and the interpolation of both algorithms but the superior versatility of the surface relaxation algorithm, this latter algorithm seemed to be the better smoothing algorithm.

Since the state of the balls in the previous simulation is used as the initial state in the following simulation to reduce the computation time of a multi-step procedure, it was shown that the *second pseudo steady state* starts around one rotation after the beginning of the simulation with the updated liner mesh.

Finally, the *multi-step* procedure is able to predict relatively accurately the liner wear evolution in 4 steps with smoothing or in 8 steps without smoothing for the 1D mesh. At least two surface relaxations are, however, necessary to obtain a sufficiently smooth shape evolution of

the fine 2D liner mesh in 4 steps. Moreover, the creation of grooves can be simulated and there is some evidence that they might reduce the liner wear rate. More detailed investigations are, however, necessary to prove this conclusion. For this reason, the following section gives some suggestions about future research objectives.

Future research

The following list summarizes some recommendations about the future research in the fields of DEM ball mill modeling and liner wear prediction:

- *DEM solver*: an important limitation of the discrete element method applied to industrial problems is the computation time. This problem has especially become apparent during the analysis of almost fully variable 2D meshes in the last chapter. Developing more efficient DEM solvers therefore seems to be an important requirement for the design of better industrial products. In particular, highly parallel solvers with a grid collision detection algorithm executed on GPU seem to be an first step in their improvement, considering that LIGGGHTS (grid collision detection) was already around 2.5 time faster than YADE (insertion sort collision detection) on CPU.

- *Fully variable geometry and boundary condition*: while relatively good predictions of the liner wear evolution were obtained for 1D meshes, it is still necessary to continue studying this topic in greater depth in order to obtain more conclusive results for almost fully variable geometries represented by fine 2D meshes. In particular, the influence of the number of operating duration steps, the smoothing algorithm, the average facet size and the boundary condition (end walls with friction, length of the axial slice, ...), on the liner wear evolution have to be studied in more detail for almost fully variable geometries.

- *Consequences of wear*: in this thesis, only the wear as such was studied. Ultimately, the consequences of wear are, however, important for optimizing the design of future liners, specifically, the influence of wear on the power draw of the mill, the lifting height and the lifespan of the liner.

- *Further applications*: due to the versatility of the discrete element method and the generality of the DEM-based procedure for predicting wear, these methods can be used to optimize ball mill liners as well as liners in totally different machines, for instance vertical shaft impactor mills. Such applications require, however, further validation studies to judge more objectively the predictive capability of the models. Once a certain expertise has, however, been acquired, these models might become very powerful tools for the development of better liners and comminution devices.

Appendix A

Analytic Validation of the Linear Spring-Slider-Damper Contact Law

In this chapter, several standard collision problems will be described. These problems are sufficiently simple to have an analytic solution. In consequence, the *linear spring-slider-damper contact law* implementation in the DEM solver YADE (see appendix C) will be *validated* on the basis of these analytic solutions (motion and power dissipation) to ensure that the software is working according to our expectations. The following problems will be studied:

- normal sphere/sphere collision
- normal sphere/facet collision
- tangential sphere/wall collision without sliding
- tangential sphere/wall collision with sliding

The values of the simulation parameters[1], which were used throughout this study are the following ones; exceptions will be mentioned[2]:

- density of the spheres: $\rho = 7640$ kg/m^3
- equivalent normal stiffness: $k_n = 10^5$ N/m
- equivalent normal damping coefficient: $c_n = 18.6$ Ns/m, i.e. the normal coefficient of restitution is equal to $\varepsilon_n = 0.3$ (sphere/sphere collision)
- equivalent tangential stiffness $k_t = 10^5$ N/m

[1] The absolute values of these parameters have no real significance in this chapter since we are only interested in finding the same analytic and numerical solution. They are, however, itemized here for the sake of completeness.

[2] These values are equal those used in [Sawley, 2003], except for the density ($\rho = 7650$ kg/m^3, negligible difference) and the time step (smaller here to neglect its influence on the results).

- equivalent tangential damping coefficient $c_t = 18.6$ Ns/m
- friction coefficient $\mu = 0.75$
- diameter of the spheres $d = 15$ mm
- time step $\Delta t = 10^{-6}$ s, i.e. sufficiently small to reduce the influence of the numerical integration

A.1 Normal sphere/sphere collision

In this section, the analytic solution of the normal collision between two spheres will be determined in order to *validate* the spring-slider-damper contact law implemented in the DEM solver YADE. Moreover, this solution will be used to establish the relation between the contact parameters and some derived parameters, i.e. the *contact time* t_c, the *normal coefficient of restitution* ε_n and the *maximum overlap* $\Delta x_{\max}$ of the spheres during their collision.

A.1.1 Analytic solution

Let m_1 and m_2 be the masses of two spherical particles moving towards each other with their respective normal velocities v_1 and v_2. The particles collide when the distance between their centers located in x_1 and x_2 becomes smaller than $z_0 = r_1 + r_2$, where r_1 and r_2 are the radii of the particles. The collision forces are then described by the normal component of the linear spring-slider-damper contact law, where the spring has a stiffness k_n and the damper a damping coefficient c_n. The figure A.1 shows the schematic representation of the contact law at the moment of the normal collision.

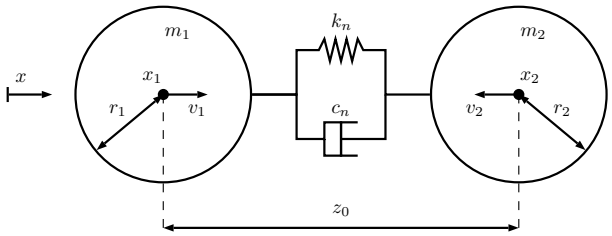

Figure A.1: Schematic representation of the normal contact law between two spherical bodies having the radii r_1 and r_2, and being initially located in x_1 and x_2 separated by a distance z_0, i.e. $z_0 = r_1 + r_2$ (adapted in the diagram). The bodies have the masses m_1 and m_2, and the opposed velocities v_1 and v_2, resulting in their contact. The normal contact law is represented by a spring of stiffness k_n in parallel with a dashpot having damping coefficient c_n.

The equations of motion of the spherical particles in the normal direction can be written as follows:

$$m_1\ddot{x}_1 + c_n(\dot{x}_1 - \dot{x}_2) + k_n(\dot{x}_1 - \dot{x}_2 + z_0) = 0 \quad (A.1)$$

$$m_2\ddot{x}_2 + c_n(\dot{x}_2 - \dot{x}_1) + k_n(\dot{x}_2 - \dot{x}_1 - z_0) = 0 \quad (A.2)$$

By taking the difference of the equation A.2 multiplied by m_1 and the equation A.1 multiplied by m_2, we obtain the equation of relative motion:

$$m_1 m_2(\ddot{x}_2 - \ddot{x}_1) + c_n(m_1 + m_2)(\dot{x}_2 - \dot{x}_1) + k_n(m_1 + m_2)(x_2 - x_1 - z_0) = 0 \quad (A.3)$$

This equation can be rewritten by introducing the relative displacement $z = x_2 - x_1$, the natural frequency $\omega_0 = \sqrt{k_n/m_{\text{eff}}}$, the effective mass $m_{\text{eff}} = m_1 m_2/(m_1 + m_2)$ and the damping ratio $\zeta = c_n/(2\sqrt{m_{\text{eff}}\, k_n})$:

$$\ddot{z} + 2\zeta\omega_0\dot{z} + \omega_0^2(z - z_0) = 0 \quad (A.4)$$

If the damping ratio satisfies the condition $0 \leq \zeta < 1$, which is usually the case, the general solution of the previous differential equation is:

$$z(t) = e^{-\zeta\omega_0 t}\,[A\cos(\omega_d t) + B\sin(\omega_d t)] + z_0 \quad \text{where} \quad \omega_d = \omega_0\sqrt{1-\zeta^2} \quad (A.5)$$

The values of the constants A and B in this equation can be determined be the initial conditions:

$$\begin{cases} z(0) = z_0 \\ \dot{z}(0) = -(v_1 + v_2) \end{cases} \Rightarrow \begin{cases} A = 0 \\ B = -\frac{v_1+v_2}{\omega_d} \end{cases} \quad (A.6)$$

The analytic solution of the normal linear spring-damper contact law is thus:

$$z(t) = z_0 - e^{-\zeta\omega_0 t}\,\frac{v_1 + v_2}{\omega_d}\sin(\omega_d t) \quad (A.7)$$

Notice that this solution obviously makes only sense from $t = 0$, i.e. the beginning of the contact, to $t = t_c$, i.e. the ending of the contact (contact time).

A.1.2 Validation

To ensure that our implementation of the spring-slider-damper contact law in YADE is working correctly, the charge motion and the power dissipated by normal damping will be validated analytically. The analytic description of the relative motion $z(t)$ between the spheres is given by the equation A.7. The power dissipation can be deduced as follows:

$$P_{\text{normal}} = c_n\,\dot{z}^2 \quad (A.8)$$

Supposing that $v_1 = 2$ m/s and $v_2 = 1$ m/s (opposed directions according to the figure A.1), the analytic and numerical solutions were determined. The figures A.2 and A.3, show that both solutions are *identical* on the domain of validity of the analytic solution, i.e. the analytic solution is not valid after the rebound since both particles continue to float in space without any interaction in the simulation. The normal contact between spheres is therefore implemented correctly. It should be mentioned that the spring-slider-damper contact law in YADE prohibits any attractive forces between two colliding particles. These forces might be created by the damper when the particles separate after the collision. To eliminate the attraction, the force between the respective particles is simply set equal to 0 in the simulation. This feature, was not validated here due to its simplicity.

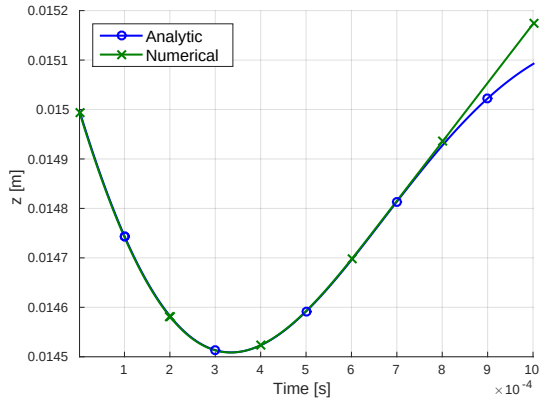

Figure A.2: Relative displacement z of the two spheres during their normal interaction obtained by the analytic formulas and the DEM solver YADE.

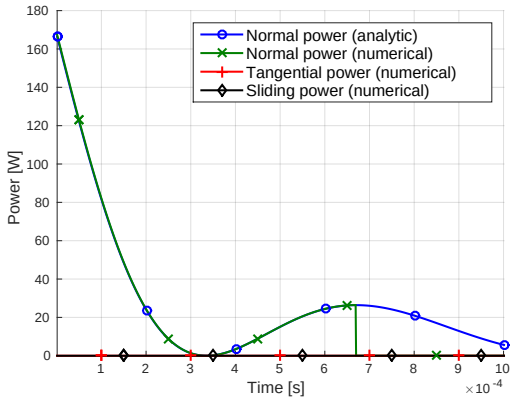

Figure A.3: Power dissipated during the normal collision of two spheres calculated by YADE, and the relevant power dissipation, which was determined by the analytic formulas.

A.1.3 Derived parameters

The *contact time* t_c is the time, when the distance between both particles is again equal to z_0 after their collision. By solving the equation $z(t) = 0$ for the first t different from 0, we obtain:

$$t_c = \frac{\pi}{\omega_d} \tag{A.9}$$

The *normal coefficient of restitution* ε_n is the ratio of the separation speed to the speed of approach:

$$\varepsilon_n = \left| \frac{z(t_c)}{z(0)} \right| = e^{-\zeta \omega_0 t_c} \tag{A.10}$$

This equation can be solved for the damping ratio ζ:

$$\zeta = -\frac{\ln(\varepsilon_n)}{\sqrt{\pi^2 + \ln^2(\varepsilon_n)}} \tag{A.11}$$

Substituting the damping ratio by it definition, the normal damping coefficient c_n can be written as a function of the normal coefficient of restitution ε_n:

$$c_n = -2\ln(\varepsilon_n)\sqrt{\frac{m_{\text{eff}}\, k_n}{\pi^2 + \ln^2(\varepsilon_n)}} \tag{A.12}$$

Finally, it is necessary to determine the *maximum overlap* $\Delta x_{\max}$ of the spheres during their impact. This can be done by noticing that the overlap is maximum, when the relative velocity $\dot{z}(t)$ is equal to zero, i.e. when $t = t_o$:

$$t_o = \frac{1}{\omega_d}\arctan\left(\frac{\sqrt{1-\zeta^2}}{\zeta}\right) \tag{A.13}$$

The maximum overlap is thus given by $\Delta x_{\max} = z_0 - z(t_o)$. If the damping is relatively low ($\zeta \to 0$), a simpler expression can be determined. In this case, the overlap is maximum for:

$$t_o^* = \frac{\pi}{2\omega_d} \tag{A.14}$$

And the *maximum overlap* for relatively low damping (indicated by the $*$) is given by:

$$\Delta x_{\max}^* = \frac{v_1 + v_2}{\omega_0} \tag{A.15}$$

Introducing the relative velocity $v_r = v_1 + v_2$ and supposing that both spheres have the same mass m, the more practical formula of maximum overlap is the following one:

$$\Delta x_{\max}^{**} = v_r\sqrt{\frac{m}{2k_n}} \tag{A.16}$$

A.2 Normal sphere/facet collision

The figure A.4 shows the second validation scenario consisting of a sphere colliding with a facet along the normal direction ($v_0 = 3$ m/s). This model was necessary to check that the facet element in YADE was implemented as expected.

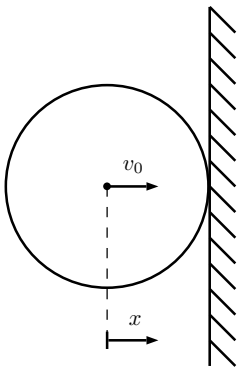

Figure A.4: Normal collision of a sphere on a facet with an initial velocity v_0.

The system of equations which describes the motion of the sphere is the following one, where m is the mass of the sphere:

$$\begin{cases} m\,\ddot{x} + c_n\,\dot{x} + k_n\,x = 0 \\ \dot{x}(0) = v_0 \\ x(0) = 0 \end{cases} \tag{A.17}$$

The analytic solution of this system is almost identical to the one in the preceding case (sphere/sphere collision). For this reasons, the definition of the natural frequency ω_0, the damping ratio ζ and the damped frequency ω_d is the same as previously, provided that m_{eff} is replaced[3] by m:

$$x(t) = \frac{v_0}{\omega_d}\, e^{-\zeta\omega_0 t}\, \sin(\omega_d t) \tag{A.18}$$

The power dissipation by normal damping is still given by the equation A.8, where $\dot{z}$ has to be replaced by $\dot{x}$.

Finally, the figures A.5 and A.6 show again that the analytic and numerical solutions are identical on the domain of validity of the analytic solution, i.e. during the contact of the sphere and the facet[4]. In conclusion, the facet element simulates the contact as expected due to the equality of the solutions.

[3]The coefficient of restitution, the contact time and the maximum overlap can also be calculated by the previous formulas, if m_{eff} is replaced by m.

[4]More precisely, the domain of validity of the analytic solution is even more restricted since the normal force is set equal to 0 in the implementation of the contact law, if it becomes attractive.

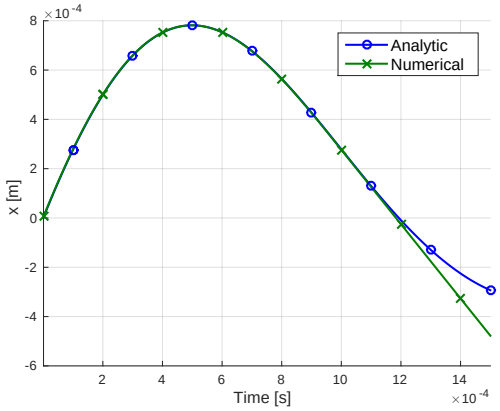

Figure A.5: Displacement x of a sphere, which normally impacts a facet, obtained by the analytic formulas and the DEM solver YADE.

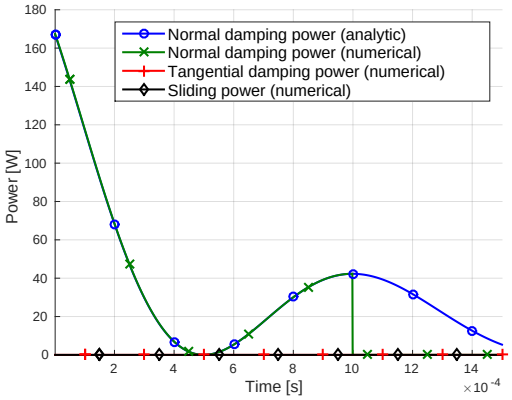

Figure A.6: Power dissipated during the normal collision of the sphere on the facet calculated by YADE, and the relevant power dissipation, which was determined by the analytic formulas.

A.3 Tangential sphere/wall collision without sliding

To validate the tangential component of the contact law analytically, it was necessary to control the interaction artificially since a *simple* analytic solution[5] can only be determined if sliding is neglected. Therefore, the friction coefficient μ was increased to 100. Simultaneously, a constant normal overlap $d_o = 1$ mm was imposed to ensure the tangential interaction, as shown in the figure A.7. Initially, the sphere moves forward with a velocity equal to $v_0 = 3$ m/s and it does not rotate.

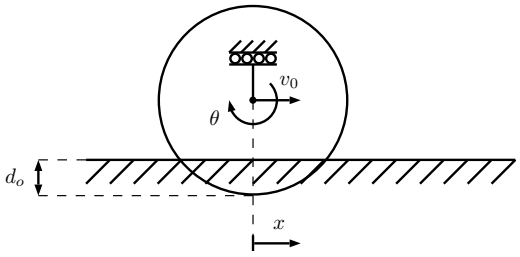

Figure A.7: Tangential collision of a sphere on a wall with an initial velocity v_0. The overlap d_o between the sphere and the wall is artificially maintained so that the tangential interaction is ensured.

The system of equations, which describes the motion of the sphere, is the following one, where m, r, $r_0 = r - d_o$ and $I = 2/5\ mr^2$ are the mass, the radius, the reduced radius and the

[5] It is obviously possible to derive an analytic solution for the combined tangential interaction with sliding but it seems not necessary to introduce this additional complexity in this validation study.

moment of inertia of the sphere:

$$\begin{cases} m\,\ddot{x} + k_t\,(x - r\theta) + c_t\,(\dot{x} - r\dot{\theta}) = 0 \\ I\,\ddot{\theta} + r\,\left(k_t\,(r\theta - x) + c_t\,(r\dot{\theta} - \dot{x})\right) = 0 \\ \dot{x}(0) = v_0 \\ x(0) = 0 \\ \dot{\theta}(0) = 0 \\ \theta(0) = 0 \end{cases} \tag{A.19}$$

The analytic solution of this system was determined by using a symbolic equation solver:

$$x(t) = m\,v_0 \left[\frac{r_0^2\,t}{I_0} + \frac{2\,I^2\,e^{-\frac{c_t\,I_0\,t}{2\,I\,m}} \sinh\left(\frac{\sqrt{I_0\,(c_t^2\,I_0 - 4\,k_t\,I\,m)}\,t}{2\,I\,m}\right)}{I^{3/2}\,\sqrt{c_t^2\,I_0 - 4\,k_t\,I\,m}} \right] \tag{A.20}$$

$$\theta(t) = m\,r_0\,v_0 \left[\frac{t}{I_0} - \frac{2\,I\,m\,e^{-\frac{c_t\,I_0\,t}{2\,I\,m}} \sinh\left(\frac{\sqrt{I_0\,(c_t^2\,I_0 - 4\,k_t\,I\,m)}\,t}{2\,I\,m}\right)}{I^{3/2}\,\sqrt{c_t^2\,I_0 - 4\,k_t\,I\,m}} \right] \tag{A.21}$$

$$\text{with} \quad I_0 = I + m\,r^2 \tag{A.22}$$

The power dissipation along the tangential direction (without sliding) is then given by the following formula (translation and rotation):

$$P_{\text{tangential}} = \dot{x}\,\left[k_n\,(x - r_0\theta) + c_n\,(\dot{x} - r_0\dot{\theta})\right] + \dot{\theta}\,r_0\,\left[k_n(r_0\theta - x) + c_n(r_0\dot{\theta} - \dot{x})\right] \tag{A.23}$$

To verify the validity of the DEM results, the wall was represented by an actual *wall element* in YADE, instead of a facet. The results in the figures A.8, A.9 and A.10 prove that the tangential contact law (without sliding) and the wall element are implemented according to our expectations.

A.4 Tangential sphere/wall collision with sliding

Since the tangential component of the contact law has been studied previously without sliding, it is necessary to analytically validate its sliding component. To reduce the complexity of the mathematical formulation, the rotation of the sphere was blocked, the tangential stiffness was increased to 10^{10} N/m and the overlap was imposed to $d_o = 1$ mm. Hence, the sphere can only slide over the wall starting with an initial velocity equal to $v_0 = 3$ m/s (figure A.11).

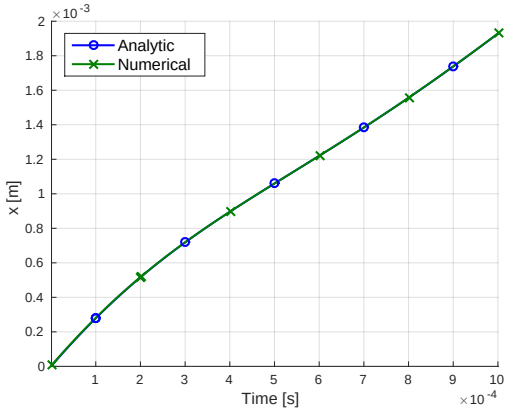

Figure A.8: Displacement x of a sphere, which tangentially collides with a wall, obtained by the analytic formulas and the DEM solver YADE (without sliding).

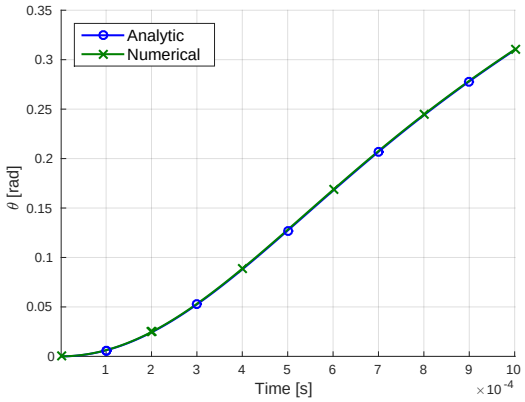

Figure A.9: Angle θ of a sphere, which tangentially collides with a wall, obtained by the analytic formulas and the DEM solver YADE (without sliding).

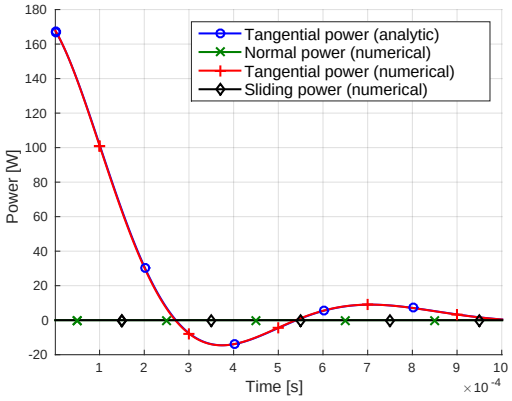

Figure A.10: Power dissipated during the tangential collision of the sphere on the wall calculated by YADE, and the relevant power dissipation, which was determined by the analytic formulas (without sliding).

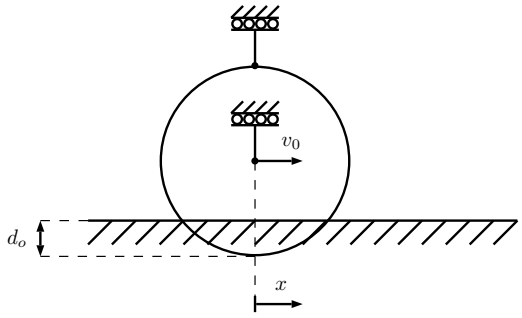

Figure A.11: Sliding collision of a sphere on a wall with an initial velocity v_0. The overlap d_o between the sphere and the wall is artificially maintained so that the tangential interaction is ensured. The rotation of the sphere is blocked.

Due to the constant overlap d_o and the blocked rotation, the tangential sliding force is equal to:

$$F_{\text{sliding}} = \mu \, k_n \, d_o \tag{A.24}$$

The displacement of the sphere is therefore the solution of the following system of equations, where m is the mass of the sphere:

$$\begin{cases} m \, \ddot{x} = F_{\text{sliding}} \\ \dot{x}(0) = v_0 \\ x(0) = 0 \end{cases} \tag{A.25}$$

The solution is easily obtained by time integration:

$$x = v_0 \, t - \frac{F_{\text{sliding}} \, t^2}{2 \, m} \tag{A.26}$$

Moreover, the power dissipated by sliding is equal to:

$$P_{\text{sliding}} = F_{\text{sliding}} \, \dot{x} \tag{A.27}$$

Determining again the displacement and the dissipated power by the analytic formulas and the DEM solver YADE, identical solutions are found on the valid domain of the analytic solution, i.e. while the sphere slides (figures A.12 and A.13).

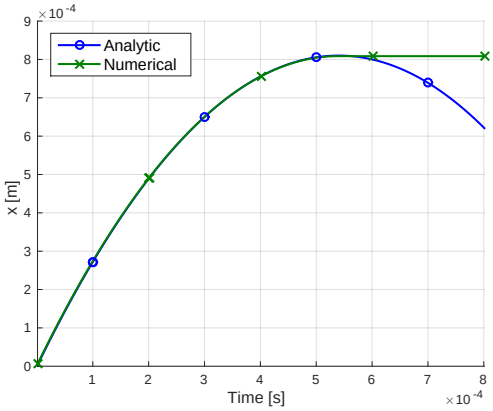

Figure A.12: Displacement x of a sphere, which slides on a facet, obtained by the analytic formulas and the DEM solver YADE.

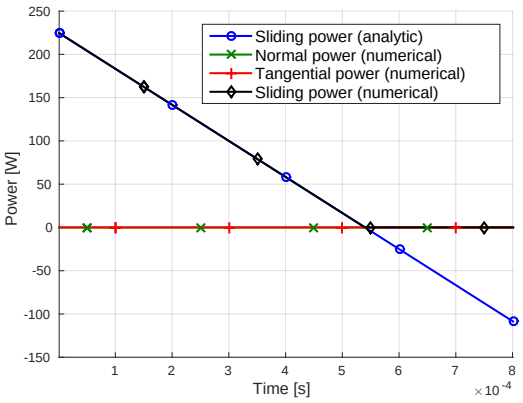

Figure A.13: Power dissipated during the sliding collision of the sphere on the wall calculated by YADE, and the relevant power dissipation, which was determined by the analytic formulas.

Appendix B

Standard Simulation Control Script of the Laboratory Mill

This chapter contains the standard PYTHON control script used to simulate the laboratory mill.

Listing B.1: Standard simulation control script of the laboratory mill - sim.py

```
################################################################################
#
# Filename:
#  sim.py
#
# Title:
#  Standard simulation control script of the laboratory ball mill
#
# Author:
#  Dominik Boemer (dominik.boemer@gmail.com)
#
# Date:
#  March 2015
#
# Description:
#  This Python script controls the simulation of the 0.8 m diameter laboratory
#  ball mill.  It is divided into the following sections:
#   - INPUT: input parameters, like the material density or the filling ratio
#   - IMPORT: import of python modules and creation of output folders
#   - MATERIAL: definition of the material
#   - MILL GEOMETRY: import of the mill geometry mesh
#   - FILLING: filling of the mill with balls
#   - SIMULATION: engines of the simulation (mill rotation, integration, ...)
#   - POST-PROCESSING: post-processing functions
#   - RUN: start of the simulation
#
# Usage:
#  dem -j nProc sim.py
#    dem is a link to the DEM solver (by default dem = yade)
#    nProc is the number of processors on which the simulation will be run
#
################################################################################
```

```
################################################################################
# INPUT
#
# This input section contains all the input parameters concerning the material,
# the geometry/filling and the simulation.  The shell liner mesh will be added
# later; its file name should be changed in the MILL GEOMETRY section.
#

# Material
rho = 7640.0 # [kg/m^3] density (of the balls)
kn  = 1.0e5  # [N/m]    equivalent normal stiffness
kt  = kn     # [N/m]    equivalent tangential stiffness
cn  = 18.6   # [Ns/m]   equivalent normal damping coefficient (equiv. en = 0.3)
ct  = cn     # [Ns/m]   equivalent tangential damping coefficient
mu  = 0.75   # [-]      friction coefficient

# Geometry/Filling
length = 0.4       # [m] axial length of the mill
rMean  = 0.772/2.0 # [m] liner profile mean radius
rBall  = 0.0075    # [m] ball radius
fRatio = 30.0      # [%] filling ratio

# Simulation
pcv   = 70.0   # [%] percentage of critical velocity
tEnd  = 5.0    # [s] total simulation time
O.dt  = 1.0e-5 # [s] fixed time step
tRec  = 1.0e-2 # [s] recording interval


################################################################################
# IMPORT
#
# In this section the Python modules necessary for reading the mesh, exporting
# the results and performing some mathematical operations are imported.  It also
# verifies that former results were deleted to ensure that they will not be
# overwritten.
#

from yade import ymport,export
import math,os

if os.path.exists('output'):
  print 'Delete old "output" directory.'
  exit()
else:
  os.makedirs('output')
  os.makedirs('output/vtk')
  os.makedirs('output/xyz')

print '\nBall Mill Simulation\n'


################################################################################
# MATERIAL
#
# In this section the material of the mill (shell liner + end walls) is defined.
# The linear spring-slider-damper contact law is used.  For this reason, the
# equivalent stiffness and damping coefficients are multiplied by 2.  In other
# words, the contact parameters of the elementary entities have to be specified;
# these parameters are internally combined by the DEM solver.
#

millMat = O.materials.append(SprSldDmpMat(knEl=2*kn,ktEl=2*kt,cnEl=2*cn,
                                          ctEl=2*ct,muEl=mu))
ballMat = O.materials.append(SprSldDmpMat(knEl=2*kn,ktEl=2*kt,cnEl=2*cn,
```

```
                                        ctEl=2*ct,muEl=mu,density=rho))
101

###############################################################################
# MILL GEOMETRY
#
106 # The mill and its end walls are added to the simulation.  The shell liner
# profile mesh is imported in the .mesh GMSH format.  The liner should be
# centered at the origine and be axially aligned with the y-axis.  It will turn
# negatively around this axis with respect to the right hand rule, i.e. looking
# in the direction of the y-axis, it turns anticlockwise. As the shell mesh was
111 # created in millimeters, a scale factor has to be applied to rescale it to
# meters.
# The end walls of the mill are modeled by infinite planes, which will be
# rotating at the same speed than the shell liner.
#
116
liner = O.bodies.append(ymport.gmsh('PerfectoABAB_dia_08_medium.mesh',
                                    material=millMat,color=(1,1,1),
                                    scale=1e-3))
walls = O.bodies.append([
121           utils.wall((0,0,0),1,material=millMat,color=(1,1,1)),
              utils.wall((0,length,0),1,material=millMat,color=(1,1,1))
            ])


126 ###############################################################################
# FILLING
#
# The number of balls is calculated on basis of the filling ratio, which gives
# the ratio of the volume occupied by the balls and their interstices (bulk
131 # density = 4580 kg/m3) with respect to the total volume of the mill (given by
# its mean diameter and its axial length).
#
# The mill will be filled by insering balls in horizontal planes which are
# progressively moving upwards until all balls have been added to the
136 # simulation.
#

vTot   = math.pi*rMean**2*length          # total volume
vBalls = vTot * fRatio * 1.0e-2           # volume of balls with interstices
141 vBall  = 4.0/3.0*math.pi*rBall**3         # volume of one ball
nBalls = int(vBalls * 4580.0/rho / vBall) # total number of balls

gap1  = 0.1*rBall # small gap to have no overlap (between balls)
gap2  = 4*rBall   # large gap to have no overlap (between liner and balls)
146
z = -rMean + rBall + gap2                      # vertical initial coordinate
x = -math.sqrt((rMean-rBall)**2 - z**2) + gap2 # horizontal initial coordinate
y = rBall + gap1                               # axial initial coordinate

151 for i in range(nBalls):
  # new axial line
  if y > length - rBall - gap1:
    y = rBall + gap1
    x = x + 2*rBall + gap1
156 # new horizontal plane
  if x > math.sqrt((rMean-rBall)**2 - z**2) - gap2:
    z = z + 2*rBall + gap1
    x = -math.sqrt((rMean-rBall)**2 - z**2) + gap2
  # append ball
161 O.bodies.append(utils.sphere(center=(x,y,z),radius=rBall,\
                                 material=ballMat,color=(1,1,1)))
  # new axial position
  y = y + 2.0*rBall + gap1
```

```
print 'Filling Ratio: '+str(fRatio)+' [%]'
print 'Number of balls: '+str(nBalls)+' [-]'


################################################################################
# SIMULATION
#
# First, the rotation speed of the mill is calculated on basis of the percentage
# of critical velocity and the mean diameter of the mill.  Then, the engines
# of the simulation are defined.  The linear spring-slider-damper contact law
# was chosen.
#
# The simulation will successively call the following engines:
#  - ForceResetter
#      The forces, torques and some energies are reset as they will be
#      calculated during the new simulation loop.
#
#  - InsertionSortCollider
#      The collisions between spheres and facets and spheres and walls are
#      detected by the insertion sort algorithm based on the axis aligned
#      bounding boxes of the different elements.
#
#  - InteractionLoop
#      The interactions loop first calculates the geometrical interaction
#      characteristics, like the overlapping of spheres.  Then, it determines
#      the interaction parameters, like the equivalent spring stiffness.
#      Finally, the forces, torques and energies of the interaction are
#      calculated by the contact law.
#
#  - NewtonIntegrator
#      The forces and torques are integrated by taking gravity into account.
#
#  - RotationEngine
#      The mesh of the shell liner and the end walls are rotated at constant
#      angular velocity about the y-axis.
#
#  - VTKRecoder and PyRunner
#      These engines are used to save the data for the post-processing at a
#      constant sampling period "tRec":
#        - center coordinates and radii of the spheres in VTK format (ParaView)
#        - center coordinates of the spheres in text format
#        - power draw of the mill
#

omegact = math.sqrt(9.81/rMean) # [rad/s] critical angular speed
omega   = pcv*1e-2*omegact      # [rad/s] angular speed
rpm     = omega*30/math.pi      # [rpm]   rotation speed

print 'Percentage of critical velocity: '+str(pcv)+' [%]'
print 'Rotation speed: '+str(rpm)+' [RPM]'

O.engines=[
  ForceResetter(),

  InsertionSortCollider([Bo1_Sphere_Aabb(),Bo1_Facet_Aabb(),Bo1_Wall_Aabb()]),

  InteractionLoop(
    [Ig2_Sphere_Sphere_ScGeom(),
     Ig2_Facet_Sphere_ScGeom(),
     Ig2_Wall_Sphere_ScGeom()],
    [Ip2_SprSldDmpMat_SprSldDmpMat_SprSldDmpPhys()],
    [Law2_ScGeom_SprSldDmpPhys_Basic()]
  ),
```

```
    NewtonIntegrator(damping=0,gravity=[0,0,-9.81]),

    RotationEngine(ids=liner,rotationAxis=[0,-1,0],rotateAroundZero=True,
                   angularVelocity=omega),
    RotationEngine(ids=walls,rotationAxis=[0,-1,0],rotateAroundZero=True,
                   angularVelocity=omega),

    VTKRecorder(fileName=os.getcwd()+'/output/vtk/',
                recorders=['spheres','facets','velocity'],
                iterPeriod=int(math.ceil(tRec/O.dt))),

    PyRunner(command='saveSphereXYZ()',iterPeriod=int(math.ceil(tRec/O.dt))),
    PyRunner(command='savePower()',iterPeriod=int(math.ceil(tRec/O.dt)))
]


################################################################################
# POST-PROCESSING
#
# In this section, the functions called by the PyRunner in the simulation loop
# are defined.  These functions calculate and save some data used for the post-
# processing.
#

# Save the position of the center of each sphere.
def saveSphereXYZ():
  out=open(os.getcwd()+'/output/xyz/'+str(O.iter/int(math.ceil(tRec/O.dt))),'w')
  output = ''
  for b in O.bodies:
    if isinstance(b.shape,Sphere):
      output+=('%g %g %g\n' \
               %(b.state.pos[0],b.state.pos[1],b.state.pos[2]))
  out.write(output)
  out.close()


# Calculate the power needed to rotate the mill and retrieve the power
# dissipated along the normal and tangential direction as well as the sliding
# dissipation
# Save this data.
def savePower():
  # Mechanical power
  power = 0;
  for i in O.interactions:
    f = Vector3(0,0,0)

    # Force by sphere on facet
    if isinstance(O.bodies[i.id1].shape,Sphere) \
        and isinstance(O.bodies[i.id2].shape,Facet):
      f = O.interactions[i.id1,i.id2].phys.normalForce \
          + O.interactions[i.id1,i.id2].phys.tangentialForce

    # Force by facet on sphere
    if isinstance(O.bodies[i.id1].shape,Facet) \
        and isinstance(O.bodies[i.id2].shape,Sphere):
      f = -O.interactions[i.id1,i.id2].phys.normalForce \
          - O.interactions[i.id1,i.id2].phys.tangentialForce

    # Force by sphere on wall
    if isinstance(O.bodies[i.id1].shape,Sphere) \
        and isinstance(O.bodies[i.id2].shape,Wall):
      f = O.interactions[i.id1,i.id2].phys.normalForce \
          + O.interactions[i.id1,i.id2].phys.tangentialForce

    # Force by wall on sphere
```

```
    if isinstance(O.bodies[i.id1].shape,Wall) \
        and isinstance(O.bodies[i.id2].shape,Sphere):
      f = -O.interactions[i.id1,i.id2].phys.normalForce \
          - O.interactions[i.id1,i.id2].phys.tangentialForce

    cp = i.geom.contactPoint

    # Power = rotation speed * torque arm x force
    power = power + Vector3(0,omega,0).dot(cp.cross(f))

  out=open(os.getcwd()+'/output/rotationPower','a')
  out.write('%g\n'%(power))
  out.close()

  # Power dissipation in the normal direction
  try:
    normalPower = O.energy['normalPower']
  except:
    normalPower = 0.0

  out=open(os.getcwd()+'/output/normalPower','a')
  out.write('%g\n'%(normalPower))
  out.close()

  # Power dissipation in the tangential direction (without sliding)
  try:
    tangentialPower = O.energy['tangentialPower']
  except:
    tangentialPower = 0.0

  out=open(os.getcwd()+'/output/tangentialPower','a')
  out.write('%g\n'%(tangentialPower))
  out.close()

  # Power dissipation due to sliding
  try:
    slidingPower = O.energy['slidingPower']
  except:
    slidingPower = 0.0

  out=open(os.getcwd()+'/output/slidingPower','a')
  out.write('%g\n'%(slidingPower))
  out.close()


################################################################################
# RUN
#
# The command in this section simply starts the simulation after indicating that
# the energy should be tracked; this is necessary to calculate the dissipated
# power.
#

O.trackEnergy = True
O.run(int(math.ceil(tEnd/O.dt))+1)
```

Appendix C

Linear Spring-Slider-Damper Contact Law Source Code Files

This chapter contains the source code of the *linear spring-slider-damper contact law* added to the YADE DEM solver in the folder `pkg/dem`.

Listing C.1: Spring-slider-damper contact law - SprSldDmpPM.hpp

```
// 2009 (c) Sergei Dorofeenko <sega@users.berlios.de> (ViscoElasticPM)
// 2015 (c) Dominik Boemer <dominik.boemer@gmail.com>

/*****************************************/
/* Linear spring-slider-damper contact law */
/*****************************************/

#pragma once

#include<core/Material.hpp>
#include<core/IPhys.hpp>
#include<pkg/common/Dispatching.hpp>
#include<pkg/dem/ScGeom.hpp>

/* Material */
class SprSldDmpMat : public Material
{
  public:
    virtual ~SprSldDmpMat();

    YADE_CLASS_BASE_DOC_ATTRS_CTOR(SprSldDmpMat,Material,
      "Material for the linear spring-slider-damper contact law.",
      ((Real,knEl,0.0,,"Elementary normal stiffness."))
      ((Real,cnEl,0.0,,"Elementary normal damping coefficient."))
      ((Real,ktEl,0.0,,"Elementary tangential stiffness."))
      ((Real,ctEl,0.0,,"Elementary tangential damping coefficient."))
      ((Real,muEl,0.0,,"Friction coefficient")),
      createIndex(););

    REGISTER_CLASS_INDEX(SprSldDmpMat,Material);
};
REGISTER_SERIALIZABLE(SprSldDmpMat);
```

```
34
   /* Interaction parameters */
   class SprSldDmpPhys : public IPhys
   {
     public:
39     virtual ~SprSldDmpPhys();

       YADE_CLASS_BASE_DOC_ATTRS_CTOR(SprSldDmpPhys,IPhys,"IPhys created from "
           ":yref:`SprSldDmpMat`, for use with "
           ":yref:`Law2_ScGeom_SprSldDmpPhys_Basic`.",
44       ((Real,kn,0.0,,"Equivalent normal stiffness."))
         ((Real,cn,0.0,,"Equivalent normal damping constant."))
         ((Real,kt,0.0,,"Equivalent tangential stiffness."))
         ((Real,ct,0.0,,"Equivalent tangential damping constant."))
         ((Real,mu,0.0,,"Friction coefficient."))
49       ((Vector3r,normalForce,Vector3r::Zero(),,
           "Normal force after previous step (in global coordinates)."))
         ((Vector3r,tangentialForce,Vector3r::Zero(),,
           "Tangential force after previous step (in global coordinates)."))
         ((Vector3r,tangentialSpringForce,Vector3r::Zero(),,
54         "Tangential spring force after previous step (in global coordinates). "
           "This variables stores the history of the tangential spring.")),
         createIndex(););

       REGISTER_CLASS_INDEX(SprSldDmpPhys,IPhys);
59 };
   REGISTER_SERIALIZABLE(SprSldDmpPhys);


   /* Extract the interaction parameters */
64 class Ip2_SprSldDmpMat_SprSldDmpMat_SprSldDmpPhys: public IPhysFunctor
   {
     public :
       virtual void go(const shared_ptr<Material>& m1,
       const shared_ptr<Material>& m2,
69     const shared_ptr<Interaction>& interaction);
       YADE_CLASS_BASE_DOC(Ip2_SprSldDmpMat_SprSldDmpMat_SprSldDmpPhys,
         IPhysFunctor, "Convert 2 instances of :yref:`SprSldDmpMat` to "
          ":yref:`SprSldDmpPhys` using the rule of consecutive connection.");

74     virtual void calculate_SprSldDmpMat_SprSldDmpMat_SprSldDmpPhys(
         const shared_ptr<Material>& m1, const shared_ptr<Material>& m2,
         const shared_ptr<Interaction>& interaction,
         shared_ptr<SprSldDmpPhys> phys);

79     FUNCTOR2D(SprSldDmpMat,SprSldDmpMat);
   };
   REGISTER_SERIALIZABLE(Ip2_SprSldDmpMat_SprSldDmpMat_SprSldDmpPhys);


84 /* Constitutive law - spring-slider-damper contact law */
   class Law2_ScGeom_SprSldDmpPhys_Basic: public LawFunctor
   {
     public :
       virtual bool go(shared_ptr<IGeom>&, shared_ptr<IPhys>&, Interaction*);
89
       YADE_CLASS_BASE_DOC_ATTRS(Law2_ScGeom_SprSldDmpPhys_Basic,LawFunctor,
         "Linear spring-slider-damper contact law operating on :yref:`ScGeom` and "
           ":yref:`SprSldDmpPhys`.",
         ((int,normalPowerIx,-1,(Attr::hidden|Attr::noSave),
94         "Index for normal damping power (with O.trackEnergy)"))
         ((int,tangentialPowerIx,-1,(Attr::hidden|Attr::noSave),
           "Index for tangential damping power (with O.trackEnergy)"))
         ((int,slidingPowerIx,-1,(Attr::hidden|Attr::noSave),
```

```
            "Index for shear power (with O.trackEnergy)")));
99
        FUNCTOR2D(ScGeom,SprSldDmpPhys);
        DECLARE_LOGGER;
    };
    REGISTER_SERIALIZABLE(Law2_ScGeom_SprSldDmpPhys_Basic);
104

    /* Contact force, torque, dissiapated power and wear calculation */
    bool computeSprSldDmp(shared_ptr<IGeom>& _geom,
      shared_ptr<IPhys>& _phys, Interaction* I, Vector3r & force,
109   Vector3r & torque1, Vector3r & torque2, Real & normalPower,
      Real & tangentialPower, Real & slidingPower);


    /* Equivalent contact parameter calculation (series) */
114 Real equivalentParameter(const Real& l1, const Real& l2);
```

Listing C.2: Spring-slider-damper contact law - SprSldDmpPM.cpp

```
// 2009 (c) Sergei Dorofeenko <sega@users.berlios.de> (ViscoElasticPM)
// 2015 (c) Dominik Boemer <dominik.boemer@gmail.com>

#include"SprSldDmpPM.hpp"
#include<core/State.hpp>
#include<core/Omega.hpp>
#include<core/Scene.hpp>
#include<pkg/common/Sphere.hpp>
#include<pkg/common/Facet.hpp>
#include<pkg/dem/ScGeom.hpp>

YADE_PLUGIN((SprSldDmpMat)
            (SprSldDmpPhys)
            (Ip2_SprSldDmpMat_SprSldDmpMat_SprSldDmpPhys)
            (Law2_ScGeom_SprSldDmpPhys_Basic));


/* SprSldDmpMat */
SprSldDmpMat::~SprSldDmpMat(){}


/* SprSldDmpPhys */
SprSldDmpPhys::~SprSldDmpPhys(){}


/* Ip2_SprSldDmpMat_SprSldDmpMat_SprSldDmpPhys */
void Ip2_SprSldDmpMat_SprSldDmpMat_SprSldDmpPhys::go(
  const shared_ptr<Material>& m1, const shared_ptr<Material>& m2,
  const shared_ptr<Interaction>& interaction)
{
  // no updates of an existing contact
  if(interaction->phys) return;
  shared_ptr<SprSldDmpPhys> phys (new SprSldDmpPhys());
  calculate_SprSldDmpMat_SprSldDmpMat_SprSldDmpPhys(m1, m2, interaction, phys);
  interaction->phys = phys;
}


/* Law2_ScGeom_SprSldDmpPhys_Basic */
bool Law2_ScGeom_SprSldDmpPhys_Basic::go(shared_ptr<IGeom>& _geom,
  shared_ptr<IPhys>& _phys, Interaction* I)
{
  // force and torque
  Vector3r force   = Vector3r::Zero();
  Vector3r torque1 = Vector3r::Zero();
  Vector3r torque2 = Vector3r::Zero();

  // energy
  Real normalPower     = 0.0;
  Real tangentialPower = 0.0;
  Real slidingPower    = 0.0;

  if (computeSprSldDmp(_geom, _phys, I, force, torque1, torque2,
       normalPower, tangentialPower, slidingPower)
       and (I->isActive))
  {
    const int id1 = I->getId1();
    const int id2 = I->getId2();

    addForce (id1,-force,   scene);
    addForce (id2, force,   scene);
    addTorque(id1, torque1, scene);
    addTorque(id2, torque2, scene);
```

```
65      // energy tracking
        if (scene->trackEnergy)
        {
          scene->energy->add(normalPower, "normalPower",
                             normalPowerIx, true);
70        scene->energy->add(tangentialPower, "tangentialPower",
                             tangentialPowerIx, true);
          scene->energy->add(slidingPower, "slidingPower",
                             slidingPowerIx, true);
        }
75
        return true;
      } else return false;
    }

80
    /* Contact force, torque, dissiapated power and wear calculation */
    bool computeSprSldDmp(shared_ptr<IGeom>& _geom,
      shared_ptr<IPhys>& _phys, Interaction* I, Vector3r & force,
      Vector3r & torque1, Vector3r & torque2, Real & normalPower,
85    Real & tangentialPower, Real & slidingPower)
    {
      SprSldDmpPhys& phys=*static_cast<SprSldDmpPhys*>(_phys.get());
      const ScGeom& geom=*static_cast<ScGeom*>(_geom.get());
      Scene* scene=Omega::instance().getScene().get();
90
      if (geom.penetrationDepth<0)
        return false;
      else
      {
95      // get bodies
        const int id1 = I->getId1();
        const int id2 = I->getId2();
        const BodyContainer& bodies = *scene->bodies;
        State& de1 = *static_cast<State*>(bodies[id1]->state.get());
100     State& de2 = *static_cast<State*>(bodies[id2]->state.get());

        // get time step
        const Real& dt = scene->dt;

105     // handle periodicity
        const Vector3r shift2 = scene->isPeriodic ?
        scene->cell->intrShiftPos(I->cellDist): Vector3r::Zero();
        const Vector3r shiftVel = scene->isPeriodic ?
        scene->cell->intrShiftVel(I->cellDist): Vector3r::Zero();
110
        // calculate relative velocity and its components (normal/tangential)
        const Vector3r c1x = (geom.contactPoint - de1.pos);
        const Vector3r c2x = (geom.contactPoint - de2.pos - shift2);

115     const Vector3r relativeVelocity = (de1.vel+de1.angVel.cross(c1x))
                                        - (de2.vel+de2.angVel.cross(c2x)) + shiftVel;
        const Real     normalVelocity     = geom.normal.dot(relativeVelocity);
        const Vector3r tangentialVelocity = relativeVelocity
                                                  - normalVelocity*geom.normal;
120

        /**********/
        /* Forces */
        /**********/
125
        // calculate normal force
        const Real normalForceScalar = phys.kn * geom.penetrationDepth
                                     + phys.cn * normalVelocity;
```

```
130       // prevent attraction due to normal damper
          if (normalForceScalar < 0)
            phys.normalForce = Vector3r::Zero();
          else
            phys.normalForce = normalForceScalar * geom.normal;
135
          // get tangential spring force history and account for the rotation
          Vector3r& tangentialSpringForce = phys.tangentialSpringForce;
          if (I->isFresh(scene)) tangentialSpringForce=Vector3r(0,0,0);
          tangentialSpringForce = geom.rotate(tangentialSpringForce);
140
          // calculate tangential forces
          tangentialSpringForce += phys.kt*tangentialVelocity*dt;
          Vector3r tangentialDamperForce = phys.ct*tangentialVelocity;
          Vector3r& tangentialForce = phys.tangentialForce;
145       tangentialForce = tangentialSpringForce + tangentialDamperForce;

          // check for Coulomb sliding
          const Real limitFt = phys.normalForce.squaredNorm() * phys.mu * phys.mu;
          bool sliding = tangentialForce.squaredNorm() > limitFt;
150       if (sliding)
          {
            /* It is necessary to calculate the following ratio in order to obtain a
             * tangential sliding force which is aligned with the tangential force
             * just before the sliding.  The spring component of the tangential force
155          * also has to be reduced due to the sliding.  In fact, this component
             * will be used at the next time step since the spring stores energy
             * (history).  Thus, it is necessary to update its value.
             */
            const Real ratio = sqrt(limitFt) / tangentialForce.norm();
160         tangentialForce *= ratio;
            tangentialSpringForce *= ratio;
          }

          // force result
165       force   =  phys.normalForce + tangentialForce;
          torque1 = -c1x.cross(force);
          torque2 =  c2x.cross(force);


170       /**********/
          /* Energy */
          /**********/

          if (scene->trackEnergy)
175       {
            // normal dissipation power
            if (normalForceScalar < 0)
              normalPower = 0;
            else
180           normalPower = phys.cn * normalVelocity * normalVelocity;

            /* Since the time step is very small, it is reasonable to suppose that
             * the energy dissipation in the tangential direction occurs either
             * exclusively by sliding or (exclusively) by tangential damping.
185          *
             * It is important to notice that the tangential force is in the
             * tangential plane even though it is the accumulated history of the
             * spring force.  The rotation of the accumulated tangential spring force
             * actually makes sure that this requirement is satisfied.  The dot
190          * product of the tangential force and the tangential velocity is,
             * however, necessary as they are not naturally aligned due to the spring
             * history.
             */
```

```
195       // sliding dissipation power (tangential direction)
          if (sliding)
            slidingPower = tangentialForce.dot(tangentialVelocity);

          // tangential damping dissipation power
200       else
            tangentialPower = tangentialForce.dot(tangentialVelocity);
        }


205     /********/
        /* Wear */
        /********/

        /* Wear will only be accumulated if:
210      *  - wear should actually be recorded;
         *  - a certain moment in time has been reached (pseudo steady state);
         *  - a sphere collides with a facet.
         */
        if (scene->trackWear
215         && scene->time > scene->recordingStartTime
            && (dynamic_cast<Facet*>(bodies[id1]->shape.get())
                || dynamic_cast<Facet*>(bodies[id2]->shape.get())))
        {
          // Get area and state of the facet
220       const int id = dynamic_cast<Facet*>(bodies[id1]->shape.get()) ? id1 : id2;
          const Facet& facet = *dynamic_cast<Facet*>(bodies[id]->shape.get());
          const Real area = facet.area;
          State& facetState = *static_cast<State*>(bodies[id]->state.get());

225       //== Energy dissipated by normal damping
          if (normalForceScalar > 0)
            facetState.energyNormalDamping +=
                              phys.cn * normalVelocity * normalVelocity * dt / area;

230       //== Energy dissipated by sliding
          if (sliding)
            facetState.energySliding +=
                                tangentialForce.dot(tangentialVelocity) * dt / area;

235       //== Energy dissipated by tangential damping
          else
            facetState.energyTangentialDamping +=
                            tangentialDamperForce.dot(tangentialVelocity) * dt / area;

240       //== Wear by the Archard equation
          facetState.archardWear +=
                     phys.normalForce.norm() * tangentialVelocity.norm() * dt / area;

          //== Wear by Finnie's law
245       if (I->isFresh(scene))
          {
            // facets do not have any mass; thus, the mass of the sphere is selected
            Real mass = de1.mass == 0.0 ? de2.mass : de1.mass;

250         // sine of the angle between the facet surface and the impact velocity
            Real sinAlpha = fabs(geom.normal.dot(relativeVelocity)
                                                          /relativeVelocity.norm());

            // cosine of the angle between the facet surface and the impact velocity
255         Real cosAlpha = sqrt(1.0 - sinAlpha*sinAlpha);

            // angular dependence
            Real f = 0.0;
```

```
          if (sinAlpha/cosAlpha > 1.0/3.0)
            f = 1.0/3.0 * cosAlpha * cosAlpha;
          else
            f = 2.0 * sinAlpha * cosAlpha - 3.0 * sinAlpha * sinAlpha;

          facetState.finnieWear +=
                                f * mass * relativeVelocity.squaredNorm() / area;
        }

        //== Excess kinetic energy wear
        if (I->isFresh(scene) && normalVelocity > 0.1)
        {
          Real mass = de1.mass == 0.0 ? de2.mass : de1.mass;
          facetState.excessKineticEnergy +=
                                  mass * normalVelocity * normalVelocity / area;
        }

      }
      return true;
    }
  }

  /* Convert material to interaction physics */
  void Ip2_SprSldDmpMat_SprSldDmpMat_SprSldDmpPhys::
    calculate_SprSldDmpMat_SprSldDmpMat_SprSldDmpPhys(
      const shared_ptr<Material>& m1, const shared_ptr<Material>& m2,
      const shared_ptr<Interaction>& interaction,
      shared_ptr<SprSldDmpPhys> phys)
  {
    SprSldDmpMat* mat1 = static_cast<SprSldDmpMat*>(m1.get());
    SprSldDmpMat* mat2 = static_cast<SprSldDmpMat*>(m2.get());

    // elementary parameters
    Real kn1 = mat1->knEl;
    Real kn2 = mat2->knEl;
    Real kt1 = mat1->ktEl;
    Real kt2 = mat2->ktEl;
    Real cn1 = mat1->cnEl;
    Real cn2 = mat2->cnEl;
    Real ct1 = mat1->ctEl;
    Real ct2 = mat2->ctEl;

    // equivalent parameters (serie)
    phys->kn = equivalentParameter(kn1,kn2);
    phys->kt = equivalentParameter(kt1,kt2);
    phys->cn = equivalentParameter(cn1,cn2);
    phys->ct = equivalentParameter(ct1,ct2);

    phys->mu = std::min(mat1->muEl, mat2->muEl);
  }

  /* Equivalent contact parameter calculation (series) */
  Real equivalentParameter(const Real& l1, const Real& l2)
  {
    if (l1>0 && l2>0) return l1*l2/(l1 + l2);
    else return 0;
  }
```

Appendix D

Wear Profile Measurements

The tables D.1 and D.2 contain the wear profile measurements used in the chapter 3 to calibrate and validate the wear model.

	0 h	2383 h	7060 h (max)	7060 h (min)	12120 h	16680 h (max)	16680 h (min)	23669 h (max)	23669 h (min)
-240	108	99	95.5	92.5	89.5	84	84	83.5	77
-220	104.5	96.5	90.5	88	82	76	76	75.5	69
-200	92.5	84	77	76	71	67	67	67	63
-180	77	71.5	67.5	68.5	65	62.5	62.5	62.5	60
-160	74	68.5	65.5	67	65	61.5	61.5	62.5	61
-140	78	71	69.5	71	69	65	65	67.5	65
-120	85	79	77.5	78.5	76	75	75	74.5	73
-100	97	90.5	89	88.5	87	89	89	88.5	84.5
-80	112	106.5	105	104.5	101	103	103	103.5	97
-60	125	120	117	116.5	112	110	108	115	106
-40	133.5	128.5	126	123.5	118	120.5	113	120	110.5
-20	138	132.5	129.5	126.5	121	124	115.5	121	111.5
0	139	134	130	127	121	123.5	115	121	111
20	138	133	129	124.5	119	122	114	119	105.5
40	133.5	128.5	124	119.5	114	107	106	106.5	92
60	125	119.5	115	108.5	101	91	91	89.5	79
80	113.5	106.5	98.5	94.5	86.5	78	78	75	68.5
100	99	91.5	84	81	75	68	68	65.5	60
120	87	78.5	73	71.5	67.5	61	61	60	55.5
140	78	70.5	66	66	63	59	59	59	55
160	74	67.5	64.5	64.5	63	60.5	60.5	61	58
180	76.5	71	69	69	68	67	67	68	65
200	92	84	81.5	80.5	80	79	79	80	73.5
220	102.5	96	92	89	86	83	83	86	76.5
240	106	99	96	91	87	85	85	85	76

Table D.1: Wear profile measurements of the liner plate (from 0 h to 23669 h) used in the chapter 3 to calibrate and validate the wear model. The first column gives the position along the x-axis (in mm), while the other columns give the respective position along the z-axis over time (in mm). The system of coordinates is defined in the figure 3.1.

	28668 h (max)	28668 h (min)	33034 h (max)	33034 h (min)	37020 h (max)	37020 h (min)	41541 h (max)	41541 h (min)	48437 h (min)
-240	74	63	66.5	60	64	51	63	51	36
-220	67	57.5	61.5	54.5	61.5	48	59	48	33.5
-200	61	53	58	52	58	46	56	46	33.5
-180	58.5	51.5	56	52	56.5	47	56	47	37.5
-160	60	53.5	58	55	58.5	49.5	58.5	50.5	43
-140	65.5	58	64	60.5	64.5	55	65	56.5	50
-120	75	66.5	73	69	75	63	75	65	58
-100	89	77	84	80.5	89	74.5	87	76	67
-80	104	88.5	98	91.5	102	85	99	85	74
-60	114	95	107	96	108	91	106	90	76
-40	117	98.5	109.5	98.5	110	94	106	92	69
-20	118	99.5	108	99	107	92.5	100	87	59
0	116	99	101.5	92	99.5	85	91	76.5	48
20	107.5	90	90.5	80	88.5	73.5	81	64.5	37.5
40	96.5	77	78	67.5	77	62	71	54	29
60	83.5	65.5	66	56.5	67	52	62.5	46.5	23.5
80	71.5	56	57	49	59	45	56	40	22
100	63	50	52.5	44.5	55	41	52	37	22
120	58.5	47	51	43.5	53.5	40	52	37	23
140	58	47	52	45.5	55.5	41	55	40	26
160	61.5	51	58	50	59.5	46	59	45	30
180	70	58	68	57	68	52	67	49.5	32
200	82.5	64	75	62	72.5	55.5	70.5	53	33.5
220	82	65	74	62	70.5	55.5	70	52.5	35
240	77	63.5	68.5	61.5	65	52.5	65	51	35

Table D.2: Wear profile measurements of the liner plate (from 28668 h to 48437 h) used in the chapter 3 to calibrate and validate the wear model. The first column gives the position along the x-axis (in mm), while the other columns give the respective position along the z-axis over time (in mm). The system of coordinates is defined in the figure 3.1.

Appendix E

Project Data Files

In order to keep the project data files for future projects, they were meticulously *archived*. Without taking into consideration the numerous scripts and output files during the testing phase, the simulation data amounts for about 540,000 files taking up around 580 GB of memory space. After removing the output data of the DEM simulations, around 1200 manually created files, like simulation, pre- and post-processing scripts remain, in addition to the 876 source files of the DEM solver YADE. This data and the document, which you are about to read, were saved on a CD distributed with this document. The directory tree of the CD is shown in the figure E.1. In the following lines, we will briefly explain how the content of the CD relates to this document.

Simulation data

The folder `SimulationData` contains:

- the PYTHON (Python 2.7.6 and IPython 1.2.1) control scripts of the DEM simulations;
- the MATLAB (R2014b) pre- and post-processing scripts;
- the FREECAD (0.14) and CATIA (V5R20) CAD files of the geometries;
- the GMSH (2.8.3) meshes;
- the PDF figures of this document.

These files are chronologically sorted by creating a folder for each major objective, like benchmarking YADE and LIGGGHTS or studying the influence of the number of processors used to run the simulation. Each folder contains in general two additional folders, which are called `input` and `output`, as well as some pre- and post-processing scripts. One of the post-processing scripts usually has a similar name to the folder in which it is saved, like `nbrProcessors.m` in the folder `2_NbrProcessors`. This script is the master script, which uses the other scripts

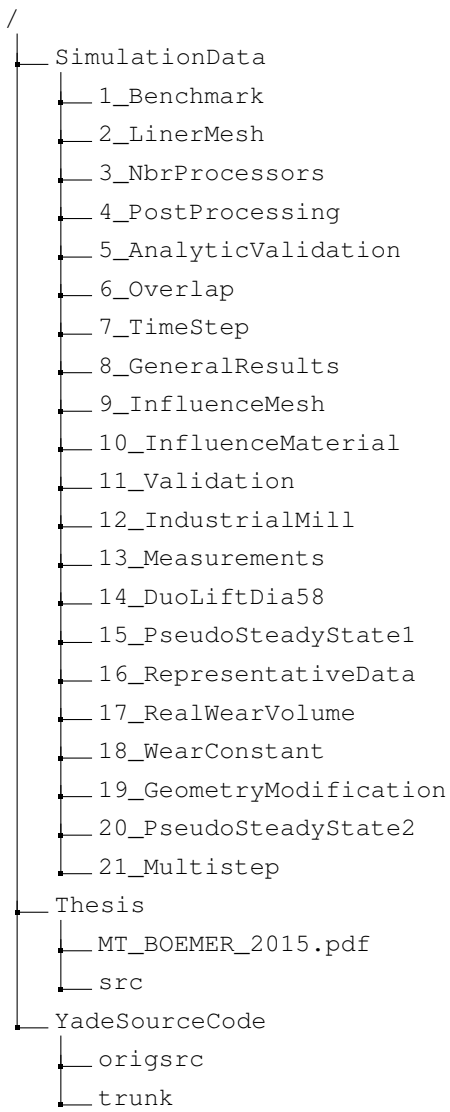

Figure E.1: Directory tree of the CD.

to create the results necessary to achieve the objective of the folder. The results are created on the basis of the input data in the `input` folder and saved in the `output` folder.

In the following list, we will summarize the major objective of each folder and indicate the related section of this document:

- `1_Benchmark` (section 2.2): comparison of the performance of LIGGGHTS and YADE;
- `2_LinerMesh` (section 2.3.2): creation of the mesh of the liner in the laboratory mill;
- `3_NbrProcessors` (section 2.3.3): influence of the number of processors on the computation time;
- `4_PostProcessing` (section 2.3.4): general explanation of the post-processing techniques, e.g. position density limits and power draw predictions;
- `5_AnalyticValidation` (section 2.4.1): analytic validation of the new spring-slider-damper contact law in YADE;
- `6_Overlap` (section 2.4.1): overlap of the discrete elements as a function of the contact parameters;
- `7_TimeStep` (section 2.4.1): determination of the time step;
- `8_GeneralResults` (section 2.4.2): general results of the simulation of the laboratory mill, like the pseudo steady state or the power draw;
- `9_InfluenceMesh` (section 2.4.2): influence of the mesh refinement on the charge motion and the power draw;
- `10_InfluenceMaterial` (section 2.4.2): influence of the material contact parameters on the charge motion and the power draw;
- `11_Validation` (section 2.4.2): validation of the predicted charge motion and power draw of the laboratory mill based on experimental data;
- `12_IndustrialMill` (section 2.4.3): extension of the results of the laboratory mill to the industrial mill;
- `13_Measurements` (section 3.1): illustration of the measurements of the real wear profiles;
- `14_DuoLiftDia58` (section 3.2.2): creation of the meshes of the Duolift liner in the 5.8 m diameter mill;
- `15_PseudoSteadyState1` (section 3.3.1): number of rotations necessary to reach the first pseudo steady state;

- `16_RepresentativeData` (section 3.3.2): accumulation of representative wear data by the simulation;
- `17_RealWearVolume` (section 3.3.3): extraction of the real wear volume from the measured wear profiles;
- `18_WearConstant` (section 3.3.4): determination of the best fitting wear model and the corresponding wear constant from the correlation of the real and predicted wear rates;
- `19_GeometryModification` (section 3.3.5): modification of the geometry due to wear;
- `20_PseudoSteadyState2` (section 3.3.6): number of rotations necessary to reach the second pseudo steady state;
- `21_Multistep` (section 3.3.7): modeling the entire liner wear evolution by a multi-step procedure and comparison of the predicted results with the real wear profiles.

Thesis

The folder `Thesis` contains the PDF version of this document as well as its LaTeX source code files in the folder `src`.

YADE source code

The folder `YadeSourceCode` contains the original and the modified source code of the DEM solver YADE in the folders `origsrc` and `trunk`, respectively. The guidelines of the installation are provided by the `INSTALL` file in these folders.

Bibliography

[Archard, 1953] Archard, J. F. (1953). **Contact and rubbing of flat surfaces**. *Journal of Applied Sciences*, 24(8), 981 – 988, doi:10.1063/1.1721448. http://dx.doi.org/10.1063/1.1721448.

[Archard, 1980] Archard, J. F. (1980). **Wear theory and mechanisms**. In M. B. Peterson & W. W.O. (Eds.), **Wear control handbook** (pp. 35 – 80). New York: ASME.

[Arekar, 2004] Arekar, C. (2004). **Real time analysis with development, simulation and validation of discrete element method models for tumbling mill charge motion and liner wear**. Master's thesis, McGill University, Canada.

[Bićanić, 2005] Bićanić, N. (2005). **Chapter 9 - Discrete element methods**. In O. C. Zienkiewicz & R. L. Taylor (Eds.), **The Finite Element Method for Solid and Structural Mechanics** (pp. 245–277). Oxford: Butterworth-Heinemann, sixth edition.

[Chandramohan & Powell, 2005] Chandramohan, R. & Powell, M. S. (2005). **Measurement of particle interaction properties for incorporation in the discrete element method simulation**. *Minerals Engineering*, 18(12), 1142 – 1151, doi:10.1016/j.mineng.2005.06.004. http://www.sciencedirect.com/science/article/pii/S0892687505001780.

[Cleary, 1998] Cleary, P. W. (1998). **Predicting charge motion, power draw, segregation and wear in ball mills using discrete element methods**. *Minerals Engineering*, 11(11), 1061 – 1080, doi:10.1016/S0892-6875(98)00093-4. http://www.sciencedirect.com/science/article/pii/S0892687598000934.

[Cleary, 2001a] Cleary, P. W. (2001a). **Charge behaviour and power consumption in ball mills: sensitivity to mill operating conditions, liner geometry and charge composition**. *International Journal of Mineral Processing*, 63(2), 79 – 114, doi:10.1016/S0301-7516(01)00037-0. http://www.sciencedirect.com/science/article/pii/S0301751601000370.

[Cleary, 2001b] Cleary, P. W. (2001b). **Modelling comminution devices using DEM**. *International Journal for Numerical and Analytical Method in Geomechanics*, 25(1), 83–105.

[Cleary, 2001c] Cleary, P. W. (2001c). **Recent advances in DEM modelling of tumbling mills**. *Minerals Engineering*, 14(10), 1295 – 1319, doi:10.1016/S0892-6875(01)00145-5. http://www.sciencedirect.com/science/article/pii/S0892687501001455.

[Cleary, 2009] Cleary, P. W. (2009). **Ball motion, axial segregation and power consumption in a full scale two chamber cement mill**. *International Journal of Minerals Engineering*, 22, 809 – 820, doi:10.1016/j.mineng.2009.02.005.

[Cleary et al., 2003] Cleary, P. W., Morrisson, R. D., & Morrell, S. (2003). **Comparison of DEM and experiment for a scale model SAG mill**. *International Journal of Mineral Processing*, 68(1–4), 129 – 165, doi:10.1016/S0301-7516(02)00065-0. http://www.sciencedirect.com/science/article/pii/S0301751602000650.

[Cleary et al., 2009] Cleary, P. W., Owen, P., Hoyer, D. I., & Marshall, S. (2009). **Prediction of mill liner shape evolution and changing operational performance during the liner life cycle: Case study of a Hicom mill**. *International Journal for Numerical Methods in Engineering*, 81, 1157 – 1179, doi:10.1002/nme.2721.

[Cleary & Sawley, 1999] Cleary, P. W. & Sawley, M. L. (1999). **Three-dimensional modelling of industrial flows**. *Second International Conference on CFD in the Minerals and Proces Industries*.

[Cleary & Sawley, 2002] Cleary, P. W. & Sawley, M. L. (2002). **DEM modelling of industrial granular flows: 3D case studies and the effect of particle shape on hopper discharge**. *Applied Mathematical Modelling*, 26(2), 89 – 111, doi:10.1016/S0307-904X(01)00050-6. http://www.sciencedirect.com/science/article/pii/S0307904X01000506.

[Cleary et al., 2008] Cleary, P. W., Sinnott, M. D., & Morrison, R. D. (2008). **DEM predicition of praticle flows in grinding processes**. *International Journal for Numerical Methods in Fluids*, 58(1), 319–353, doi:10.1002/fld.1728.

[Cundall, 1971] Cundall, P. A. (1971). **A computer model for simulating progressive large scale movement in blocky rock systems**. *Proceedings Symp. Intl. Society of Rock Mechanics*, 1, Paper II–8.

[Cundall & Strack, 1979] Cundall, P. A. & Strack, O. D. L. (1979). **A discrete numerical model for granular assemblies**. *Géotechnique*, 29(1), 47–65.

[Datta et al., 1999] Datta, A., Mishra, B. K., & Rajamani, R. K. (1999). **Analysis of power draw in ball mills by the discrete element method**. *Canadian Metallurgical Quarterly*, 38(2), 133 – 140, doi:10.1016/S0008-4433(98)00039-1. http://www.sciencedirect.com/science/article/pii/S0008443398000391.

[Djordjevic, 2005] Djordjevic, N. (2005). **Influence of charge size distribution on net-power draw of tumbling mill based on DEM modelling**. *Minerals Engineering*, 18(3),

375 – 378, doi:10.1016/j.mineng.2004.06.001. http://www.sciencedirect.com/science/article/pii/S0892687504001414.

[Djordjevic et al., 2004] Djordjevic, N., Shi, F. N., & Morrison, R. (2004). **Determination of lifter design, speed and filling effects in AG mills by 3D DEM**. *Minerals Engineering*, 17(11-12), 1135 – 1142, doi:10.1016/j.mineng.2004.06.033. http://www.sciencedirect.com/science/article/pii/S0892687504002067.

[Dong & Moys, 2002] Dong, H. & Moys, M. H. (2002). **Assessment of discrete element method for one ball bouncing in a grinding mill**. *International Journal of Mineral Processing*, 65(3–4), 213 – 226, doi:10.1016/S0301-7516(01)00083-7. http://www.sciencedirect.com/science/article/pii/S0301751601000837.

[Edelsbrunner et al., 1983] Edelsbrunner, H., Kirkpatrick, D. G., & Seidel, R. (1983). **On the shape of a set of points in the plane**. *Information Theory, IEEE Transactions*, 29(4), 551–559, doi:10.1109/TIT.1983.1056714. http://ieeexplore.ieee.org/xpl/articleDetails.jsp?arnumber=1056714.

[Feng & Owen, 2004] Feng, Y. T. & Owen, D. R. J. (2004). **A 2D polygon/polygon contact model: algorithmic aspects**. *Engineering Computations*, 21(2/3/4), 265 – 277, doi:10.1108/02644400410519785.

[Finnie, 1972] Finnie, I. (1972). **Some observations on the erosion of ductile metals**. *Wear*, 19(1), 81 – 90, doi:10.1016/0043-1648(72)90444-9. http://www.sciencedirect.com/science/article/pii/0043164872904449.

[Finnie et al., 1992] Finnie, I., Stevick, G. R., & Ridgely, J. R. (1992). **The influence of impingement angle on the erosion of ductile metals by angular abrasive particles**. *Wear*, 152(1), 91 – 98, doi:10.1016/0043-1648(92)90206-N. http://www.sciencedirect.com/science/article/pii/004316489290206N.

[FLSmidth, 2015] FLSmidth (2015). http://www.flsmidth.com.

[Franke et al., 2015] Franke, J., Cleary, P. W., & Sinnott, M. D. (2015). **How to account for operating condition variability when predicting liner operating life with DEM – A case study**. *Minerals Engineering*, 73(0), 53 – 68, doi:10.1016/j.mineng.2014.11.009. http://www.sciencedirect.com/science/article/pii/S0892687514003756.

[Glover & De Beer, 1997] Glover, G. & De Beer, J. C. K. (1997). **The application of the discrete element method to the optimization of mill liner systems**. *Proceedings of the XX International Mineral Processing Congress*, (pp. 219–228).

[Govender, 2005] Govender, I. (2005). **X-ray motion analysis of charge particles in a laboratory mill**. PhD thesis, University of Cape Town, Cape Town.

[Herbst & Nordell, 2001] Herbst, J. A. & Nordell, L. (2001). **Optimization of the Design of SAG Mill Internals Using High Fidelity Simulation**.

[Jin et al., 2005] Jin, S., Lewis, R. R., & West, D. (2005). **A comparison of algorithms for vertex normal computation**. *The Visual Computer*, 21(1-2), 71–82, doi:10.1007/s00371-004-0271-1. http://dx.doi.org/10.1007/s00371-004-0271-1.

[Kalala, 2008] Kalala, J. T. (2008). **Discrete element method modelling of forces and wear on mill lifters in dry ball milling**. PhD thesis, University of the Witwatersrand, Johannesburg. http://wiredspace.wits.ac.za/bitstream/handle/10539/6031/Johnny%20Kalala%20PhD%20_20Sept2008.pdf?sequence=1.

[Kalala et al., 2008] Kalala, J. T., Breetzke, M., & H., M. M. (2008). **Study of the influence of liner wear on the load behaviour of an industrial dry tumbling mill using the Discrete Element Method (DEM)**. *International Journal of Mineral Processing*, 86(1–4), 33 – 39, doi:10.1016/j.minpro.2007.10.001. http://www.sciencedirect.com/science/article/pii/S0301751607002190.

[Kalala et al., 2005a] Kalala, J. T., Bwalya, M. M., & Moys, M. H. (2005a). **Discrete element method (DEM) modelling of evolving mill liner profiles due to wear. Part I: DEM validation**. *Minerals Engineering*, 18(15), 1386 – 1391, doi:10.1016/j.mineng.2005.02.009. http://www.sciencedirect.com/science/article/pii/S0892687505000919.

[Kalala et al., 2005b] Kalala, J. T., Bwalya, M. M., & Moys, M. H. (2005b). **Discrete element method (DEM) modelling of evolving mill liner profiles due to wear. Part II. Industrial case study**. *Minerals Engineering*, 18(15), 1392 – 1397, doi:10.1016/j.mineng.2005.02.010. http://www.sciencedirect.com/science/article/pii/S0892687505000920.

[Kalala & Moys, 2004] Kalala, J. T. & Moys, M. H. (2004). **Discrete element method modelling of liner wear in dry ball milling**. *Journal of the South African Institute of Mining and Metallurgy*, 104(10), 597 – 602. http://www.saimm.co.za/Journal/v104n10p597.pdf.

[Kawatra, 2006] Kawatra, S. K. (2006). **Advances in comminution**. Littleton, Colorado, USA: Society for Mining, Metallurgy, and Exploration, Inc.

[Khanal & Morrison, 2008] Khanal, M. & Morrison, R. (2008). **Discrete element method study of abrasion**. *Minerals Engineering*, 21(11), 751 – 760, doi:10.1016/j.mineng.2008.06.008. http://www.sciencedirect.com/science/article/pii/S0892687508001684.

[Kozicki & Donzé, 2009] Kozicki, J. & Donzé, F. V. (2009). **YADE-OPEN DEM: an open-source software using a discrete element method to simulate granular material**. *Engineering Computations*, 26(7), 786 – 805, doi:10.1108/02644400910985170. http://www.emeraldinsight.com/doi/abs/10.1108/02644400910985170.

[Longding, 2015] Longding (2015). http://www.made-in-ld.com.

[Magotteaux S.A., 2015] Magotteaux S.A. (2015). http://www.magotteaux.com.

[Makokha et al., 2007] Makokha, A. B., Moys, M. H., Bwalya, M. M., & Kimera, K. (2007). **A new approach to optimising the life and performance of worn liners in ball mills: Experimental study and DEM simulation**. *International Journal of Mineral Processing*, 84(1–4), 221 – 227, doi:10.1016/j.minpro.2006.09.009. Special Issue To Honor The Late Professor R. Peter King. http://www.sciencedirect.com/science/article/pii/S0301751606002158.

[McBride & Powell, 2006] McBride, A. T. & Powell, M. S. (2006). **A structured approach to modelling SAG mill liner wear – numerical modelling of liner evolution**. *International autogenous and semi autogenous grinding technology*, 3, 120 – 132. http://www.infomine.com/library/publications/docs/McBride2006.pdf.

[Meng & Ludema, 1995] Meng, H. C. & Ludema, K. C. (1995). **Wear models and predictive equations: their form and content**. *Wear*, 181-183, 443 – 457, doi:10.1016/0043-1648(95)90158-2. http://www.sciencedirect.com/science/article/pii/0043164895901582.

[Šmilauer et al., 2014] Šmilauer, V., et al. (2014). **Yade Documentation**. The Yade Project, release 2014-08-08.git-b1621bc edition. http://yade-dem.org/doc/.

[Mishra, 2003a] Mishra, B. K. (2003a). **A review of computer simulation of tumbling mills by the discrete element method: Part I — contact mechanics**. *International Journal of Mineral Processing*, 71(1–4), 73 – 93, doi:10.1016/S0301-7516(03)00032-2. http://www.sciencedirect.com/science/article/pii/S0301751603000322.

[Mishra, 2003b] Mishra, B. K. (2003b). **A review of computer simulation of tumbling mills by the discrete element method: Part II — Practical applications**. *International Journal of Mineral Processing*, 71(1–4), 95 – 112, doi:10.1016/S0301-7516(03)00031-0. http://www.sciencedirect.com/science/article/pii/S0301751603000310.

[Mishra & Rajamani, 1992] Mishra, B. K. & Rajamani, R. K. (1992). **The discrete element method for the simulation of ball mills**. *Applied Mathematical Modelling*, 16(11), 598 – 604, doi:10.1016/0307-904X(92)90035-2. http://www.sciencedirect.com/science/article/pii/0307904X92900352.

[Morrison & Cleary, 2004] Morrison, R. D. & Cleary, P. W. (2004). **Using DEM to model ore breakage within a pilot scale SAG mill**. *Minerals Engineering*, 17(11–12), 1117 – 1124, doi:10.1016/j.mineng.2004.06.016. http://www.sciencedirect.com/science/article/pii/S0892687504001815.

[Morrison & Cleary, 2008] Morrison, R. D. & Cleary, P. W. (2008). **Towards a virtual comminution machine**. *Minerals Engineering*, 21(11), 770 – 781, doi:10.1016/j.mineng.2008.06.005. http://www.sciencedirect.com/science/article/pii/S0892687508001623.

[Moys et al., 2000] Moys, M. H., Van Nierop, M. A., Van Tonder, J. C., & Glover, G. (2000). **Validation of the discrete element method (DEM) by comparing predicted load behaviour of a grinding mill with measured data**. In P. Massacci (Ed.), **Oral Session Proceedings of the XXI International Mineral Processing Congress**, volume 13 of *Developments in Mineral Processing* (pp. C3–39 – C3–44). Elsevier. http://www.sciencedirect.com/science/article/pii/S0167452800800149.

[Munjiza, 2005] Munjiza, A. A. (2005). **The combined finite-discrete element method**. England: John Wiley & Sons, Ltd, first edition.

[O'Sullivan & Bray, 2004] O'Sullivan, C. & Bray, J. D. (2004). **Selecting a suitable time step for discrete element simulations that use the central difference time integration scheme**. *Engineering Computations*, 21(2-4), 278 – 303, doi:10.1108/02644400410519794. http://www.emeraldinsight.com/doi/abs/10.1108/02644400410519794.

[Pournin et al., 2001] Pournin, L., Liebling, T. M., & Mocellin, A. (2001). **Molecular-dynamics force models for better control of energy dissipation in numerical simulations of dense granular media**. *Phys. Rev. E*, 65(1), 278 – 303, doi:10.1103/PhysRevE.65.011302. http://lipn.univ-paris13.fr/~pournin/PourninLieblingMocellinPRE65.pdf.

[Powell et al., 2008] Powell, M. S., Govender, I., & McBride, A. T. (2008). **Applying DEM outputs to the unified comminution model**. *Minerals Engineering*, 21(11), 744 – 750, doi:10.1016/j.mineng.2008.06.010. http://www.sciencedirect.com/science/article/pii/S0892687508001775.

[Powell & McBride, 2006] Powell, M. S. & McBride, A. T. (2006). **What is required from DEM simulations to model breakage in mills?** *Minerals Engineering*, 19(10), 1013 – 1021, doi:10.1016/j.mineng.2006.03.009. http://www.sciencedirect.com/science/article/pii/S0892687506000914.

[Powell & Morrison, 2007] Powell, M. S. & Morrison, R. D. (2007). **The future of comminution modelling**. *International Journal of Mineral Processing*, 84(1–4), 228 – 239, doi:10.1016/j.minpro.2006.08.003. Special Issue To Honor The Late Professor R. Peter King. http://www.sciencedirect.com/science/article/pii/S0301751606001888.

[Powell et al., 2006] Powell, M. S., Smit, I., Radziszewski, P., Cleary, P., Rattray, B., Eriksson, K., & Schaeffer, L. (2006). **The selection and design of mill liners**. In S. K. Kawatra (Ed.), **Advances in comminution** (pp. 331 – 376). Littleton, Colorado, USA: Society for Mining, Metallurgy, and Exploration, Inc.

[Powell et al., 2011] Powell, M. S., Weerasekara, N. S., Cole, S., LaRoche, R. D., & Favier, J. (2011). **DEM modelling of liner evolution and its influence on grinding rate in ball mills**. *Minerals Engineering*, 24(3–4), 341 – 351, doi:10.1016/j.mineng.2010.12.012. http://www.sciencedirect.com/science/article/pii/S0892687510003535.

[Prignon & Lepoint, 2001] Prignon, X. & Lepoint, F. (2001). **Perfecto and XLift Project**. Laboratoire Slegten: Magotteaux s.a.

[Qiu et al., 2001] Qiu, X., Potapov, A., Song, M., & Nordell, L. (2001). **Predictions of wear and mill lifters using discrete element method**.

[Rabinowicz, 1995] Rabinowicz, E. (1995). **Friction and wear of materials**. Canada: John Wiley & Sons, Inc., second edition.

[Radziszewski, 1997] Radziszewski, P. (1997). **Predictive model for ball mill wear**. *Canadian Metallurgical Quarterly*, 36(2), 87 – 93, doi:10.1016/S0008-4433(96)00045-6. http://www.sciencedirect.com/science/article/pii/S0008443396000456.

[Radziszewski, 1999] Radziszewski, P. (1999). **Comparing three DEM charge motion models**. *Minerals Engineering*, 12(12), 1501 – 1520, doi:10.1016/S0892-6875(99)00137-5. http://www.sciencedirect.com/science/article/pii/S0892687599001375.

[Radziszewski & Morrell, 1998] Radziszewski, P. & Morrell, S. (1998). **Fundamental discrete element charge motion model validation**. *Minerals Engineering*, 11(12), 1161 – 1178, doi:10.1016/S0892-6875(98)00103-4. http://www.sciencedirect.com/science/article/pii/S0892687598001034.

[Radziszewski & Tarasiewicz, 1993a] Radziszewski, P. & Tarasiewicz, S. (1993a). **Modelling and simulation of ball mill wear**. *Wear*, 160(2), 309 – 316, doi:10.1016/0043-1648(93)90435-O. http://www.sciencedirect.com/science/article/pii/004316489390435O.

[Radziszewski & Tarasiewicz, 1993b] Radziszewski, P. & Tarasiewicz, S. (1993b). **Simulation of ball charge and liner wear**. *Wear*, 169(1), 77 – 85, doi:10.1016/0043-1648(93)90393-Z. http://www.sciencedirect.com/science/article/pii/004316489390393Z.

[Radziszewski et al., 2005] Radziszewski, P., Varadi, R., Chenje, T., Santella, L., & Sciannamblo, A. (2005). **Tumbling mill steel media abrasion wear test development**. *Minerals Engineering*, 18(3), 333 – 341, doi:10.1016/j.mineng.2004.06.006. http://www.sciencedirect.com/science/article/pii/S0892687504001475.

[Rajamani et al., 2000a] Rajamani, R. K., Mishra, B. K., Venugopal, R., & Datta, A. (2000a). **Discrete element analysis of tumbling mills**. *Powder Technology*, 109(1–3), 105 – 112, doi:10.1016/S0032-5910(99)00230-2. http://www.sciencedirect.com/science/article/pii/S0032591099002302.

[Rajamani et al., 2014] Rajamani, R. K., Rashidi, S., & Dhawan, N. (2014). **Advances in discrete element method application to grinding mills**. *Mineral Processing and Extractive Metallurgy*, (pp. 117 – 128). http://content.lib.utah.edu/cdm/ref/collection/uspace/id/10649.

[Rajamani et al., 2000b] Rajamani, R. K., Songfack, P., & Mishra, B. K. (2000b). **Impact energy spectra of tumbling mills**. *Powder Technology*, 108(2–3), 116 – 121, doi:10.1016/S0032-5910(99)00208-9. http://www.sciencedirect.com/science/article/pii/S0032591099002089.

[Rezaeizadeh et al., 2010a] Rezaeizadeh, M., Fooladi, M., Powell, M. S., Mansouri, S. H., & Weerasekara, N. S. (2010a). **A new predictive model of lifter bar wear in mills**. *Minerals Engineering*, 23(15), 1174 – 1181, doi:10.1016/j.mineng.2010.07.016. http://www.sciencedirect.com/science/article/pii/S0892687510001974.

[Rezaeizadeh et al., 2010b] Rezaeizadeh, M., Fooladi, M., Powell, M. S., & Weerasekara, N. S. (2010b). **An experimental investigation of the effects of operating parameters on the wear of lifters in tumbling mills**. *Minerals Engineering*, 23(7), 558 – 562, doi:10.1016/j.mineng.2009.12.010. http://www.sciencedirect.com/science/article/pii/S0892687509003070.

[Sawley, 2003] Sawley, M. L. (2003). **Numerical simulation of a ball mill using DEM. Report on a preliminary validation study in collaboration with Magotteaux-Slegten**. *Report TR-01-03*.

[Sawley, 2006] Sawley, M. L. (2006). **Study of non-spherical particles in a ball mill**. *Report MA-01-06*.

[Sawley, 2008] Sawley, M. L. (2008). **Influence on axial ball motion of the internal geometry of a SAG mill**. *Report MA-07-01*.

[Sawley, 2014] Sawley, M. L. (2014). **Liner wear in a ball mill. Literature survey of wear models**. *Report TR-14-01*.

[Sheldon & Kanhere, 1972] Sheldon, G. L. & Kanhere, A. (1972). **An investigation of impingement erosion using single particles**. *Wear*, 21(1), 195 – 209, doi:10.1016/0043-1648(72)90257-8. http://www.sciencedirect.com/science/article/pii/0043164872902578.

[Thornton et al., 2013] Thornton, C., Cummins, S. J., & Cleary, P. W. (2013). **An investigation of the comparative behaviour of alternative contact force models during inelastic collisions**. *Powder Technology*, 233(0), 30 – 46, doi:10.1016/j.powtec.2012.08.012. http://www.sciencedirect.com/science/article/pii/S0032591012005670.

[Timoshenko & Goodier, 1951] Timoshenko, S. & Goodier, J. N. (1951). **Theory of elasticity**. McGraw-Hill.

[Van Nierop et al., 2001] Van Nierop, M. A., Glover, G., Hinde, A. L., & Moys, M. H. (2001). **A discrete element method investigation of the charge motion and power draw of an experimental two-dimensional mill**. *International Journal of Mineral Processing*, 61(2), 77–92, doi:10.1016/S0301-7516(00)00028-4. http://www.sciencedirect.com/science/article/pii/S0301751600000284.

[Wahba, 1990] Wahba, G. (1990). **Spline models for observational data**. Philadelphia, Pennsylvania, USA: Society for industrial and applied mathematics.

[Weerasekara et al., 2013] Weerasekara, N. S., et al. (2013). **The contribution of DEM to the science of comminution**. *Powder Technology*, 248(0), 3 – 24, doi:10.1016/j.powtec.2013.05.032. http://www.sciencedirect.com/science/article/pii/S0032591013003902.

[Wellinger & Breckel, 1969] Wellinger, K. & Breckel, H. (1969). **Kenngrössen und Verschleiss beim Stoss metallischer Werkstoffe**. *Wear*, 13(4–5), 257 – 281, doi:10.1016/0043-1648(69)90249-X. http://www.sciencedirect.com/science/article/pii/004316486990249X.

[Wikipedia, 2015] Wikipedia (2015). **Cement mill**. http://en.wikipedia.org/wiki/File:LDFMBallMill.jpg.

[Wills & Napier-Munn, 2005] Wills, B. & Napier-Munn, T. J. (2005). **Wills' mineral processing technology**. Oxford: Butterworth-Heinemann, seventh edition. http://www.sciencedirect.com/science/book/9780750644501.

[Zehnder, 2012] Zehnder, A. T. (2012). **Fracture Mechanics**. Netherlands: Springer, first edition.